ON MEDICAL IMAGE PROCESSING, ANALYSIS, RETRIEVAL AND SECURITY MANAGEMENT

Thesis submitted for the degree of
Doctor of Philosophy (Technology)
in
Computer Science and Engineering

by

SUDEB DAS

Department of Computer Science and Engineering
University of Calcutta

2014

To my family.

Acknowledgments

I express my sincere thanks to my supervisor Prof. Malay Kumar Kundu who introduced me to the world of images, visions and patterns. With a deep sense of gratitude, I remain obliged for his unconditional support and guidance during the course of my research works. I greatly acknowledge his valuable conceptual suggestions during the research works. Prof. Kundu gave me the freedom to explore a variety of topics. Whenever I struggled, his generous support always came at just the right time. It is my privilege to work under the supervision of a person like him of profound knowledge and humble personality.

I want to thank the professors of the Machine Intelligence Unit – Prof. S. K. Pal, Prof. S. Mitra and Prof. A. Ghosh for their constructive suggestions and comments. Also my thanks go to Dr. D. P. Mandal, Prof. R. K. De, Dr. S. N. Biswas, Prof. S. Bandopadhyay, Dr. B. U. Shankar and Dr. K. Ghosh. I am also thankful to Prof. C. A. Murthy and Dr. P. Maji for helping me in my research work by providing fruitful academic suggestions.

I would never forget the company I had from my fellow researchers M. Chowdhury, Dr. B. N. Subudhi, K. R. Murthy, Dr. R. Das, Dr. M. Das, T. Basu, P. P. Kundu, A. Mondal, A. Gorai, R. Roy, A. Banerjee, C. Parmer, A. Bakshi, J. Modal, D. Karmakar and friends. Special note of thanks goes to late Mr. J. Gupta, Mr. B. Sharma, Mr. I. Dutta, Dr. S. Choudhury, Mrs. M. De, Mr. S. Das, Mrs. N. Das, Mr. S. Das, Mr. B. Porel, Mr. S. R. Pyne and Mr. J. K. Kahal for providing me all kinds of facility whenever needed. My vote of thanks goes to the Machine Intelligence Unit, Indian Statistical Institute, Kolkata-108 for providing all facilities to perform the research works. I am also grateful to the members of the Ph.D. committee of the Department of Computer Science and Engineering, University of Calcutta. Special thanks goes to Dr. P. K. Das (MD) for subjectively evaluating the effectiveness of the solutions reported in this thesis (from a medical expert perspective) and providing useful suggestions.

I thank my parents and all elders in my family, who taught me the values of hard work and patience. I am also grateful to my wife and in-laws who provided continuous family support and valuable personal advices during my research period. I would like to share this moment of happiness with my twin daughters Debangshi and Ditipriya and all my family members and well-wishers.

.....

(Sudeb Das)

Abstract

Medical imaging is undoubtedly one of the most impacting technologies in modern society. In the last few decades, various domains of medical imaging paradigm have advanced remarkably. Despite all these advancements, there still exist several inherent problems that need to be solved. Finding effective solutions to these problems require significant advancements in various fields of medical image processing, analysis and management paradigm. The main objective of this thesis is to study and improve certain aspects of the medical image computing domain. Emphasis is given on developing various pre/post-processing enhancement schemes for diverse modalities of medical images. Specifically, the high computational cost of popular non-local means filtering scheme for magnetic resonance image is reduced without compromising the denoising performance. The advantages of non-local means and pulse coupled neural networks are combined to achieve this goal. To effectively integrate complementary information from multimodal medical images, medical image fusion schemes are proposed based on multiscale geometric analysis of non-subsampled contourlet transform and pulse coupled neural network. Importance has also been given to effective management and distribution issues of medical images. In this regard, novel classification and retrieval systems are proposed for diverse modalities of medical images based on various multiscale geometric analysis tools. Attempts have been made to represent the content of medical images through compact and robust feature vectors. This results in classification and retrieval systems which work efficiently even in the presence of common medical imaging artifacts. Various critical and ethical issues regarding medical images and related information like security, authenticity, integrity, confidentiality and non-repudiation are handled by novel medical image watermarking techniques. The proposed schemes exhibit high payload and imperceptibility characteristics. Extensive experiments and comparisons with state-of-the-art schemes are carried out to qualitatively as well as quantitatively evaluate the performance effectiveness of the proposed solutions. The above mentioned novel developments are suitable for inclusion as services in a comprehensive integrated medical imaging system.

Contents

1 Introduction **1**

1.1 The Medical Image Computing Paradigm 1

1.2 Background and Related Works 4

1.2.1 Medical Image Enhancement: MRI Denoising 5

1.2.2 Multimodal Medical Image Fusion 9

1.2.3 Medical Image Classification and Retrieval 11

1.2.4 Medical Image Watermarking 14

1.3 Theoretical Preliminaries 17

1.3.1 Multiscale Image Transforms 17

1.3.1.1 Contourlet Transform 19

1.3.1.2 Nonsubsampled Contourlet Transform 22

1.3.1.3 Type-I Ripplet Transform 24

1.3.2 Pulse Coupled Neural Network 27

1.3.3 Least Square-Support Vector Machine 30

1.3.4 Earth Mover's Distance 31

1.3.5 Image Quality and Quantitative Performance Measures 34

1.4 Scope and Contributions of the Thesis 41

1.4.1 Problem Definitions 42

1.4.2 Contributions 43

1.5 Organization of the Thesis 44

2 Medical Image Enhancement: MRI Denoising **47**

2.1 Introduction 47

2.2 Noise in MRI 48

2.3 NLM in MR Image Denoising 50
2.4 PCNN for Image Denoising 53
2.5 Proposed Method 55
2.6 Results and Discussion 56
2.6.1 Experimental Setup 57
2.6.2 Analysis and Discussion 58

3 Multimodal Medical Image Fusion 69

3.1 Introduction 69
3.2 *Scheme 1*: NSCT-based Multimodal MIF using PCNN and MSF . . 72
3.2.1 Modified Spatial Frequency 73
3.2.2 Proposed Method 74
3.2.2.1 Fusing Low Frequency Subbands 74
3.2.2.2 Fusing High Frequency Subbands 74
3.2.2.3 Algorithm 75
3.2.3 Results and Discussion 77
3.2.3.1 Experimental Setup 77
3.2.3.2 Subjective Analysis and Discussion 79
3.2.3.3 Objective Analysis and Discussion 81
3.3 *Scheme 2*: A Neuro-Fuzzy Approach for Medical Image Fusion . . . 84
3.3.1 Reduced Pulse Coupled Neural Network 85
3.3.2 Proposed Method 86
3.3.2.1 Fuzzy Adaptive Linking Strength 86
3.3.2.2 Algorithm 89
3.3.3 Results and Discussion 90
3.3.3.1 Experimental Setup 90
3.3.3.2 Subjective Analysis and Discussion 92

3.3.3.3 Objective Analysis and Discussion 94

4 Medical Image Classification and Retrieval 98

4.1 Introduction 98

4.2 Brain MR Image Classification 100

4.2.1 *Scheme 1*: Proposed Method 103

4.2.1.1 Feature Reduction 104

4.2.1.2 Offline Phase 105

4.2.1.3 Online Phase 105

4.2.2 *Scheme 2*: Proposed Improvement over '*Scheme 1*' 106

4.2.3 Results and Discussion 108

4.2.3.1 *Scheme 1*: Experimental Results and Comparisons 108

4.2.3.2 *Scheme 2*: Experimental Results and Comparisons 116

4.3 Content based Retrieval System for Medical Radiographs 119

4.3.1 Proposed Method 121

4.3.1.1 Image Signature Computation 121

4.3.1.2 Training by LS-SVM 122

4.3.1.3 Algorithm 123

4.3.2 Results and Discussion 124

5 Medical Image Watermarking 128

5.1 Introduction 128

5.2 *Scheme 1*: Spatial Domain MIW Technique 131

5.2.1 Proposed Method 132

5.2.1.1 Hash of Region of Interest 132

5.2.1.2 Dispersion of Watermark Bits 133

5.2.1.3 Tamper Localization 134

5.2.1.4 Watermark Generation and Insertion 137

5.2.1.5 Watermark Extraction and Verification 140
5.2.2 Results and Discussion 143
5.3 *Scheme 2*: Transform Domain MIW Technique 155
5.3.1 Proposed Method 156
5.3.1.1 Watermark Generation and Insertion 156
5.3.1.2 Watermark Extraction and Verification 160
5.3.2 Results and Discussion 162

6 Conclusion and Future Work **170**
6.1 Contributions 170
6.2 Future Work 174

Bibliography **177**

Author's Publications **228**

List of Abbreviations

ADF : Anisotropic Diffusion Filter
AES : Advanced Encryption Standard
ANN : Artificial Neural Network
AWGN : Additive White Gaussian Noise
BCH : Bose-Chaudhuri-Hocquengham
BER : Bit Error Rate
BIC : Binary Identification Code
BLM : Binary Location Map
CAD : Computer Aided Diagnosis
CBIR : Content Based Image Retrieval
CBMIR : Content Based Medical Image Retrieval
CBS : Content Based Search
CF : Column Frequency
CNT : Contourlet Transform
CT : Computed Tomography
CVT : Curvelet Transform
DCT : Discrete Cosine Transform
DE : Differential Evolution
DF : Directional Frequency
DFB : Directional Filter Bank
DFT : Discrete Fourier Transform
DIC : Doctor's Identification Code
DICOM : Digital Imaging and Communications in Medicine
DW : Diffusion-Weighted
DWM : Digital Watermarking
DWT : Discrete Wavelet Transform
EA : Evolutionary Algorithm
ECG : Electrocardiography
ECT : Emission Computed Tomography
EHR : Electronic Health Record
EMD : Earth Mover's Distance
EN : Entropy
fMRI : Functional Magnetic Resonance Imaging

FCM : Fuzzy C-Means
FDG : Fluorodeoxyglucose
FL : Fuzzy Logic
FLAIR : Fluid Attenuated Inversion Recovery
FN : False Negative
FP : False Positive
FP-ANN : Feed Forward Back-Propagation ANN
FT : Fourier Transform
GA : Genetic Algorithm
HFS : High Frequency Subband
HIS : Hospital Information System
HPS : High Pass Subband
HVS : Human Visual System
IDFT : Inverse Discrete Fourier Transform
IF : Image Fusion
IHS : Intensity-Hue-Saturation
INDX : Indexing Keywords
IRMA : Image Retrieval for Medical Applications
IUNLM : Improved Unbiased Non-Local Means
JPEG : Joint Photographic Experts Group
K-NN : K-Nearest Neighbor
LAE : Local Average Energy
LFS : Low Frequency Subband
LIE : Local Information Entropy
LP : Laplacian Pyramid
LPS : Low Pass Subband
LSB : Least Significant Bit
LS-SVM : Least Square-Support Vector Machine
m-PCNN : Multichannel-Pulse Coupled Neural Network
MGA : Multiscale Geometric Analysis
MI : Mutual Information
MIF : Medical Image Fusion
MIS : Medical Information System
MIW : Medical Image Watermarking
MR : Magnetic Resonance

MRA : Multiresolution Analysis
MRI : Magnetic Resonance Imaging
MSD : Multiscale Decomposition
MSE : Mean-Square-Error
MSF : Modified Spatial Frequency
MSSIM : Mean Structural Similarity Index
NC : Normalized Correlation
NEMA : National Electrical Manufactures Association
NFHF-CNT : Neuro Fuzzy Hybrid Fusion based on CNT
NFHF-CVT : Neuro Fuzzy Hybrid Fusion based on CVT
NFHF-NSCT : Neuro Fuzzy Hybrid Fusion based on NSCT
NLM : Non-Local Means
NSCT : Nonsubsampled Contourlet Transform
NSDFB : Non-subsampled Directional Filter Bank
NSFB : Non-subsampled Filter Bank
NSPFB : Non-subsampled Pyramid Filter Bank
NVF : Noise Visibility Function
PACS : Picture Achieving and Communication Systems
PCA : Principal Component Analysis
PCNN : Pulse Coupled Neural Network
PCNNNI : Pulse Coupled Neural Network with Null Interconnection
PCNNNI_IUNLM : PCNNNI Adaptive IUNLM
PDE : Partial Differential Equation
PDF : Probability Density Function
PDFB : Pyramidal Directional Filter Bank
PET : Positron Emission Tomography
POC : Point-of-Care
PSNR : Peak-Signal-to-Noise-Ratio
QFB : Quincunx Filter Bank
QILV : Quality Index based on Local Variance
QP : Quadratic Programming
RDM : Recursive Dither Modulation
RF : Row Frequency
RMSE : Root-Mean-Square-Error
ROE : Region-of-Embedding

ROI	: Region of Interest
RONI	: Region of Non-Interest
RPCNN	: Reduced Pulse Coupled Neural Network
RT	: Type-I Ripplet Transform
SBS	: Semantic Based Search
SF	: Spatial Frequency
SHA-256	: Secure Hash Algorithm-256
SNR	: Signal-to-Noise Ratio
SOM	: Self-Organizing Map
SPECT	: Single-Photon Emission Computed Tomography
STD	: Standard Deviation
SVD	: Singular Value Decomposition
TBS	: Text Based Search
TN	: True Negative
TP	: True Positive
TPE	: Total Perceptual Error
UNLM	: Unbiased Non-Local Means
USG	: Ultrasonography
WPSNR	: Weighted Peak-Signal-to-Noise-Ratio
WT	: Wavelet Transform

List of Figures

1.1 Different body structures: (a) The human body[1], (b) The glass frog[2]. 2
1.2 Modules of medical image computing paradigm. 4
1.3 Need of image fusion: (a) Source Image 1: T1-weighted MR; (b) Source Image 2: MR angiography; (c) Fused image. 9
1.4 Laplacian pyramid scheme: (a) Analysis and (b) Synthesis. 19
1.5 Construction of DBF. 21
1.6 Frequency partition of contourlet transform. 21
1.7 Contourlet transform of *Barbara* image. 22
1.8 NSCT (a) NSFB structure that implements the NSCT. (b) Frequency partitioning obtained with the proposed structure. 23
1.9 Structure of PCNN. 28
1.10 Organization of the thesis. 44

2.1 Block diagram of PCNNNI_IUNLM. 55
2.2 Sample MR images: original images (Row 1), noisy images with Rician noise level = 9% (Row 2) and denoised images (Row 3). MRI images: (a) Synthetic, (b) real 1, (c) real 2 and (d) real 3. . . . 59
2.3 Effect of the "*denoising parameter*" (t). 59
2.4 Synthetic image data T1-weighted MR image: (a) Noise-free image, (b) noisy image (noise level = 9%), (c) NLM-output [46], (d) UNLM-output [42], (e) PCNNNI_IUNLM output, (f) Time Matrix, (g) actual noise, (h) residual of NLM, (i) residual of UNLM, (j) residual of PCNNNI_IUNLM. 61
2.5 Real MR image 1: (a) Noise-free image, (b) noisy image (noise level = 9%), (c) NLM-output [46], (d) UNLM-output [42], (e) PCNNNI_IUNLM output, (f) Time Matrix, (g) actual noise, (h) residual of NLM, (i) residual of UNLM, (j) residual of PCNNNI_IUNLM. 62
2.6 Real MR image 2: (a) Noise-free image, (b) noisy image (noise level = 9%), (c) NLM-output [46], (d) UNLM-output [42], (e) PCNNNI_IUNLM output, (f) Time Matrix, (g) actual noise, (h) residual of NLM, (i) residual of UNLM, (j) residual of PCNNNI_IUNLM. 63

2.7 Real MR image 3: (a) Noise-free image, (b) noisy image (noise level = 9%), (c) NLM-output [46], (d) UNLM-output [42], (e) PCNNNI_IUNLM output, (f) Time Matrix, (g) actual noise, (h) residual of NLM, (i) residual of UNLM, (j) residual of PCNNNI_IUNLM. 63
2.8 Zoomed in portion of the real MR image 1: (a) noise free, (b) NLM [46], (c) UNLM [42], and (d) PCNNNI_IUNLM. 64
2.9 Performance comparison in terms of RMSE with different noise levels and image types: (a) synthetic MR image, (b) real MR image 1, (c) real MR image 2, (d) real MR image 3. 65
2.10 Performance comparison in terms of PSNR with different noise levels and image types: (a) synthetic MR image, (b) real MR image 1, (c) real MR image 2, (d) real MR image 3. 65
2.11 Performance comparison in terms of MSSIM with different noise levels and image types: (a) synthetic MR image, (b) real MR image 1, (c) real MR image 2, (d) real MR image 3. 66
2.12 Performance comparison in terms of QILV with different noise levels and image types: (a) synthetic MR image, (b) real MR image 1, (c) real MR image 2, (d) real MR image 3. 66
2.13 Performance comparison in terms of time requirement with different noise levels and image types: (a) synthetic MR image (143×181), (b) real MR image 1 (256×256), (c) real MR image 2 (256×256), (d) real MR image 3 (176×141). 67

3.1 Block diagram of the proposed '*Scheme–1*' MIF method. 76
3.2 Source images (top two rows) with fusion results of '*Scheme 1*' (last row): $x1$ = CT, $y1$ = MRI, $x2$ = T1-weighted MR, $y2$ = MR Angiography , $x3$ = CT, $y3$ = T1-weighted MR-GAD, $x4$ = T1-weighted MR, $y4$ = T2-weighted MR, $x5$ = CT, $y5$ = Proton Density (PD) weighted MR. 78
3.3 Fusion results of '*Scheme 1*' on image combinations $C1$ and $C5$: (a)(g) Method NSCT_PCNN_SF, (b)(h) Method of [361], (c)(i) Method of [114], (d)(j) Method of [124], (e)(k) Method of [127] and (f)(l) Method of [123]. 80
3.4 Block Diagram of the proposed '*Scheme–2*' MIF method. 89

3.5 Visual results for the five pairs (ak, bk) of source images, $(k = 1, 2, 3, 4, 5)$. Fused images obtained: $c1$-$c5$ by scheme [124], $d1$-$d5$ by scheme [114], $e1$-$e5$ by scheme [361], $f1$-$f5$ by scheme [127], $g1$-$g5$ by scheme [123], $h1$-$h5$ by NFHF-CNT, $i1$-$i5$ by NFHF-CVT, $j1$-$j5$ by '*Scheme 2*'. 91
3.6 Performance comparison of CNT, CVT and NSCT. Zoomed in versions of '*Group 1*' fused images of Fig. 3.5: (a) $h1$ for CNT, (b) $i1$ for CVT and (c) $j1$ for NSCT. 94
3.7 Objective performance comparisons of '*Scheme 2*. 96

4.1 Block diagram of '*Scheme 1*'. 104
4.2 Block diagram of '*Scheme 2*'. 107
4.3 Sample brain MR images used in the experiments of '*Scheme 1*': (a) normal, (b) glioma, (c) meningioma, (d) sarcoma, (e) Pick's disease, (f) Huntington's disease, (g) Alzheimer's disease, (h) Alzheimer's disease with visual agnosia, (i) chronic subdural hematoma, (j) cerebral toxoplasmosis, (k) herpes encephalitis, (l) multiple sclerosis. . . 110
4.4 Performance evaluation of '*Scheme 1*' in terms of sensitivity. 111
4.5 Performance evaluation of '*Scheme 1*' in terms of specificity. 112
4.6 Performance evaluation of '*Scheme 1*' in terms of classification accuracy. 113
4.7 ROC curves of performance evaluation of '*Scheme 1*': (a) Dataset-66 (b) Dataset-160 and (c) Dataset-255. 114
4.8 Sample brain MR images used in the experiments of '*Scheme 2*' (row 1) with corresponding rotated (row 2) and dynamic range (row 3) modified versions: (a) normal, (b) glioma, (c) meningioma, (d) sarcoma, (e) Pick's disease, (f) Huntington's disease, (g) Alzheimer's disease, (h) Alzheimer's disease with visual agnosia. 118
4.9 Performance comparison of '*Scheme 2*' with different wavelet combinations. 119
4.10 Performance comparison of '*Scheme 2*' with different MGA tools. . 120
4.11 Block diagram of the described CBMIR system. 123
4.12 Query-by-example experiments: Query images (left) and Retrieved images in decreasing order of similarity (right). 125
4.13 Average Precision vs Average Recall (frame size 5, 10, 15 and 20). . 126
4.14 Class-wise Average precision and Average Recall. 127

5.1 Manipulation of medical image. 129
5.2 Hash of the ROI using $SHA-256$. 132
5.3 Dispersion of the watermark bits for $k = 23$, $n = 100$ and $h = 50$. . 133
5.4 Embedding of the tamper localization information. 134
5.5 Tamper localization in case of no tampering. 135
5.6 Tamper localization in case of tampering (shaded pixels). 136
5.7 Watermark generation and insertion in '*Scheme 1*'. 138
5.8 Watermark extraction and verification in '*Scheme 1*'. 141
5.9 An example of EHR used in the experiment. 144
5.10 Sample medical images used in the experiments of '*Scheme 1*': (a) original images, (b) watermarked images, (c) watermark extracted images. 146
5.11 Performance of '*Scheme 1*' in terms of watermark capacity versus ROI size (% original image pixels). 147
5.12 Tamper localization capability of '*Scheme 1*': (a) original watermarked image, (b) tampered watermarked image, (c) tampered region. 151
5.13 Watermark generation and insertion in '*Scheme 2*'. 157
5.14 Watermark extraction and verification in '*Scheme 2*'. 161
5.15 Original images (above ((a1)-(e1)) and their corresponding watermarked images produced by '*Scheme 2*' (below ((a2)-(e2)). 164
5.16 Watermarking strength factor (α) vs PSNR (dB). 167
5.17 Watermarking strength factor (α) vs JPEG Quality Factor. 167

List of Tables

3.1 Performance evaluation of '*Scheme 1*' MIF method 82
3.2 Performance comparison of '*Scheme 1*' using image combinations $C1$ and $C5$ 83
3.3 Performance evaluation of '*Scheme 2*' MIF method 94

4.1 Setting of one pass of 6-fold stratified CV for Dataset-66. 111
4.2 Setting of one pass of 5-fold stratified CV for Dataset-160. 111
4.3 Setting of one pass of 5-fold stratified CV for Dataset-255. 112
4.4 Performance comparison of '*Scheme 1*' using the three datasets. . . 115

5.1 Performance evaluation of '*Scheme 1*' 145
5.2 Performance of '*Scheme 1*' for DICOM images. 149
5.3 Performance comparison of '*Scheme 1*' 153
5.4 Performance of '*Scheme 2*' when no ROI is specified 165
5.5 Performance of '*Scheme 2*' when ROI is specified 165
5.6 Attacks where '*Scheme 2*' successfully extracted the watermark . . 168

Chapter 1

Introduction

"*The 19th century poet Emily Dickinson was reclusive to the point that she would allow a doctor to examine her only from a distance of several feet as she walked past an open door. If she were alive today, it's likely that she would benefit from advances in medical imaging that could accommodate her standoffishness while still diagnosing the Bright's disease that ended her life at age 55.*" [1].

1.1 The Medical Image Computing Paradigm

Medical science – is one of the most important fields of natural science. It is the quest for understanding the structures and functions of the human body under all conditions of health, illness and injury [2]. This quest results in various models of human health which are immensely helpful in detecting and diagnosing illness and abnormalities, preventing diseases and disabilities, and designing therapies/treatments to alleviate the pain and suffering of the patients. Advancement toward these objectives has been so remarkable that nowadays, the average life span of humans in developed countries is almost twice its expected value a century ago [2, 3].

The human body as shown by the schematic image in Fig. 1.1(a), is an incredibly complex system. In this regard, the major challenges to clinicians as well as researchers are the questions: how to acquire, process and display the massive amount of data regarding the static and dynamic properties of this human body.

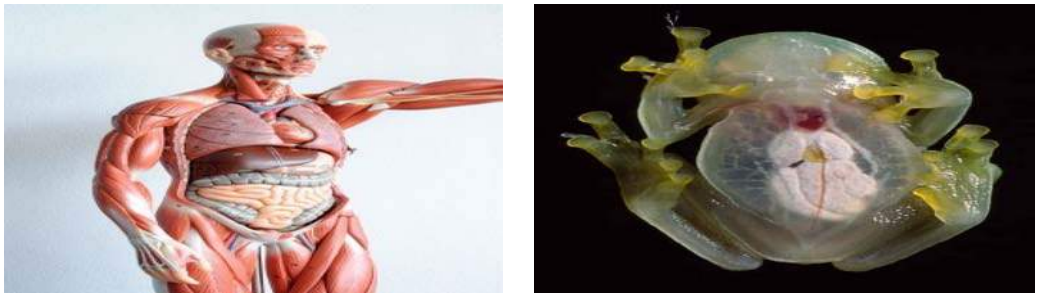

(a) (b)

Figure 1.1: Different body structures: (a) The human body[1], (b) The glass frog[2].

Effective *acquisition*, *processing* and *visualization* of this data is extremely necessary, since this results in information that can be assimilated, interpreted and utilized in an efficient way to yield more useful diagnostic methods and treatment procedures [4]. Most of the times, the presentation of information as an '*image*' is the most efficient approach to address these challenges [5, 6].

Unlike the '*Glass Frog*', shown in Fig. 1.1(b), we cannot see through our skin to look at our organs. The skin that covers our bodies and protects our organs makes it difficult for doctors to see what is going on inside our bodies. Medical image computing tools allow doctors to see inside the human body in a non-invasive manner, so that they can diagnose and treat diseases. Different modalities (e.g. X-ray, Emission Computed Tomography (ECT), Positron Emission Tomography (PET), Single-Photon Emission Computed Tomography (SPECT), Magnetic Resonance Imaging (MRI), Ultrasonography (USG) and Computed Tomography (CT) etc.) of medical images reveal various characteristics of the human body. Some of these important characteristics are transmissivity, opacity, emissivity, reflectivity, conductivity, magnetizability etc. and changes in these characteristics with time [3, 4].

[1]Courtesy by Thitiya Mangprayool (downloaded from `http://www.123rf.com/photo_13930940_human-anatomy.html`)

[2]Courtesy by Steffen Reichle–The Nature Conservancy (downloaded from `http://www.nature.org/cs/groups/webcontent/@web/@bolivia/documents/media/prd_021484.jpg`)

This information is essential for improving human health through detection and diagnosis of illness and injury [2–4, 7].

Since the discovery of X-rays by Wilhelm Conrad Rontgen in 1895, the continuous and remarkable development as well as advancement of existing and new image acquisition techniques provide different and much more important views of the anatomical, functional and molecular properties of a human body [2–4, 8]. In the medical image computing paradigm, the main issue in the early years of research and development was regarding the storage and transfer of images due to limited computing capacity. The speed of pixel manipulation algorithms was an essential challenge [9–11]. At present, a method-driven modeling approach dominates and algorithms are developed on a methodological level in order to support diagnostic decisions or intervention planning. The characteristics of radiological work has gone through significant change: from the subjective interpretation of images towards diagnosis based on objective quantitative image parameters [11]. What is perhaps most remarkable about these advances is the fact that this required significant innovations in nearly all aspects of image processing, analysis and management domains [4, 7]. The development of image computing and analysis systems for diagnostic support, operation planning and computer-aided surgery is a complex interdisciplinary process. Therefore, a multidisciplinary culture of research, including clinical practice, medical and biomedical research, image acquisition and image computing is needed [11]. Moreover, in an application-oriented integrative approach, advanced image processing, analysis and management methods have to be developed so that image-based medical diagnostics and patient treatment can be improved in the future.

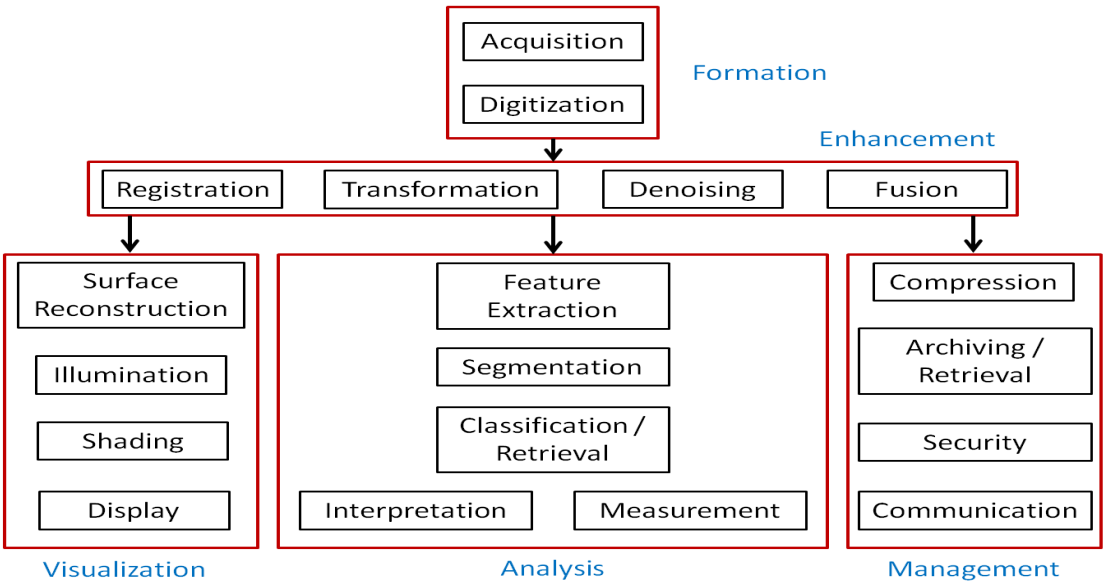

Figure 1.2: Modules of medical image computing paradigm.

1.2 Background and Related Works

The commonly used term '*medical image computing*' means the utilization of digital image processing and analysis techniques for medical images used in diagnosis and treatment. In general, medical image computing paradigm covers the following five major domains as shown in Fig. 1.2 [12]. The first major domain namely *image formation*, includes all the steps from capturing the image to forming a digital image matrix. Generally, the output images obtained by different image formation schemes are of sub-optimal quality and not readily suitable for further use. In most cases, these images are undergone through some form of *image enhancement*. This refers to all types of manipulation of the obtained images, resulting in optimized and improved output images. The domain of *image visualization* indicates realistic visualization of the image data specifically in 2D, 3D and 4D format. The *image analysis* domain encompasses diverse sorts of techniques which are used for quantitative measurements and abstract interpretations of biomedical images. The last domain namely *image management*, sums up all

schemes that provide efficient and secure storage, communication, archiving, and access of medical images. Even though, in the last few decades, every aspect of the above mentioned domains of medical image computing paradigm has advanced significantly, but we still require substantial research activities for not only improving the existing schemes, but also to develop novel and intelligent techniques for known and hitherto unknown/unsolved problems.

Among the various domains of medical imaging paradigm described in Fig. 1.2, the present thesis contains some possible solutions to problems of four different sub-domains namely – MRI denoising, multimodal medical image fusion, classification/retrieval of medical images, effective and ethical management of digital medical images and related information through digital image watermarking techniques. The following section contains a brief review of some of the existing works related to these sub-domains.

1.2.1 Medical Image Enhancement: MRI Denoising

Generally, due to various sources of interference and other physical phenomena that affect the underlying measurement processes in imaging and data acquisition systems, medical images get deteriorated by different types of artifacts [3, 13]. Some of the main artifacts in medical images are different types of noise (Rician in MRI, Speckle in USG and Poisson in SPECT etc.), limited contrast, motion artifacts and bias field etc. These artifacts limit the visual quality of the medical images. As a result, it becomes difficult for medical experts to analyze and interpret comprehensive and accurate information from the underlying medical images. Moreover, these artifacts also cause problems in subsequent high level image processing and analysis tasks. For example, the small differences that may exist between normal and abnormal tissues in a mammogram are confounded by

noise and other artifacts, often making it difficult to directly analyze and interpret the acquired images. Therefore, it is of paramount importance to improve the appearance and visual quality of the medical images by some image enhancement techniques [14–18].

In recent years, among the different modalities of medical images, MRI has gained popularity in diagnosis and treatment planning [19,20]. Over the years MRI technology has advanced significantly to be more cost-effective, providing improved spatio-temporal resolution as well as reducing the acquisition time. However, the quest of any of these objectives results in images with low signal-to-noise ratio (SNR) and exhibits significant artifacts (e.g, noise, partial voluming, background inhomogeneity and bias field etc.) which are undesirable [21, 22]. These artifacts limit the accuracy of computer-aided diagnosis (CAD), clinical visual inspection and performance of subsequent high level post-processing procedures (e.g. segmentation, registration, tracking etc.). Therefore, pre/post-acquisition enhancement steps are essential for reducing these artifacts in MR images [19, 23–25].

MR images contain varying amounts of noise of diverse origins: noise from stochastic variation, numerous physiological processes, eddy currents, artifacts from the magnetic susceptibilities between neighboring tissues, rigid body motion, non-rigid motion, thermal noises from the patient and electronic noises from the MRI device [14, 15]. One of the main noise component in MRI is due to thermal noise of the scanned object [19, 25, 26]. The variance of thermal noise can be described as the sum of noise variances from independent stochastic processes representing the body, the coil and the electronics [25, 27]. The inverse discrete Fourier transform (IDFT) of the raw magnetic resonance (MR) data is normally used to construct the image in a single channel signal acquisition system. The signal component of the acquired measurement exists in both real and imaginary channels. Both of these orthogonal channels are affected by additive white Gaus-

sian noise (AWGN) [28]. Generally, the magnitude of the reconstructed MR image is utilized for visual inspection and subsequent computer aided analysis. In [29], it was shown that as the magnitude of the MRI signal is the square root of the sum of the squares of two independent Gaussian variables, it follows Rician distribution. In multichannel MRI the MR image is reconstructed by combining complex images and the noise distribution can be described by non-central Chi distribution. Based on the reconstruction mechanism, the noise amplitude varies according to the spatial location of the image and can follow Rician or Chi distribution in case of parallel imaging [30].

Over the years, many approaches have been proposed to address the difficult problem of MR image denoising. Generally, these existing schemes can be grouped into three different categories: filtering approach, transform domain approach and statistical approach [25]. In filtering approach, various linear and non-linear filters are used to denoise the MR images. Some of the remarkable techniques of this category are: spatial and temporal filtering, anisotropic diffusion filtering, combination of domain and range filtering and non-local means filtering etc. In [14], McVeigh et al. have proposed the spatial and temporal filter for reducing the Gaussian noise in MR images. This filtering scheme suffers from various problems: edge blurring, loss of spatial resolution and aliasing artifacts etc. To overcome these problems, Perona et al. have developed a multiscale smoothing and edge detection scheme called the anisotropic diffusion filter (ADF) [31]. ADF significantly improves the image quality by preserving object boundaries. ADF and its variants have been successfully applied to denoise MR images by various researchers [32–35]. As a non-iterative alternative to ADF, the bilateral filter was proposed by Tomasi et al. [36]. This filter is a combination of two Gaussian filters: domain and range filters. It does not involve the solution of partial differential equation (PDE) and can be implemented in single iteration. This filtering technique is applied for MRI

denoising by Walker et al. [37] and Xie et al. [38]. Wong et al. have proposed the trilateral filtering scheme for reducing noise in medical images [39, 40]. This filtering technique uses the local structural similarity along with the geometric and photometric similarities of bilateral filter. Recently, the popular non-local means (NLM) filter for denoising natural images has come up as an effective scheme for denoising MR images [25, 41–45]. The NLM filter exploits the redundancy of information contained within an image to remove the noise [46]. Several modifications of the original NLM algorithm have been proposed by various researchers for denoising MR images [25, 42, 43, 47–56].

In transform domain based denoising approaches various multiresolution analysis (MRA) and multiscale geometric analysis (MGA) tools are used to decompose the MR images into different frequency components that can be studied with a resolution matched to their scale. Wavelets, curvelet and contourlet transforms are some of the widely used transforms for image denoising. Wavelet transform (WT) and it's variants have been widely used for MR image denoising by various researchers [16, 57–63]. The denoising methods based on WT, are not suitable for describing the signals which have high dimensional singularities such as edges and corners. To overcome the shortcomings of WT, and to detect, represent and process high dimensional data, some new advanced transforms have been proposed [64, 65]. Recently, these transforms have been used by several researchers for denoising MR images [66–68].

A few works have been reported in the literature for MR image denoising based on statistics/estimation methods [28, 69, 70]. The schemes of this category can be further divided into several sub-groups: maximum likelihood approach [71–75], linear minimum mean square error estimation approach [76, 77] and non-parametric estimation method [24, 78–82] etc.

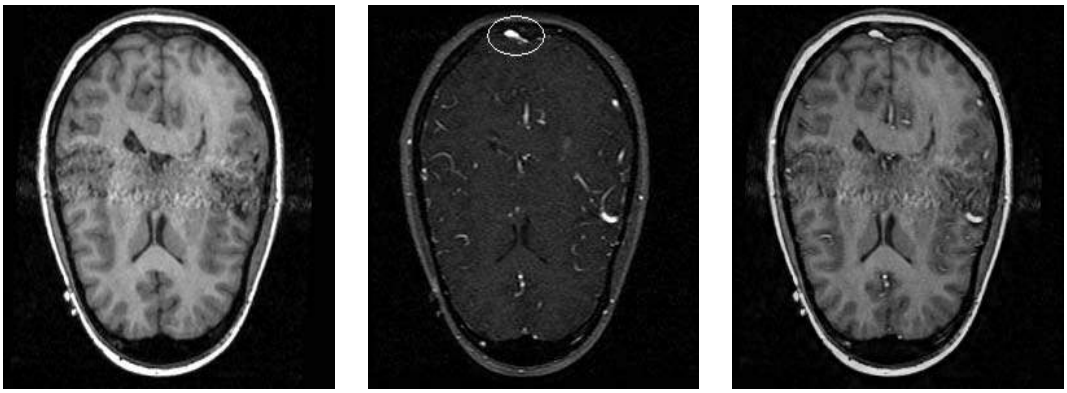

(a) (b) (c)

Figure 1.3: Need of image fusion: (a) Source Image 1: T1-weighted MR; (b) Source Image 2: MR angiography; (c) Fused image.

1.2.2 Multimodal Medical Image Fusion

Even though, the visual qualities of different modalities of medical images are improved by various image enhancement techniques. It is often not possible for a single modality of medical image to provide the medical experts with comprehensive and accurate information. The rapid and extraordinary advances in various technology domains (e.g. sensor, electrical, electronics and communication etc.) and modern instrumentations have brought an urgency for processing techniques that can efficiently integrate information from these different sources into a single composite form for interpretation. Multiple imaging modalities can complement each other to provide more information to understand the real worlds of objects than the use of a single modality [83–86]. Fig. 1.3, shows an example describing the need of such image fusion (information integration). The T1-weighted MR image in Fig. 1.3(a), contains information about soft tissues and it also shows a lesion in the brain. But, the vascular nature of the lesion is not clear. The vascular nature of the lesion is evident in the magnetic resonance angiography image of Fig. 1.3(b), but the tissue information is low. Both the lesion and its vascular nature along with the soft tissues information are evident in the fused image of the

Fig. 1.3(c). Lower cost, less time, accurate as well as reliable information are some of the immediate potential advantages of image fusion (IF). Moreover, it enables features to be distinguished that are impossible to perceive with any individual sensor. These advantages correspond to the notions of *redundant*, *complementary*, *more timely*, and *less costly* information [84, 85].

As a subset of IF techniques, multimodal medical image fusion (MIF) is the integration of complementary information from multimodal source medical images. The fused images are more suitable for human visual perception and further computer processing and analysis tasks [87, 88]. The combination of images from different modalities, leads to additional clinical information which is not apparent in the separate imaging modalities. A successful fusion should extract complete information from source images into the result, without introducing any artifacts or inconsistencies [89–92]. Generally, depending on the merging scheme used, existing MIF schemes can be classified into three levels [93]: pixel level, feature level, and decision level. MIF usually employs the techniques at pixel level. According to whether multiscale decomposition (MSD) is applied, the pixel level fusion methods can be roughly classified into MSD-based [94–99] or non-MSD-based methods [100–103]. Compared to the latter, the former performs better, because it can capture salient image features at different scales, which are more suitable to the mechanism of human vision [91, 98, 104–108].

The MIF schemes based on the methodology of simplest pixel averaging methods, normally result in undesirable side effects such as reduced contrast, loss of image fine details and unwanted degradation etc. [100, 101, 109–111]. In more robust weighted averaging approaches for pixel level fusion, the fused pixel is estimated as the weighted average of the corresponding input pixels. However, the weight estimation usually requires a user-specific threshold. Many other MIF methods have been developed based on intensity-hue-saturation (IHS), principal

component analysis (PCA), and the Brovey transform etc. [102, 103, 112, 113]. These techniques are easy to understand and implement. But, these schemes suffer from spectral degradation; that is, they can yield high spatial resolution fused image, but they overlook important spectral information. Soft-computing techniques (e.g., artificial neural network (ANN), fuzzy logic (FL), genetic algorithm (GA) and evolutionary algorithm (EA) etc.) have also been introduced to produce better fused images [114–120]. However, the performance of these soft-computing schemes depends on the sample images and this is not an appealing characteristic.

Because, real-world objects usually contain structures at many different scales or resolutions and multiresolution or multiscale approaches can provide a means to exploit this fact. The multiresolution techniques have attracted more and more interest in IF. WT and its variants are used in MIF extensively by various researchers [94, 121–125]. Recently, several novel MGA tools, like, curvelet, contourlet, ripplet etc. are found to offer better advantages of directionality, localization, anisotropy and multiscale properties, which cannot be perfectly achieved by traditional multiscale analysis like WT [64, 65, 126]. As a consequence, MIF schemes based on these transform domains result in superior fused images than produced by WT [95–98, 127–129].

1.2.3 Medical Image Classification and Retrieval

Nowadays, modern hospitals and health-care centers are producing large number (sometimes, 100, 000 images a day; this is about 100 GB of data) of medical images of diverse modalities. This generates huge repositories of valuable information, which in many cases is difficult to process and manage appropriately [12, 130–135]. Development of automated diagnostic tools to draw quicker and easier inferences from these huge databases has become an important area of research in biomedical

engineering [136–145]. Very often, an important initial step in developing such tools is the search (classification/retrieval) of potential subjects from different categories of medical images stored in databases, before an adequate course of action can be suggested for pathological subjects.

At present, medical images can be searched in three different ways: text based search (TBS), content based search (CBS) and semantic based search (SBS) methods [136, 146, 147]. Sometimes, a combination of these above mentioned schemes are also used for medical image search purpose [148–151]. In TBS schemes, images are classified/retrieved by manually annotated and previously stored text descriptions and traditional database techniques. Even though, TBS systems are fast and easy to develop, but these have several inherent shortcomings: incompleteness or inability to search due to ambiguous or missing descriptions in the file headers, dependency on time-consuming and subjective annotation procedures, and ineffectiveness of natural language of diagnostic reports in representing the true content of the medical images [140, 147, 152–156]. Thus, to support effective image searching, various methods based on image content have been developed.

In CBS systems, images are indexed and retrieved from databases based on their visual content (low level image features) such as color, texture, shape, salient points, patches and visual words etc. [131, 136, 153, 157–163]. Initially, medical images were included in the content based image retrieval (CBIR) field as a subdomain for trials [142, 164–167]. These efforts have been embodied in several content-based medical image retrieval (CBMIR) systems [131, 168–172]. Some of the remarkable CBMIR systems are: Automatic Search and Selection Engine with Retrieval Tools (ASSERT) [173], Image Indexing by Content (I^2C) [164], COntent-Based Retrieval Architecture (COBRA) [174], GNU Image Finding Tool for Medical images (MedGIFT) [175], Medical Image Access and Presentation System (MIAPS) [176], Spine Pathology and Image Retrieval System (SPIRS) [177]

and Image Retrieval for Medical Applications (IRMA) [178–180] etc. There are promising CBIR-based CAD systems, mostly specialized on a particular application domain, e.g. MR brain volumes [181, 182], lung cancer [183], mammography [184], chest CT [185], or bone age assessment [186], etc. Flexible image retrieval engine (FIRE) system handles different kinds of medical data as well as non-medical data like photographic databases [187]. Some very good reviews of the works done in this domain can be found in [131,136,146,149,152,153,166,188–191].

One of the major problems in CBS for image data is '*semantic gap*'. The '*semantic gap*' is the lack of coincidence between the information that one can extract from the visual data and the interpretation that the same data have for a user in a given situation. User seeks semantic similarity, but the database can only provide similarity by data processing [147,149,192,193]. An alternative to CBMIR is the semantics based medical image retrieval, where the main goal is to obtain the semantics of the images, by means of automatic image annotation [147, 149, 150, 192–195]. The current state-of-the-art in medical image search approaches has been presented in [131, 190].

Among the different modalities of medical images, the non-invasive nature of MRI together with its rich information provision, makes it the widely used method for diagnosis and treatment planning [20, 196]. Various researchers are not only trying to improve the MR image quality, but also seeking novel methods for easier and quicker inference from the images. In recent years, MRI has emerged as one of the popular choice to study the human brain [197, 198]. This necessitates the requirement of developing automated diagnosis tools to draw quicker and easier inferences from the brain MR images [135, 197, 199–203]. In recent years, various approaches of brain MR image classification [204–215] and retrieval [216–225] have been proposed by different researchers.

A lot of research works are going on for developing effective classification and

retrieval systems for medical images. Various research groups are increasingly attracted to medical image classification and retrieval problem. Many international competitions are now emerging to assist in the benchmark of feature sets, retrieval and classification schemes. One such annual competition is known as Cross Language Evaluation Forum of Image (ImageCLEF[1]). Since 2004, the ImageCLEF competition has conducted text-based as well as image-based retrieval each year. The tasks increasingly involved more data, a higher number of classes, and a more complicated class structure. In 2005, it has also included a medical image annotation task. Competitions are mainly based on the IRMA project X-ray library [153, 170, 178, 226], which consists of medical radiographs taken from clinical routine at the Department of Diagnostic Radiology, Aachen University Hospital, Germany. Images are classified by medical experts according to the imaging modality, the examined region, the image orientation with respect to the body and the biological system under evaluation [137, 180, 226–234]. Some of the remarkable medical image search systems based on this IRMA radiographic images can be found in [137, 154, 170, 194, 226, 235–244].

1.2.4 Medical Image Watermarking

Due to its importance in clinical diagnosis, treatment, research and other commercial and non-commercial applications, medical information is highly valuable and critical. The modern integrated health-care delivery systems (such as hospital information systems (HISs), medical information system (MISs), Picture Archiving and Communication Systems (PACS) etc.) provide easier access, effective manipulation and efficient distribution of medical information [245–251]. On the other hand, these advances have introduced new risks for inappropriate use of medical information, given the ease with which digital form of data could be

[1]http://imageclef.org

manipulated [252–256]. Consequently, there is a need to design a system for effective storage, access controlling and manipulation restriction of medical images and related information, keeping the authenticity, integrity and confidentiality requirements of medical data intact, for effective management purpose [255, 257, 258].

Recently, studies show that digital watermarking (DWM) is a promising way to facilitate sharing and remote handling of information in the digital world in a secure and private manner [259–266]. Medical image watermarking (MIW) is a subset of digital watermarking, where medical information is embedded in medical images and/or videos. When digital watermarking techniques are used in medical domain, these schemes must follow some specific requirements [257]: imperceptibility, robustness, capacity, authenticity, reversibility, intactness of region of interests (ROIs) and complexity etc. MIW schemes have several applications in medical data management domain: saving digital data storage and network bandwidth, avoid detachment of medical images and related information, confidentiality and security of patient record, non-repudiation, integrity control, authentication, indexing, access control and captioning etc. [252, 267].

In the last few decades, researchers have developed a number of MIW schemes both in spatial [268–278] as well as in transform domain [**?**, 279–286]. Various researchers have classified these existing MIW techniques differently based on their applicability or working methodology. For example in [255], G. Coatrieux et al. have mentioned that three different kinds of MIW schemes are available. The first class groups methods that embed information within region of non-interest (RONI) in order not to compromise the diagnosis capability [253, 269, 273, 280, 287, 288]. The second approach corresponds to reversible watermarking [269, 284, 285, 289, 290]. The third approach consists in using classical watermarking methods while minimizing the distortion [246, 291, 292].

According to Navas et al. [257], MIW algorithms reported in literature can be

divided into two categories: The algorithms that focus on tamper detection and authentication [272, 280, 287–289, 293–296]. The tamper detection algorithms use such watermarks which are able to localize the changes or alterations where the tampering was done. The second category of algorithms focus on electronic health record (EHR) data hiding [246, 254, 269, 280, 286, 292, 297–299]. These techniques give more importance in hiding higher payload in image, keeping the imperceptibility very high.

Researchers proposed watermarking techniques and reported findings in the literature to satisfy both integrity and confidentially requirements [247, 300–307], while hiding EHR in medical image to make it more usable. Both fragile and robust watermarking techniques are used for integrity control and EHR hiding. Anand et al. have used least significant bit (LSB) plane technique in spatial domain to insert patient information encrypted using a log function in medical images [246]. In [254], Cho et al. have applied non-blind watermarking method to medical images both in spatial and transform domain. Zhou et al. have presented a MIW scheme that attaches digital signature and EHR into the mammographic images using the LSB replacing technique [291]. Chao et al. have proposed a secure data hiding technique based on bipolar multiple-base conversion to allow a variety of EPR data to be hidden within the same mark image [300]. In [292], Acharya et al. have adapted MIW for interleaving patient information and graphical signals with medical images to reduce storage and transmission overheads. Nayak et al. [298] have extended the work of Acharya et al. [292] in transform domain (discrete Fourier transform (DFT), discrete cosine transform (DCT) and discrete wavelet transform (DWT)). In this scheme, text files are encrypted using Rijndael algorithm and Electrocardiographic (ECG) signal is encrypted by differential pulse code modulation technique, prior to interleaving.

Shih et al. [280], have proposed a MIW technique embedding a fragile water-

mark and textual data around the ROI of a medical image based on GA in DCT domain. In [288], Giakoumaki et al. have presented a wavelet based multiple MIW approach for addressing the confidentiality protection and both origin and data authentication problems. Luo et al. have presented a lossless scheme for medical image processing [308]. Their method provides relatively high data embedding rate and original image can be recovered distortion free. Memon et al. have proposed a method to embed the watermark information in RONI. Encryption of the embedded data is also done to provide additional security using Bose-Chaudhuri-Hocquengham (BCH) in their method [303]. In [285], a robust, reversible, blind and double watermarking scheme that embeds/extracts watermarks using recursive dither modulation (RDM) scheme and differential evolution (DE) optimization in DWT domain based on singular value decomposition (SVD) is proposed. Extensive reviews on different MIW schemes can be found in [255, 257, 258, 309].

1.3 Theoretical Preliminaries

In this thesis work, several mathematical tools/techniques have been used to develop different solutions to various problems of medical image computing subdomains. The following section begins with the theoretical preliminaries of the different tools/techniques used in the thesis. A brief description of the different quantitative measures used to objectively evaluate the performances of the proposed solutions is also included in this section.

1.3.1 Multiscale Image Transforms

Efficient representation of visual information lies at the foundation of many image processing and analysis tasks, including compression, filtering, and feature extraction etc. Efficiency of a representation refers to the ability to capture significant

information of an object of interest in a small description [310,311]. Moreover, for human visual system (HVS), it is well-known that the receptive fields in the visual cortex are characterized as being *localized*, *oriented*, and *bandpass* [312]. Various experiments in searching for the sparse components of (both still and time-varying) natural images produced basis images that closely resemble the aforementioned characteristics of the visual cortex [313]. More importantly, the results suggest that for a computational image representation to be efficient, it should have the following properties [310, 311]: *multiresolution*, *localization*, *critical sampling*, *directionality* and *anisotropy*. Among these desiderata, the first three are successfully provided by the separable wavelet system. However, the last two require new challenging nonseparable constructions.

A key distinguishing feature of natural images is that they have intrinsic *geometric structures*. In particular, visual information is mainly contained in the geometry of object boundaries or edges. Edges or boundaries of objects cause discontinuities or singularities in image intensity. How to efficiently represent singularities in images poses a great challenge in image processing. The well known Fourier transform (FT) can only provide an efficient representation for smooth images but not for images that contain edges. It is also well known that 1D singularities in a function (which has finite duration or is periodic) destroy the sparsity of Fourier series representation of the function, which is known as *Gibbs phenomenon*. In contrast, WT is able to efficiently represent a function with 1D singularities [314, 315]. In particular, wavelets are good at isolating the discontinuities at edge points. However, as a result of their construction by separable extension from 1D bases, wavelets in 2D cannot "*see*" the smoothness along the contours. In addition, separable wavelets can capture only limited directional information, which is an important and unique feature of multi-dimensional signals.

Ridgelet transform overcomes the limitations of WT [316]. It can resolve 1D

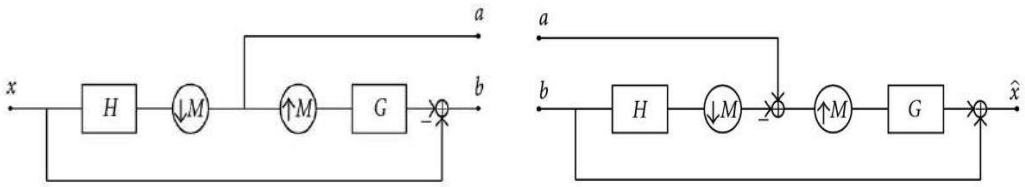

Figure 1.4: Laplacian pyramid scheme: (a) Analysis and (b) Synthesis.

singularities along an arbitrary direction (including horizontal and vertical direction). But, since ridgelet transform is not able to resolve 2D singularities, Candes and Donoho have proposed the first generation *curvelet* transform based on multiscale ridgelet [64]. Curvelet transform can resolve 2D singularities along smooth curves. Similar to curvelet, *contourlet* [65] and *ripplet* [126] transforms were proposed to resolve 2D singularities. In the following section brief descriptions are given about some of MRA/MGA tools used in this thesis.

1.3.1.1 Contourlet Transform

The major drawback of WT in two dimensions is its limited ability in capturing directional information. In light of this, Do and Vetterli [65] have developed the CNT, based on an efficient 2D multiscale and directional filter bank (DBF). CNT not only possess the main features of DWT, but also offer a high degree of directionality and anisotropy. It allows for different and flexible number of directions at each scale, while achieving nearly critical sampling. In addition, CNT uses iterated filter banks, which makes it computationally efficient ($O(N)$ operations for an N-pixels image).

CNT gives a multiresolution, local and directional expansion of image using pyramidal DFB (PDFB). The PDFB combines Laplacian pyramid (LP) which captures the point discontinuities, with a DFB which links these discontinuities into linear structures.

LP scheme is shown in Figure 1.4. Here, the input image x is first lowpass filtered by analysis filter H and then downsampled to produce a coarse approximation a. It is then interpolated and passed through the synthesis filter G. The resulting image is subtracted from the original image x to obtain the bandpass image b. This process can be iterated repeatedly on the coarser version of the image a. LP is a multiscale decomposition of $L^2(R^2)$ into series of increasing resolution subspaces which are orthogonal complements of each other as follows [317]:

$$L^2(R^2) = V_{j_0} \oplus (\bigoplus_{j=J_0}^{-\infty} W_j) \tag{1.1}$$

where, V_{j_0} is the approximation subspace at the scale 2^{j_0}, W_j is the detail in the finer scale 2^{j-1}. In the LP, each subspace W_j is spanned by a frame $\mu_{j,n}(t)_{n\varepsilon Z^2}$ that utilizes a uniform grid on R^2 of intervals $2^{j-1} \times 2^{j-1}$.

In 1992, Bamberger and Smith constructed a 2D DFB that can be maximally decimated while achieving perfect reconstruction [318]. It is used in the second stage of CNT to link the edge points into linear structures, which involves modulating the input image and using quincunx filter banks (QFB) with diamond-shaped filters. A l-level tree-structured DFB is equivalent to a 2^l parallel channel filter bank with equivalent filters and overall sampling matrices as shown in Figure 1.5. As shown in Figure 1.5, corresponding to the subbands indexed, the equivalent analysis and synthesis filters are denoted using H_k and G_k, $0 \leq k < 2^m$.

A l-level DFB generates a perfect directional basis for discrete signal in $l^2(Z^2)$ that is composed of the impulse responses of 2^l directional synthesis filters and their shift. They can be represented as follows:

$$g_k^{(l)}[n - S_k^{(l)} n]_{0 \leq k < 2^l, n\varepsilon Z^2} \tag{1.2}$$

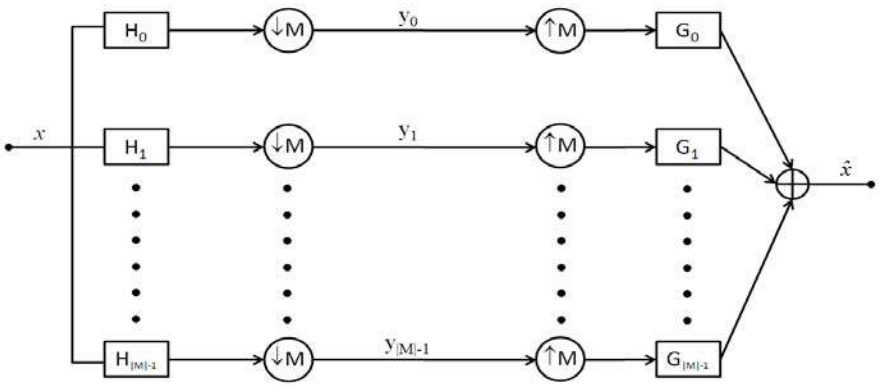

Figure 1.5: Construction of DBF.

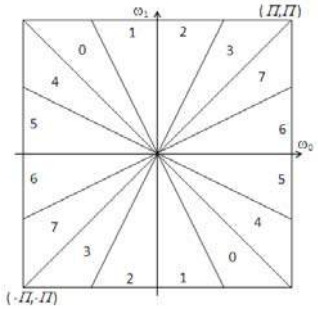

Figure 1.6: Frequency partition of contourlet transform.

$$g[n] = \frac{2\Pi}{n_1}[\psi(\frac{n_1(l+1)}{N} + n_2) - \psi(\frac{n_1 l}{N} + n_2)] \tag{1.3}$$

where, $N = 2^{n-2}$ and $\psi(x)$ is similar to the common *sin* function.

$$\psi(x) = \frac{1 - cos(\pi x)}{\pi x} \tag{1.4}$$

In CNT, applying a l_j-level DBF to the detail subspace W_j results in a decomposition with 2^{l_j} directional subspaces as follows:

$$W_j = \bigoplus_{k=0}^{2^{l_j}-1} W_{j,k}^{l_j} \tag{1.5}$$

A DFB is designed to capture the high frequency content like smooth contours and directional edges. Fig. 1.6, shows the frequency partition of CNT, and Fig. 1.7,

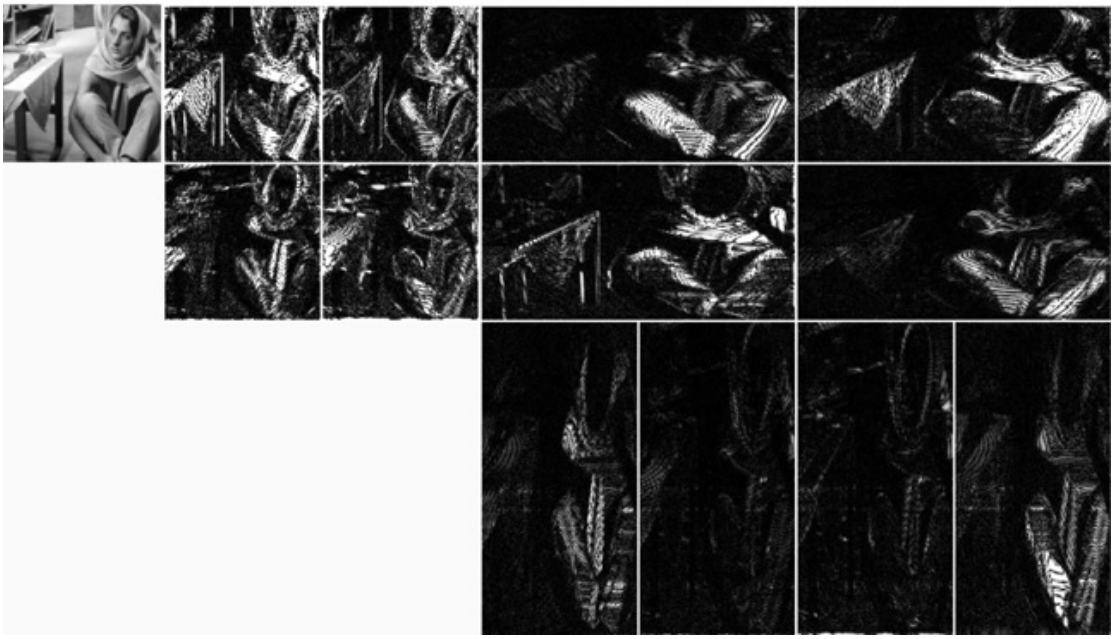

Figure 1.7: Contourlet transform of *Barbara* image.

presents an image along with its subbands after decomposition by CNT.

1.3.1.2 Nonsubsampled Contourlet Transform

In 2006, Arthur L. da Cunha et al. have proposed an overcomplete transform called the NSCT [319]. NSCT is a fully shift-invariant, multiscale and multi-direction expansion that has a fast implementation. The CNT is not shift invariant due to the presence of the down-samplers and up-samplers in both the LP and DFB stages of CNT [319]. NSCT achieves shift-invariance property by using the Non-subsampled pyramid filter bank (NSPFB) and the Non-subsampled DFB (NSDFB).

NSPFB is a shift-invariant filtering structure accounting for the multiscale property of NSCT. This is achieved by using two-channel non-subsampled 2D filter banks. It has no downsampling or upsampling and hence shift-invariant. Perfect

reconstruction is achieved provided the filters satisfy the following identity

$$H_0(z)G_0(z) + H_1(z)G_1(z) = 1 \tag{1.6}$$

where, $H_0(z)$ is the lowpass decomposition filter, $H_1(z)$ is the highpass decomposition filter, $G_0(z)$ is the lowpass reconstruction filter, and $G_1(z)$ is the highpass reconstruction filter.

In order to obtain the multiscale decomposition, NSPFB are constructed by iterated non-subsampled filter banks. For the next level all filters are upsampled by 2 in both dimensions. Therefore, they also satisfy the perfect reconstruction identity. The equivalent filters of a k-th level cascading NSPFB are given by

$$H_n^{eq}(z) = \begin{cases} H_1(z^{2^{n-1}}) \prod_{j=0}^{n-2} H_0(z^{2^j}), & 1 \leq n < 2^k \\ \prod_{j=0}^{n-1} H_0(z^{2^j}) & , \ n = 2^k \end{cases} \tag{1.7}$$

where, z^j stands for $[z_1^j, z_2^j]$.

The NSDFB is constructed by eliminating the downsamplers and upsamplers of the DFB by switching off the downsamplers/upsamplers in each two channel filter bank in the DFB tree structure and upsampling the filters accordingly [319]. The outputs of the first level and second level filters are combined to get the four directional frequency decomposition. The synthesis filter bank is obtained similarly. All filter banks in the NSDFB tree structure are obtained from a single non-subsampled filter bank (NSFB) with fan filters. To obtain multidirectional decomposition, NSDFBs are iterated and to get the next level decomposition all filters are up sampled by a quincunx matrix given by

$$QM = \begin{bmatrix} 1 & 1 \\ 1 & -1 \end{bmatrix} \tag{1.8}$$

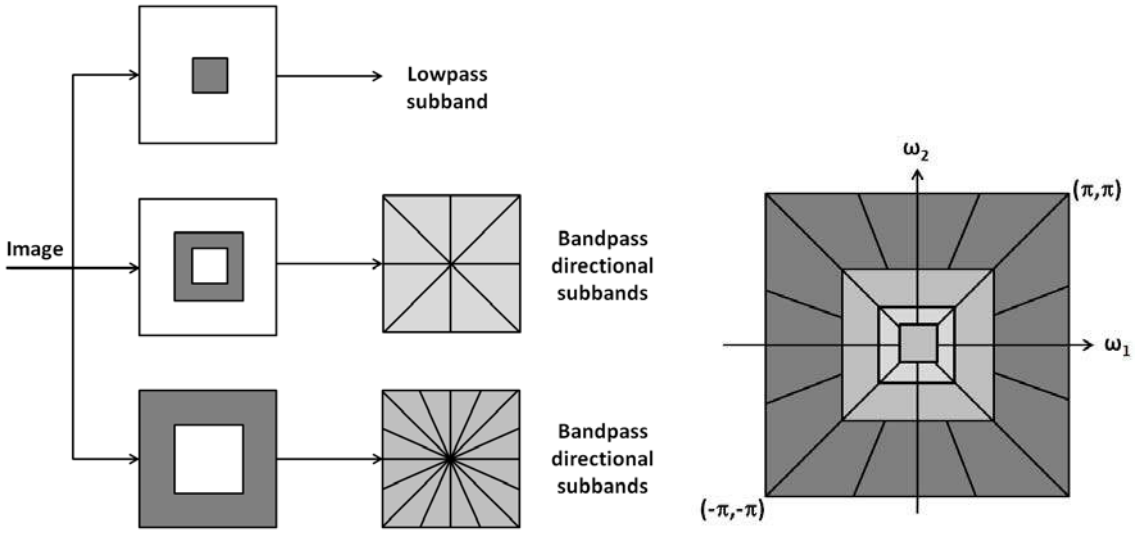

Figure 1.8: NSCT (a) NSFB structure that implements the NSCT. (b) Frequency partitioning obtained with the proposed structure.

NSCT is obtained by combining NSPFB and NSDFB as described by the Fig. 1.8(a). The resulting filtering structure approximates the ideal partition of the frequency plane displayed in Fig. 1.8(b). It must be noted that different from the contourlet expansion NSCT has a redundancy given by $R = \sum_{j=0}^{j} 2^{l_j}$, where 2^{l_j} is the number of directions at scale j.

1.3.1.3 Type-I Ripplet Transform

DWT and its variants have been used extensively for image processing applications. But the problem with DWT is that it is inherently non-supportive to directionality and anisotropy. To address these problems, Jun Xu *et al.* have proposed a new MGA tool called RT [126]. RT is a higher dimensional generalization of the curvelet transform (CVT), capable of representing images or $2D$ signals at different scales and different directions. To achieve anisotropic directionality, CVT uses a parabolic scaling law [64]. From the perspective of micro-local analysis, the anisotropic property of CVT guarantees resolving $2D$ singularities along

C^2 curves. Whereas, RT provides a new tight frame with sparse representation for images with discontinuities along C^d curves [126].

There are two questions regarding the scaling law used in CVT: 1) Is the parabolic scaling law optimal for all types of boundaries? and if not, 2) What scaling law will be optimal? To address these questions, Jun Xu *et al.* have generalized the scaling law of CVT, which resulted in RT. RT generalizes CVT by adding two parameters, i.e., support c and degree d. CVT is just a special case of RT with $c = 1$ and $d = 2$. The anisotropy capability of representing singularities along arbitrarily shaped curves of RT, is due to these two new parameters c and d.

As digital image processing needs discrete transform instead of continuous transform, here we describe the discretization of RT [126]. The discretization of continuous RT is based on the discretization of the parameters of ripplet functions. The scale parameter a is sampled at dyadic intervals. The position parameter b and the rotation parameter θ are sampled at equal-spaced intervals. a_j, $\overrightarrow{b}_k$ and θ_l substitute a, $\overrightarrow{b}$ and θ, respectively, and satisfy that $a_j = 2^{-j}$, $\overrightarrow{b}_k = [c \cdot 2^{-j} \cdot k_1, 2^{-j/d} \cdot k_2]^T$ and $\theta_l = \frac{2\Pi}{c} \cdot 2^{-\lfloor j(1-1/d) \rfloor} \cdot l$, where $\overrightarrow{k} = [k_1, k_2]^T$, and j, k_1, k_2, $l \in \mathbb{Z}$. $(\cdot)^T$ denotes the transpose of a vector. $d \in \mathbb{R}$, since any real number can be approximated by rational numbers, so we can represent d with $d = n/m$, $n, m \neq 0 \in \mathbb{Z}$. Usually, we prefer $n, m \in \mathbf{N}$ and n, m are both primes. In the frequency domain, the corresponding frequency response of ripplet function is in the form

$$\widehat{\rho}_j(r, \omega) = \frac{1}{\sqrt{c}} a^{\frac{m+n}{2n}} W(2^{-j} \cdot r) V(\frac{1}{c} \cdot 2^{-\lfloor j \frac{m-n}{n} \rfloor} \cdot \omega - l) \tag{1.9}$$

where, W and V are the *radial-window* and the *angular-window*, respectively.

These two windows satisfy the following admissibility conditions:

$$\sum_{j=0}^{+\infty} |W(2^{-j} \cdot r)|^2 = 1 \tag{1.10}$$

$$\sum_{l=-\infty}^{+\infty} |V(\frac{1}{c} \cdot 2^{-\lfloor j(1-1/d) \rfloor} \cdot \omega - l)|^2 = 1 \tag{1.11}$$

given c, d and j. These two windows partition the polar frequency domain into 'wedges'. The 'wedge' corresponding to the ripplet function in the frequency domain is

$$H_{j,l}(r,\theta) = \{2^j \leq |r| \leq 2^{2j}, |\theta - \frac{\pi}{c} \cdot 2^{-\lfloor j(1-1/d) \rfloor} \cdot l| \leq \frac{\pi}{2} 2^{-j}\} \tag{1.12}$$

The discrete RT of an $M \times N$ image $X(m,n)$ is as follows:

$$R_{j,\overrightarrow{k},l} = \sum_{m=0}^{M-1} \sum_{n=0}^{N-1} X(m,n) \overline{\rho_{j,\overrightarrow{k},l}(m,n)} \tag{1.13}$$

where, $R_{j,\overrightarrow{k},l}$ are the ripplet coefficients.

As a generalized version of CVT, RT is not only capable of resolving 2D singularities, but it also has some useful properties:

1. It forms a new tight frame in a function space. Having good capability of localization in both spatial and frequency domain, it provides a more efficient and effective representation for images or 2D signals.

2. It has general scaling with arbitrary degree and support, which can capture 2D singularities along different curves in any directions.

Jun Xu *et al.* have showed that RT can provide a more effective representation for images with singularities along smooth curves [126]. It outperforms DCT and DWT in nonlinear approximation, when the number of retained coefficients is

small. RT can achieve roughly 2 dB higher Peak-Signal-to-Noise Ratio (PSNR) on average than Joint Photographic Experts Group (JPEG), and provide better visual quality than JPEG2000 at low bit-rates, when applied to image compression. In case of image denoising application, RT performs better than CVT and DWT. RT produces high quality fused images, when applied in the medical image fusion domain [107]. All these experiments show that RT based image coding is suitable for representing texture or edges in images.

1.3.2 Pulse Coupled Neural Network

Biological systems have always been an inspiration for developing computer vision, image and video processing algorithms. In late 1980s, during the study of cat visual cortex, Eckhorn et al. discovered that the midbrain in an oscillating way creates binary images that could extract different features from the visual impression [320]. Based on these binary images the actual image is created in the cat's brain. To simulate this behavior, they developed a neural network, called Eckhorn's model. Similar neural behavior was also found by Rybak et al. based on study of the visual cortex of guinea pig and they developed a neural network, called Rybak's model [321]. Because these models provide a simple, effective way for studying synchronous pulse dynamics in networks, these were recognized as being very potential in image processing [322–326]. Johnson et al. carried on a number of modifications and variations to tailor this model's performance in image processing algorithms [323, 327]. This modified neural model is called PCNN.

The PCNN is a single layer, two-dimensional, laterally connected network of integrate-and-fire neurons, with a 1:1 correspondence between the image pixels and network neurons. This is an unsupervised neural network with self-organizing capability. The output images at different iterations typically represent some

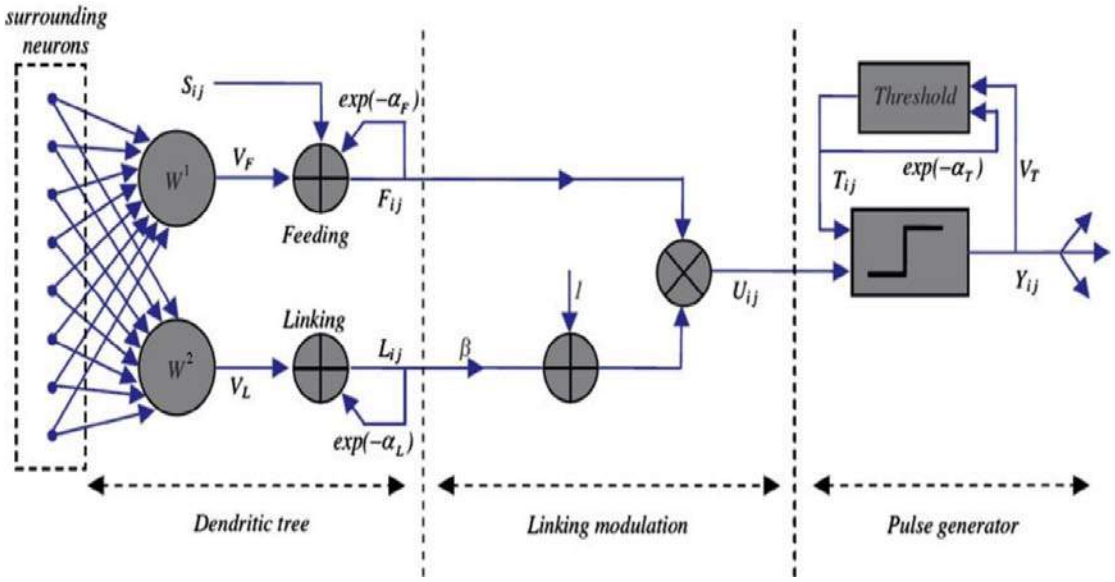

Figure 1.9: Structure of PCNN.

segments or edges information of the input image. The PCNN neuron's structure is shown in Fig. 1.9. The neuron consists of an input part (dendritic tree), linking part and a pulse generator. The neuron receives the input signals from feeding and linking inputs. Feeding input is the primary input from the neuron's receptive area. The neuron receptive area consists of the neighboring pixels of corresponding pixel in the input image. Linking input is the secondary input of lateral connections with neighboring neurons. The difference between these inputs is that the feeding connections have a slower characteristic response time constant than the linking connections. The standard PCNN model is described as iteration by the following equations [322, 325]:

$$F_{m,n}[t] = e^{-\alpha_F} F_{m,n}[t-1] + V_F \sum_{k,l} W^1_{m,n,k,l} Y_{m,n}[t-1] + S_{m,n} \tag{1.14}$$

$$L_{m,n}[t] = e^{-\alpha_L} L_{m,n}[t-1] + V_L \sum_{k,l} W^2_{m,n,k,l} Y_{m,n}[t-1] \tag{1.15}$$

$$U_{m,n}[t] = F_{m,n}[t](1 + \beta L_{m,n}[t]) \tag{1.16}$$

$$Y_{m,n}[t] = \begin{cases} 1, & U_{m,n}[t] > \theta_{m,n}[t] \\ 0, & \text{otherwise} \end{cases} \tag{1.17}$$

$$\theta_{m,n}[t] = e^{-\alpha_\theta}\theta_{m,n}[t-1] + V_\theta Y_{m,n}[t] \tag{1.18}$$

In Eq.(1.14) to Eq.(1.18), the indexes m and n refer to the pixel location in the image, k and l refer to the dislocation in a symmetric neighborhood around one pixel, and t denotes the current iteration (discrete time step). Here t varies from 1 to T (total number of iterations). The dendritic tree is given by Eqs.(1.14)–(1.15). The two main components F and L are called feeding and linking, respectively. $W^1_{m,n,k,l}$ and $W^2_{m,n,k,l}$ are the synaptic weight coefficients and S is the external stimulus. V_F and V_L are normalizing constants. α_F and α_L are the time constants; generally, $\alpha_F < \alpha_L$. The linking modulation is given in Eq.(1.16), where $U_{m,n}[t]$ is the internal state of the neuron and β is the linking parameter. The pulse generator determines the firing events in the model in Eq.(1.17). $Y_{m,n}[t]$ depends on the internal state and threshold. The dynamic threshold of the neuron is Eq.(1.18), where V_θ and α_θ are normalized constant and time constant, respectively. Generally, the firing time output (time matrix) of PCNN is used for different image processing and analysis applications. The time matrix is computed as follows:

$$G(m,n) = \sum_{t=1}^{T} Y_{m,n}[t] \tag{1.19}$$

The time matrix G of PCNN includes the information of the image intensity distribution as well as the spatial geometrical structures of the image, which makes it suitable for various image processing and analysis applications.

The working mechanism of PCNN can be described as follows: the input stimulus (pixel intensity) is received by the feeding element and the internal activation element combines the feeding element with the linking element. The value of

internal activation element is compared with a dynamic threshold that gradually decreases at iteration. The internal activation element accumulates the signals until it surpasses the dynamic threshold and then fires the output element and the dynamic threshold increases simultaneously strongly. The output of the neuron is then iteratively fed back to the element with a delay of one iteration. Based on the application and requirements, various modifications are made in the original PCNN. More information about PCNN can be found in [325, 326].

1.3.3 Least Square-Support Vector Machine

Recently, support Vector Machines (SVM) have been shown to be effective for many classification problems [328]. For binary-class classifications, SVM constructs an optimal separating hyperplane between the positive and negative classes with the maximal margin. It can be formulated as a quadratic programming (QP) problem involving inequality constraints. The most critical drawback of SVM is its high computational complexity for high dimensional data sets. To reduce the computational demand, the least square version of SVM (LS-SVM) is developed which attempts to minimize the least square error on the training samples while simultaneously maximizing the margin between two classes. LS-SVM avoids solving quadratic programming problem and simplifies the training procedure. While in classical SVM's many support values are zero (nonzero values correspond to support vectors), in LS-SVM, the support values are proportional to the errors. A two-norm is taken with equality instead of inequality constraints so as to obtain a linear set of equations instead of a QP problem in the dual space [329, 330]. Given a training set:

$$\{(x_i, y_i)\}_{i=1}^{N} \quad and \quad y_i = \{+1, -1\} \tag{1.20}$$

where, x_i is an n-dimensional vector and y_i is the label of this vector. LS-SVM can be formulated as the optimization problem:

$$\min_{w,b,e} \mathcal{J}(w,b,e) = \frac{1}{2}w'w + \frac{1}{2}C\sum_{i=1}^{n} e_i^2 \tag{1.21}$$

subject to the equality constraints

$$y_i[w'\varphi(x_i) + b] = 1 - e_i \tag{1.22}$$

where, $C > 0$ is a regularization factor, b is a bias term, w is the weights vector, e_i is the difference between the desired output and the actual output and $\varphi(x_i)$ is a mapping function.

The lagrangian for problem of Eq.(1.21) is defined as follows:

$$\mathcal{L}(w,e_i,b,\alpha_i) = \min_{w,b,e} \mathcal{J}(w,b,e) - \sum_{i=1}^{n} \alpha_i\{y_i[w'\varphi(x_i) + b] - 1 + e_i\} \tag{1.23}$$

where, α_i are Lagrange multipliers. The Karush-Kuhn-Tucker (KKT) conditions for optimality: $\frac{\partial \mathcal{L}}{\partial w} = 0 \rightarrow w = \sum_{i=1}^{n} \alpha_i y_i \varphi(x_i)$; $\frac{\partial \mathcal{L}}{\partial e_i} = 0 \rightarrow \alpha_i = Ce_i$; $\frac{\partial \mathcal{L}}{\partial b} = 0 \rightarrow \sum_{i=1}^{n} \alpha_i y_i = 0$; $\frac{\partial \mathcal{L}}{\partial \alpha_i} = 0 \rightarrow y_i[w'\varphi(x_i) + b] - 1 + e_i = 0$, is the solution to the following linear system

$$\begin{bmatrix} 0 & -Y \\ Y & \varphi\varphi' + C^{-1}I \end{bmatrix} \begin{bmatrix} b \\ \alpha \end{bmatrix} = \begin{bmatrix} 0 \\ \overline{1} \end{bmatrix} \tag{1.24}$$

where, $\varphi = [\varphi(x_1)'y_1, ..., \varphi(x_n)'y_n], Y = [y_1, ..., y_n]$,
$\overline{1} = [1, ..., 1]$, and $\alpha = [\alpha_1, ..., \alpha_n]$.

For a given kernel function K(,) and a new test sample point x, the LS-SVM

classifier is given by

$$f(x) = sgn[\sum_{i=1}^{n} \alpha_i y_i K(x, x_i) + b] \tag{1.25}$$

1.3.4 Earth Mover's Distance

In computer vision applications, feature distributions are often used to summarize the content of an image. Consequently, it becomes important to define a distance between two distributions. This requires in turn a notion of distance between the basic elements that appear in the distributions. EMD is such a consistent measure of distance, or dissimilarity, between two distributions of points in a space for which a *'ground distance'* (distance measure between single features) is given [331].

Intuitively, given two distributions, one of them can be seen as a mass of earth properly spread in space, the other as a collection of holes in that same space. The EMD measures the least amount of work needed to fill the holes with earth. Here, a unit of work corresponds to transporting a unit of earth by a unit of ground truth. A distribution can be represented by a set of clusters where each cluster is represented by its cluster center (e.g., mean, mode etc.), and by the fraction (weight) of the distribution that belongs to that cluster. Such a representation is called *signature* of the distribution. Signatures can be of variable or fixed size. EMD reflects the minimal cost that must be paid to transform one signature into the other. The EMD has many desirable properties: it is more robust in comparison to other histogram matching techniques, in that it suffers from no arbitrary quantization problems due to the fixed binning of the latter. It allows for partial matching, and it can be applied to signatures with different sizes. When used to compare distributions that have the same overall mass, the EMD is a true metric.

Computing the EMD is based on a solution to the well known transportation problem. Assuming, that several suppliers, each with a given amount of goods, are required to supply several consumers, each with a given limited capacity. For each supplier-consumer pair, the cost of transporting a single unit of goods is given. The transportation problem is then to find a least expensive flow of goods from the suppliers to the consumers that satisfies the consumer's demand. Matching signatures can be naturally cast as transportation problem by defining one signature as the supplier and the other as the consumer, and by setting the cost for a supplier-consumer pair to equal the ground distance between an element in the first signature and an element in the second. Intuitively, the solution is then the minimum amount of *work* required to transform one signature into the other.

Let, $P = \{(p_1, w_{p_1}), ..., (p_m, w_{p_m})$ be the first signature with m clusters where p_i represents a cluster representative and w_{p_i} indicates the weight of the cluster. Similarly, $Q = \{(q_1, w_{q_1}), ..., (q_n, w_{q_n})$ be the second signature with n clusters. Also let, $D = [d_ij]$ be the *ground distance* matrix, where $d_ij = d(p_i, q_j)$ indicates the ground distance between clusters p_i and q_j, chosen according to the task at hand.

Computing EMD thus becomes finding a flow $F = [f_{ij}]$ with f_{ij} representing the flow between p_i and q_j which minimizes the overall cost.

$$WORK(P, Q, F) = \sum_{i=1}^{m} \sum_{j=1}^{n} d(p_i, q_j) f_{ij} \tag{1.26}$$

subject to the constraints:

$$f_{ij} \geq 0, 1 \leq i \leq m, 1 \leq j \leq n \tag{1.27}$$

$$\sum_{j=1}^{n} f_{ij} \leq w_{p_i}, 1 \leq i \leq m \tag{1.28}$$

$$\sum_{i=1}^{m} f_{ij} \leq w_{q_j}, 1 \leq j \leq n \tag{1.29}$$

$$\sum_{i=1}^{m}\sum_{j=1}^{n} f_{ij} = min(\sum_{i=1}^{m} w_{p_i}, \sum_{j=1}^{n} w_{q_j}) \tag{1.30}$$

Constraint Eq.(1.27) ensures movement of goods from suppliers to consumers and not the other way. Constraint Eq.(1.28) defines the upper bound on the capacity of the suppliers while Eq.(1.29) represents the upper bound on the capacity of the consumers. Constraint Eq.(1.30) ensures that maximum possible supplies to be moved from suppliers (P) to consumers (Q), called the *total flow*. Once the solution to optimal flow is obtained EMD is defined as the work normalized by the total flow:

$$EMD(P,Q) = \frac{\sum_{i=1}^{m}\sum_{j=1}^{n} d(p_i, q_j) f_{ij}}{\sum_{i=1}^{m}\sum_{j=1}^{n} f_{ij}} \tag{1.31}$$

EMD by its definition extends to distance between sets or distributions of elements, thereby facilitating partial matches. It can be shown that, EMD is a metric, if the ground distance is a metric and the total weights of two signatures are equal.

1.3.5 Image Quality and Quantitative Performance Measures

In this thesis, the performance effectiveness of various proposed solutions, overcoming different problems of medical image processing, analysis and management sub-domains have been evaluated through extensive experiments and comparisons. Both subjective (qualitative) as well as objective (quantitative) measures have been used for this purpose. All the solutions reported in subsequent parts of this thesis have been implemented in MATLAB, and experiments have been carried out on a PC with 2.10 GHz CPU and 2 GB RAM. In the following section, brief descriptions of the different image quality and quantitative performance measures

are given, which have been used to objectively evaluate the effectiveness of the proposed solutions.

For evaluating the performance effectiveness of the proposed medical image enhancement scheme, the image quality and quantitative performance measures used are:

Root-Mean-Square-Error (RMSE): RMSE is computed by the following formula:

$$RMSE = \sqrt{\frac{1}{M \times N} \sum_{m=1}^{M} \sum_{n=1}^{N} (X(m,n) - Y(m,n))^2} \tag{1.32}$$

where, X and Y are two images of size $M \times N$ and $X(m,n)$ indicates the gray-value of the pixel of image X at position (m,n). In case of denoising applications, one of the two images is the denoised image and the other one is the noise-free (reference) image. Lower value of RMSE indicates better denoised results.

Peak-Signal-to-Noise-Ratio (PSNR): PSNR is an approximation to human perception of reconstruction quality. Higher value of PSNR represents better output image and it is computed as follows:

$$PSNR = 10 \times log_{10}(\frac{MAX_L^2}{MSE}) \tag{1.33}$$

where, MAX_L indicates the maximum possible gray value of the images (in case of 8-bit gray image this is 255) and MSE represents the mean-square-error between two images (X and Y) of size $M \times N$ and is computed by the following formula:

$$MSE = \frac{1}{M \times N} \sum_{m=1}^{M} \sum_{n=1}^{N} (X(m,n) - Y(m,n))^2 \tag{1.34}$$

Mean Structural Similarity Index (MSSIM): It is a method for measuring the similarity between two images X and Y [332].

$$MSSIM(X,Y) = \frac{1}{B}\sum_{b=1}^{B} SSIM(x_j, y_j) \tag{1.35}$$

where, x_j and y_j are the image contents at the j-th local window; and B is the number of local windows in the image. The SSIM metric is calculated on various windows of an image. The measure between two windows x and y of common size $N \times N$ is:

$$SSIM(x,y) = \frac{(2\mu_x\mu_y + c_1)(2\sigma_{xy} + c_2)}{(\mu_x^2 + \mu_y^2 + c_1)(\sigma_x^2 + \sigma_y^2 + c_2)} \tag{1.36}$$

where, μ_p and σ_p^2 represents the average and variance of p, respectively; $p = \{x, y\}$. The term σ_{xy} indicates the covariance of x and y. $c_1 = (k_1 L)^2$, $c_2 = (k_2 L)^2$ are two variables to stabilize the division with weak denominator and L indicates the dynamic range of the pixel-values with $k_1 = 0.01$ and $k_2 = 0.03$ by default. Higher value of MSSIM represents better output.

Quality Index based on Local Variance (QILV): Based on the assumption that a great amount of the structural information of an image is codded in its local variance distribution, QILV for two images X and Y is defined as follows [333]:

$$QILV(X,Y) = \frac{2\mu_{V_X}\mu_{V_Y}}{\mu_{V_X}^2 + \mu_{V_Y}^2} \cdot \frac{2\sigma_{V_X}\sigma_{V_Y}}{\sigma_{V_X}^2 + \sigma_{V_Y}^2} \cdot \frac{\sigma_{V_X V_Y}}{\sigma_{V_X}\sigma_{V_Y}} \tag{1.37}$$

where, $\sigma_{V_X V_Y}$ represents the covariance between the variances of X and Y, σ_{V_Y} denotes the standard deviation of the local variance and μ_{V_X} indicates the mean of the local variance with locality defined as a window of size B

(default $B = 11$). High value of $QILV$ means better results.

The selected image quality and quantitative performance measures used in the objective analysis for evaluating the proposed MIF schemes are as follows:

Standard Deviation (STD): It measures the contrast of the fused image. An image with high contrast would have a high standard deviation. It is calculated as follows:

$$STD = \sqrt{\frac{1}{M \times N} \sum_{m=1}^{M} \sum_{n=1}^{N} (X(m,n) - \overline{X})^2} \tag{1.38}$$

where, $M \times N$ denotes the size of the image X and

$$\overline{X} = \frac{1}{M \times N} \sum_{m=1}^{M} \sum_{n=1}^{N} |X(m,n)| \tag{1.39}$$

Entropy (EN): The entropy of an image is a measure of its information content. It is the average number of bits needed to quantize the intensities in the image. It is defined as

$$EN = -\sum_{g=0}^{L-1} p(g) \log_2 p(g) \tag{1.40}$$

where $p(g)$ is the probability of grey-level g, and the range of g is [0,.....,L-1]. An image with high information content would have high entropy.

Spatial Frequency (SF): Spatial frequency can be used to measure the overall activity and clarity level of an image. Larger SF value denotes better fusion result and it is calculated as follows:

$$SF = \sqrt{RF^2 + CF^2} \tag{1.41}$$

where, RF is the row frequency and CF is the column frequency:

$$RF = \sqrt{\frac{1}{M \times (N-1)} \sum_{m=0}^{M-1} \sum_{n=0}^{N-2} (X(m, n+1) - X(m, n))^2} \tag{1.42}$$

and

$$CF = \sqrt{\frac{1}{(M-1) \times N} \sum_{m=0}^{M-2} \sum_{n=0}^{N-1} (X(m+1, n) - X(m, n))^2} \tag{1.43}$$

Mutual Information (MI): It measures the degree of dependence between two images. A larger measure implies better quality. In case of MIF, given the fused image Z and two source images X and Y of size $M \times N$ each, MI is defined as [334]:

$$MI = MI(X, Z) + MI(Y, Z), \tag{1.44}$$

where,

$$MI(X, Z) = \sum_{u=1}^{L} \sum_{v=1}^{L} h_{X,Z}(u, v) log_2 \frac{h_{X,Z}(u, v)}{h_X(u) h_Z(v)} \tag{1.45}$$

where, h_X, h_Z are the normalized gray level histograms of X and Z, respectively. $h_{X,Z}$ is the joint gray level histogram of X and Z, and L is the number of bins. $MI(X, Z)$ indicates how much information the fused image Z conveys about the reference X. Thus, the higher the mutual information between Z and X, the more likely Z resembles the ideal X.

$\mathbf{Q^{\frac{XY}{Z}}}$: Given the fused image Z and two source images X and Y of size $M \times N$ each, C. S. Xydeas et al. proposed an objective image fusion performance measure $Q^{XY/Z}$ as follows [335]:

$$Q^{XY/Z} = \frac{\sum_{m=1}^{M} \sum_{n=1}^{N} (Q^{XZ}(m, n) w^X(m, n) + Q^{YZ}(m, n) w^Y(m, n))}{\sum_{m=1}^{M} \sum_{n=1}^{N} (w^X(m, n) + w^Y(m, n))} \tag{1.46}$$

where, $Q^{XZ}(m,n) = Q_g^{XZ}(m,n)Q_\alpha^{XZ}(m,n)$. $Q_g^{XZ}(m,n)$ and $Q_\alpha^{XZ}(m,n)$ are the edge strength and orientation preservation values, respectively. $Q^{YZ}(m,n)$ is similarly computed. $w^X(m,n)$ and $w^Y(m,n)$ reflect the importance of $Q^{XZ}(m,n)$ and $Q^{YZ}(m,n)$, respectively. The dynamic range of $Q^{XY/Z}$ is $[0,1]$, and it should be as close to 1 as possible.

Q_0: It is a universal image quality index proposed by Wang et al. [335]. Q_0, between the source image X and the fused image Z is defined as follows:

$$Q_0(X,Z) = \frac{2\sigma_{XZ} \cdot 2\bar{X}\bar{Z}}{(\sigma_X^2 + \sigma_Z^2) \cdot (\bar{X}^2 + \bar{Z}^2)} \tag{1.47}$$

where, σ_{XZ} represents the covariance between X and Z. σ_X, σ_Z indicate the standard deviations of X and Z; and $\bar{X}$, $\bar{Z}$ represent the mean value of X and Z, respectively. $Q_0(X,Y,Z)$ is the average between $Q_0(X,Z)$ and $Q_0(Y,Z)$:

$$Q_0(X,Y,Z) = \frac{Q_0(X,Z) + Q_0(Y,Z)}{2} \tag{1.48}$$

Note that $-1 \leq Q_0 \leq 1$, and it should be also as close to 1 as possible.

Quantitative evaluation of the proposed image classification and retrieval systems and their performance comparison with other state-of-the-art techniques have been analyzed using the following statistical measures:

Sensitivity (true positive fraction): is the probability that a diagnostic test is positive, given that the person has the disease.

$$Sensitivity = Recall = \frac{TP}{TP + FN} \tag{1.49}$$

Specificity (true negative fraction): is the probability that a diagnostic test

is negative, given that the person does not has the disease.

$$Specificity = \frac{TN}{TN + FP} \tag{1.50}$$

Precision (positive predictive value): is the probability that a person truly has the disease given that his diagnostic test was positive.

$$Precision = \frac{TP}{TP + FP} \tag{1.51}$$

Accuracy: is the probability that a diagnostic test is correctly performed.

$$Accuracy = \frac{TP + TN}{TP + TN + FP + FN} \tag{1.52}$$

where,

TP (True Positive) - correctly classified positive cases,

TN (True Negative) - correctly classified negative cases,

FP (False Positive) - incorrectly classified negative cases, and

FN (False Negative) - incorrectly classified positive cases.

The image quality and quantitative performance measures used to evaluate the performance of the proposed MIW schemes are:

Weighted Peak Signal to Noise Ratio (WPSNR): It uses the principle of redundancy of HVS toward high frequency components in images. WPSNR is nothing but PSNR weighted by HVS parameter and is expressed as:

$$WPSNR = 10 \times log_{10}(\frac{MAX_L^2}{NVF \times MSE}) \tag{1.53}$$

where, NVF is the noise visibility function defined as

$$NVF = NORM(\frac{1}{1+\delta^2_{block}}) \tag{1.54}$$

where, δ_{block} is the standard deviation of block of pixels having a specific size (8×8) and $NORM$ is normalization function used to normalize the NVF value in the range from zero to unity.

Total Perceptual Error (TPE): In this thesis, visual degradation due to watermark embedding is quantitatively measured using the TPE measurement calculated from the Watson Metric [336, 337]. Lower the value of TPE the better the result.

1.4 Scope and Contributions of the Thesis

In this thesis work, several novel solutions have been proposed to solve some diverse problems from four different fields of medical image computing paradigm: medical image enhancement (MRI denoising), multimodal MIF, classification and retrieval of medical images and effective and ethical management of digital medical images and related information through digital watermarking technique.

The guiding motivation behind this thesis work can be summarized as follows: generally, the visual quality of medical images produced by different imaging instruments get deteriorated by various types of noise. This is due to various sources of interference and other physical phenomena that affect the underlying measurement processes in imaging and data acquisition systems. Therefore, it is of paramount importance to improve the visual quality of medical images by some image enhancement techniques. Even though, assuming a medical personnel has high quality medical images for diagnosis and treatment planning. It is

often not possible for a single modality of medical image to provide the medical personnel comprehensive and accurate information. Most of the time, the medical personnel has to observe and analyze multiple medical images of different and same modalities (with different parameter settings), simultaneously, to get the required information. The use of multiple imaging modalities on a single patient, for example MRI and CT or PET requires sophisticated image fusion algorithms to get the complete and quite often complementary information. Moreover, because of the huge amount of imaging data, the existing manual methods of analysis and interpretation of medical images are tedious, time consuming, costly and subject to experience of human observer. This necessitates the requirement of developing automatic classification and retrieval techniques to draw quicker and easier inferences from the medical images. Finally, the widespread and convenient availability of digital data has spurred the search for efficient and ethical management technique for medical images and related information. Consequently, there is a need to design a system for effective storage, access controlling and manipulation restriction of medical images and related information, keeping the authenticity, integrity and confidentiality requirements of medical data intact for effective and ethical management purposes.

1.4.1 Problem Definitions

Within the previously described scope of the thesis, few problems in various medical image computing sub-domains have been identified. Specifically, the problems for which some novel efficient solutions have been proposed in this thesis can be listed as follows:

1. This problem is related to MR image denoising by the popular NLM filtering technique. Specifically, the problem is how to reduce the computational

complexity of NLM filtering technique without sacrificing the denoising performance.

2. What could be an effective saliency measure to identify the important information (pixel/coefficents/features etc.) from multimodal source medical images? Moreover, how to incorporate intrinsic subtle details of the source medical images into the fused image to improve the result? Furthermore, how to automatically estimate the proper values of the parameters used in MIF techniques?

3. How to construct compact and effective feature vector representations by capturing the intrinsic subtle details of the medical images for efficient classification and retrieval purposes?

4. How can MIW technique be used as an all-in-one solution tool to effectively and ethically manage various critical issues of medical images and its related information? Moreover, to increase the applicability of MIW scheme, how could we make it robust to high compression and various common watermarking attacks?

1.4.2 Contributions

The research work presented in this thesis, advances knowledge in certain areas of medical image processing, analysis and management domains. Some potential contributions of the research outcomes are noted below.:

1. Novel denoising technique for MR images, which is not only computationally efficient but also at the same time capable of producing better/comparable denoised results.

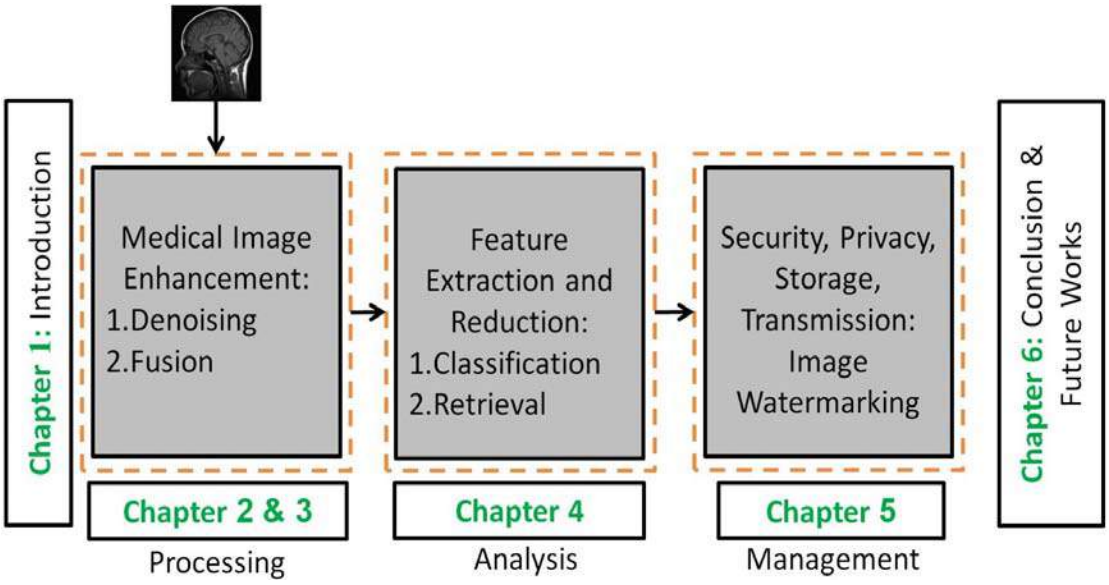

Figure 1.10: Organization of the thesis.

2. Development of novel automatic MIF schemes to integrate complementary and contrasting information from multimodal source medical images for the purpose of better diagnosis and treatment planning.

3. Designing of novel robust classification and retrieval systems for diverse modalities of medical images.

4. Development of novel blind, highly secure MIW techniques for effective and ethical management of medical images and related information.

1.5 Organization of the Thesis

The present thesis comprises of six chapters, four of which describe novel contributions. Chapter-wise organization of the thesis is depicted in the flow diagram of Fig. 1.10 and is described briefly next:

- ***Chapter 1: Introduction***

The present chapter is the first one in this thesis work. This chapter contains the introductory discussion, brief review of related works and overview of rest of the following thesis. A brief theoretical exposition of various techniques/tools used in this thesis is also included here.

- ***Chapter 2: Medical Image Enhancement: MRI Denoising***

  The first contributory chapter of this thesis work present a novel noise removal approach based on PCNN adaptive improved unbiased NLM filter to overcome some of the shortcomings of existing NLM based MR image denoising techniques.

  Some portions of the material in this chapter are from the articles [338, 339] *published by the author.*

- ***Chapter 3: Multimodal Medical Image Fusion***

  This chapter presents two novel multimodal MIF schemes to overcome some of the shortcomings of state-of-the-art MIF methods. The first proposed method is based on MGA of NSCT and modified spatial frequency (MSF) motivated PCNN. The second MIF scheme is also based on NSCT and a reduced PCNN (RPCNN). This approach explores the use of fuzzy logic for building an efficient MIF technique based on HVS response model.

  Some portions of the material in this chapter are from the articles [340, 341] *published by the author.*

- ***Chapter 4: Medical Image Classification and Retrieval***

  In this chapter, two different solutions are proposed for two different medical imaging problems: brain MRI classification and medical image retrieval. The first solution is for classifying normal and abnormal brain MR images based on RT. This method is then improved by making it robust against common

MRI artifacts (rotation, varying dynamic range etc.). The second part of this chapter contains a possible solution to overcome certain shortcomings of the existing CBMIR systems. Here, a novel CBMIR scheme is proposed based on NSCT, clustering mechanism and EMD to retrieve medical images similar to the given query image.

Some portions of the material in this chapter are from the articles [342–344] *published by the author.*

- ***Chapter 5: Medical Image Watermarking***

  Chapter 5 of this thesis work contains two different solutions to problems regarding effective and ethical management of digital medical images and related information. This results in two novel MIW approaches: the first one is based on spatial domain and the other on transform domain.

  Some portions of the material in this chapter are from the articles [345, 346] *published by the author.*

- ***Chapter 6: Conclusion and Future Work***

  The final chapter of the present thesis contains the concluding remarks and direction of future scopes of research.

Chapter 2

Medical Image Enhancement: MRI Denoising

2.1 Introduction

Generally, medical images are corrupted by various types of noise and degradations during their acquisition and transmission. The presence of noise not only produces undesirable visual quality but also lowers the visibility of low-contrast objects. This limits the accuracy of any qualitative as well as quantitative measurements from the medical images [3,13–15,17,19]. As mentioned in the previous chapter that among the different available medical imaging modalities, MRI as a low-risk, fast, non-invasive imaging technique with no ionizing radiation hazard, have become popular in medical domain. Although the resolution, SNR and acquisition speed of MRI technology have improved remarkably over the past several years. Still, presence of noise is one of the main problems of MR images [3, 16, 18, 25]. A brief review of the state-of-the-art MRI denoising schemes is provided in Section 1.2.1 of the previous chapter. Recently, the MRI denoising techniques based on NLM filtering scheme have proven to outperform many of the existing denoising methods. Even though, NLM based MR image denoising schemes provide superior quality denoised MR images, but have some inherent shortcomings. The main problem with NLM based MRI denoising schemes is their

high computational burden. Moreover, negative contributions of non-significant pixels in the denoising procedure also result in sub-optimal quality denoised images [25, 42, 48, 52]. In this chapter, an attempt has been made to overcome these problems by combining the advantages of NLM and PCNN together and develop a novel MRI denoising method[1]. Extensive (both quantitative and qualitative) experiments and comparisons with state-of-the-art MRI denoising techniques have been carried out to evaluate the performance of the developed scheme.

The rest of the chapter is organized as follows. In Section 2.2, noise characteristics of MR images is described. The state-of-the-art of MR image denoising schemes based on NLM method is briefly reviewed in Section 2.3. In Section 2.4, we briefly describe how PCNN can be used for image denoising applications. The developed MR image denoising technique is outlined in Section 2.5. Experimental results and comparisons are presented in Section 2.6.

2.2 Noise in MRI

MRI technology is based on the working principles of nuclear magnetic resonance, in mapping the spatial location and corresponding properties of specific nuclei or protons of the examined subject. This is done using the interaction between an electromagnetic field and nuclear spin. The human body is largely composed of fat and water molecules. Each water molecule has two hydrogen nuclei or protons. These hydrogen protons are usually imaged to describe the physiological or pathological alterations of human tissues [2, 19, 20, 25]. MRI detects and processes the signals generated when hydrogen atoms are placed in strong magnetic field and excited by a resonant magnetic excitation pulse.

As mentioned in the previous chapter that various kinds of artifacts can occur

[1]Details can be found in [338, 339]

in MRI, some affecting the diagnostic quality, while others may be confused with pathology [3,21,22]. The main source of noise in MRI images is the thermal noise in the examined object [14,22,28]. The MR image is commonly reconstructed by computing the IDFT of the raw data. The signal component of the measurements is present in both real and imaginary channels; each of the two orthogonal channels is affected by AWGN. The noise in the reconstructed complex-valued data is thus complex white Gaussian noise [14,21,25,27,29]. Generally, the magnitude of the reconstructed MR image is used for visual inspection and for automatic computer analysis. Since the magnitude of the MRI signal is the square root of the sum of the squares of two independent Gaussian variables, it follows a Rician distribution. In low intensity (dark) regions of the magnitude image, the Rician distribution tends to a Rayleigh distribution and in high intensity (bright) regions it tends to a Gaussian distribution. A practical consequence is a reduced image contrast: noise increases the mean value of pixel intensities in dark image regions [13,29,30].

The complex valued raw MR data acquired in the Fourier domain is characterized by a zero mean Gaussian probability density function (PDF). Due to the linearity and the orthogonality properties of FT, after the inverse FT, the noise distribution in the real and imaginary components still remains Gaussian. However, it is common practice to transform the complex valued images into magnitude and phase images. Since computation of a magnitude (or phase) image is a non-linear operation, the PDF of the MR data changes and it becomes Rician distributed. If A is the original signal amplitude, then the PDF of the reconstructed magnitude image M will be [14,27–29]:

$$p_M(M|A,\sigma) = \frac{M}{\sigma^2} e^{-(\frac{M^2+A^2}{2\sigma^2})} I_0(\frac{AM}{\sigma^2})\varepsilon(M) \tag{2.1}$$

where, $I_0(\cdot)$ represents the 0-th order modified Bessel function of the first kind, $\varepsilon(\cdot)$

the Heaviside step function and σ^2 indicates the noise variance. In high SNR i.e., high intensity (bright) regions of the magnitude imaged, the Rician distribution tends to a Gaussian distribution with mean $\sqrt{A^2+\sigma^2}$ and variance σ^2 can be given as

$$p_M(M|A,\sigma) \approx \frac{1}{\sqrt{2\Pi}\sigma^2} e^{-(\frac{M^2-\sqrt{A^2+\sigma^2}}{2\sigma^2})} \varepsilon(M) \tag{2.2}$$

In case of image background, where SNR is 0 due to the lack of water proton density in the air, the Rician PDF simplifies to a Rayleigh distribution with PDF

$$p_M(M|A,\sigma) = \frac{M}{\sigma^2} e^{-(\frac{M^2}{2\sigma^2})} \varepsilon(M) \tag{2.3}$$

To effectively remove noise from the MR images, the variance of the complex Gaussian noise needs to be estimated. The estimated noise variance gives a measure of the quality of the MR image. In the literature, various methods have been proposed, some needing high SNR regions in the noisy image while others a background region to estimate the noise variance [26, 27, 58, 76, 82].

2.3 NLM in MR Image Denoising

Recently, among these existing noise removal schemes for MR images, methods based on NLM paradigm have gained remarkable popularity [25, 42–45, 52–56]. Originally proposed by Buades et al. [41, 46], NLM is a very simple and effective way to reduce noise while minimally affecting the intrinsic original structures of the image. Based on the concept of natural redundancy of patterns exists in the images, NLM filters estimate the noise-free intensity of a given pixel as a weighted linear combination of the other image pixels' intensities.

In the standard formulation of NLM, given an image X, the filtered value

$NLM(X(p))$ at pixel p with intensity value $X(p)$ is calculated as [41, 46]:

$$NLM(X(p)) = \sum_{\forall q \in \Omega} w(p,q)X(q) \tag{2.4}$$

where, Ω is a large '*search window*' centered at pixel p (in [41, 46] Ω is considered to be the entire image i.e., $\Omega = X$) and $w(p,q)$ is the weight assigned to pixel q with respect to pixel p, according to the similarity between two patches N_p and N_q centered at p and q, respectively, and is calculated:

$$w(p,q) = \frac{1}{Z(p)} e^{-\frac{d(p,q)}{h^2}} \tag{2.5}$$

$$Z(p) = \sum_{q \in \Omega} e^{-\frac{d(p,q)}{h^2}} \tag{2.6}$$

where, $Z(p)$ is a normalizing constant: $\sum_q w(p,q) = 1$, and $0 \leq w(p,q) \leq 1$. The parameter h is an exponential decay control parameter and d is the Gaussian weighted Euclidean distance of all the pixels of each neighborhood:

$$d(p,q) = G_p ||X(N_p) - X(N_q)||^2_{R_{sim}} \tag{2.7}$$

where, G_p is a normalized Gaussian weighting function with zero mean and σ standard deviation (usually set to 1). $X(N_p)$ is defined as a square '*neighborhood window*' centered around pixel p with a user-defined radius R_{sim}. When $p = q$, the self similarity is very high and thus can produce an over-weighting effect in Eq.(2.4). To solve this problem, $w(p,p)$ is calculated as:

$$w(p,p) = max(w(p,q) \forall q \neq p) \tag{2.8}$$

In [42], Manjon et al. have proposed a Rician-adapted version of the NLM

filter for MR images, overcoming the problem of signal dependant noise bias of MRI. Their scheme, called the unbiased NLM (UNLM) follows the idea of [58], that in the squared magnitude MR image, the noise bias ($2\sigma^2$) is no longer signal-dependant and can be easily removed:

$$UNLM(X) = \sqrt{NLM(X)^2 - 2\sigma^2} \tag{2.9}$$

Several modifications of the original NLM algorithm have been proposed by various researchers for denoising MR images [25]. In [44], Manjon et al. have used a modified version of the original NLM filter for denoising the multi-spectral MRI. In [48], Coupe et al. have proposed a faster, optimized and parallelized (multi-threading) implementation of the NLM filter for 3D MRI denoising. Later, in [43], the authors have extended their work for developing a fully automated and optimized block wise NLM filter for denoising 3D MRI. Wiest-Daessle et al. [52] have modified the NLM algorithm for removing Rician noise from diffusion tensor MRI. To avoid eliminating diagnostically important details/structures from the MR image, Gal et al. have proposed a dynamic NLM filter for denoising dynamic contrast enhanced MR images [53]. The method proposed by Liu et al. [45], outperforms the original NLM and the UNLM. This scheme is an enhancement of the NLM with pre-processing for removing Rician noise in 3D MR images. Manjon et al. [54] have proposed an adaptive NLM for denoising MR images with spatially varying noise levels, such as those obtained by parallel imaging and surface coil acquisitions. Again, in [55], Manjon et al. have described another 3D MR image denoising scheme by exploiting the sparseness and self-similarity properties of the underlying images. In [56], Coupe et al. have proposed an adaptive multi-resolution block wise NLM filter for denoising 3D MR images. A good review of several other variations of NLM filter for MR image denoising is given in [25].

The main drawback of the existing MRI denoising schemes based on NLM filter is the need for very intensive computations due to the reckoning of the squared distance between the comparison pixels. The reason is that the calculation for the similarity weights is performed in a full-space of neighborhood. Moreover, the accuracy of the similarity weights will be affected by the noise and many neighborhood pixels which are remarkably similar to the central pixel are assigned slight results. This leads to bring side effects to the denoising results: image's tissue regions may be weakened, especially small structural details and the distinct edge features etc. For this reason, some alternative techniques have been proposed in the literature to speedup the computation of non-local averages, both for textured or non-textured images [43, 49, 50]. The main objective of this chapter is to describe an efficient way of further reducing NLM filter's computational burden without sacrificing the denoising performance of NLM. For achieving this goal, a novel MR image denoising scheme is proposed, combining together the advantages of NLM (specifically, improved unbiased version of NLM termed as IUNLM) and PCNN. In this regard, our main contribution is the use of image's time matrix information obtained by applying PCNN with null interconnection (PCNNNI) on the image, to pre-select significant pixels in the search window of NLM. In the proposed technique this pre-selection helps in finding the significant pixels only for which the distances are calculated in the subsequent phase of the method. As a result of this pre-selection not only the computational burden of NLM filter reduces, but also comparable/better denoised MR images are obtained.

2.4 PCNN for Image Denoising

PCNN is an excellent tool for image processing [322,325,326]. The most convincing evidence comes from its outstanding performance in image denoising. One of the

important properties of PCNN is that it is equally effective in removing impulse as well as Gaussian noise [347–352]. According to the working principle of PCNN, if a neuron is activated at some iteration, at the next iteration those pixels having approximate intensity around it will be activated too. Whereas, if the gray value of a pixel has apparent difference with that of the pixels around it, the neuron corresponding to the pixel will be activated before or after the neurons around it. That is to say it cannot be activated synchronously with the neurons around it. As we know, except for the edges and other directional structures most of the local areas of an image have high correlation. Therefore, if a neuron cannot fires synchronously with others around it, it can be thought that the gray value of the pixel has been degraded by noise, and proper subsequent algorithms should be taken to restore it. The standard PCNN model is described in the previous chapter in Section 1.3.2.

In the proposed scheme, a simplified PCNN is adopted which is known as PCNN with null-interaction (PCNNNI) [322, 350, 353]:

$$U_{m,n}[t] = G_{Feed}e^{-\alpha_F}F_{m,n}[t-1] + S_{m,n} + Y_{m,n}[t-1] \tag{2.10}$$

$$\theta_{m,n}[t] = e^{-\alpha_\theta}\theta_{m,n}[t-1] + V_\theta Y_{m,n}[t] \tag{2.11}$$

$$Y_{m,n}[t] = \begin{cases} 1, & U_{m,n}[t] > \theta_{m,n}[t] \\ 0, & \text{otherwise} \end{cases} \tag{2.12}$$

where, G_{Feed} is the feed gain. The purpose of these modifications is to keep the response of the neuron dependent mainly on the image information and to avoid influence of other neighbor neurons. This allows that the firing time and firing frequency of each neuron depends more directly on the intensity value of the pixel associated to the the neuron element and the temporal information of

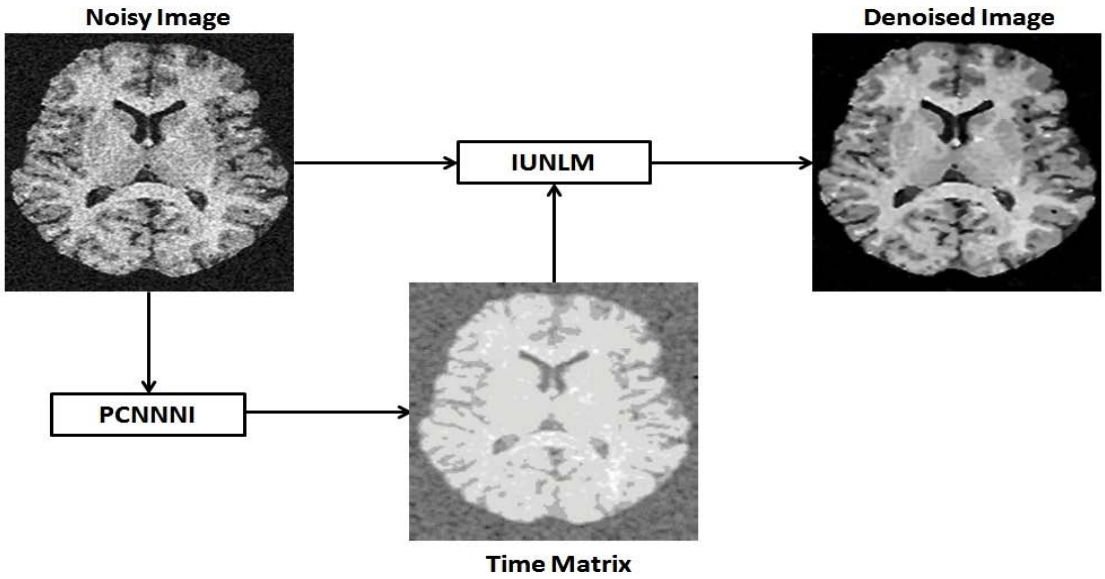

Figure 2.1: Block diagram of PCNNNI_IUNLM.

the neuron [322, 350, 353]. Another reason is that PCNNNI has less number of adjustable parameters than the original PCNN. Finding proper values of these adjustable parameters, itself is a challenging task. Moreover, due to the sensitivity of the HVS to edges and directional features exist in an image, it is observed that the use of single pixel value to activate the neuron of PCNN results in sub-optimal output. Therefore, in the proposed scheme, instead of using the value of a single pixel to motivate one neuron, the local average gray value considering a window surrounding the pixel of interest is used as the input to the PCNNNI's neuron.

2.5 Proposed Method

Integrating the advantages of NLM and PCNN, in this chapter, a novel and efficient MRI denoising scheme is described based on IUNLM and PCNNNI. For simplicity the proposed technique is termed as 'PCNNNI_IUNLM'. The block diagram of PCNNNI_IUNLM scheme is shown in Fig. 2.1. The salient steps of the proposed scheme are as follows:

1. Estimate the noise of the image (noise estimation is described later).

2. Input the normalized and local averaged (considering a window) pixel values of the noisy MR image (X) to motivate the neurons of the PCNNNI and generate pulse of neurons using Eqs.(2.10)–(2.12).

3. Record the PCNNNI's output (time matrix) information G using Eq.(1.19).

4. For every pixel $X(p)$ in the image X use Eq.(2.4) to compute the filtered value following the condition:

$$w(p,q) = \begin{cases} \frac{1}{Z(p)} e^{-\frac{d(p,q)}{h^2}}, & \text{if } Cond_1 \text{ or } Cond_2 \\ 0, & \text{otherwise} \end{cases} \tag{2.13}$$

where,

$$Cond_1 : |G(p) - G(q)| \leq t\sigma \tag{2.14}$$

and,

$$Cond_2 : |Mean(X(N_p)) - Mean(X(N_q))| \leq t\sigma \tag{2.15}$$

where, t represents a "*denoising parameter*". It controls the tradeoff between the denoising performance and computational cost. The parameter σ denotes the standard deviation of the noise.

5. For every pixel in the image calculate the unbiased value by applying Eq.(2.9).

2.6 Results and Discussion

Extensive experiments and comparisons with state-of-the-art methods have been carried out to evaluate the performance of the proposed MRI denoising scheme.

2.6.1 Experimental Setup

To evaluate and compare PCNNNI_IUNLM with state-of-the-art techniques, experiments have been conducted on various $2D$ MR images (both synthetic and real). Parameters of PCNNNI have been set to $\alpha_F = 0.5$, $\alpha_\theta = 0.5$, $V_\theta = 5$, $N = 300$. The value of the denoising parameter t is set to 0.5. These parameter values have been found to provide satisfactory results and estimated experimentally. The parameters of NLM filter have been set as $R_{sim} = 2$, $R_{search} = 5$ and $h = 1.2\sigma$ (as mentioned in [42]). The quantitative measures used in the experiments and comparisons are: RMSE (Eq.(1.32)), PSNR (Eq.(1.33)), MSSIM (Eq.(1.35)) and QILV (Eq.(1.37)). While RMSE and PSNR describe how well noise is removed, MSSIM and QILV indicates how well intrinsic subtle structures are preserved, providing complimentary information. Moreover, among the above mentioned quantitative measures, MSSIM and QILV are more suitable to represent the visual quality of the denoised images as perceived by human. Lower value of RMSE indicates better noise removal performance. Whereas, higher values of PSNR, MSSIM and QILV represent better denoised image. The values of MSSIM and QILV lie in the range of [0,1].

The Rician noise is built from white Gaussian noise in the complex domain:

$$X_r(p) = X_0(p) + \eta_1(p), \eta_1(p) \sim \mathcal{N}(0, \sigma) \tag{2.16}$$

$$X_i(p) = \eta_2(p), \eta_2(p) \sim \mathcal{N}(0, \sigma) \tag{2.17}$$

where X_0 is the “ground truth" and σ is the standard deviation of the added white Gaussian noise. Finally, the noisy image is computed as follows:

$$X_N(p) = \sqrt{X_r(p)^2 + X_i(p)^2} \tag{2.18}$$

During the experiments, MR images have been contaminated by several levels of Rician noise $[1\%, 3\%, 5\%, 7\%, 9\%, 11\%, 13\%, 15\%]$. In this regard, $x\%$ represents the standard deviation $(xb/100)$ of the added zero-mean white Gaussian noise, where b is the value of the brightest tissue in the image.

The demonstrated denoising scheme has been compared with the standard NLM implementation proposed by Buades et al. [46] and the unbiased version of NLM (UNLM) proposed by Manjon et al. [42]. In literature, there exists several modified NLM filters with improved computational complexity (based on PCA, block selection etc.) [43, 50, 54]. But in this chapter, we only choose to compare PCNNNI_IUNLM with the above mentioned schemes, because our goal is to propose an alternate way of pixel pre-selection, and we believe this modification can be incorporated with more improved versions of the NLM filters–resulting in further improvement. Moreover, as we have only concentrated on 2D MR images, therefore, it would be improper to compare the described technique with existing schemes for 3D MR images.

2.6.2 Analysis and Discussion

Both qualitative as well as quantitative evaluation have been performed to find out the effectiveness of PCNNNI_IUNLM. Some of the denoised MR images obtained by PCNNNI_IUNLM are shown in Fig. 2.2. In Fig. 2.2, the original noise-free images are shown in the first row and the corresponding noisy (Rician noise level = 9%) images are shown in the second row, respectively. The denoised images obtained by PCNNNI_IUNLM, are shown in the third row of Fig. 2.2.

In the described denoising technique the "*denoising parameter*" t plays an important role. It affects both the visual quality of the denoised image as well as the time requirement of PCNNNI_IUNLM. The graphs of Fig. 2.3, show the perfor-

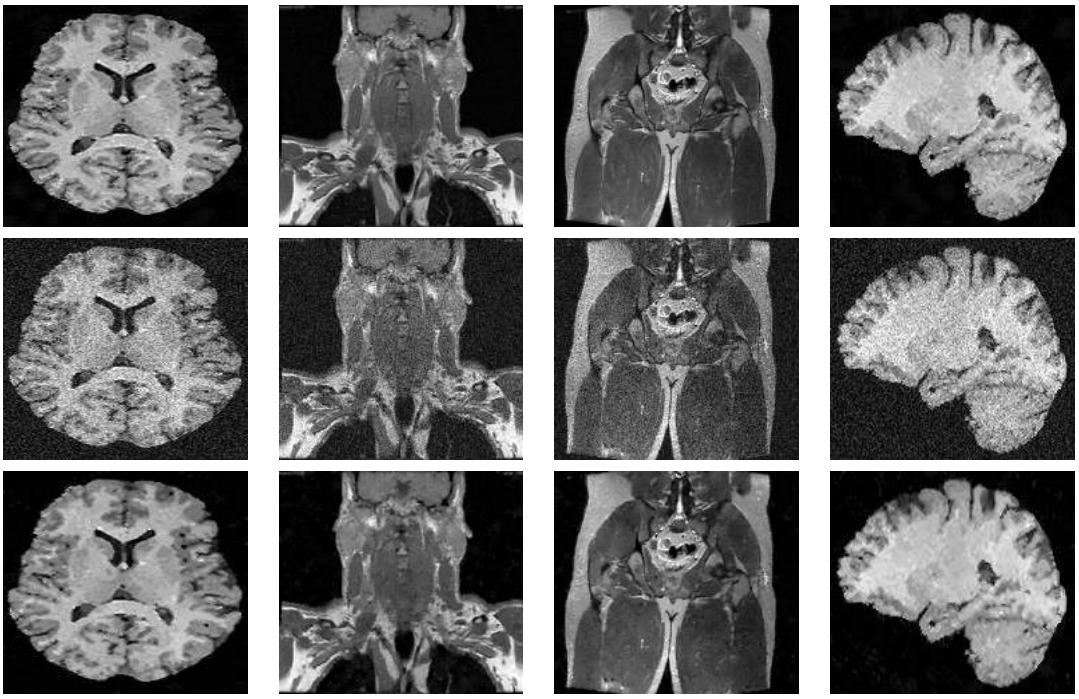

(a) (b) (c) (d)

Figure 2.2: Sample MR images: original images (Row 1), noisy images with Rician noise level = 9% (Row 2) and denoised images (Row 3). MRI images: (a) Synthetic, (b) real 1, (c) real 2 and (d) real 3.

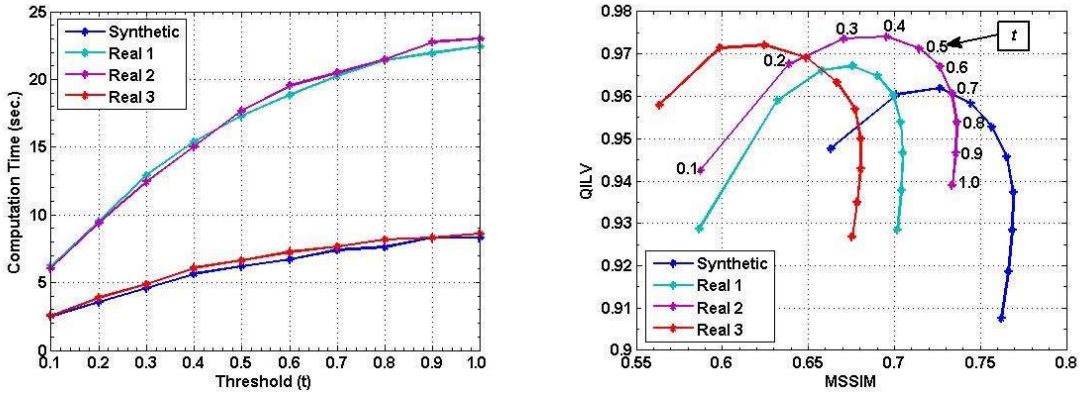

(a) (b)

Figure 2.3: Effect of the "*denoising parameter*" (t).

mance of PCNNNI_IUNLM considering the MR images shown in Fig. 2.2 with different values of t for a fixed noise level 9%. In both the graphs of the Fig. 2.3, the value of t is incremented from 0.1 to 1.0 by step value 0.1. The graph of the Fig. 2.3(a) describes the relationship between t and the time requirement of PCNNNI_IUNLM. It shows that increasing the value of t results in higher computational time requirement by PCNNNI_IUNLM. The reason is that for small value of t, according to Eq.(2.13), we only have to calculate the Gaussian weighted Euclidean distance (by Eq.(2.7)), when the neighborhoods N_p and N_q are very similar to each other. This results in increase in the number of pre-selected pixels for which we do not have to compute the distances by Eq.(2.7). As a result, the time requirement of the described denoising scheme decreases. On the other hand, when t's value is set high, then even for very dissimilar neighborhoods (N_p and N_q), we have to compute the distances, and this results in higher time requirement. Moreover, considering only very similar (low t value) or very dissimilar (high t value) neighborhoods in the weight calculation by Eq.(2.13) affects the denoising performance of PCNNNI_IUNLM. The visual quality (represented by MSSIM and QILV) of the denoised images obtained by PCNNNI_IUNLM with different values of t is shown in the graph of the Fig. 2.3(b). It can be observed from the graph of Fig. 2.3(b) that the visual quality of the denoised images initially improves with different values of t starting from 0.1 up to 0.3. Then, in between 0.4 to 0.6 the visual quality remains more or less similar, and from 0.7 it decreases. From the obtained results shown in Fig. 2.3, it can be said that the optimal value of t lies between 0.4 to 0.6, both inclusive. This leads us to set the value of the "*denoising parameter*" t to 0.5 in PCNNNI_IUNLM.

In order to evaluate the performance of PCNNNI_IUNLM for synthetic MR data, tests have been carried out on the images of BrainWeb database [354, 355]. Experiments have been conducted on 2D slices of 3D image volumes. The images

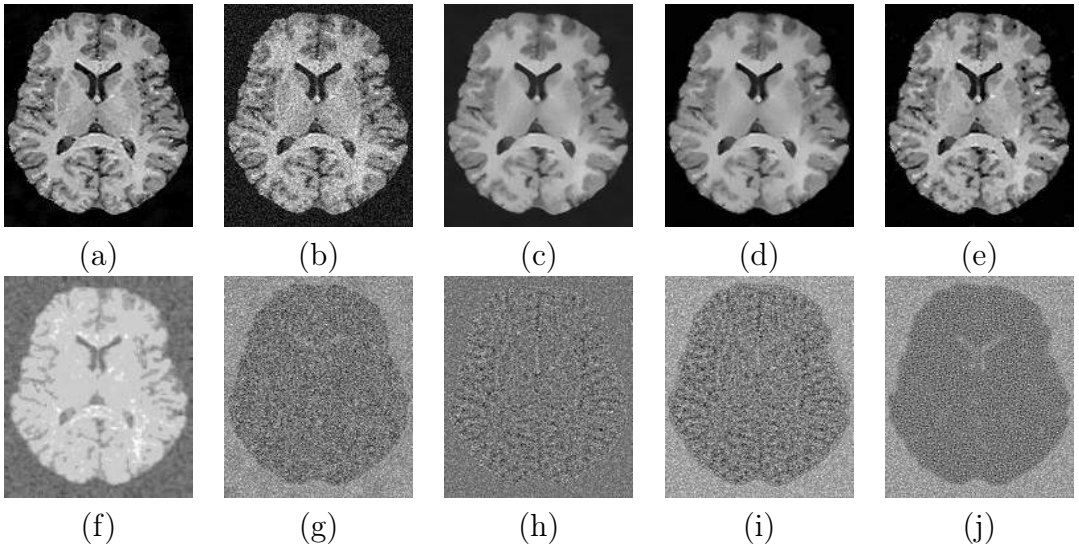

Figure 2.4: Synthetic image data T1-weighted MR image: (a) Noise-free image, (b) noisy image (noise level = 9%), (c) NLM-output [46], (d) UNLM-output [42], (e) PCNNNI_IUNLM output, (f) Time Matrix, (g) actual noise, (h) residual of NLM, (i) residual of UNLM, (j) residual of PCNNNI_IUNLM.

of the Fig. 2.4(c)-(e) show the visual results for a 2D slice of a T1-weighted MR image volume ($181 \times 143 \times 181$ with $1mm^3$ resolution) obtained by PCNNNI_IUNLM method as well as several state-of-the-art existing denoising schemes. It can be observed from the time matrix's image given in Fig. 2.4(f) that even from the noisy image PCNNNI can segregate similar/dissimilar image regions effectively. This helps in pre-classifying the pixels in PCNNNI_IUNLM. The residual images are also shown in (Fig. 2.4(h)-(j)) which are obtained by subtracting the denoised images from the noisy images. Residual images are required to verify the traces of anatomical information removed during denoising: this reveals the excessive smoothing and the blurring of small structural details contained in the images. As can be observed from the residual images of Fig. 2.4 that the schemes NLM [46] and UNLM [42] have removed more anatomical information from the MR image compared to PCNNNI_IUNLM. Moreover, comparing the denoised images shown in Fig. 2.4(c)-(e), it can be clearly observed that the existing NLM and UNLM methods result in a more smoothed/blurred denoised image compared

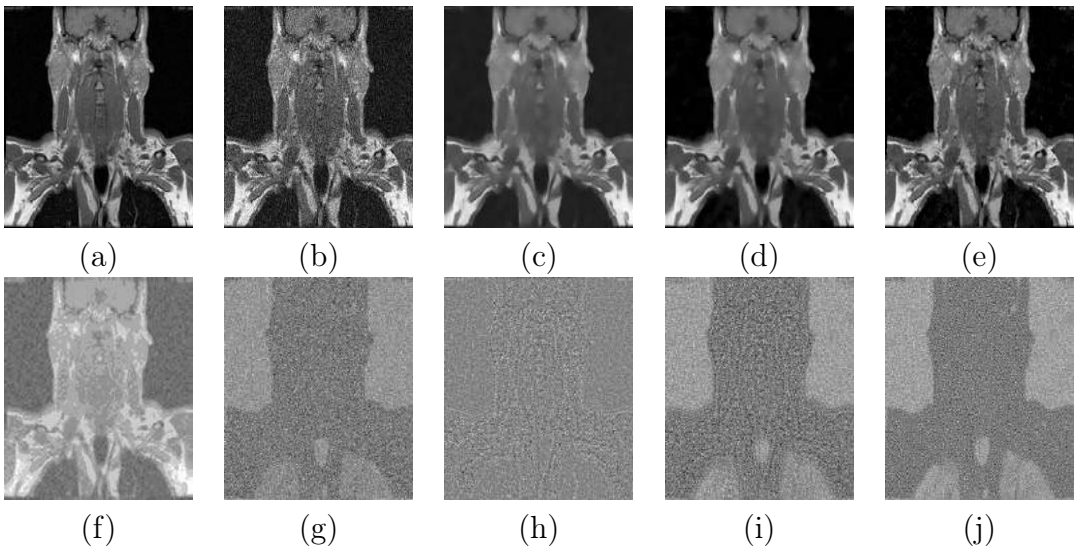

Figure 2.5: Real MR image 1: (a) Noise-free image, (b) noisy image (noise level = 9%), (c) NLM-output [46], (d) UNLM-output [42], (e) PCNNNI_IUNLM output, (f) Time Matrix, (g) actual noise, (h) residual of NLM, (i) residual of UNLM, (j) residual of PCNNNI_IUNLM.

to PCNNNI_IUNLM.

To apply the PCNNNI_IUNLM on real[2] magnitude MR images the standard deviation of the complex Gaussian noise needs to be estimated. In the experiments the noise estimation has been carried out by the method proposed by Rajan et al. [73]. Figs. 2.5-2.7 show the visual performance of PCNNNI_IUNLM in case of real MR images. These figures also contain the denoised and residual images obtained from the different compared denoising techniques for visual comparison. From all the given results for real MR images, it can be easily observed that the denoised images obtained by PCNNNI_IUNLM are producing the superior results compared than the other techniques. This is also evident from the residual images given in Figs.2.5-2.7. It can be clearly seen form these residual images that PCNNNI_IUNLM results in less anatomical information loss and smoothing effects in the denoised images.

The images of the Fig. 2.8, further demonstrate the visual quality improvement of PCNNNI_IUNLM over the existing schemes. The Fig. 2.8 contains the zoomed

[2]Downloaded from http://bigwww.epfl.ch/luisier/MRIdenoising/TestImages.zip

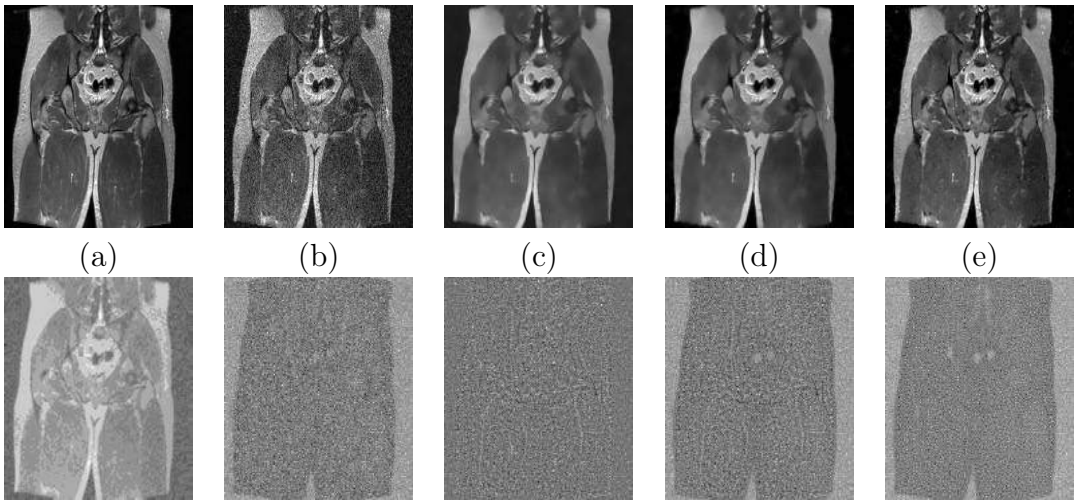

Figure 2.6: Real MR image 2: (a) Noise-free image, (b) noisy image (noise level = 9%), (c) NLM-output [46], (d) UNLM-output [42], (e) PCNNNI_IUNLM output, (f) Time Matrix, (g) actual noise, (h) residual of NLM, (i) residual of UNLM, (j) residual of PCNNNI_IUNLM.

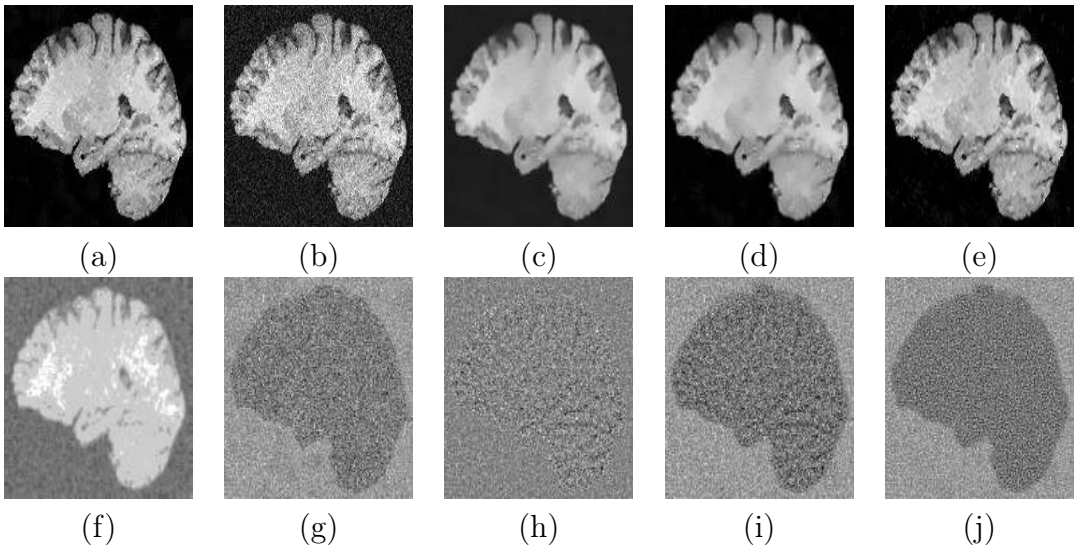

Figure 2.7: Real MR image 3: (a) Noise-free image, (b) noisy image (noise level = 9%), (c) NLM-output [46], (d) UNLM-output [42], (e) PCNNNI_IUNLM output, (f) Time Matrix, (g) actual noise, (h) residual of NLM, (i) residual of UNLM, (j) residual of PCNNNI_IUNLM.

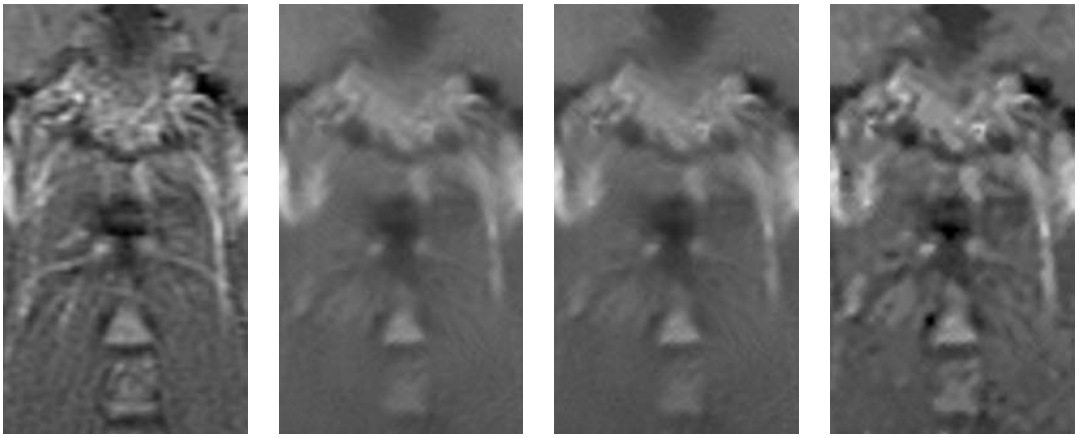

(a) (b) (c) (d)

Figure 2.8: Zoomed in portion of the real MR image 1: (a) noise free, (b) NLM [46], (c) UNLM [42], and (d) PCNNNI_IUNLM.

in portions of the noise free and denoised images of the real MR image 1. From these images, it can be clearly observed that the schemes NLM and UNLM result in over-smoothing of the fine textural and structural details as compared to PCNNNI_IUNLM. Due to the absence of this over-smoothing the denoised images obtained through PCNNNI_IUNLM are visually better than the resultant images obtained by the existing schemes.

The graphs of the Figs. 2.9-2.12, show the performance comparisons of PCNNNI_IUNLM with the existing techniques NLM and UNLM in terms of the quantitative measures RMSE, PSNR, MSSIM and QILV respectively. These graphs show the effectiveness of the different denoising methods with increasing level of noise. In all the cases we have also included the corresponding quantitative measures for the noisy images (represented by the 'red' lines in the graphs). It is clear from the graphs of the Figs. 2.9-2.12 that PCNNNI_IUNLM has superior performance over NLM and UNLM in all the cases. Moreover, it can also be observed from these graphs that the performance of PCNNNI_IUNLM improves significantly for higher level of noise.

The real superiority of the PCNNNI_IUNLM over the other compared meth-

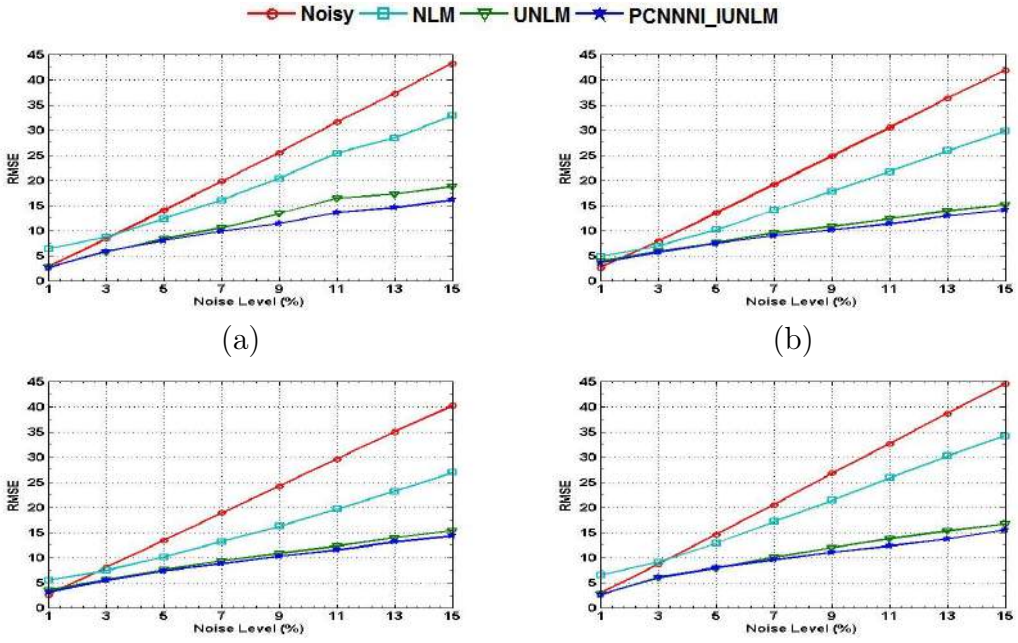

Figure 2.9: Performance comparison in terms of RMSE with different noise levels and image types: (a) synthetic MR image, (b) real MR image 1, (c) real MR image 2, (d) real MR image 3.

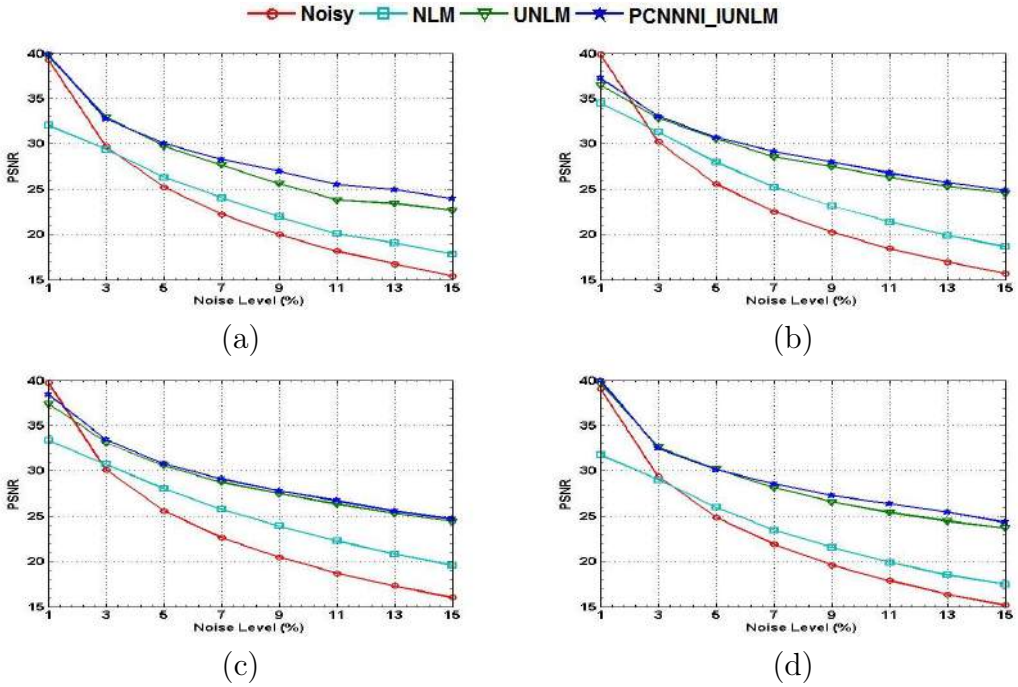

Figure 2.10: Performance comparison in terms of PSNR with different noise levels and image types: (a) synthetic MR image, (b) real MR image 1, (c) real MR image 2, (d) real MR image 3.

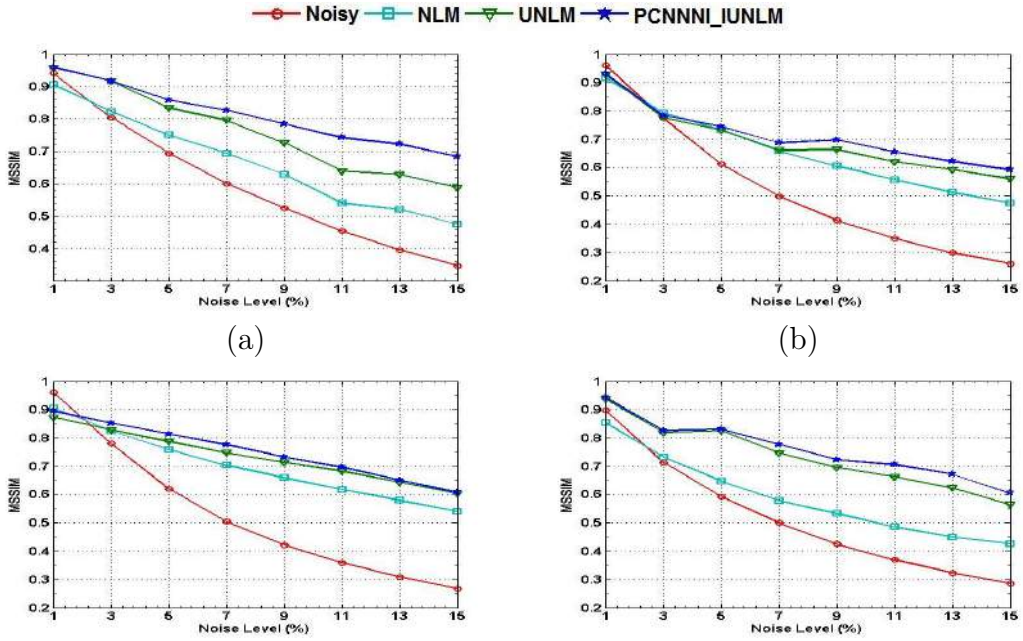

Figure 2.11: Performance comparison in terms of MSSIM with different noise levels and image types: (a) synthetic MR image, (b) real MR image 1, (c) real MR image 2, (d) real MR image 3.

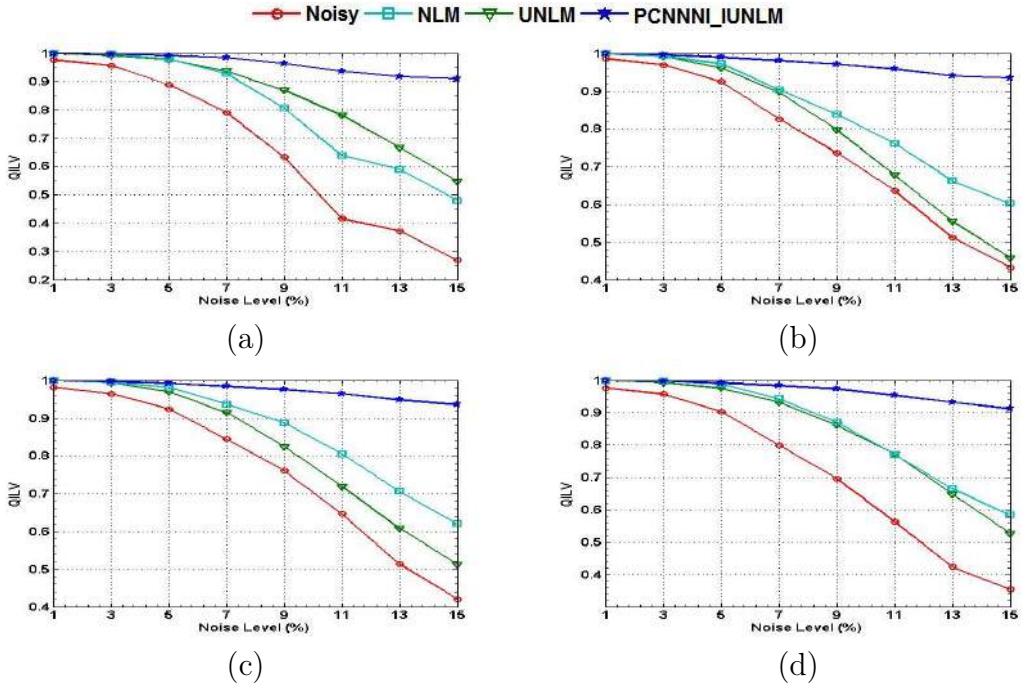

Figure 2.12: Performance comparison in terms of QILV with different noise levels and image types: (a) synthetic MR image, (b) real MR image 1, (c) real MR image 2, (d) real MR image 3.

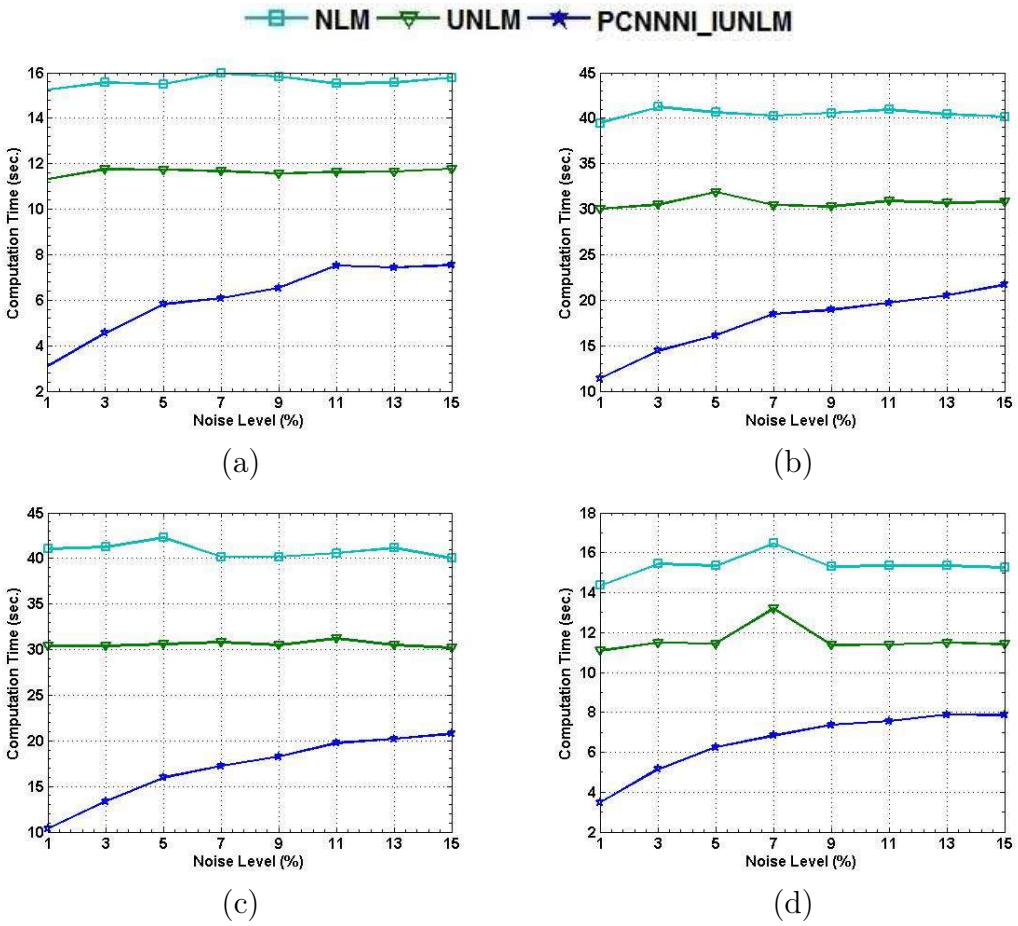

Figure 2.13: Performance comparison in terms of time requirement with different noise levels and image types: (a) synthetic MR image (143 × 181), (b) real MR image 1 (256 × 256), (c) real MR image 2 (256 × 256), (d) real MR image 3 (176 × 141).

ods comes in the form of computational efficiency. This is evident from the graphs of Fig. 2.13. The performance comparison of PCNNNI_IUNLM over the aforementioned existing denoising techniques in terms of actual 'Time (sec.)' requirements are given in Fig. 2.13. It is clear from the Fig. 2.13 that for all the MR images used in the experiments PCNNNI_IUNLM is the least computationally expensive scheme as compared to NLM and UNLM. We can see from the Fig. 2.13 that the denoising methods NLM and UNLM require the near about same amount of time irrespective of the noise amount. But, for PCNNNI_IUNLM the time re-

quirements increases with increase in the noise amount. The obtained results and comparisons with state-of-the-art techniques suggest that the PCNNNI_IUNLM is effective in MRI denoising. The described MR image denoising method not only provides better denoised results, but also is less computationally expensive. Moreover, as both the NLM and the PCNN is highly parallelizable the processing time associated with PCNNNI_IUNLM can be further reduced using distributed computing and more advanced version of the NLM filter.

Even though, noise removal improves the visual quality of the medical images, it is often not possible for a single modality of medical image to provide the medical expert with complete and accurate information. Most of the times, the medical expert has to observe and analyze multiple images (of different modalities or same modality with different settings) of the patient for proper diagnosis and treatment planning. It would be very helpful for the medical expert to have a tool that can efficiently integrate information (complementary and quite often contrasting) from multimodal medical images into a single one. This is a problem of '*information fusion*', and in the next chapter attempts have been made to deal with this problem by some novel MIF schemes.

Chapter 3

Multimodal Medical Image Fusion

3.1 Introduction

With the rapid and significant development in technologies and modern instrumentations, medical imaging is taking on an increasingly critical and vital role in a large number of health-care applications including diagnosis, research, treatment etc. To provide support to the physicians on their clinical diagnosis and treatment, an increasing number of medical image modalities have become available [84–86]. We have seen in the previous chapters that various pre and post processing (enhancement) techniques are required to improve the visual quality of these diverse modalities of medical images. Enhancing the visual quality of the medical images results in higher information content and improves the interpretability, but, as the image formation principles of various medical imaging technologies and instrumentations are different [88, 90–92], they reflect different information of human organs and tissues, and have their respective application ranges. As a consequence, it is often not possible for a single modality of medical image to provide comprehensive and accurate information. For instance, structural images like MRI, CT, USG, magnetic resonance angiography etc. provide high-resolution images containing anatomical information. On the other hand, functional images such as PET, SPECT and functional MRI (fMRI) etc., provide low-spatial resolution images with functional information. While X-ray, CT is the primary modality for most image-based treatment planning, other modalities such as MRI, PET and

SPECT and USG can provide important data that may improve overall patient management [87–89, 107]. As a result, combining multimodal medical images to provide much more useful information through image fusion has become the focus of imaging research and processing [88]. Multiple imaging modalities can complement each other to provide more information for understanding the real world of objects than the use of a single modality. Image fusion aims to generate a single fused image, which contains more precise and reliable visualization of the objects than any one of its source images. Such a fused image should provide extended information and better perception for human vision or computerized vision tasks [83–86].

In recent years, many IF and MIF techniques have been proposed by various researchers. It has been found that the pixel-level spatial domain methods usually lead to contrast reduction. Approaches based on IHS, PCA, and the Brovey transform offer better results, but suffer from spectral degradations. Pyramidal IF schemes fail to introduce any spatial orientation selectivity in the decomposition process, and hence often cause blocking effects [104]. The problem with widely used WT is that it can preserve spectral information efficiently but cannot express spatial characteristics well [105, 123, 124]. As a result, WT based fusion schemes fail to preserve the salient features of the source images efficiently and introduce artifacts and inconsistencies in the fused results [127]. Recently, to overcome these problems, many improved IF/MIF methods based on MGA tools (like curvelet, contourlet, ripplet etc.) are proposed [107, 127]. However, measuring the importance/contribution of individual source image in the fused image, and finding effective way of combining them is still an open problem. Most of the above mentioned schemes are modality specific with their own limitations [114]. The field of MIF is quite different from that of multifocus and visible/infrared IF. Most of the times, there are very subtle differences between the features of

the source medical images. Special care has to be taken during the fusion process of these fine details. Therefore, we need a MIF scheme that can simultaneously handle the problems of contrast reduction, loss of image details and unwanted image degradations. It has been observed that PCNN based IF schemes outperform the conventional IF methods [111, 356–360]. Even though there exists several IF schemes based on transform domain and PCNN, most of these methods suffer from various problems. In [114] Z. Wang. et al. have proposed a fast MIF scheme based on a multi-channel PCNN (m-PCNN) model with easy extensibility capability, producing fused images with high information content, but suffering from the problems of contrast reduction and loss of image fine details. Q. X.-Bo et al. have developed an IF method based on spatial frequency (SF) motivated PCNN in NSCT domain [361]. It works well for multifocus IF and visible/infrared IF, but the absence of directional information in SF and the use of same fusion rule for both the subbands cause contrast reduction and loss of image details. The IF technique proposed by G. Xin et al. based on dual-layer PCNN model with a negative feedback control mechanism in the NSCT domain has shown promising results in multifocus IF [362]. In [359] M. M. Deepika et al. have proposed a combined method of MIF and edge deduction based on NSCT and PCNN. This scheme also suffers from the problems of contrast reduction and unwanted image degradations. The technique proposed by K. Feng et al. in [111] based on bi-dimensional empirical mode decomposition and m-PCNN, shows good result in preserving the source images fine details in the fused image, but suffers from contrast reduction. In most of the existing IF methods based on PCNN the value of a single pixel (coefficient) in spatial or transform domain is used to motivate one neuron [114, 359, 362]. But this simple use of pixels (coefficients) in spatial or transform domain is not effective enough, because humans are sensitive to edges and directional features. In this chapter, two novel MIF techniques ('*Scheme*

1'[1] and '*Scheme 2*'[2]) are presented as possible solutions to the above mentioned information (image) integration problem.

The rest of the chapter is organized as follows: Section 3.2 first introduces the MIF method of '*Scheme 1*'. Subsection 3.2.1 contains the description of modified spatial frequency, which is used as the saliency measure in '*Scheme 1*'. The MIF technique of '*Scheme 1*' is described in Subsection 3.2.2. In Subsection 3.2.3, the experimental and comparative results of '*Scheme 1*' are included. Section 3.3, introduces the second MIF technique ('*Scheme 2*'). In Subsection 3.3.1, a simplified PCNN model is described and the working principles of '*Scheme 2*' is explained in Subsection 3.3.2. The Subsection 3.3.3 contains the experimental results and discussion of '*Scheme 2*'.

3.2 *Scheme 1*: NSCT-based Multimodal MIF using PCNN and MSF

To overcome from the above mentioned shortcomings of the existing MIF schemes, in the next section a novel MIF method ('*Scheme 1*') is described. The main contribution of '*Scheme 1*' is the use of shift-invariance, multiscale and multidirectional properties of NSCT along with the modified spatial frequency (capable of capturing the fine details present in the image) motivated PCNN in such a way that can capture the subtle differences and the fine details present in the source medical images that result in fused images with high contrast, clarity and information content.

[1]Details can be found in [340]
[2]Details can be found in [341]

3.2.1 Modified Spatial Frequency

Spatial frequency (SF) proposed by Eskicioglu et al. is calculated by row and column frequencies [363]. It reflects the whole activity level of an image which means: the larger the SF the higher the image resolution. A modified version of SF is used in '*Scheme 1*'. The MSF consists of row frequency (RF), column frequency (CF) and diagonal frequency (DF). The original SF lacks the directional information present in the image which results in the loss of important fine details of the image. Whereas, MSF incorporates this directional information and this results in an image clarity/activity level measure capable of capturing the fine details present in the image [364]. For an $M \times N$ pixel image X the MSF is defined as

$$MSF = \sqrt{RF^2 + CF^2 + DF^2}, \tag{3.1}$$

where,

$$RF = \sqrt{\frac{1}{M(N-1)} \sum_{m=1}^{M} \sum_{n=2}^{N} [X(m,n) - X(m,n-1)]^2}, \tag{3.2}$$

$$CF = \sqrt{\frac{1}{(M-1)N} \sum_{m=2}^{M} \sum_{n=1}^{N} [X(m,n) - X(m-1,n)]^2}, \tag{3.3}$$

and,

$$DF = P + Q, \tag{3.4}$$

where,

$$P = \sqrt{\frac{1}{(M-1)(N-1)} \sum_{m=2}^{M} \sum_{n=2}^{N} [X(m,n) - X(m-1,n-1)]^2}, \tag{3.5}$$

and,

$$Q = \sqrt{\frac{1}{(M-1)(N-1)} \sum_{m=2}^{M} \sum_{n=2}^{N} [X(m-1,n) - X(m,n-1)]^2}, \tag{3.6}$$

3.2.2 Proposed Method

The notations used in this section are as follows: X, Y, Z represent the two source images and the resultant fused image, respectively. $I = (X, Y, Z)$. L_G^I indicates the low-frequency subband (LFS) of the image I at the coarsest scale G. $D_{g,h}^I$ represents the high-frequency subband (HFS) of the image I at scale g, $(g = 1, ..., G)$ and direction h. (m, n) denotes the spatial location of each coefficient. The method can be easily extended to more than two images.

3.2.2.1 Fusing Low Frequency Subbands

The LFSs coefficients are fused using '*max selection*' rule. According to this fusion rule, select the frequency coefficients from L_G^X or L_G^Y with greater absolute value as the fused coefficients:

$$L_G^Z(m,n) = \begin{cases} L_G^X(m,n), & |L_G^X(m,n)| \geq |L_G^Y(m,n)|, \\ L_G^Y(m,n), & \text{otherwise}, \end{cases} \tag{3.7}$$

3.2.2.2 Fusing High Frequency Subbands

The HFSs of the source images are fused using PCNN. As humans are sensitive to features such as edges, contours etc., so instead of using PCNN in NSCT domain directly (i.e., using individual coefficients), MSF in NSCT domain is considered as the image feature to motivate the PCNN. Let, $MSF_{m,n}^{g,h,I}$ be the modified spatial frequency corresponding to a coefficient $D_{g,h}^I(m,n)$, measured by using an overlapping window around the concerned coefficient where $I = (X, Y)$. In order to reduce the computational complexity, we use a simplified PCNN:

$$F_{m,n}^{g,h,I}[t] = MSF_{m,n}^{g,h,I}, \tag{3.8}$$

$$L_{m,n}^{g,h,I}[t] = e^{-\alpha_L} L_{m,n}^{g,h,I}[t-1] + V_L \sum_{k,l} W_{m,n,k,l}^{g,h,I}\ Y_{m,n,k,l}^{g,h,I}[t-1], \tag{3.9}$$

$$U_{m,n}^{g,h,I}[t] = F_{m,n}^{g,h,I}[t](1 + \beta L_{m,n}^{g,h,I}[t]), \tag{3.10}$$

$$Y_{m,n}^{g,h,I}[t] = \begin{cases} 1, & U_{m,n}^{g,h,I}[t] > \theta_{m,n}^{g,h,I}[t], \\ 0, & \text{otherwise}, \end{cases} \tag{3.11}$$

$$\theta_{m,n}^{g,h,I}[t] = e^{-\alpha_\theta} \theta_{m,n}^{g,h,I}[t-1] + V_\theta Y_{m,n}^{g,h,I}[t], \tag{3.12}$$

where, the feeding input $F_{m,n}^{g,h,I}$ is equal to the modified spatial frequency $MSF_{m,n}^{g,h,I}$. The linking input $L_{m,n}^{g,h,I}$ is equal to the sum of neurons firing times in linking range. $W_{m,n,k,l}^{g,h,I}$ is the synaptic gain strength and subscripts k and l are the size of linking range in the PCNN. α_L is the decay constant. β is the linking strength, V_L and V_θ are the amplitude gains. $U_{m,n}^{g,h,I}$ is the total internal activity and $\theta_{m,n}^{g,h,I}$ is the threshold. If $U_{m,n}^{g,h,I}$ is larger than $\theta_{m,n}^{g,h,I}$, then the neuron will generate a pulse $Y_{m,n}^{g,h,I} = 1$, also called one firing time. The sum of $Y_{m,n}^{g,h,I} = 1$ in t iteration (namely the firing times), is used to represent the image information. Here, rather than $Y_{m,n}^{g,h,I}[t]$, the time matrix ($G_I^{g,h}(m,n)$) information is analyzed, since neighboring coefficients with similar features represent similar firing times in a given iteration time, and it is calculated by the following equation:

$$G_I^{g,h}(m,n) = \sum_{t=1}^{T} Y_{m,n}^{g,h,I}[t], \tag{3.13}$$

3.2.2.3 Algorithm

The medical images to be fused must be registered to assure that the corresponding pixels are aligned. The block diagram of the proposed MIF scheme is shown in Fig. 3.1. Here the salient steps of '*Scheme 1*' is outlined here:

1. Decompose the registered source medical images A and B by NSCT to get

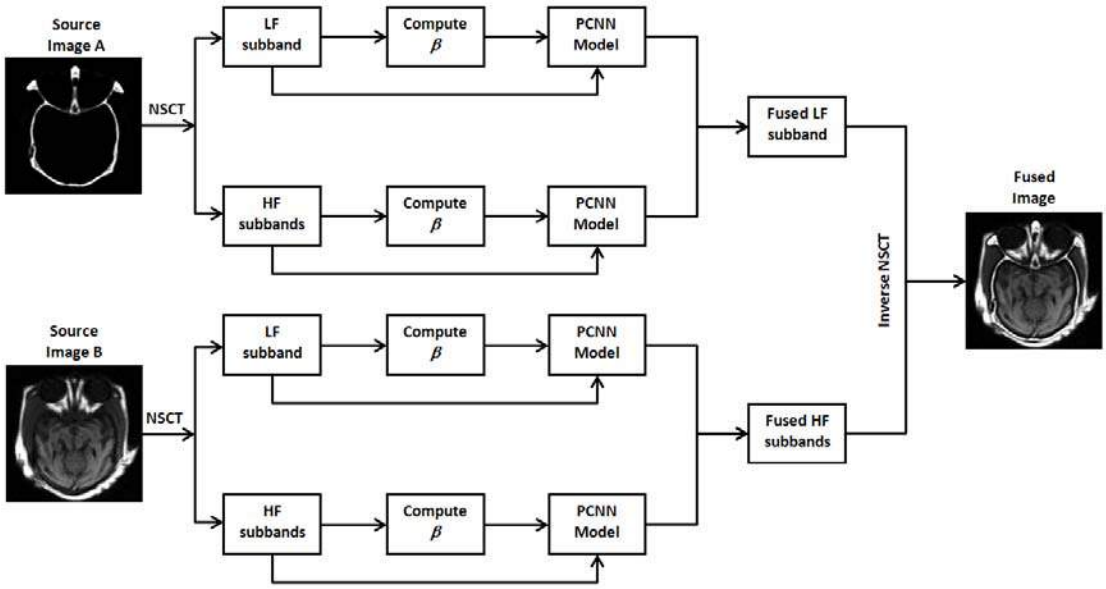

Figure 3.1: Block diagram of the proposed '*Scheme–1*' MIF method.

the LFSs and HFSs.

2. Fused the coefficients of LFSs using the 'max selection' rule described in Section 3.2.2.1, to get the fused LFS.

3. Compute the MSF as described in Section 3.2.1, using overlapping window on the coefficients in HFSs.

4. Input MSF of each HFS to motivate the PCNN and generate pulse of neurons with Eqs.(3.8)–(3.12), and compute the firing times $G_{m,n}^{g,h,I}[t]$ by Eq.(3.13).

5. If $t = T$, then iteration stops. Then fuse the coefficients of the HFSs by the following fusion rule:

$$D_{g,h}^{Z}(m,n) = \begin{cases} D_{g,h}^{X}(m,n), & G_{X}^{g,h}(m,n) \geq G_{Y}^{g,h}(m,n), \\ D_{g,h}^{Y}(m,n), & \text{otherwisee}, \end{cases} \tag{3.14}$$

6. Apply inverse NSCT (INSCT) on the fused LFS and HFSs to get the final fused medical image.

3.2.3 Results and Discussion

To evaluate the performance of '*Scheme 1*', extensive experiments have been carried out on various modalities of medical images. Both objective as well as subjective analysis have been conducted to show the effectiveness of the proposed MIF technique.

3.2.3.1 Experimental Setup

In the experiments regarding the performance evaluation of '*Scheme 1*', the decomposition parameter of NSCT has been set to $levels = [1, 2, 4]$. The '*pyrexc*' and '*vk*' are used as the pyramid filter and orientation filter, respectively. Parameters of PCNN have been set as $k \times l = 3 \times 3$, $\alpha_L = 0.06931$, $\alpha_\theta = 0.2$, $\beta = 0.2$, $V_L = 1.0$, $V_\theta = 20$, $W = [0.707\ 1\ 0.707,\ 1\ 0\ 1,\ 0.707\ 1\ 0.707]$, and $T = 200$. The quantitative measures used in the experiments are STD (Eq.(1.38)), EN (Eq.(1.40)), SF (Eq.(1.41)), MI (Eq.(1.45)), $Q^{XY/Z}$ (Eq.(1.46)) and Q_0 (Eq.(1.48)). To support our choice of MSF over SF, an experiment has been performed, where all the other configurations of '*Scheme 1*' are kept same, only SF has been used instead of MSF (named NSCT_PCNN_SF for convenience).

The Fig. 3.2, shows five pairs of source medical images[3] of different modalities used in the experiments along with the corresponding fused results obtained by '*Scheme 1*'. In Fig. 3.2, Ci $(i = 1, 2, ..., 5)$ indicates the image combinations: $Ci = (xi, yi, zi)$, xi and yi are the two groups of source images and zi represents the fused results. The CT image in Fig. 3.2(x1) shows the bones and the MRI image in Fig. 3.2(y1) displays the soft tissue information. The T1-weighted MR image in Fig. 3.2(x2) contains the soft tissues and it also shows a lesion in the brain, but the vascular nature of the lesion is not clear. The vascular nature of the lesion

[3]Source images are downloaded from http://www.imagefusion.org/; http://www.med.harvard.edu/aanlib/home.html.

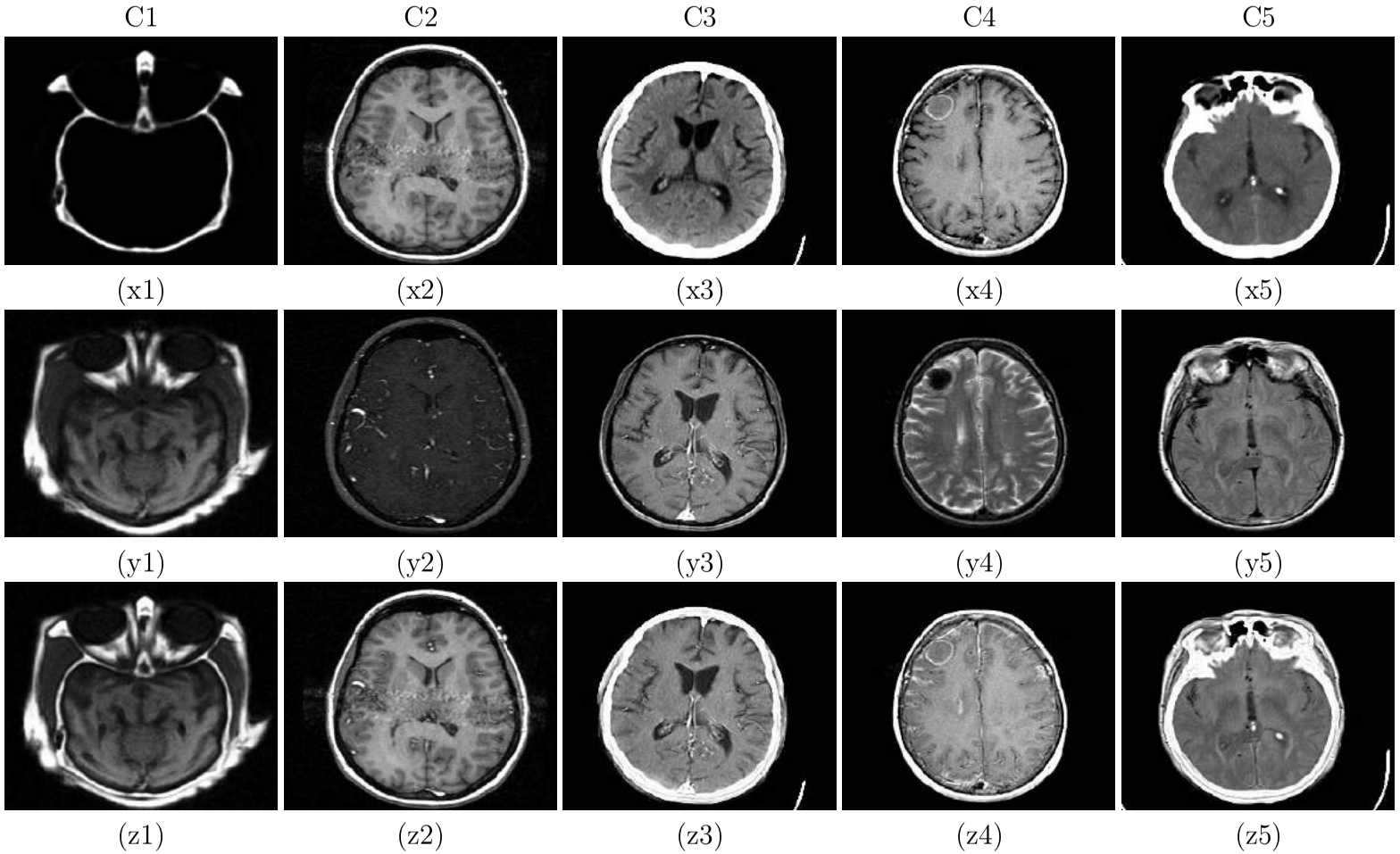

Figure 3.2: Source images (top two rows) with fusion results of '*Scheme 1*' (last row): $x1$ = CT, $y1$ = MRI, $x2$ = T1-weighted MR, $y2$ = MR Angiography , $x3$ = CT, $y3$ = T1-weighted MR-GAD, $x4$ = T1-weighted MR, $y4$ = T2-weighted MR, $x5$ = CT, $y5$ = Proton Density (PD) weighted MR.

is evident in MR Angiography of Fig. 3.2(y2), but the tissue information is low. In Fig. 3.2(x3) and Fig. 3.2(y3), CT image demonstrates the calcification and the MR image reveals several focal lesions involving basal ganglia with some surrounding edema, respectively. Both the MR images of Fig. 3.2(x4) and Fig. 3.2(y4) show a lesion in the frontal lobe. The CT image in Fig. 3.2(x5) indicates a medial left occipital infarct involving the left side of the splenium of the corpus callosum and the MR image in Fig. 3.2(y5) reveals only mild narrowing of the left posterior cerebral artery.

For the five source medical images of Fig. 3.2, the detail quantitative evaluation is given in Table 3.1. The Table 3.2 shows the performance comparisons of '*Scheme 1*' against some of the existing MIF schemes using the images of the image combinations $C1$ and $C5$ as the source images. Fused images for the image combinations $C1$ and $C5$ obtained by the compared methods of Table 3.2 are shown in Fig. 3.3.

3.2.3.2 Subjective Analysis and Discussion

An expert radiologist has been asked to subjectively evaluate the effectiveness of the proposed MIF method. After careful manual inspection of the images of the Fig. 3.2, the radiologist has conformed to the effectiveness of '*Scheme 1*'. He has found that the fused images obtained by '*Scheme 1*' are more clear, informative and have higher contrast than the source medical images that is helpful in visualization as well as interpretation. The fused image of image combination $C1$ contains both the bone structure (from Fig. 3.2(x1)) and the soft tissue information (from Fig. 3.2(y2)). Both the lesion and its vascular nature along with the soft tissue information are evident in the fused image (Fig. 3.2(z2)) of the image combination $C2$. Similarly, the fused images of the other image combinations ($C3$, $C4$ and $C5$) contain information from both the corresponding source images. The

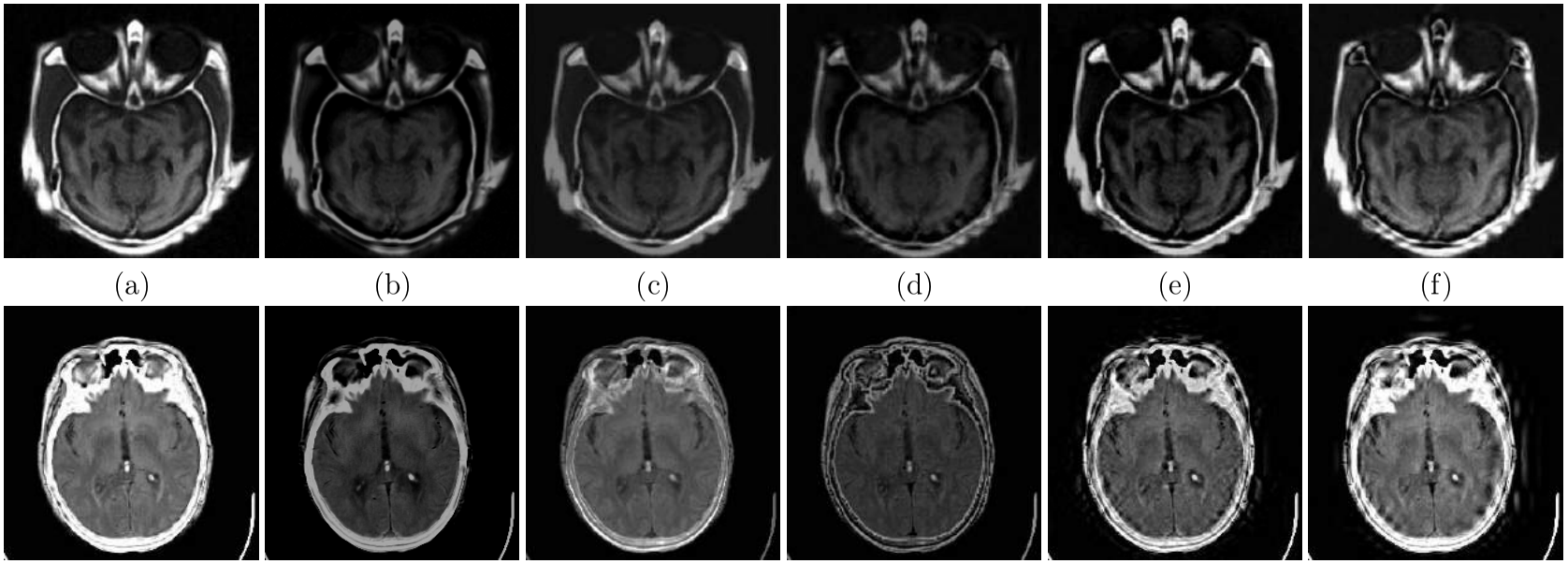

Figure 3.3: Fusion results of '*Scheme 1*' on image combinations $C1$ and $C5$: (a)(g) Method NSCT_PCNN_SF, (b)(h) Method of [361], (c)(i) Method of [114], (d)(j) Method of [124], (e)(k) Method of [127] and (f)(l) Method of [123].

resultant fused images of Fig. 3.3 obtained by the compared methods of Table 3.2 have been also shown to the radiologist. The resultant fused images obtained by NSCT_PCNN_SF are visually very much similar to the fused images obtained by '*Scheme 1*' (as can be seen from the fused images of Figs. 3.2(z1),(z5) and Figs. 3.3(a)(g)). But during the quantitative analysis, it has been found that the fused images obtained by '*Scheme 1*' have higher quantitative results than the method of NSCT_PCNN_SF. All the compared methods of Fig. 3.3 except the schemes of [123] and NSCT_PCNN_SF suffer from the problem of contrast reduction. It is clear from the images of Fig. 3.3 that the methods of [361], [124] and [127] (Figs. 3.3(b)(h),(d)(j) and (e)(k)) have lost large amount of image details. As can be easily seen from the images of Figs. 3.3(d)(j) and Figs. 3.3(f)(l), the methods of [124] and [123] suffer from the problems of blocking effects (as evident from the lower portions of the images) and contain unwanted image degradations.It is also clear from the resultant images given in Fig. 3.2 and Fig. 3.3 that '*Scheme 1*' results in low contrast reduction, high clarity and high information content. The '*Scheme 1*' also causes less unwanted degradations in the fused images, as well as is free from the problem of blocking effects. Therefore, it is clear from the subjective analysis of the fused images that '*Scheme 1*' is very effective in fusing multi-modality medical images and superior than many state-of-the-art MIF techniques.

3.2.3.3 Objective Analysis and Discussion

In Table 3.1, columns 3 to 5 show the spatial frequencies, entropies and standard deviations of the source medical images, and columns 6 to 11 give the values of the different quantitative measures of the fused images obtained by '*Scheme 1*'. The **'bold'** values indicate the highest values in the Table 3.1 for that quantitative measure. The higher values of SF for the image combinations $C1$ to $C4$ indicate

Table 3.1: Performance evaluation of '*Scheme 1*' MIF method

Comb.	Name	SF	EN	STD	Fused Image MI	SF	EN	STD	$Q^{AB/F}$	Q_0
C1	a1	4.4316	1.7126	44.7519	4.8300	**6.9434**	**6.7724**	**65.8646**	0.7771	0.5286
	b1	6.2600	5.6013	58.8283						
C2	a2	7.7005	4.1524	**69.1972**	5.0067	**7.8946**	**6.0659**	68.9896	0.6699	0.6646
	b2	6.4901	4.3310	25.5812						
C3	a3	6.0280	3.3019	79.2907	3.1200	**6.8315**	**4.5234**	**82.3317**	0.5180	0.8990
	b3	7.2990	3.4385	61.7932						
C4	a4	6.9383	3.3046	77.1245	3.4700	**6.9678**	**4.0450**	**79.5945**	0.5410	0.8883
	b4	6.5795	3.2856	52.6946						
C5	a5	4.8089	2.9001	79.8634	3.0593	6.3261	**4.3645**	**83.7037**	0.5338	0.8796
	b5	**6.8405**	3.6014	61.9829						

that the fused images obtained by '*Scheme 1*' have more activity and clarity level than the source images (Fig. 3.2(z5)). Only the proton density weighted MR image (Fig. 3.2(y5)) of image combination $C5$ has the higher value of SF than the fused image (Fig. 3.2(z5)). The reason behind it may be that the CT image (Fig. 3.2(x5)) of the image combination $C5$ contains a thick whitish outer-boundary which become predominant in the fused result. Similarly the higher values of EN for the fused images show that the fused images obtained by '*Scheme 1*' have more information content than the source images. We can also see from the Table 3.1 that the standard deviation's values of the resultant images for 4 out of 5 source image combinations are higher than their corresponding source images, which indicates that the fused images obtained by our proposed MIF method have higher contrast than the corresponding source images. Only in case of image combination $C2$ the STD value of one of the source image Fig. 3.2(x2) (T1-weighted MR) is greater than the fused image (Fig. 3.2(z2)). It may be because of the fact that the other source image Fig. 3.2(y2) (MR Angiograph) of the image combination $C2$ has very low contrast (indicated by low STD value) causing the fused image (Fig. 3.2(z2)) to have a lower STD value (lower by very

Table 3.2: Performance comparison of '*Scheme 1*' using image combinations $C1$ and $C5$

Scheme	Comb.	MI	SF	EN	STD	$\mathbf{Q^{AB/F}}$	$\mathbf{Q_0}$
Scheme [361]	$c1$	2.6817	5.0373	6.2781	29.7318	0.6859	0.4762
	$c5$	2.6651	5.9269	4.2015	55.6347	0.3163	0.7626
Scheme [114]	$c1$	**5.4036**	5.3194	5.8783	33.7291	0.7527	0.5212
	$c5$	**3.1076**	5.9834	4.1933	55.1152	0.4958	0.8578
Scheme [124]	$c1$	2.0575	5.6108	4.9822	33.6529	0.4019	0.4527
	$c5$	2.8041	6.2651	4.1899	56.2076	0.4850	0.7529
Scheme [127]	$c1$	2.5295	6.5575	6.3877	53.8200	0.4537	0.4976
	$c5$	2.4406	6.2136	4.2635	56.5361	0.4371	0.4981
Scheme [123]	$c1$	2.7148	6.6591	6.7295	57.9787	0.5219	0.5071
	$c5$	2.6217	6.1865	4.3216	78.4728	0.4210	0.6150
Scheme NSCT_PCNN_SF	$c1$	4.7477	6.9326	6.7704	65.8304	0.7754	0.5272
	$c5$	2.9788	6.2938	4.3528	81.9448	0.5007	0.8751
'*Scheme 1*'	$c1$	4.8300	**6.9434**	**6.7724**	**65.8646**	**0.7771**	**0.5286**
	$c5$	3.0593	**6.3261**	**4.3645**	**83.7037**	**0.5338**	**0.8796**

small amount). Therefore, it is clear from Table 3.1 that the fused images obtained by '*Scheme 1*' are more clear, informative and have higher contrast which is helpful in visualization and interpretation.

In Table 3.2, the **'bold'** values indicate the highest values. It is clear from the Table 3.2 that '*Scheme 1*' has all the highest quantitative results except for MI. The method of [114] has the highest value for the MI measure. It may be because of the fact that the method of [114] is based on m-PCNN in the spatial (pixel) domain. It preserves the information from both the source images better than '*Scheme 1*'. But since '*Scheme 1*' is based on modified spatial frequency motivated PCNN in NSCT domain, hence it is superior in capturing the fine details of the source images into the fused image. The highest value of SF indicates that the fused image obtained by '*Scheme 1*' has more activity and clarity level than the source images. Similarly the highest values of EN and STD for the fused images show that the fused images obtained by the proposed scheme have more information as well as higher contrast than the source images. It is also clear

from the Table 3.2 that the fused image obtained by NSCT_PCNN_SF has lower quantitative results than the results obtained by '*Scheme 1*' MIF technique. For the other image combinations used in the experiments similar kind of results are obtained.

Although, PCNN based IF/MIF methods outperform other conventional schemes, these approaches have one main shortcoming: PCNN has several parameters with complex structures, and optimal estimation of these parameters is a major limitation for automation and generalization of PCNN based IF/MIF methods. Moreover, from literature it is known that IF/MIF techniques based on HVS response provide better fused results. Incorporating the advantages of PCNN and HVS response, in the next section, a novel MIF scheme ('*Scheme 2*') is described based on a novel parameter estimation technique for PCNN.

3.3 *Scheme 2*: A Neuro-Fuzzy Approach for Medical Image Fusion

In most of the PCNN based IF/MIF techniques, the parameters of PCNN model are kept same and set as a constant. But, according to HVS, the responses to a region with notable features are stronger than a region with non-notable features. Thus, the parameters of PCNN's neurons should be related to the importance (significance) of the features of either the corresponding pixel (in spatial domain) or coefficient (in transform domain) of the image [365–367]. But, the problem remains: how to measure the importance (significance) of the pixel (coefficient) in the corresponding image. Therefore, we not only need a way to adaptively and automatically set the values of the parameters of the PCNN, but also to make the fusion scheme free from the common problems faced by the existing

techniques [368]. In the next section, fuzzy logic is used for building a simultaneous fusion and enhancement technique based on the HVS model to address these above mentioned problems. In this regard, the main contributions of '*Scheme 2*' are as follows: (1) A novel MIF scheme employing NSCT and reduced PCNN (RPCNN) with adaptive linking strengths based on the corresponding image's local features. (2) Following the subjectivity of HVS, fuzzy logic is used to enable the proposed scheme to produce high quality fused images with higher contrast, more clarity and more useful subtle detail information. (3) Without involving any prior training and trials the less complex RPCNN having less number of parameters leads to computational efficiency, which is suitable for real time image processing applications (like point-of-care (POC) health care technologies).

3.3.1 Reduced Pulse Coupled Neural Network

Considering the applications of multimodal MIF, and in order to improve the computational efficiency (in terms of reducing the number of optimizable parameters), in '*Scheme 2*', a simplified model of PCNN known as RPCNN is adapted slightly from [369]:

$$F_{m,n}[t] = S_{m,n}, \tag{3.15}$$

$$L_{m,n}[t] = \sum_{k,l} W_{m,n,k,l} Y_{m,n}[t-1], \tag{3.16}$$

$$U_{m,n}[t] = F_{m,n}[t](1 + \beta L_{m,n}[t]), \tag{3.17}$$

$$Y_{m,n}[t] = \begin{cases} 1, & U_{m,n}[t] > \theta_{m,n}[t], \\ 0, & \text{otherwise}, \end{cases} \tag{3.18}$$

$$\theta_{m,n}[t] = e^{-\alpha_\theta}\theta_{m,n}[t-1] + V_\theta Y_{m,n}[t], \tag{3.19}$$

where, the symbols used in Eqs.(3.15)-(3.19) have usual meaning as described in Section 1.3.2.

Compared to the 9 parameters of the standard PCNN model, the RPCNN contains only 4 key parameters: $W_{m,n,k,l}$, $\beta_{m,n}$, V_θ and α_θ [322,325,369]. Moreover, $W_{m,n,k,l}$ is usually kept unchanged and we set these to the reciprocal of square distance between two pixels (coefficients). Among the remaining three parameters, the linking coefficient β can vary the weighting of the linking channel in the internal activity, and hence is application dependant. Keeping this in mind, the values of the linking strengths (β) are adaptively set based on fuzzy logic approach, and set the values of the other two parameters, heuristically.

3.3.2 Proposed Method

In '*Scheme 2*', coefficients of both LFSs and HFSs are fused in a similar way using RPCNNs with fuzzy-adaptive linking strengths. The notations used are as follows: $I = (X, Y, Z)$ where X, Y, Z represents the two source images and the resultant fused image, respectively. The value $B^I_{g,h}(m, n)$ indicates a coefficient of the subband B of the image I at the scale g $(= 1, ..., G)$ and direction h, where S is the coarsest scale, and (m, n) denotes the spatial location of the coefficient in the subband. The method can be easily extended to more than two images.

3.3.2.1 Fuzzy Adaptive Linking Strength

From PCNN related literature it is known that the linking strength (β) reflects the pixel's (coefficient) characteristics, and should be adaptive to the importance (significance) of the corresponding pixel (coefficient). Moreover, from the HVS model related literature, it has been found that the contrast enhancement mechanism and incremental visual threshold can be effectively model as a non-linear

system, which following the HVS decide visually significant or insignificant pixels with respect to its neighbors [366,370,371]. The uncertainty exists in deciding the visual quality (significance) of the image's pixel (coefficient) and the subjectivity of the HVS response is successfully handled by fuzzy logic approaches [367, 372].

Keeping these in mind, a novel fuzzy based technique is described to adaptively set the value of β, by estimating each coefficient's significance (importance) in the corresponding image. If a coefficient's '*local average energy*' is large or its '*local information entropy*' is large, then the coefficient has more importance in the image. In '*Scheme 2*', $LAE^I_{g,h}(m,n)$ and $LIE^I_{g,h}(m,n)$ are considered as the representations of a coefficient's '*local average energy*' and its '*local information entropy*', respectively. LAE gives information about the existence of edges, contours and textures in an image. Similarly, LIE indicates the complexity or unpredictability of a local region. Regions corresponding to high signal complexity tend to have flatter distributions hence higher entropy and these regions are considered to be the important regions (edges, contours and texture information) of the image [373]. Two fuzzy membership values are computed corresponding to each coefficient $B^I_{g,h}(m,n)$ using the 'S-type' membership function. Considering, $\mu_1(B^I_{g,h}(m,n))$ and $\mu_2(B^I_{g,h}(m,n))$ as the fuzzy membership values associated with $LAE^I_{g,h}(m,n)$ and $LIE^I_{g,h}(m,n)$, respectively, $\mu(B^I_{g,h}(m,n))$ is computed as the membership value associated with the coefficient's larger '*local average energy*' or larger '*local information entropy*'. This $\mu(B^I_{g,h}(m,n))$, reflecting the importance of the coefficient $B^I_{g,h}(m,n)$ in the corresponding image I, is used as the linking strength $\beta^{g,h,I}_{m,n}$.

For a coefficient $B^I_{g,h}(m,n)$, $LAE^I_{g,h}(m,n)$ and $LIE^I_{g,h}(m,n)$ are computed according to the Eq. (3.20) and Eq. (3.21), respectively, considering a window of size

$M \times N$ centered around the coefficient:

$$LAE^I_{g,h}(m,n) = \frac{1}{M \times N} \sum_{m=1}^{M} \sum_{n=1}^{N} B^I_{g,h}(m,n)^2, \tag{3.20}$$

$$LIE(B^I_{g,h}(m,n)) = -\sum p(B^I_{g,h}(m,n)) \log_2 p(B^I_{g,h}(m,n)), \tag{3.21}$$

where, $p(B^I_{g,h}(m,n))$ is the probability of occurrence of the coefficient $B^I_{g,h}(m,n)$.

The fuzzy membership values $\mu_1(B^I_{g,h}(m,n))$ and $\mu_2(B^I_{g,h}(m,n))$ are computed as follows:

$$\mu_1(B^I_{g,h}(m,n)) = \begin{cases} 0, & LAE^I_{g,h}(m,n) \leq a_1, \\ 2(\frac{LAE^I_{g,h}(m,n)-a_1}{c_1-a_1})^2, & a_1 \leq LAE^I_{g,h}(m,n) \leq b_1, \\ 1-2(\frac{LAE^I_{g,h}(m,n)-a_1}{c_1-a_1})^2, & b_1 \leq LAE^I_{g,h}(m,n) \leq c_1, \\ 1, & LAE^I_{g,h}(m,n) \geq c_1, \end{cases} \tag{3.22}$$

and

$$\mu_2(B^I_{g,h}(m,n)) = \begin{cases} 0, & LIE^I_{g,h}(m,n) \leq a_2, \\ 2(\frac{LIE^I_{g,h}(m,n)-a_2}{c_2-a_2})^2, & a_2 \leq LIE^I_{g,h}(m,n) \leq b_2, \\ 1-2(\frac{LIE^I_{g,h}(m,n)-a_2}{c_2-a_2})^2, & b_2 \leq LIE^I_{g,h}(m,n) \leq c_2, \\ 1, & LIE^I_{g,h}(m,n) \geq c_2, \end{cases} \tag{3.23}$$

where,

$$b_1 = average(LAE^I_{g,h}) \tag{3.24}$$

$$c_1 = b_1 + max(|b_1 - max(LAE^I_{g,h})|, |b_1 - min(LAE^I_{g,h})|) \tag{3.25}$$

$$a_1 = 2b_1 - c_1 \tag{3.26}$$

and similarly,

$$b_2 = average(LIE^I_{g,h}) \tag{3.27}$$

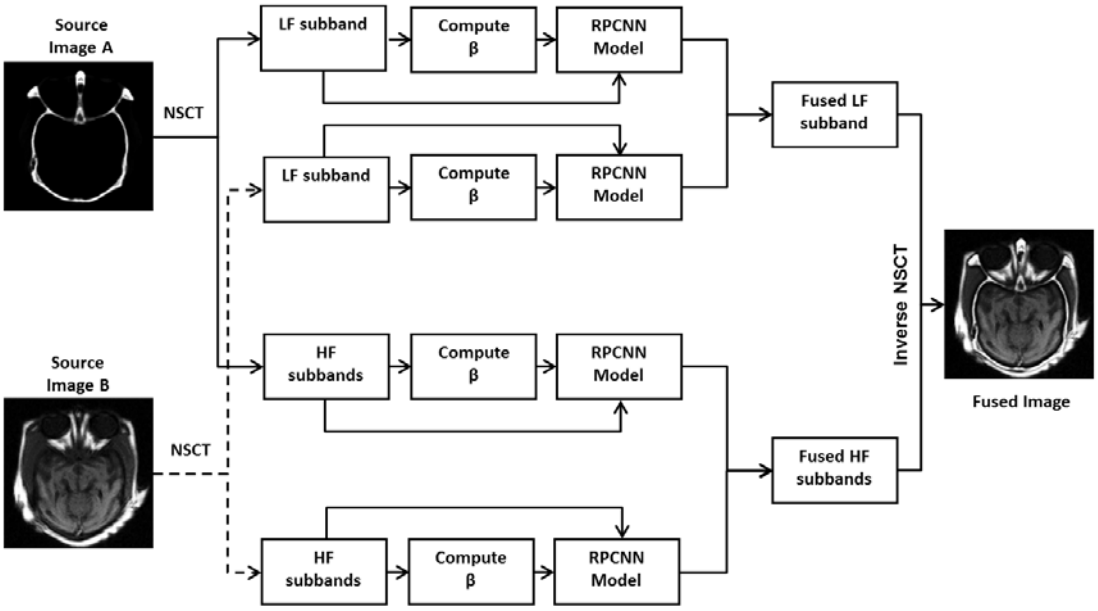

Figure 3.4: Block Diagram of the proposed '*Scheme–2*' MIF method.

$$c_2 = b_2 + max(|b_2 - max(LIE^I_{g,h})|, |b_2 - min(LIE^I_{g,h})|) \tag{3.28}$$

$$a_2 = 2b_2 - c_2 \tag{3.29}$$

where b_i is the cross-over point, c_i is the shoulder point and a_i is the feet point of S type membership curve, $i = 1, 2$ (considering two source images).

The linking strength $\beta^{g,h,I}_{m,n}$ corresponding to the coefficient $B^I_{g,h}(m,n)$ is then computed as follows:

$$\beta^{g,h,I}_{m,n} = max(\mu_1(B^I_{g,h}(m,n)), \mu_2(B^I_{g,h}(m,n))), \tag{3.30}$$

3.3.2.2 Algorithm

The block diagram of '*Scheme 2*' is shown in Fig. 3.4. Assuming that the medical images to be fused are co-registered to ensure that the corresponding pixels are aligned, the salient steps of the '*Scheme 2*' is outlined here:

1. Decompose the registered source medical images P and Q by NSCT to get the LFSs and HFSs.

2. Compute the linking strengths $\beta_{m,n}^{g,h,I}$, $I = (X, Y)$ as described in Section 3.2.2.1.

3. Input the coefficients of the subbands to motivate the RPCNNs and generate pulse of neurons using Eqs.(3.15)–(3.19), and compute the firing times $G_{g,h}^{I}(m,n)$ by Eq. 1.19.

4. At $t = T$ (total number of iterations), determine the fused coefficient $B_{g,h}^{Z}(m,n)$ following the fusion rule:

$$B_{g,h}^{Z}(m,n) = \begin{cases} B_{g,h}^{X}(m,n), & G_{g,h}^{X}(m,n) \geq G_{g,h}^{Y}(m,n), \\ B_{g,h}^{Y}(m,n), & \text{otherwise}, \end{cases} \tag{3.31}$$

5. Apply inverse NSCT on the fused coefficients to get the final fused medical image Z.

3.3.3 Results and Discussion

To evaluate the performance of '*Scheme 2*', extensive experiments have been carried out on various modalities of medical images. Both objective as well as subjective analysis have performed to show the effectiveness of '*Scheme 2*'.

3.3.3.1 Experimental Setup

Parameters of PCNN $k \times l$, α_T, V_T, W and T have been set to the values described in '*Scheme 1*'. The size of the window for computing the local average energy and the local information entropy, has been set as 3×3. The quantitative measures used in these experiments are same as that of the '*Scheme 1*'.

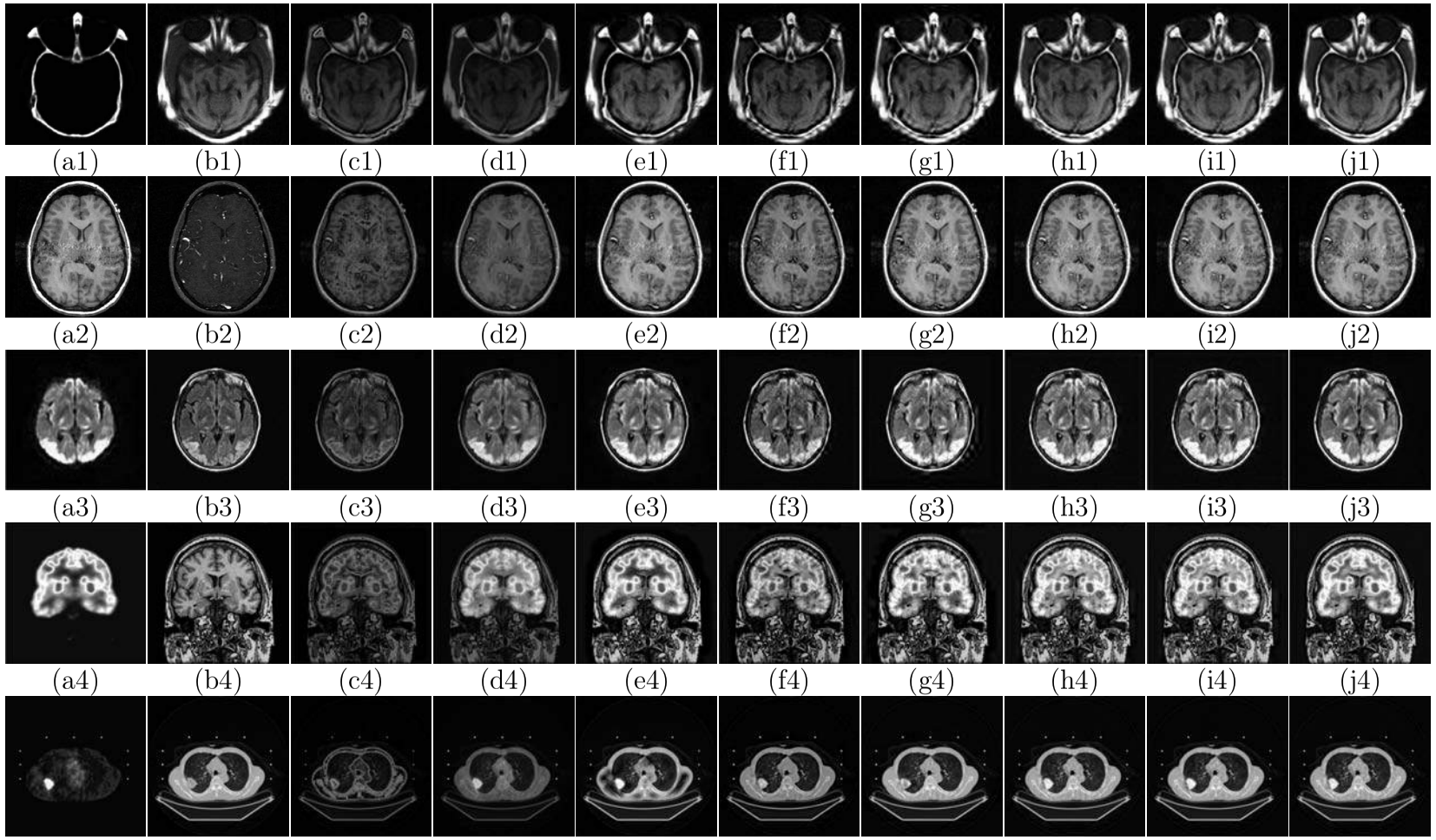

Figure 3.5: Visual results for the five pairs (ak, bk) of source images, $(k = 1, 2, 3, 4, 5)$. Fused images obtained: $c1$-$c5$ by scheme [124], $d1$-$d5$ by scheme [114], $e1$-$e5$ by scheme [361], $f1$-$f5$ by scheme [127], $g1$-$g5$ by scheme [123], $h1$-$h5$ by NFHF-CNT, $i1$-$i5$ by NFHF-CVT, $j1$-$j5$ by '*Scheme 2*'.

The visual and quantitative results for 5 pairs of source images from 5 different combinations are given in this section. For simplicity, the five pairs of source medical images are termed as '*Group 1*' to '*Group 5*', and these are shown in the first two columns of Fig. 3.5. In '*Group 1*' the CT image in Fig. 3.5(a1) shows the bone structure, and the MRI image in Fig. 3.5(b1) displays the soft tissue information. The T1-weighted MR image in Fig. 3.5(a2) contains the soft tissues, and a lesion in the brain, but the vascular nature of the lesion is not clear. The vascular nature of the lesion is evident in MR Angiography of Fig. 3.5(b2), but the tissue information is low. The fluid attenuated inversion recovery (FLAIR) MR image of Fig. 3.5(a3) shows symmetrical signal hyper-intensity of the occipito-parietal cortical ribbon, and the diffusion-weighted (DW) image of Fig. 3.5(b3) shows increased signal in the areas of the FLAIR abnormality. In Fig. 3.5(a4) the coronal F-18 fluorodeoxyglucose (FDG)-PET image provides the metabolic information, whereas, the coronal MR-T1 image of Fig. 3.5(b4) shows the structural information. The FDG-PET image of Fig. 3.5(a5) shows a lesion in the right lung that indicates increased FDG uptake, and the CT image of Fig. 3.5(b5) shows the structural information with exact location of the lesion within the right lung. The '*Scheme 2*' has been compared with five state-of-the-art MIF schemes both subjectively and objectively. The performance of '*Scheme 2*' is also compared with the effectiveness of other MGA-tools such as CNT and CVT. Keeping all the other configurations same NSCT is replaced from '*Scheme 2*' by CNT and CVT for this purpose. In the following discussion, these two MIF techniques are termed as NFHF-CNT and NFHF-CVT, respectively. Even though the visual and quantitative results are provided only for 5 pairs of medical images, for the other source images similar results are obtained.

3.3.3.2 Subjective Analysis and Discussion

An expert radiologist has been asked to subjectively evaluate the effectiveness of '*Scheme 2*. Both the fused images obtained by '*Scheme 2*, and the fused images obtained by the compared schemes are shown to the radiologist. According to the clinician opinion, it can be seen from the given results of Fig. 3.5, that apart from '*Scheme 2*' (Fig. 3.5: j1-j5) and the schemes of [123] (Fig. 3.5: g1-g5) and [361] (Fig. 3.5: e1-e5), all the other compared techniques suffer from the problem of contrast reduction. Moreover, he has found that the fused images obtained by the schemes of [124] (Fig. 3.5: c1-c5), [361] (Fig. 3.5: e1-e5), [127] (Fig. 3.5: f1-f5) and [123] (Fig. 3.5: g1-g5) have lost large amount of image details. Furthermore, he observed that the methods of [127] (Fig. 3.5: f1-f5) and [123] (Fig. 3.5: g1-g5) suffer from the problem of blocking effect (as evident from the lower portions of the images) and contain unwanted image degradations. Whereas, in his opinion, the fused image Fig. 3.5(j1) obtained '*Scheme 2*' for '*Group 1*' source images, contains both the bone structure (from the CT image of Fig. 3.5(a1)) and the soft tissue information (from the MRI image of Fig. 3.5(b1)). The lesion and its vascular nature along with the soft tissue information are evident in the fused image Fig. 3.5(j2) of '*Group 2*'. Both the complementary information from the source images of '*Group 3*' can be clearly seen in the fused image Fig. 3.5(j3). For '*Group 4*', the fused image shown in Fig. 3.5(j4) contains the metabolic information from the FDG-PET image of Fig. 3.5(a4) and the structural information from the T1-weighted MR image of Fig. 3.5(b4). The fused image Fig. 3.5(j5) of '*Group 5*' shows both the structural information (exact location) and the metabolic activity of the lesion in the same image. Finally, after careful inspection of all the resultant images, the clinician has conformed to the effectiveness of '*Scheme 2*. He has found that the fused images obtained by '*Scheme 2*, are clearer, informative and have higher

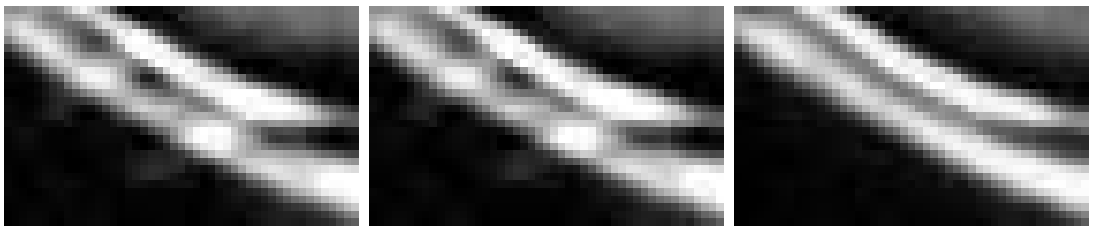

(a) (b) (c)

Figure 3.6: Performance comparison of CNT, CVT and NSCT. Zoomed in versions of '*Group 1*' fused images of Fig. 3.5: (a) $h1$ for CNT, (b) $i1$ for CVT and (c) $j1$ for NSCT.

contrast than the source medical images. For evaluating the efficiency of NSCT over CNT and CVT (NFHF-CNT and NFHF-CVT, respectively), the zoomed in versions of the fused images produced by these MIF schemes are shown to the clinician. The zoomed in version resultant images of '*Group 1*' images, obtained by NFHF-CNT, NFHF-CVT and NFHF-NSCT are shown in '*Scheme 2*. The clinician has conformed that even though, the fused images obtained by NFHF-CNT and NFHF-CVT look similar to the fused images produced by '*Scheme 2*. But, both of these image (CNT and CVT) transforms result in blurring of edges and unwanted image degradations as shown in Fig. 3.6. It can be seen from the resultant images given in Fig. 3.5 and Fig. 3.6 that '*Scheme 2*' results in low contrast reduction, high clarity and high information content. The '*Scheme 2*' also causes less unwanted degradations in the fused images, as well as is free from the problem of blocking effects.

3.3.3.3 Objective Analysis and Discussion

For the five pairs of source medical images the detailed quantitative evaluations are given in Table 3.3. Columns 3 to 5 in the Table 3.3, show the SF, EN and STD of the source medical images, respectively. The values of these quantitative measures of the fused images obtained by '*Scheme 2*' are given in columns 6 to 8 of Table 3.3. The **'bold'** values indicate the highest values in Table 3.3, for that

Table 3.3: Performance evaluation of '*Scheme 2*' MIF method

	Source Image				Fused Image		
Group	**No.**	**SF**	**EN**	**STD**	**SF**	**EN**	**STD**
1	a1	4.4316	1.7126	44.7519	**7.2512**	**6.7918**	**64.6989**
	b1	6.2600	5.6013	58.8283			
2	a2	7.7005	4.1524	**69.1972**	**7.9600**	**6.3514**	69.1150
	b2	6.4901	4.3310	25.5812			
3	a3	10.4970	2.4263	59.7992	10.5607	**5.8155**	**64.4903**
	b3	**12.7502**	2.6375	49.6101			
4	a4	5.1728	3.2840	67.1263	**9.5685**	**6.6329**	**74.2056**
	b4	9.3992	5.3682	64.4280			
5	a5	2.8705	1.9766	19.8552	**5.8448**	**4.9837**	56.5273
	b5	5.6831	5.0498	**56.8748**			

quantitative measure. The highest values of SF for the images of Groups 1,2,4 and 5 indicate that the fused images obtained by '*Scheme 2*' have more activity and clarity level than the source images. Similarly the highest values of EN for the fused images indicate that the fused images obtained by '*Scheme 2*, have more information content than the source images. It can be observed from Table 3.3 that the STD values of the fused images for 3 out of 5 source image combinations are higher than their corresponding source images. This shows that the '*Scheme 2*' produces higher contrast fused images. Only in case of image groups 2 and 5, the STD values of one of the corresponding source images (Fig. 3.5(a2) and Fig. 3.5((b5)) are greater than the fused images. It may be because of the fact that the other source images (Fig. 3.5(b2) and Fig. 3.5(a5)) of the image groups 2 and 5, have very low contrast (indicated by low STD values), causing the fused images to have lower STD values (lower by very small amount). Therefore, it is evident from Table 3.3, that the fused images obtained by '*Scheme 2*' are more clear, informative and have higher contrast which is helpful in visualization and interpretation.

The quantitative performance comparisons of '*Scheme 2*' against some of the

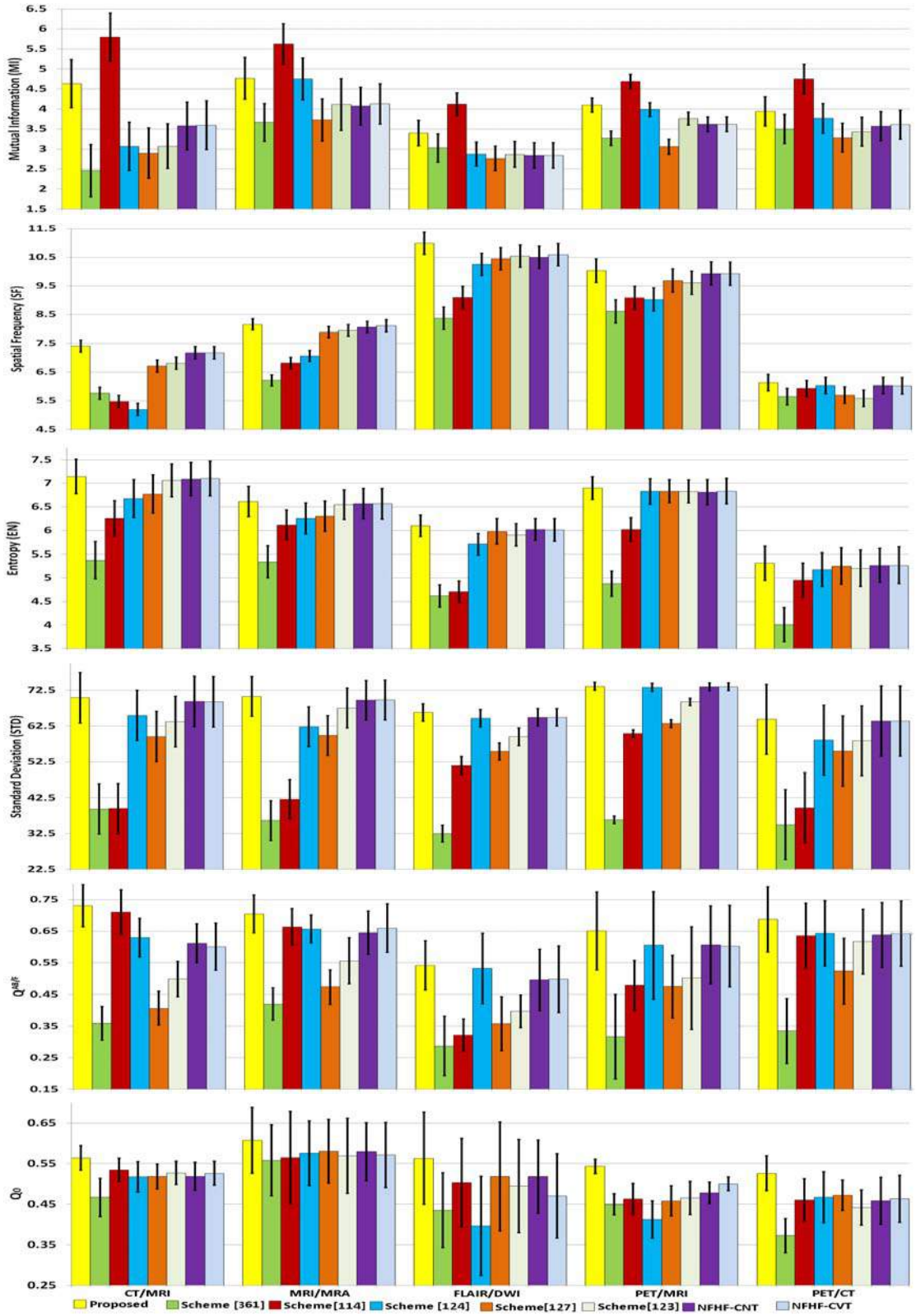

Figure 3.7: Objective performance comparisons of '*Scheme 2*.

existing MIF schemes are given in the Fig. 3.7 in the form of “error bar" plots. Fig. 3.7 shows the average and the standard deviation values of the different measures used in the experiments for all the 7 pairs of source images for all the 5 different groups. It can be seen from Fig. 3.7 that ‘*Scheme 2*’ has all the largest objective measures (5 out of 6), which is obviously better than the other methods. The highest values of SF indicate that the fused images obtained by ‘*Scheme 2*, have more activity and clarity level than the other schemes. Similarly the highest values of EN and STD for the fused images show that the fused images obtained by ‘*Scheme 2*, have more information, as well as higher contrast than the other compared methods. It is also clear that the method [114] is better than ‘*Scheme 2*’ in respect of the quantitative measure MI. It may be because that the method of [114] is based on a multi-channel PCNN in spatial domain, which can retain the source image information in the fused image better than ‘*Scheme 2*. But, ‘*Scheme 2*’ is superior for all other quantitative measures. Moreover, the RPCNN used in ‘*Scheme 2*’ having less complex structure and parameters is computationally efficient than the original PCNN. This helps in reducing the computational cost of the overall system. Specifically, ‘*Scheme 2*’ requires approximately 45 to 55 seconds to fuse a pair of source medical images of size 512×512, irrespective of their modalities. Therefore, it is obvious from Table 3.3 and Fig. 3.7, that the fused images obtained by ‘*Scheme 2*’ MIF method based on hybrid neuro-fuzzy technique and NSCT, are more clear, informative and have higher contrast than the existing mentioned MIF methods.

Even though, the visual quality of the different modalities of medical images are enhanced by some enhancement techniques (denoising, contrast improvement, bias correction, fusion etc.), because of the huge amount of digital medical images (growing every hours), it is often not possible for a medical expert to quickly and correctly search and retrieve relevant information from these vast information

repositories. Development of automated diagnostic tools to draw quicker and easier inferences from these huge databases has become an important area of research in biomedical engineerin. In the next chapter, this '*effective information retrieval*' paradigm in medical domain is explored.

Chapter 4

Medical Image Classification and Retrieval

4.1 Introduction

Due to the large amount of medical images produced every hour, the existing manual methods of analysis and interpretation of these images have become tedious, time consuming, costly and subject to the experience of the human observer. This necessitates the requirement of developing automated diagnosis tools to draw quicker and easier inferences from the medical image repositories [131,136,168,190]. Most often, these diagnostic tools are based on acquisition of relevant, meaningful signals or images from potential subjects and then utilization of certain powerful signal or image processing techniques for automated analysis. The suggested methods for segregation of subjects can vary depending on the type of potential abnormality or disease the subject is suffering from, and the type of signals or images acquired, on the basis of which the inferences have to be drawn [130, 137–139]. As mentioned in Chapter 1, the text based search methodology has several inherent shortcomings. Moreover, it has been found that an effective information retrieval system should have semantics based search capability. But, semantics based information retrieval is still in its infancy stage [374]. As a result, most of the current state-of-the-art medical information retrieval systems are based on search tech-

niques depending on content (low level features) of the underlying subject (text, image, video etc.).

Content based medical image classification and retrieval is a pattern recognition problem in which different images are categorized into several groups based on some similarity measure, by calculating the similarity/dissimilarity between the contents of an image database [131, 169–171]. Apart from high accuracy, the convergence rate of the automated system must also be practically feasible [131, 136, 153, 158, 159]. One important aspect of content based medical image classification and retrieval system is that it is very difficult to construct a generalized feature vector which can represent the contents of diverse modalities of medical images equally effectively. Based on these criteria, several automated systems have been developed for medical image classification and retrieval, mostly specialized on a particular application domain [135, 153, 170, 181, 183–185].

In this chapter, attempts have been made to provide two different solutions to this '*effective information retrieval*' problem in the medical domain. The first solution ('*Scheme 1*'[1]) addresses the automatic classification of normal brain MR images from the abnormal ones. The classification technique of '*Scheme 1*' has been improved in '*Scheme 2*'[2], by making it much more robust in the presence of common MRI artifacts. The second part of this chapter is concerned about efficient content based medical image retrieval, considering diverse modalities of medical images[3].

The rest of the chapter is organized as follows: the brain MR image classification problem is introduced in Section 4.2. '*Scheme 1*' and its improvement, '*Scheme 2*', are described in Section 4.2.1 and Section 4.2.2, respectively. In Section 4.2.3, results obtained by '*Scheme 1*' and '*Scheme 2*' are analyzed and

[1]Details can be found in [342]
[2]Details can be found in [343]
[3]Details can be found in [344]

discussed. The medical image retrieval domain is introduced in Section 4.3. An effective solution to the problems of this field is presented in Section 4.3.1. Performance effectiveness of this solution is discussed in Section 4.3.2.

4.2 Brain MR Image Classification

MRI is a low-risk, fast, non-invasive imaging technique with no ionizing radiation hazard. It provides high quality and high contrast images of anatomical structures as well as functional images of different organs [19, 196]. Soft tissue structures (heart, lungs, liver, brain and other organs) are clearer and more detailed with MRI than other medical imaging modalities. The non-invasive nature of MRI together with its rich information provision, makes MRI the widely used method for diagnosis and treatment planning [20, 196]. Various researchers are not only trying to improve the MR image quality, but also seeking novel methods for easier and quicker inference from these images. In recent years, MRI has emerged as one of the popular choice to study the human brain [197, 198]. MRI can detect a variety of conditions of the brain such as cysts, tumors, bleeding, swelling, developmental and structural abnormalities, infections, inflammatory conditions, or problems with the blood vessels, etc. It can determine whether a shunt is working or not, and detect damage to the brain caused by an injury or a stroke.

However, because of the huge amount of imaging data, the existing manual methods of analysis and interpretation of brain images are tedious, time consuming, costly and subject to fatigue of human observer. This necessitates the requirement of developing automated diagnosis tools to draw quicker and easier inferences from the MR images. These automated systems can be of great help for the medical personnel in diagnosis, prognosis, pre-surgical and post-surgical procedures, etc. [135, 199, 200, 202, 203, 206–210]. One of the most distinguishable

feature of a normal human brain is the symmetry, which is obvious in the axial and the coronal brain MR images. Whereas, asymmetry in an axial MR brain image strongly indicates abnormality/disorder [200,201]. This symmetry-asymmetry can be modeled by various image and signal processing techniques, which can be used to classify the normal and abnormal brain MR images [135, 197, 201].

In recent years, various approaches of brain MR image classification have been proposed by different researchers [205, 210–215]. One of the first solutions was proposed by Chaplot et al. [201]. They have achieved 94% and 98% accuracies on a database consisted of 52 MR images of which 6 are of normal brain and 46 are of abnormal brain, through classifiers based on self-organizing map (SOM) and SVM, respectively. They have used 2 level DWT with '*Db4*' as the mother wavelet for feature extraction. Maitra et al. [204] have employed an improved version of orthogonal DWT called Slantlet transform for MR image feature extraction. They have suggested that Slantlet transform [375] has better time localization properties along with shorter supports for the filters, which is important for capturing the subtle distinguishable features of brain MR images. For each two-dimensional MR image, they have computed its intensity histogram and Slantlet transform is applied on this histogram signal. Then a feature vector, for each image, is created by considering the magnitudes of Slantlet transform outputs corresponding to 6 spatial positions, chosen according to a specific logic. The features hence derived are used to train a neural network based binary classifier, which can automatically infer whether the image is that of a normal brain or a pathological brain, suffering from Alzheimer's disease. Again in [206] they have proposed another unsupervised brain MR image classification system based on fuzzy c-means (FCM) clustering approach and achieving excellent accuracy. In [207], the authors have argued that classification of MRI image along with skull in MR images results in reduction of efficiency to a great extent. Thus, they have proposed a scheme based on skull

stripping prior to classification using gray-level co-occurrence features. Dahshan et al. have proposed a hybrid technique for classification of brain MR images based on reduced (by PCA) DWT features using two different classifiers: feed forward back-propagation artificial neural network (FP-ANN) and K-nearest neighbor (K-NN) [208]. They have achieved 97% and 98% classification accuracy with FP-ANN and K-NN classifier, respectively. In [135], the authors have proposed two novel NNs namely modified counter propagation ANN and modified Kohonen ANN for brain MR image segregation. These novel ANNs are iteration free which ultimately improves the convergence rate besides yielding accurate results.

Zhang et al. have proposed several advanced techniques for brain MR image classification based on various optimization schemes [202, 203, 209]. In [209], they have constructed a 19-dimensional DWT based texture feature vector for every brain MR image and used it to train a feed-forward artificial neural network whose parameters are optimized via adaptive chaotic particle swarm optimization. On a MR brain image database of 160 images (20 normal and 140 abnormal) they have achieved 98.75% classification accuracy. Similarly, in [202] Zhang et al. have used the scaled conjugate gradient technique for faster convergence of the back-propagation neural network classifier and simultaneously achieving high accuracy in classifying normal and abnormal brain MR images. Again, in [200], they have utilized a scaled chaotic artificial bee colony scheme to optimized the parameters of an ANN for brain MR image classification. In, [203] Kernel SVM is used as the classifier by Zhang et al. achieving a classification accuracy of 99.38%.

Exploring the literature of state-of-the-art brain MR image classification techniques, it has been found that most of these schemes suffer from several shortcomings:

- These systems are based on DWT or variants of DWT, which has several inherent problems: limited directionality, non-supportiveness to anisotropy,

etc. As a result, DWT cannot capture the subtle and intrinsic details of the brain MR images, which are required for segregating normal and abnormal cases.

- Although, most of the state-of-the-art schemes utilize PCA for feature reduction to achieve computational efficiency. Because of the DWT + PCA combination, the dimension of the reduced feature vector is still comparatively high.

- Moreover, most of these schemes use neural network with complex weight optimization techniques, which leads to high computational complexity.

- Furthermore, most of the existing techniques lack the generalization capability, as these systems work well on small particular dataset, but, fail to work efficiently for different datasets of various sizes with varying classes of diseases.

The main motivation of the following works is to develop an automatic brain MR image classification system with less computational complexity and high classification accuracy. The other motivation is to make the classification technique general, so that it can work equally efficiently for different brain MR datasets, consisting varying number of disease classes. In general, most of the existing classification systems for brain MR images, consist of three main modules: feature extraction, feature reduction and classification, respectively. Both the classification techniques of '*Scheme 1*' and its improvement in '*Scheme 2*' (described next) consist of similar process blocks.

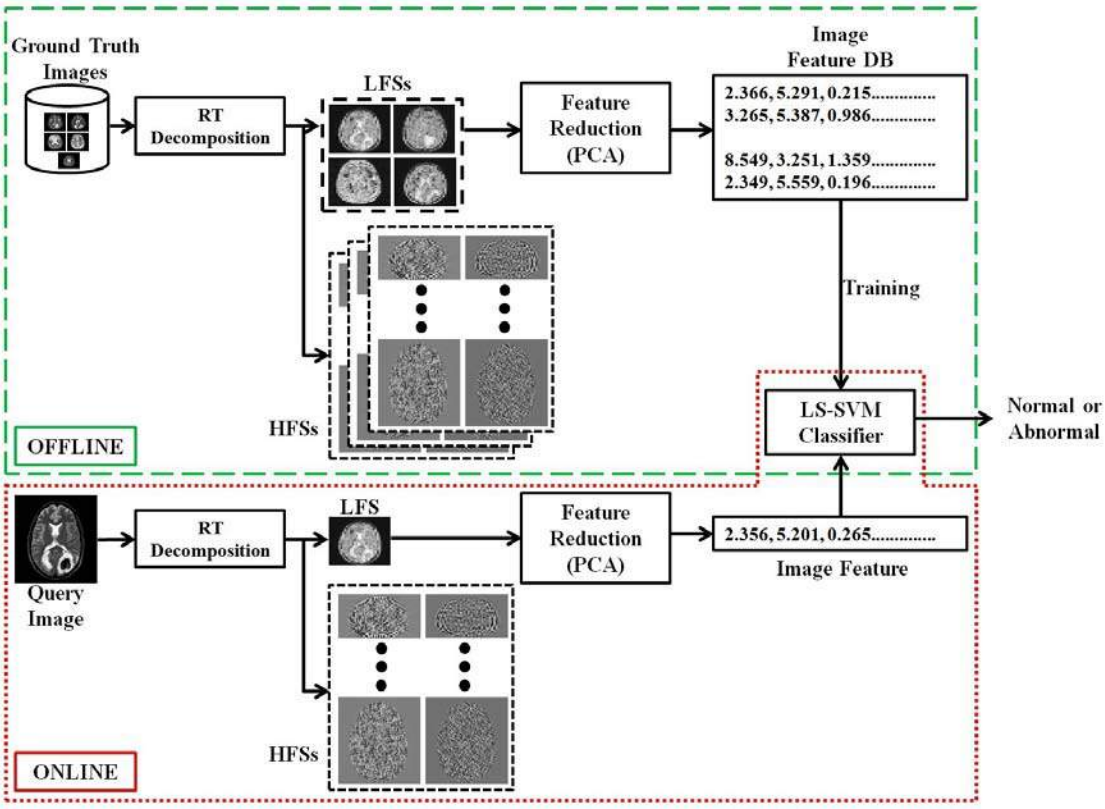

Figure 4.1: Block diagram of '*Scheme 1*'.

4.2.1 *Scheme 1*: Proposed Method

In this section, firstly, the working methodology of '*Scheme 1*' is described. The '*Scheme 1*' consists of two phases as shown in the block diagram of Fig. 4.1– an offline phase and an online phase. Both the phases, consist of the following modules: feature extraction based on RT (Section. 1.3.1.3), feature reduction through PCA [376] and classification by LS-SVM classifier (Section 1.3.3).

4.2.1.1 Feature Reduction

There are two different feature reduction phases in '*Scheme 1*'. Here, these phases are described briefly.

Let, $N \times N$ be the size of a brain MR image I, $N = 2m$, $m \, \varepsilon \, \mathbb{Z}^+$. After applying RT on I, let the size of the decomposed LFS be $M \times M$, $M = 2p$, $p \, \varepsilon \, \mathbb{Z}^+$.

Therefore, the first feature reduction happens for the transition: $N \times N \rightarrow M \times M$, $M < N$.

The second feature reduction is achieved using PCA [376]. Let, T_{var} be the total variance of the original feature set, and S_{var} be the total variance of the reduced feature set having dimension d, $d \ll M^2$. The proper value of d is selected: $\frac{S_{var}}{T_{var}} \backsimeq 0.9$. Let, PER_{red} be the achieved feature reduction percentage.

$$\therefore PER_{red} = \frac{N^2 - d}{N^2} \times 100\ \% \tag{4.1}$$

4.2.1.2 Offline Phase

Let, n be the number of training images of size $N \times N$, $N = 2m$, $m \varepsilon \mathbb{Z}^+$. The salient steps of the offline (training) phase are listed next:

Step 1: The training images are decomposed by RT to get the LFSs and HFSs. Only the LFSs (one LFS/image) are used as features. Let, $M \times M$ ($M < N$) be the size of each LFS, $M = 2p$, $p \varepsilon \mathbb{Z}^+$. A feature matrix X of size $n \times M^2$ is constructed by the coefficients of the LFSs. Each row of X consists of M^2 coefficients belonging to a particular LFS, representing feature vector of dimension M^2 of that image.

Step 2: The dimension of the feature vectors representing the training images is reduced by applying PCA on X from M^2 to d (say), where $d \ll M^2$, following the criteria mentioned in Section 4.2.1.1.

Step 3: The set of reduced feature vectors, along with the class information are used to train a LS-SVM classifier [329]. Cross validation is used for improving the generalization capability of the system.

4.2.1.3 Online Phase

The online phase of '*Scheme 1*' consists of the following steps:

Step 1: The user (doctors, radiologist etc.) inputs the brain MR image of size $N \times N$ to be classified. RT is applied on the input image to get the LFS of size $M \times M$.

Step 2: The dimension of the feature vector representing the input query image is reduced from M^2 to d by applying PCA.

Step 3: This reduced feature vector of dimension d is used as input to the previously trained LS-SVM classifier. The classifier classified the input query image as normal or abnormal.

4.2.2 *Scheme 2*: Proposed Improvement over '*Scheme 1*'

The widely used feature representation scheme for MR image classification based on LFS coefficients of WT is found to be less effective in presence of common MRI artifacts (small rotation, low dynamic range etc.). The directional information presents in the HFSs can be used to improve the performance. Moreover, little attention has been paid to find out the performance effectiveness of the newly developed MGA tools (curvelet, contourlet, and ripplet etc.) in classifying brain MR images. This section presents the improvement strategy '*Scheme 2*' applied to our previously proposed '*Scheme 1*' overcoming the above mentioned problems. In '*Scheme 2*', both the LFS and the HFSs are used to construct image representative feature vector robust to common MRI artifacts. Moreover, the findings of a performance comparison study on various MRA/MGA transforms (such as traditional WT, curvelet, contourlet and ripplet) for brain MR image classification is also discussed here. The investigations presented in this section, include the effect

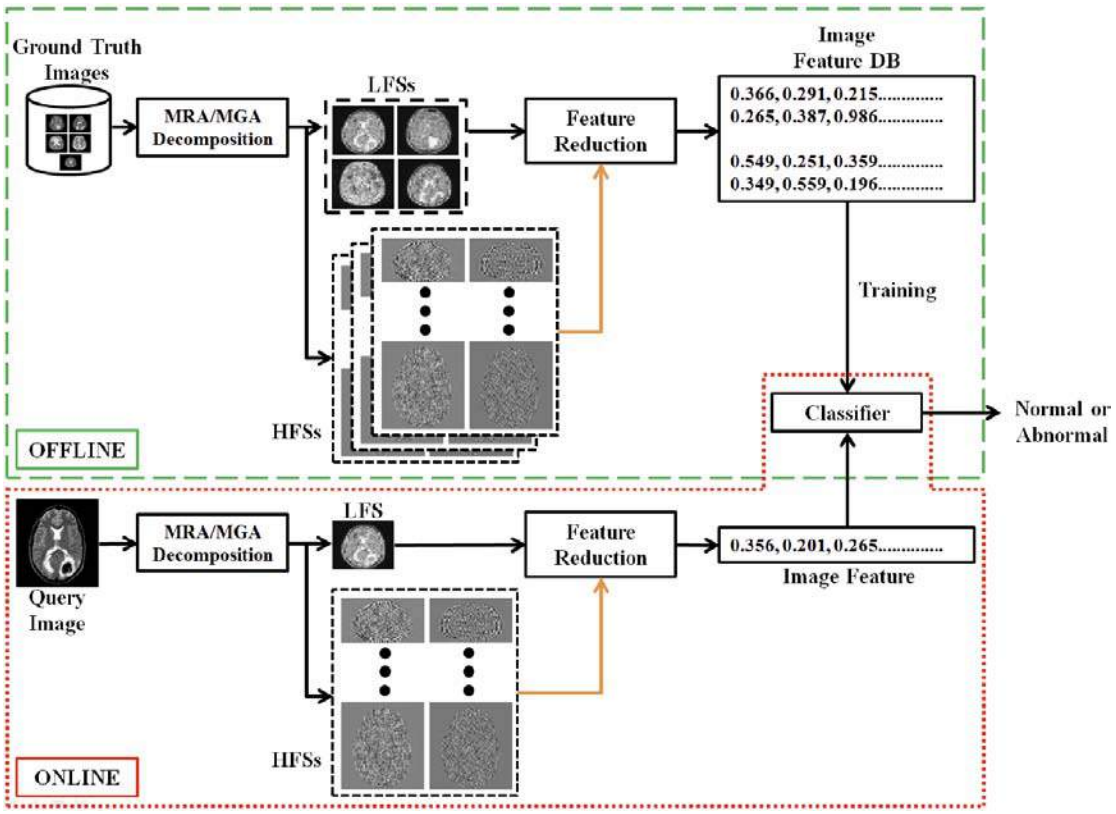

Figure 4.2: Block diagram of '*Scheme 2*'.

of different decomposition levels and filters in classification performance.

Small rotation, low dynamic range, noise etc. are the common artifacts present in today's MR images. The existing brain MR image classification schemes work efficiently for images free from common MRI artifacts, but their performance decrease in presence of these artifacts. The commonly used LFS for representing MR images is ineffective in capturing the subtle details and directional information present in the images. To tackle this problem, in '*Scheme 2*', both the LFS and HFSs coefficients are used during feature extraction. After decomposing the images of the training set through a MRA/MGA transform, the subband's energy for each HFSs are calculated as follows:

$$ENG_s^d = \frac{1}{M \times L} \sum_{x=1}^{M} \sum_{y=1}^{L} |I_s^d(x,y)|^2 \tag{4.2}$$

where, I_s^d is the subband of size $M \times L$ at scale s and direction d, $s = 1, 2, ..., S$, $d = 1, 2, ..., D$. Then the coefficients of the LFSs and the HFSs energies' are passed to PCA for feature reduction, which results in the feature vector of dimension 10 (this value is chosen experimentally). The novel use of HFSs information for feature representation is indicated by "*orange*" colored lines in the block diagram of Fig. 4.2. As can be seen from the block diagram of Fig. 4.2, all the other steps of '*Scheme 2*' are same as '*Scheme 1*' described in Section 4.2.1.

4.2.3 Results and Discussion

Extensive experiments have been carried out to evaluate the performance of the '*Scheme 1*' and its improvement '*Scheme 2*', in brain MR image classification. In the following section the experimental results of '*Scheme 1*' are discussed first, and then, the performance improvement obtained by the '*Scheme 2*' is described.

4.2.3.1 *Scheme 1*: Experimental Results and Comparisons

In the experiments carried out to evaluate the performance of '*Scheme 1*', the decomposition parameter of RT has been set to levels = $[1, 2, 4, 4]$, and '9/7' and '*pkva*' have been used as the pyramid filter and orientation filter, respectively. Three (3) different MR image datasets have been used in the experiments. All the datasets consist of T2-weighted MR brain images in axial plane and 256×256 in-plane resolution, which are downloaded from the website of Harvard Medical Schools[4]. The first two datasets are benchmark datasets, widely used in brain MR image classification problem, and consist of abnormal images from 7 types of diseases along with the normal images. The abnormal brain MR images of the benchmark datasets consist images of the following diseases: glioma, meningioma, Alzheimer's disease, Alzheimer's disease plus visual agnosia, Pick's disease, sar-

[4]URL: http://med.harvard.edu/AANLIB/

coma and Huntington's disease. The first benchmark dataset (Dataset-66) consists of 66 (18 normal and 48 abnormal) brain MR images. There are in total 160 (20 normal and 140 abnormal) brain MR images in the second benchmark dataset (Dataset-160). The third new larger dataset (Dataset-255) consists of 255 (35 normal and 220 abnormal) brain MR images. Abnormal brain MR images of the third dataset are from 11 types of diseases, among which 7 types of diseases are same as the two benchmark datasets, mentioned before. The third dataset also consists abnormal images of 4 new types of diseases: chronic subdural hematoma, cerebral toxoplasmosis, herpes encephalitis and multiple sclerosis. Each of the 11 types of diseases' consists of 20 abnormal brain MR images. Fig. 4.3, shows samples of the brain MR images used in the experiments.

To make the LS-SVM classifier more reliable and generalize to independent datasets, 5×5-fold and 5×6-fold stratified cross validations (CV) are employed. 5× 6-fold stratified CV is used for Dataset-66, and for the other two datasets 5×5-fold stratified CV is carried out. For training of the LS-SVM, we have used the Radial Basis Function: $K(x_i, x_j) = exp(-\gamma \parallel x_i - x_j \parallel^2), \gamma > 0$, as the kernel. There are two tunable parameters of RBF kernel in LS-SVM classifier: C and γ. The kernel parameter γ controls the shape of the kernel and regularization parameter C controls the tradeoff between margin maximization and error minimization. It is not known beforehand which values of C and γ are the best for the classification problem at hand. Hence, various pairs of (C, γ) have been tried with over the course of the CV procedure, and the one with the lowest CV error rate is picked, where $C\ \varepsilon\ [1, 10]$ and $\gamma\ \varepsilon\ [1, 3]$. After finding the best values for the parameters C and γ, these values are used to train the LS-SVM model, and the test set is used to measure the error rate of the classification system. Tables 4.1-4.3, show the settings of the training and the validation images for the datasets used in the experiments.

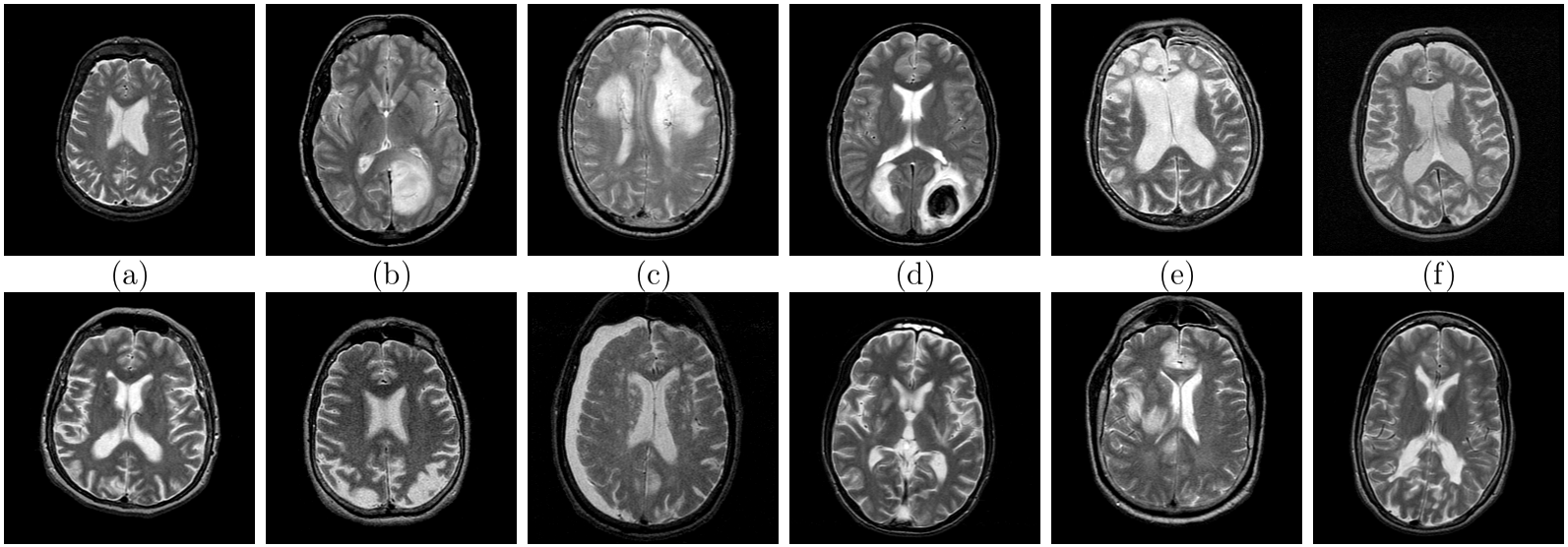

Figure 4.3: Sample brain MR images used in the experiments of '*Scheme 1*': (a) normal, (b) glioma, (c) meningioma, (d) sarcoma, (e) Pick's disease, (f) Huntington's disease, (g) Alzheimer's disease, (h) Alzheimer's disease with visual agnosia, (i) chronic subdural hematoma, (j) cerebral toxoplasmosis, (k) herpes encephalitis, (l) multiple sclerosis.

Table 4.1: Setting of one pass of 6-fold stratified CV for Dataset-66.

Total No. of Images		Training (55)		Validation (11)	
Normal (18)	Abnormal (48)	Normal	Abnormal	Normal	Abnormal
66		15	40	3	8

Table 4.2: Setting of one pass of 5-fold stratified CV for Dataset-160.

Total No. of Images		Training (128)		Validation (32)	
Normal (20)	Abnormal (140)	Normal	Abnormal	Normal	Abnormal
160		16	112	4	28

To compare the performance of '*Scheme 1*' with the state-of-the-art techniques, several other existing schemes have been implemented. Quantitative evaluation of '*Scheme 1*' and it's performance comparison with other state-of-the-art techniques are analyzed using the following statistical measures: Sensitivity (Eq.(1.49)), Specificity (Eq.(1.50)) and Accuracy (Eq.(1.52)). Several different experiments are carried out to evaluate the performance of '*Scheme 1*' in light of feature reduction efficiency, classification accuracy, comparisons with other state-of-the-art schemes and computation complexity analysis.

The '*Scheme 1*' is based on the MGA of the LFS coefficients obtained by RT decomposition. With the above mentioned RT decomposition configuration, the size of the LFS is 32×32. PCA is used to reduce the feature vector size to only 9, where these 9 features are the first 9 principal components, preserving $\simeq$ 90% of total variance of the RT decomposed features. This reduced feature set is only 0.88% and 0.014% of the initial feature set considering LFS and original image, respectively. Therefore, due to the RT+PCA combination 99% feature reduction have been achieved. The systems proposed in [200, 202, 203, 209] have used 19 principal components as the image representing feature vector. We have

Table 4.3: Setting of one pass of 5-fold stratified CV for Dataset-255.

Total No. of Images		Training (204)		Validation (51)	
Normal (35)	Abnormal (220)	Normal	Abnormal	Normal	Abnormal
255		28	177	7	43

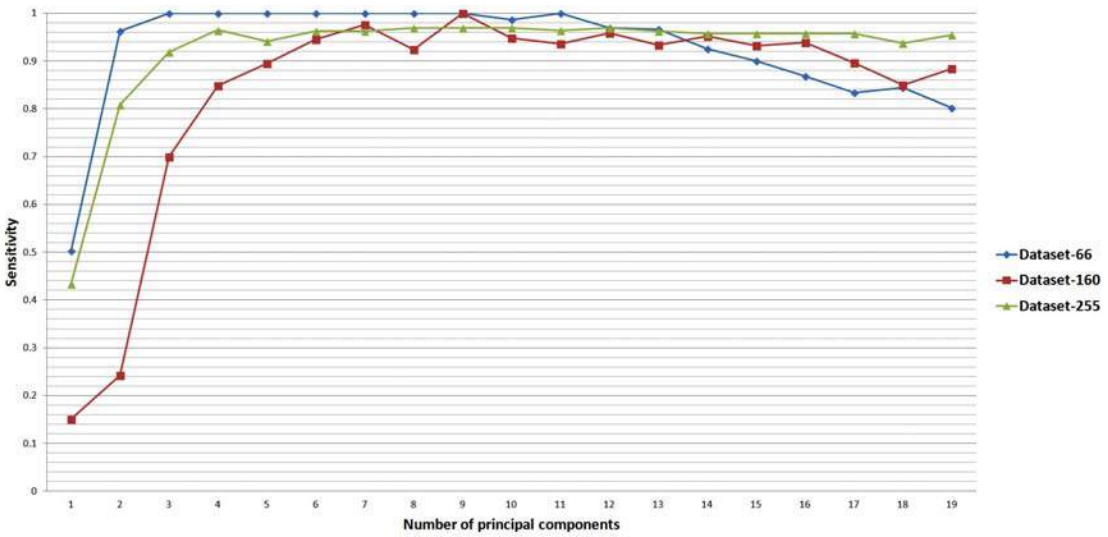

Figure 4.4: Performance evaluation of '*Scheme 1*' in terms of sensitivity.

not only achieved 47.39% feature reduction from the state-of-the-art brain MR image classification techniques, but also higher performance in terms of accuracy. To find out the proper number of principal components, which give the best result, the performance of '*Scheme 1*' is experimented with different numbers of principal components $(1 - 19)$. The graphs of the Figs. 4.4, 4.5, and 4.6, show the performance of '*Scheme 1*' in terms of sensitivity, specificity and classification accuracy for the three datasets used in the experiments with different numbers of principal components, respectively. It is clear from the results given in Figs. 4.4, 4.5, and 4.6, that '*Scheme 1*' works efficiently for all the three datasets using only 9 principal components for image representation. The best results are achieved for all the statistical measures used to evaluate the performance of '*Scheme 1*', considering only 9 principal components: sensitivity $(1.00, 1.00, 0.97)$,

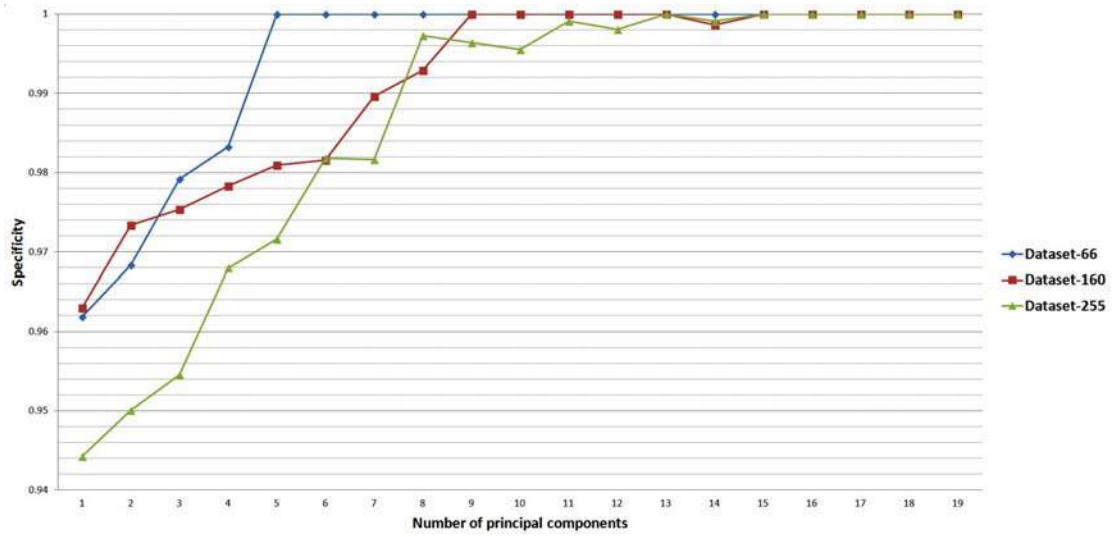

Figure 4.5: Performance evaluation of '*Scheme 1*' in terms of specificity.

specificity $(1.00, 1.00, 0.99)$ and classification accuracy $(100\%, 100\%, 99.39\%)$, for the datasets-66, 160 and 255, respectively. The classification accuracy of '*Scheme 1*' is also evaluated through receiver operating characteristic (ROC) curves, shown in Fig. 4.7. The '*Scheme 1*' correctly classified the MRI images of Dataset-66 and Dataset-160 with an average area under curve (AUC) of 100%, with 0% standard deviation. For the Dataset-255, AUC of 99.45% ($\pm$0.0046%) is achieved.

The performance of '*Scheme 1*' is compared with 13 state-of-the-art brain MR image classification schemes. The performance comparisons of the implemented methods are evaluated using all the three datasets. The obtained comparison results are shown in Table 4.4. The Table 4.4, also shows the feature vector dimension for each of the schemes. The schemes described in [201] give the worst performance results in terms of accuracy. Moreover, these methods have the highest feature dimension (4761 features/image), which results in high computational complexity. The dimension (7) of the feature vector used in [208], is less than '*Scheme 1*' (9). But it is obvious from the results of Table 4.4, that the method described in [208] is less efficient and general than the proposed scheme, in terms

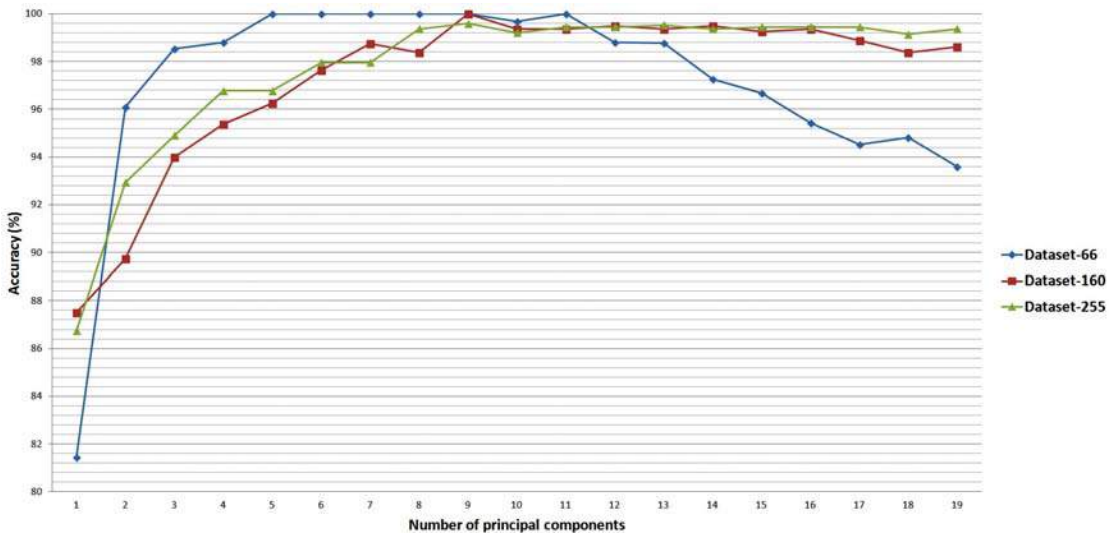

Figure 4.6: Performance evaluation of '*Scheme 1*' in terms of classification accuracy.

of classification accuracy. The techniques described in [200, 202, 203, 209] show improved results in brain MR image classification, with lower feature vector dimension (19). But, these schemes use various complex weight optimization techniques, which themselves require high computational complexity. Whereas, '*Scheme 1*' only requires feature vector of dimension 9, with the highest retrieval accuracies.

During time requirement analysis, all the images of all the three datasets are used for computing the overall time requirement of '*Scheme 1*'. The computation times (except the LS-SVM training) of all the constituting stages (feature extraction, feature reduction and classification) of '*Scheme 1*' are recorded, and the average values are used as the time requirement. The feature extraction, feature reduction and LS-SVM classification average time requirements for an MRI image of size 256×256 are 0.026 seconds, 0.014 seconds and 0.002 seconds, respectively. The overall average computation time for each MRI image of size 256×256 is about 0.042 seconds. Even though, the time requirement for feature extraction through RT is slightly greater than DWT, but due to the use of LS-SVM with only 9 principal components results in lower overall time requirement. Moreover,

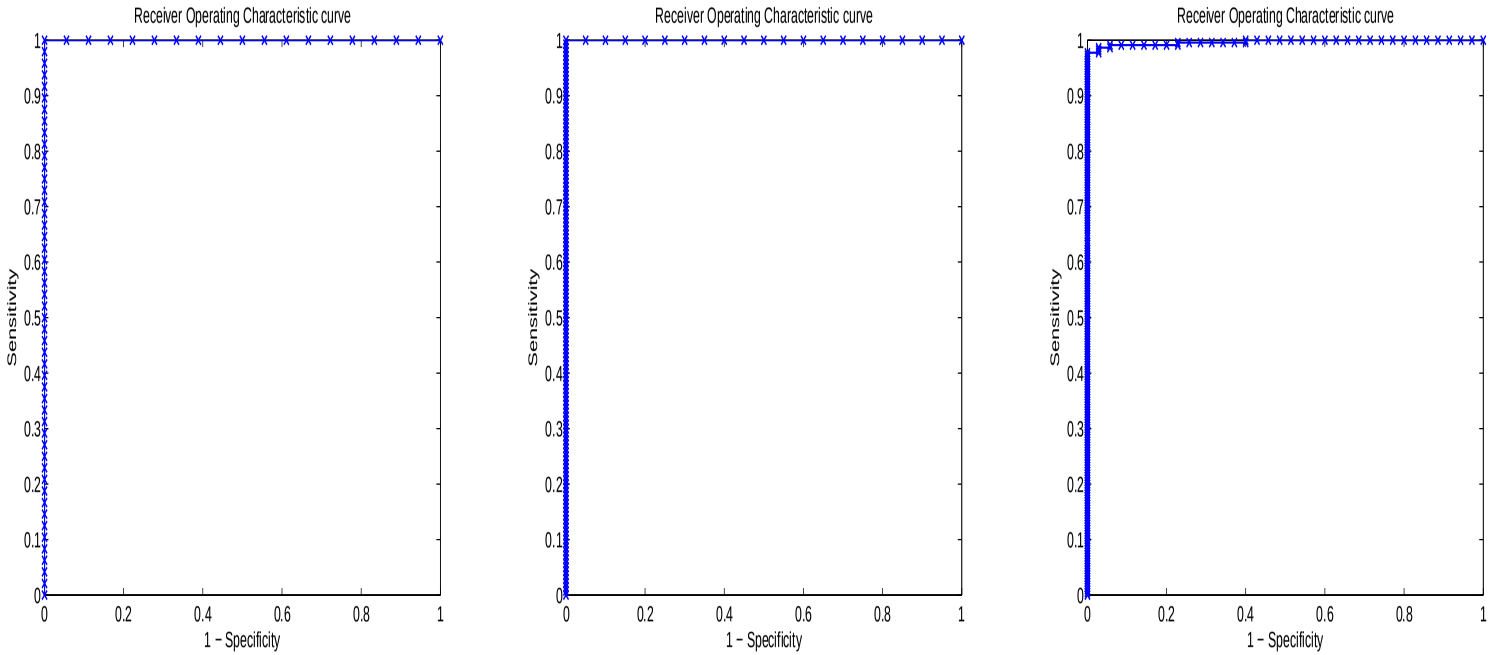

(a) (b) (c)

Figure 4.7: ROC curves of performance evaluation of '*Scheme 1*': (a) Dataset-66 (b) Dataset-160 and (c) Dataset-255.

Table 4.4: Performance comparison of '*Scheme 1*' using the three datasets.

Scheme	Feature dimension	Accuracy (%)		
		Dataset-66	Dataset-160	Dataset-255
DWT+SOM [201]	4761	94.00	93.17	91.65
DWT+SVM+LIN [201]	4761	96.15	95.38	94.05
DWT+SVM+POLY [201]	4761	98.00	97.15	96.37
DWT+SVM+RBF [201]	4761	98.00	97.33	96.18
DWT+PCA+FNN [208]	7	97.00	96.98	95.29
DWT+PCA+kNN [208]	7	98.00	97.54	96.79
DWT+PCA+FNN+ACPSO [209]	19	100.00	98.75	97.38
DWT+PCA+BPNN+SCG [202]	19	100.00	98.29	97.14
DWT+PCA+FNN+SCABC [200]	19	100.00	98.93	97.81
DWT+PCA+KSVM+LIN [203]	19	96.01	95.00	94.29
DWT+PCA+KSVM+HPOLY [203]	19	98.34	96.88	95.61
DWT+PCA+KSVM+IPOLY [203]	19	100.00	98.12	97.73
DWT+PCA+KSVM+GRB [203]	19	100.00	99.38	98.82
'*Scheme 1*'	9	**100.00**	**100.00**	**99.39**

with 9 dimensional feature vector for each training image, the storage cost of stored image feature database is also reduced. From the above mentioned results and discussions, it is clear that '*Scheme 1*' not only performs the best, among all the mentioned state-of-the-art brain MR image classification techniques, but also works efficiently with different sizes' of datasets and various disease classes.

4.2.3.2 *Scheme 2*: Experimental Results and Comparisons

The performance of the improved brain MR classification technique termed as '*Scheme 2*', is evaluated using the brain MR images of the 'Dataset–66' described in the Table 4.1. The images of this dataset are rotated through 5 different angles 5° to 25° in clockwise direction, and the dynamic ranges of the images are modified to 5 different levels (150,10) to (250,30), respectively. Therefore, the total number of images used in experiments is 726. To compare the performance of

the DWT using different numbers of decomposition levels and wavelet bases, we have considered 3 wavelet families: Daubechies (dbN, N = 1, 8), Coiflets (coifN, N = 1, 5), and Biorthogonal (biorN.N, N.N = 1.3, 6.8). For each wavelet basis, the number of decomposition levels from 1 to 4 is considered. For the other three transforms, 6 different pyramidal and directional filter combinations (from {'9/7', '5/3'} and {'9/7', '5/3', 'pkva'}) are considered with different number of decomposition levels. To classify the images K-Nearest Neighbors (K-NN) classifier is used with $k = 1$. To avoid overfitting problem, K-fold CV is integrated into our method with $K = 5$, which make '*Scheme 2*' reliable and generalize to other independent datasets. Fig. 4.8, shows samples of the brain MR images used in the experiments.

Different number of principal components (PCs) are considered to reduce the dimension of the feature vector. After extensive experiments it has been found that 10 number of PCs (preserving $> 80\%$ of the total variance) is providing acceptable results. Therefore, different MRA/MGA transforms are compared considering only 10 PCs. Fig. 4.9 illustrates the performance comparison of WT with different decomposition levels and mother wavelets. For CNT, CVT and RT the best results are obtained for decomposition orientations {4, 8, 8}, {4, 4} and {2, 4}, respectively. The graph of Fig. 4.10 shows the results for CNT, CVT and RT with different filter combinations and the above mentioned best decomposition orientations.

The graph of Fig. 4.9, shows that 'bior1.3' mother wavelet at decomposition level 3 provides the best performance ($\approx 88\%$) among different WT configurations. This is because of the high smoothness, small support, high vanishing moments, linear phase and near orthogonal properties of 'bior' wavelet compared to others. The performance decreases near about $10\%-12\%$, when we only used LFS features for classification. From the graph of Fig. 4.10, it can be clearly seen that the

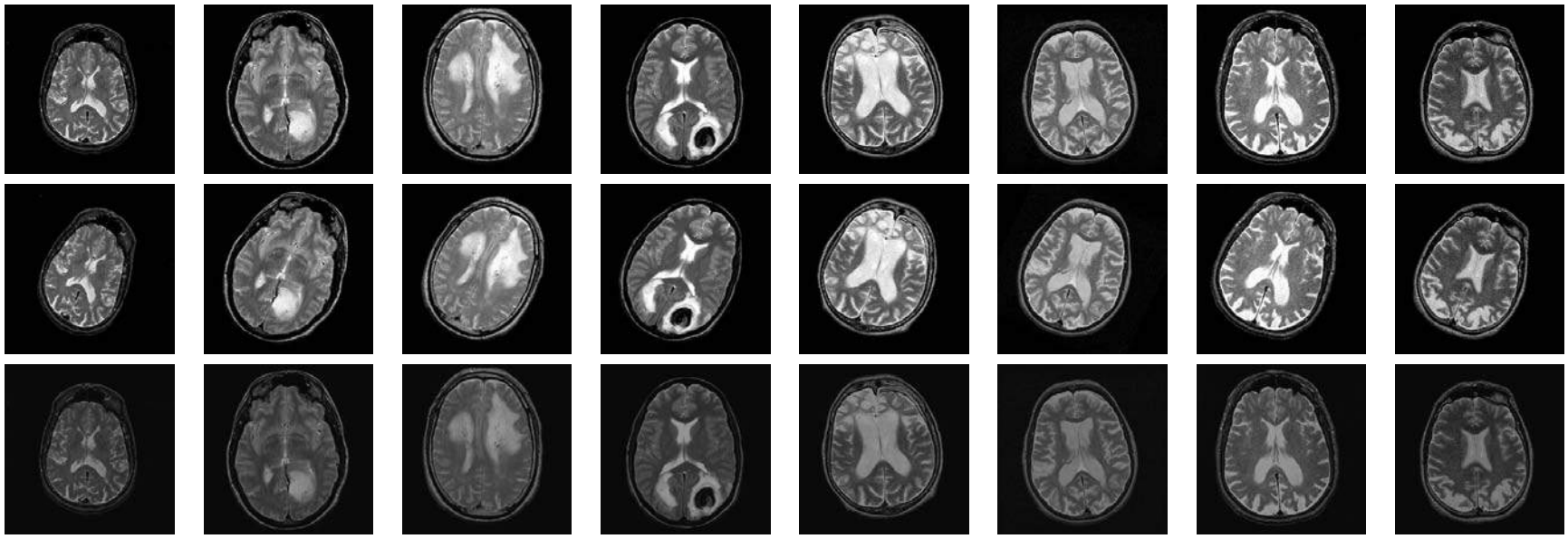

Figure 4.8: Sample brain MR images used in the experiments of '*Scheme 2*' (row 1) with corresponding rotated (row 2) and dynamic range (row 3) modified versions: (a) normal, (b) glioma, (c) meningioma, (d) sarcoma, (e) Pick's disease, (f) Huntington's disease, (g) Alzheimer's disease, (h) Alzheimer's disease with visual agnosia.

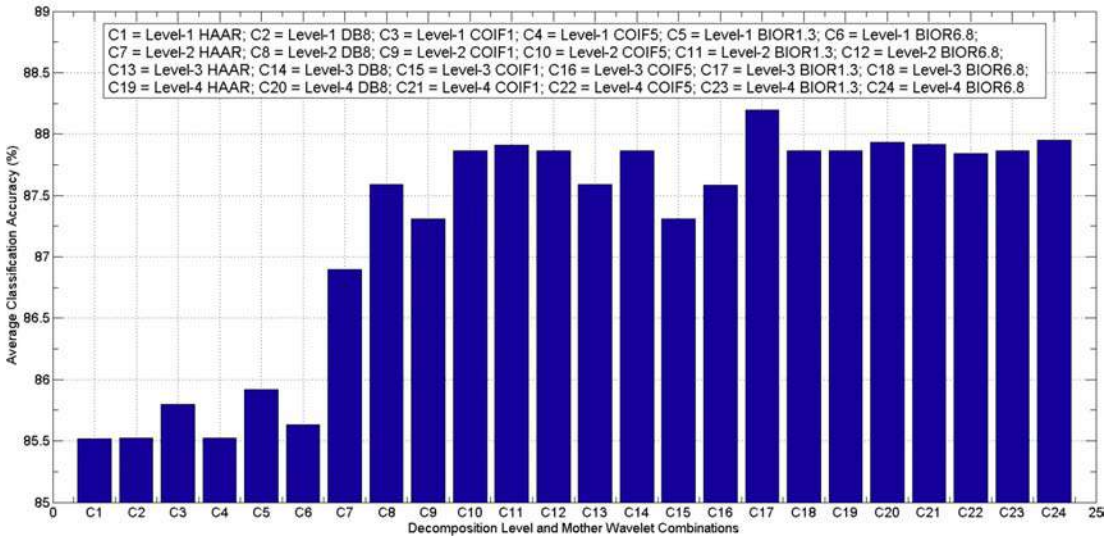

Figure 4.9: Performance comparison of '*Scheme 2*' with different wavelet combinations.

filter combination '9/7' (pyramidal) and 'pkva' (directional) performs the best for CNT, CVT and RT. The '9/7' filters are linear phase and are close to being orthogonal and thus carries more subtle image information. Whereas, the ladder structure 'pkva' filters are more effective because of its superior edge direction localization property. Moreover, among these three transforms CNT performs the best in terms of average classification accuracy of $\geq 93\%$. When we use only LFS features obtained from these three transforms for classification, the performance decreases near about $6\% - 7\%$.

4.3 Content based Retrieval System for Medical Radiographs

The second solution regarding the '*effective information retrieval*' problem in medical domain is related to efficient image retrieval from a database consisting diverse modalities of radiographic medical images. Over the past few decades, with the rapid proliferation of various modalities of images in the medical domain, retriev-

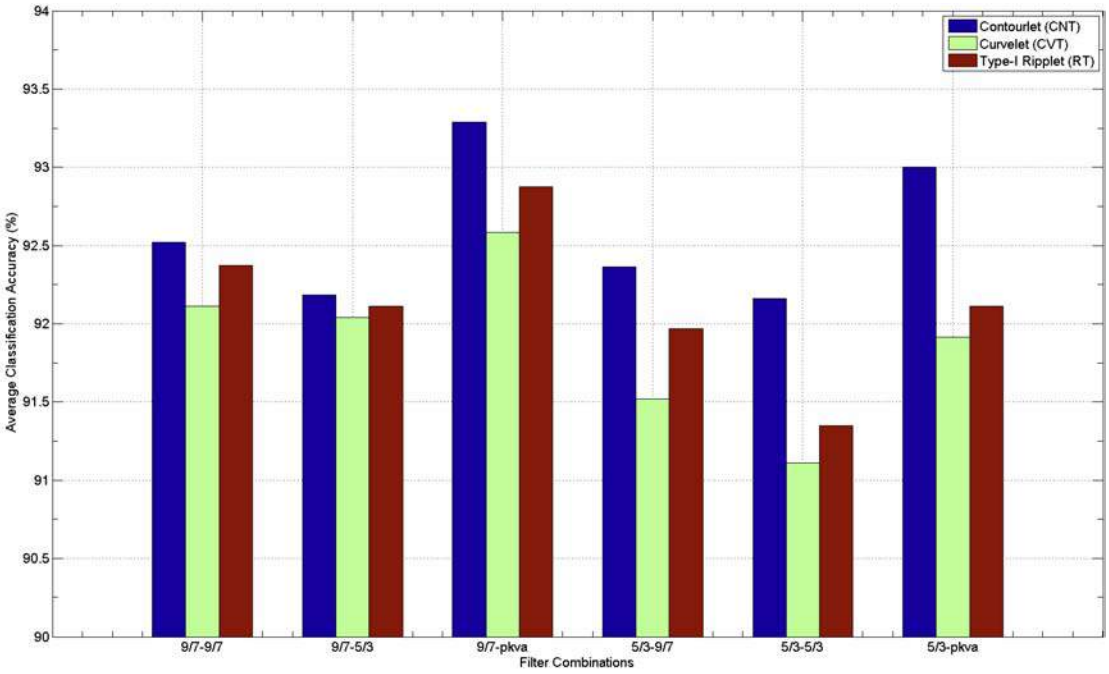

Figure 4.10: Performance comparison of '*Scheme 2*' with different MGA tools.

ing medical images from large repositories to aid radiological image interpretation is becoming one of the most active research fields [140, 143, 174, 178]. Due to its critical and ethical values, medical image interpretation requires high accuracy. Currently, radiologists rely on both knowledge and heuristics to accomplish this procedure [136, 166, 377]. As a result of perceptual, training and fatigue differences among radiologists, there are variations in the interpretations made by different medical personnel to the same image [131, 190, 378]. Moreover, with the wide deployment of modern medical imaging devices in hospitals, large numbers of medical images are produced every day, placing an additional burden on radiologists. On one hand, they have to render accurate diagnoses for each image; on the other, they have to interpret large amounts of medical images within a limited time frame [168, 188, 230].

An open challenge for automatic retrieval of medical images is the inter-class vs. intra-class variability problem: an image that belongs to the same visual class

might look very different, while images that belong to different visual classes might look very similar [137, 178, 240]. Several CBMIR prototypes have been proposed to address this problem using local and global features [173, 177, 233]. Majority of these systems are developed around a specific imaging modalities and retrieval methods in these systems are task and modality specific. There are few systems that have a global CBIR system for diverse image collections. The current state-of-the-art in CBMIR approach has been presented in [131, 190].

Most of the existing CBMIR systems require high dimensional image representative feature vector. CBMIR utilizes multiple visual features to represent images, which brings the problem of the "*curse of dimensionality*" [144, 187, 239, 241, 379]. Though conventional dimensional reduction methods can be employed to tackle this problem, but these solutions ignore the fact that different visual features have a range of physical meanings. Moreover, these existing systems often have to search the entire image database to retrieve the similar images. These result in high computational complexity. In the CBMIR system described next, NSCT and FCM (fuzzy-C-means) algorithm is used in such a way that results in an image representative feature vector having comparatively very low dimension. Moreover the computational complexity is further reduced using a LS-SVM based pre-classification mechanism. Experimental studies on a radiographic medical image database (IRMA-2009) show promising retrieval result.

4.3.1 Proposed Method

In this section, various parts of the novel CBMIR system is described briefly.

4.3.1.1 Image Signature Computation

The medical images are mostly gray-scale images having different size. During the retrieval process, the images of the medical database (DB) are resized to size $M \times N$. NSCT (described in Section 1.3.1.2) is applied to each image I of the database. A l-level NSCT decomposition of an image I, results in 2^l sub-bands, each having the same size $M \times N$. Let the sub-bands of each image I be denoted by S_b^I, where $b = 1, 2, 3, \cdots, 2^l$.

For each sub-band S_b^I, a feature map FM_b^I is computed by using Eq. (4.3) utilizing the concept of '*local energy*' over a neighborhood W_{ij} of size $p \times q$, centered around a coefficient with coordinates (i, j). The size of the window W_{ij}, is determined using the Spectral Flatness Measure (SFM).

$$FM_b^I(i,j) = \sum_{(p,q)\varepsilon W_{ij}} |S_b^{Ip}(p,q)| G(i-p, j-q) \tag{4.3}$$

where, $G(i, j)$ is a Gaussian low-pass (smoothing) filter.

After computing the feature maps for an image I of the database, each feature map is clustered using FCM algorithm, into m different clusters. In the proposed CBIR system, an image I is represented in terms of a signature:

$$Sig^I = \{(C_1, w_{C_1}), (C_2, w_{C_2}), ..., (C_m, w_{C_m})\} \tag{4.4}$$

where, C_k represents k-th cluster centroid ($k = 1, 2, ..., m$) and w_{C_k} indicates the fraction of pixels belonging to the cluster C_k. C_k constitutes the NSCT features over b feature maps and is represented by

$$C_k = [f_1^k, ..., f_b^k] \tag{4.5}$$

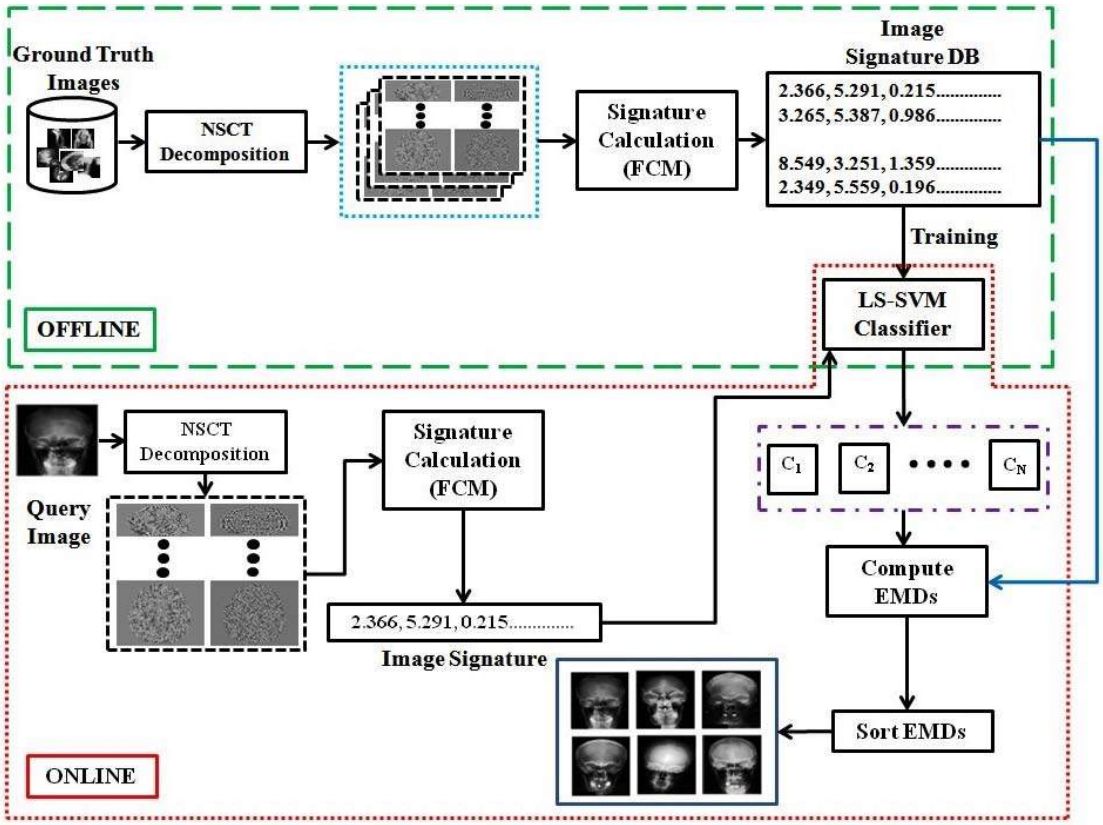

Figure 4.11: Block diagram of the described CBMIR system.

4.3.1.2 Training by LS-SVM

LS-SVM classifier (described in Section 1.3.3) is trained with 70% and tested with 30% of the leveled data using stratified random sampling method.The Radial Basis Function (RBF) kernel is used with 10 fold cross validation (CV) procedure to find the best values of tunable parameters C and σ^2. The value of kernel parameter (σ^2) is changed between 0.2 and 20 and value of regularization parameter (C) is changed between 1 and 1000 for optimization purpose using grid-search method. After finding the best values of the parameters $C = 100$ and $\sigma^2 = 0.6$ of the RBF kernel with a CV accuracy of 76%, they are utilized for the final training to generate the local concepts model.

4.3.1.3 Algorithm

The block diagram of the content based radiograph retrieval system is shown in Fig. 4.11. As can be seen from the Fig. 4.11 that the retrieval system works on two different phases: 'OFFLINE' and 'ONLINE'. In the 'OFFLINE' phase the sample radiographs from the training dataset are used to train the LS-SVM classifier. Cross validation is used for improving the generalization capability of the system (described in Section 4.3.1.2). The salient steps of the 'ONLINE' phase of the CBMIR system are as follows:

1. The user enters the query image to the system.
2. Image signature (representing the content) of the query image based on NSCT is computed as described in Section 4.3.1.1.
3. Class identification of the query image is done by the LS-SVM classifier (Section 4.3.1.2).
4. The distances between the query image and all the images in the identified class are computed using the EMD (described in Section 1.3.4).
5. After sorting the distances in ascending order, the system retrieves the top 20 ranked images from the database and presents them to the user.

4.3.2 Results and Discussion

To evaluate the performance of the described CBMIR scheme a subset of IRMA 2009[5] radiographic image database (ImageCLEF-2009) [178–180, 229] has been used in the experiments. A database of 1550 radiographic images from 31 different classes (each having 50 images) has been constructed. Images of this database are

[5]IRMA 2009 medical image data set is courtesy of T. M. Deserno, Dept. of Medical Informatics, RWTH, Aachen, Germany.

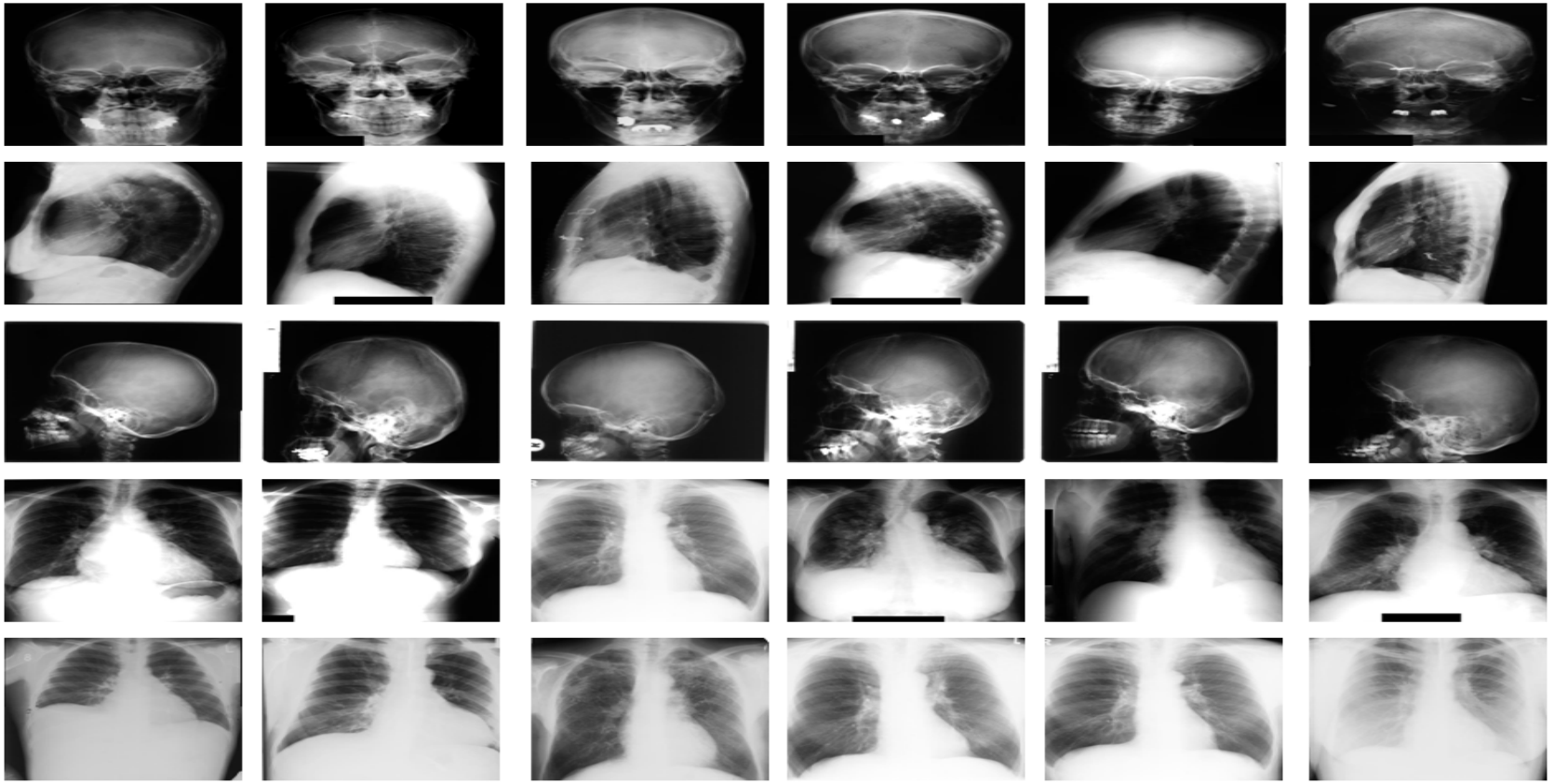

Figure 4.12: Query-by-example experiments: Query images (left) and Retrieved images in decreasing order of similarity (right).

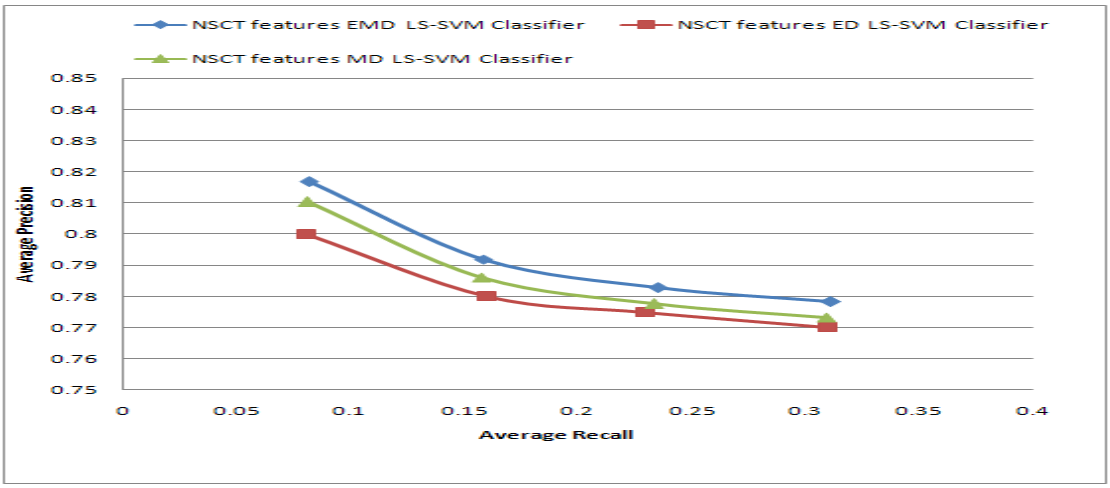

Figure 4.13: Average Precision vs Average Recall (frame size 5, 10, 15 and 20).

classified by medical experts according to the imaging modality, the examined region, the image orientation with respect to the body and the biological system under evaluation [137,180,226–234]. Two commonly used statistical measures have been computed to assess the proposed system's performance, namely precision and recall.

A query-by-example experiment is shown in Fig. 4.12 (database of 1550 images). The left image in each row is the query image. The five images on the right are ordered by decreasing similarity from left-to-right, according to the EMD measure. The results demonstrate that all the retrieved images are from the same class as the query image. Moreover, it is interesting to note that the response to a normal chest image query (fourth row) is a set of normal chest images. Whereas, a pathological chest image (fifth row) retrieved chest image examples of non-normal appearance (visually similar to the query input).

The graph of Fig. 4.13, shows the performance of the proposed method in terms of Precision vs. Recall (PR) graph. The average precision and recall is computed over all the images of database. The results are taken for the retrieved image frame sizes of 5, 10, 15 and 20. The graph also shows the performance comparisons of

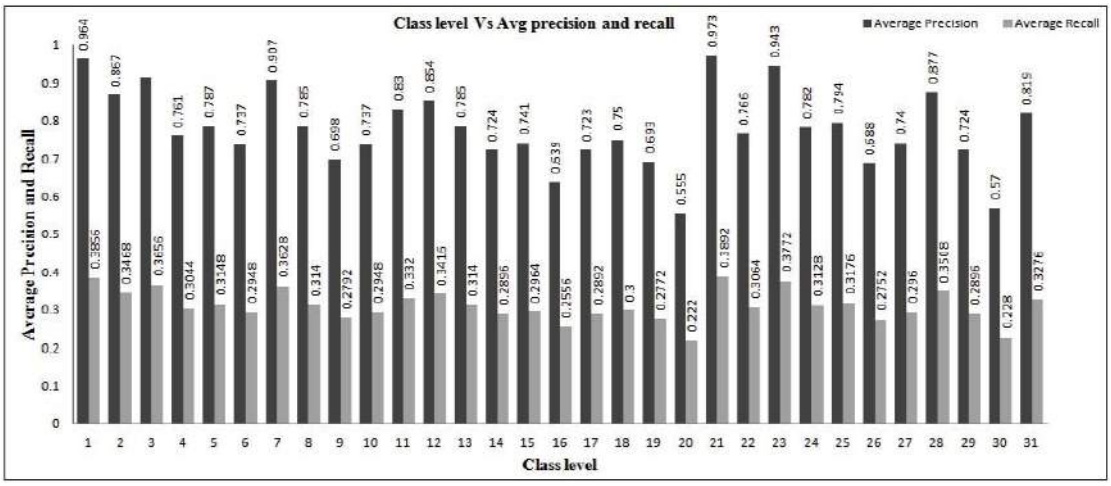

Figure 4.14: Class-wise Average precision and Average Recall.

three different similarity measures namely Euclidean Distance (ED), Manhattan Distance (MD) and EMD. It is clear from the graph of Fig. 4.13 that the proposed CBMIR system based on EMD perform satisfactorily. The graph of Fig. 4.14 shows the class wise average precision and average recall performance of 1550 images of 31 different modalities of medical images. It is to be noted that the dimension of the feature vector (image signature) used to represent the content of a radiograph is 36. This feature vector dimension is comparatively very low than most of the state-of-the-art CBMIR systems [141, 154, 232]. Even with this low dimensional feature vector, the above described system performs satisfactorily in radiographic medical image retrieval. Moreover, the use of LS-SVM as a pre-classifier also reduces the computational burden of the system as compared to other existing schemes.

The rapid and significant advancements of information and communication technologies have initiated several novel applications in the field of medical information management and improved the existing applications. But, along with these remarkable advancements, there have also emerged several new threats. The ease with which digital form of data can be acquired and manipulated in an open-

environment, like the Internet, lies at the root cause of these new vulnerabilities. Moreover, medical information management contains several demanding ethical issues regarding the sort of manipulation that can be applied on medical images and related information. In the next chapter, digital image watermarking technique is utilized for answering several of the above mentioned issues regarding the effective and ethical management of medical images and related information.

Chapter 5

Medical Image Watermarking

5.1 Introduction

As mentioned earlier, medical information is highly valuable and critical due to its importance in clinical diagnosis, treatment, research, education and other commercial/non-commercial applications, both for private and government organizations. During the last few years, due to rapid and significant advancements of information and communication technologies, medical data distribution and management systems have undergone a significant change, both in concepts as well as in applications [245, 250]. HIS and PACS based on the Digital Imaging and Communications in Medicine (DICOM) standard (as advised by National Electrical Manufacturers Association (NEMA)), form the base of the modern integrated and sophisticated health-care delivery systems [245, 247–250]. These systems provide easier access, effective manipulation and efficient distribution of medical information between hospitals. There are number of reasons for this medical information exchange, for example, tele-medicine applications (ranging from tele-consulting, tele-diagnosis and tele-surgery) and distant learning of medical personnel [250, 276–278]. EHR technology has replaced the inefficient paper records paradigm and is available in various forms such as diagnostic reports, images and vital sign signals etc. It can also contain the health history information of a patient, such as demographic data, physical examination information, laboratory test results, treatment procedures, and prescriptions etc., which are highly

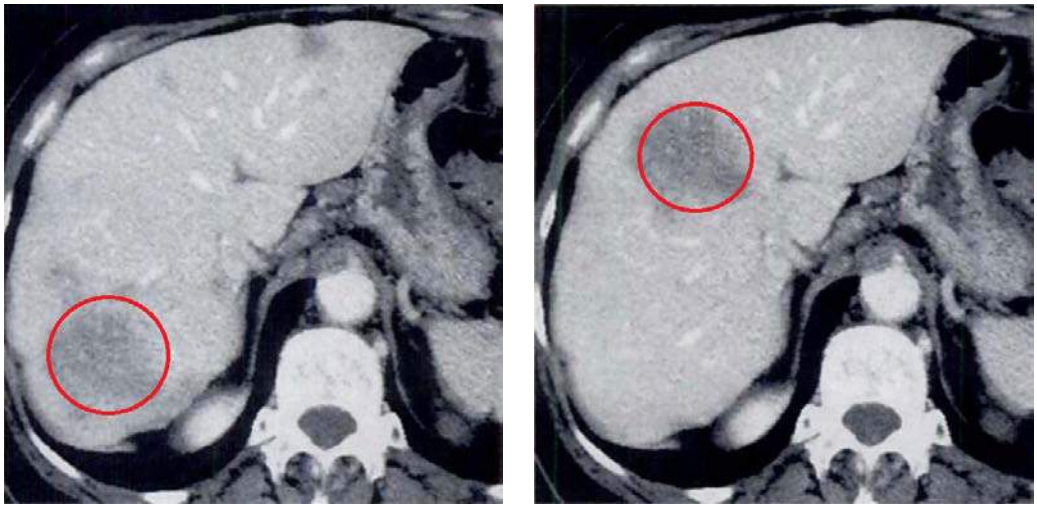

(a) (b)

Figure 5.1: Manipulation of medical image.

confidential in nature [256].

On the other hand, these advances have introduced new risks for inappropriate use of medical information, given the ease with which digital forms of data can be manipulated [252–256]. For example, consider the following case of medical image manipulation as shown in Fig. 5.1. This example shows the fraudulent use of digital medical image manipulation of a CT scan image by changing the location of an infected region of the liver. This raises the question: how this type of manipulation can be detected? In fact, it is nearly impossible, even for expert medical personnel, to detect such plausible manipulations that contain totally fabricated abnormalities by merely observing the images [251]. Moreover, medical images have special characteristics and requirements. As well as, it is also concerned with legal and ethical issues regarding the allowable operations and disclosures that can be undertaken on them, since any degradation of the quality of the images could result in misdiagnosis [252, 253, 288].

Therefore, it is of paramount importance to prevent unauthorized access and manipulation of medical data, as well as to protect its confidentiality. This neces-

sitates the design of a system for effective storage, access control and restricted manipulation of medical information, keeping the authenticity, integrity and confidentiality requirements of medical data intact for effective and ethical information management purposes.

Digital watermarking (DWM) which imperceptibly embeds information (watermark) within a host signal (cover) such as image, audio or video, is an emerging research area of multimedia data management [259, 265]. Original motivation of this technique was to protect copyright, but it has also been applied to a wider range of multimedia applications [260, 264]. When it is applied to medical images, necessary steps are taken so that after watermark embedding, the medical images can still conform to the DICOM format [247]. DWM techniques have the potentiality of becoming an all-in-one solution tool, providing alternative and/or complementary solutions for a wide number of ethical issues related to medical information management and distribution [252, 253, 257, 258, 261, 262, 276–278].

Keeping these aforementioned issues in mind, in this chapter, two MIW techniques are described for effective and ethical management of digital medical images and related information. The first MIW technique ('*Scheme 1*'[1]) is based on spatial domain LSB plane replacement methodology. Whereas, the second method ('*Scheme 2*'[2]) is based on MGA of contourlet transform.

The rest of the chapter is organized as follows: the spatial domain MIW technique of '*Scheme 1*' is introduced in Section 5.2. Various steps of '*Scheme 1*' are described in Subsection 5.2.1. In Subsection 5.2.2, the experimental results obtained by '*Scheme 1*' and its comparisons with several state-of-the-art MIW techniques are discussed. The second MIW scheme ('*Scheme 2*)', based on CNT is introduced in Section 5.3. Subsection 5.3.1, contains the description of the work-

[1]Details can be found in [345]
[2]Details can be found in [346]

ing methodology of '*Scheme 2*'. Obtained experimental results and comparisons of '*Scheme 2*' with existing MIW methods are included in Subsection 5.3.2.

5.2 *Scheme 1*: Spatial Domain MIW Technique

Even though, there exist several MIW techniques, but most of these schemes have several disadvantages:

- Most of these existing MIW schemes are image modality specific i.e., some of these techniques only work for MRI images, whereas, others work for CT or X-ray images.
- In case of medical images, two of the major desirable requirements are high payload capacity and no or unnoticeable visual degradation. Achieving these two conflicting criteria is proven to be very difficult. Often, the existing MIW methods have either low payload capacity with reasonable imperceptibility, or vice versa.
- Moreover, most of the time the existing MIW schemes lack the proper security measures which are required for safeguarding the valuable and often sensitive patient's personal health information.
- Furthermore, most of these existing MIW techniques do not have any proper tamper localization and recovery mechanism.

Keeping these above mentioned issues in mind, the first MIW scheme ('*Scheme 1*') described next, is a novel blind, fragile watermarking technique capable of preserving integrity, authenticity and confidentiality of the medical information.

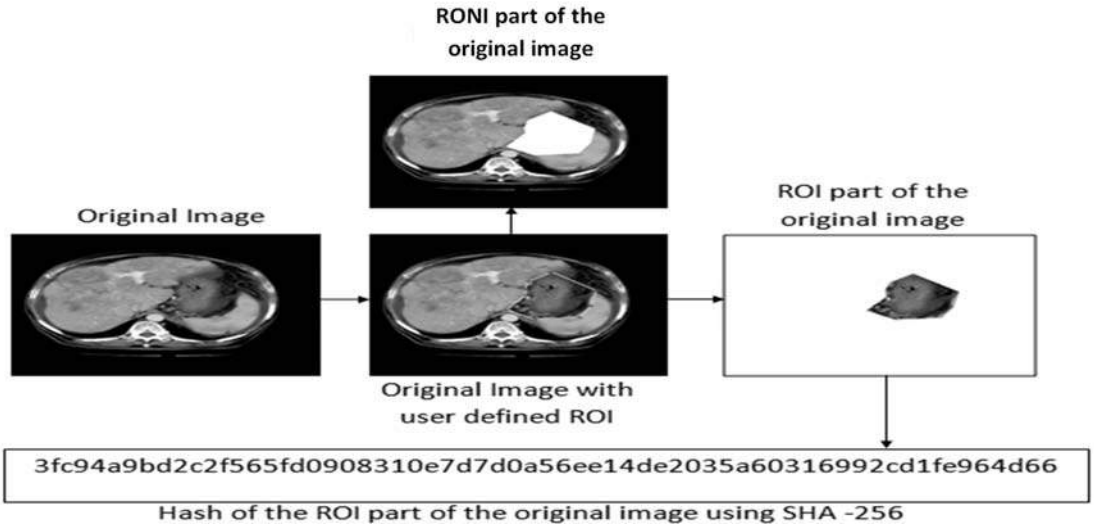

Figure 5.2: Hash of the ROI using $SHA-256$.

5.2.1 Proposed Method

Several standard security tools and compression technique are used in '*Scheme 1*', like Secure Hash Algorithm-256 ($SHA-256$) [380], Advanced Encryption Standard (AES) [381] and arithmetic coding compression [382]. $SHA-256$ is used to compute the hash of the ROI of the medical image. This hash is used as a message digest to verify the integrity of the medical image. In '*Scheme 1*', AES cryptographic method is used to encrypt/decrypt the EHR/DICOM metadata part to achieve better security. To reduce the payload's size, arithmetic coding compression technique is used to losslessly compressed the watermark. In the following sections, various modules of '*Scheme 1*' are described:

5.2.1.1 Hash of Region of Interest

The ROI is the most important part in a medical image. It contains the most valuable information of the medical image and should not undergo any modification [252, 255, 272, 277, 291]. There can be several disjoint ROIs in a medical image and several ways exist to define them: manual, automatic and semiauto-

0	0	40	10	0	50	20	0	0	30
0	0	27	0	0	37	7	0	47	17
0	44	14	0	0	24	0	0	34	4
0	31	1	0	41	11	0	0	21	0
48	18	0	0	28	0	0	38	8	0
35	5	0	45	15	0	0	25	0	0
22	0	0	32	2	0	42	12	0	0
9	0	49	19	0	0	29	0	0	39
0	0	36	6	0	46	16	0	0	26
0	0	23	0	0	33	3	0	43	13

Figure 5.3: Dispersion of the watermark bits for $k = 23$, $n = 100$ and $h = 50$.

matic. In the standard DICOM format, if the ROI is present then its description is embedded in a tag of the DICOM header. In '*Scheme 1*', a polygonal ROI can be interactively defined by the user (physician, clinician, etc.). The reason of choosing polygonal ROI is that in most of the cases, ROI in a medical image is of irregular shape. A polygonal ROI can be completely characterized by the number of vertices n_v and their coordinates $v(x, y)$. Although, in '*Scheme 1*' we have only concentrated on single ROI, this method can also work on multiple ROIs. After the selection of the ROI, the hash of the ROI is computed using the $SHA - 256$ cryptographic hash function, which produces a 64 character (256 bits) message digest as shown in Fig. 5.2.

5.2.1.2 Dispersion of Watermark Bits

To increase the security of '*Scheme 1*', an one-to-one mapping function is used to disperse the bits of the watermark payload into the embedding region, depending on a secret prime key. For example, one function that may be used for this purpose is given below:

$$f(x) = (kx \ mod \ n) + 1 \tag{5.1}$$

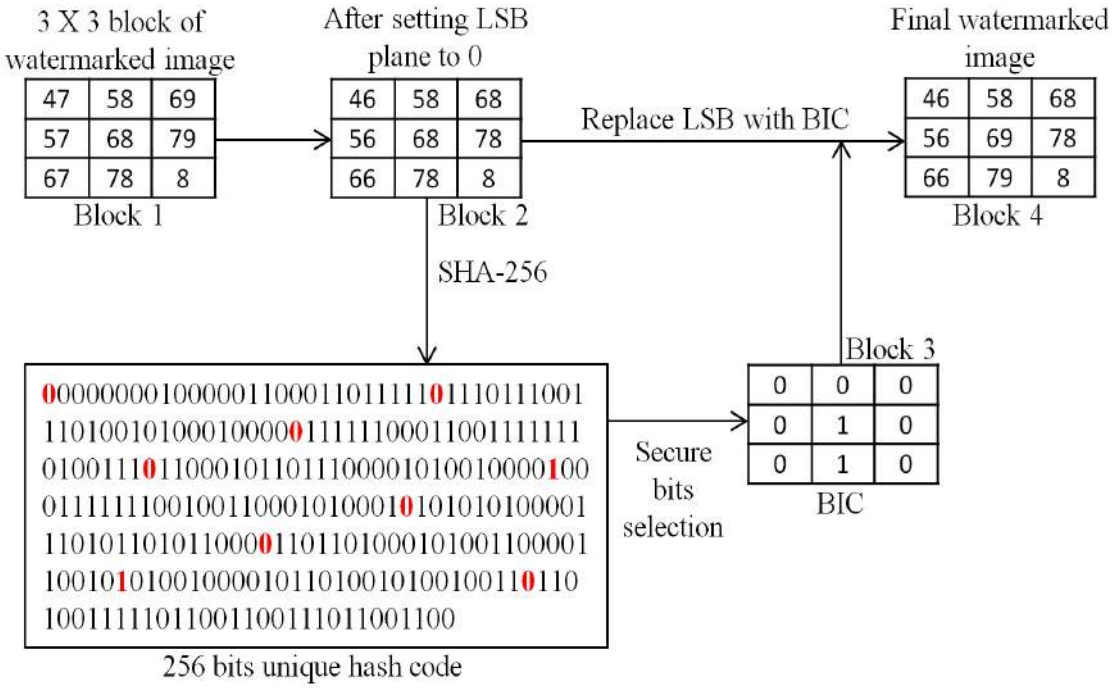

Figure 5.4: Embedding of the tamper localization information.

where, for an image of size $P \times Q$ and watermark payload of h bits, $n = P \times Q$; k is a prime number $\in [1, n]$; x is the bit position in the watermark payload and $x \in [1, h]$. As an example, if we take $k = 23$, $n = 100$ (say 10×10 pixels image) and $h = 50$, then the dispersion of the watermark bits in the cover image is shown in Fig. 5.3.

5.2.1.3 Tamper Localization

The '*Scheme 1*' is equipped with a novel image content dependent block based tamper localization mechanism. Considering, Bp as the LSB plane of the image, after embedding the first watermark in the penultimate LSB plane (say $Bp + 1$), the LSB plane Bp of the watermarked image is filled with 0's. The modified watermarked image of size $P \times Q$ is then divided into 3×3 blocks in a non-overlapping manner. If the image size is not a multiple of 3, then some more rows and/or columns with all values 0 are added to the image to get an extended image.

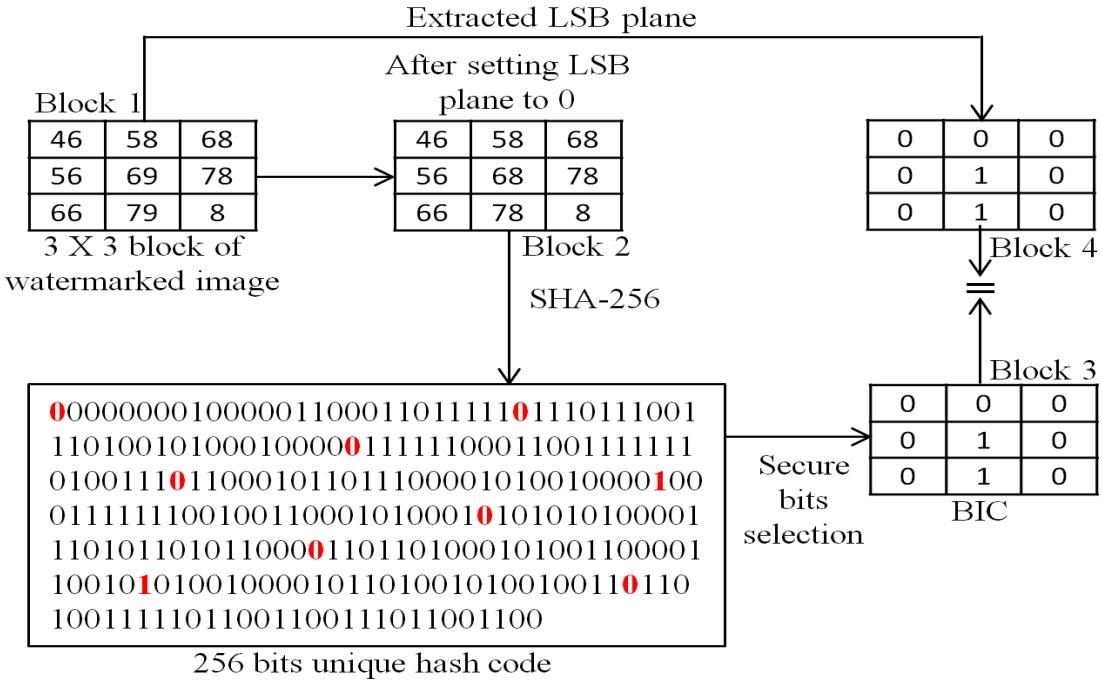

Figure 5.5: Tamper localization in case of no tampering.

A binary location map (BLM) of the same size as the image or the extended image is formed for tamper localization purpose. For every 3×3 image block a 9 bits block identification code (BIC) is calculated using a cryptographic hash function. For example if we use SHA-256, for a block we will get a BIC of 256 bits. Among these 256 bits, 9 bits are selected. The selection of 9 bits among 256 bits is same for both the watermark insertion and extraction procedures. This selection of 9 bits also provides a level of security. The BLM constructed by all the block's $BICs$, is embedded in the LSB plane Bp of the modified watermarked image. Considering, a 3×3 image block as an example, Fig. 5.4 describes this method. In this example, we have used $SHA-256$ to compute the BIC of the block. We have chosen the 1st, 28th, 56th, 84th, 112th, 140th, 168th, 196th and 224th bits as the selected 9 bits out of the 256 bits to construct the BIC. The $Block-1$ in Fig. 5.4 is the image after embedding the first watermark in the $Bp+1$ bitplane of the original image. After setting the LSB (Bp) plane of the Block 1 to 0, the $Block-2$

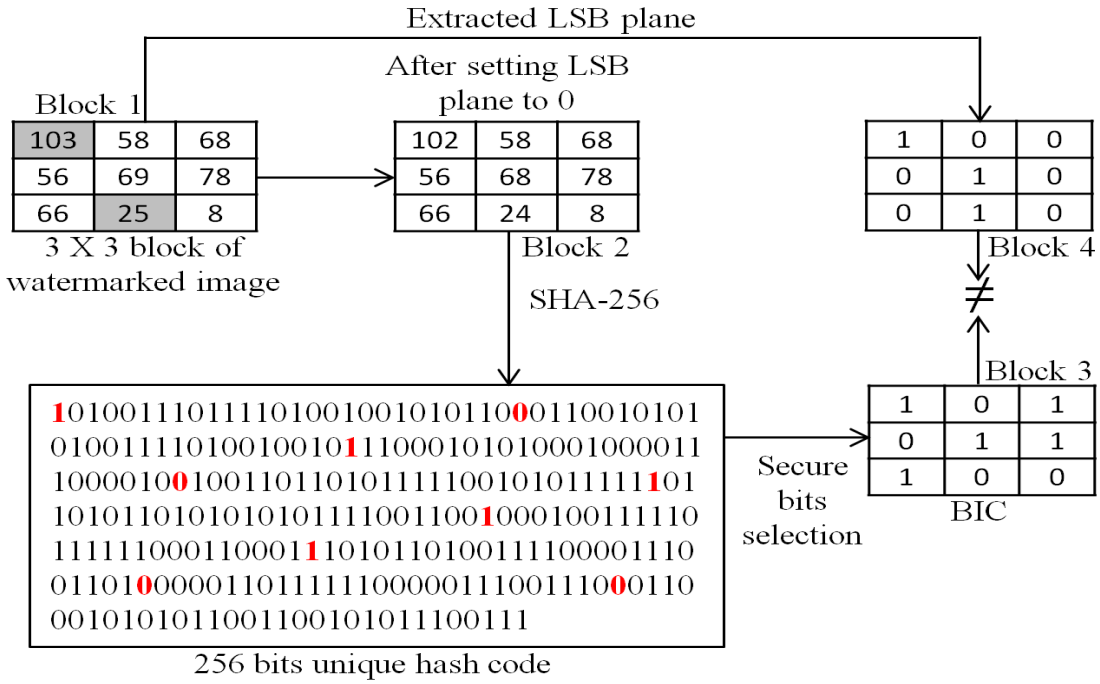

Figure 5.6: Tamper localization in case of tampering (shaded pixels).

will always contains only even numbers. In this case, only the odd numbers of the $Block-1$ will be reduced to next lower even numbers. $SHA-256$ hashing is used on $Block-2$ to get the 256 bits unique hash code as shown in Fig. 5.4. Among these 256 bits only 9 bits are selected to form the BIC ($Block-3$ in Fig. 5.4). The selected bits are shown in red color in Fig. 5.4. This BIC is used to construct the BLM. The BP plane of the $Block-2$ (which only contains 0) is replaced by this BIC (BLM for the whole image) to get the final watermarked image ($Block-4$ in Fig. 5.4). Replacing the Bp plane of $Block-2$ by the BIC ($Block-3$) bits will change the pixel values of $Block-2$ in the following manner: if the bit at the (i,j)th position of BIC ($Block-3$) is 1 then increase the (i,j)th pixel value of $Block-2$ by 1 to the next higher odd value. For example, the BIC ($Block-3$) shown in Fig. 5.4, contains 1 bit at $(2,2)$ and $(3,2)$ positions. Therefore, only the pixel values 68 and 78 at the corresponding positions $(2,2)$ and $(3,2)$ of $Block-2$ are increased by 1 to the next higher odd values 69 and 79s, respectively.

During watermark extraction procedure, the LSB plane Bp ($Block-4$ in Fig. 5.5 and 5.6) from the watermarked image ($Bloc-1$ in Fig. 5.5 and 5.6) is extracted. Following the same procedure as described above, a BIC/BLM is formed ($Block-3$ in Fig. 5.5 and 5.6). If there is no tampering to the watermarked image ($Block-1$ in Fig. 5.5), then the extracted bit-plane ($Block-4$ in Fig. 5.5) and the BIC/BLM ($Block-3$ in Fig. 5.5) are going to be same as shown in Fig. 5.5. Fig. 5.6 shows that for any modification in the watermarked image (shaded pixels are the modified pixels of $Block-1$ in Fig. 5.6), the extracted bit-plane ($Block-4$ in Fig. 5.6) and the BIC/BLM ($Block-3$ in Fig. 5.6) is not going to be same. The difference between the extracted bit-plane and the BLM, will give the tampered locations.

5.2.1.4 Watermark Generation and Insertion

As mentioned earlier, two different watermarks are embedded in medical images in '*Scheme 1*'. The first watermark is used to insert the encrypted EHR/DICOM metadata, indexing keywords, doctor's identification code, ROI information and the side information used during the watermark extraction procedure. The ROI information consists of the number of vertices n_v and their corresponding coordinates $v(x, y)$ of the polygonal ROI. It also contains the bits of the LSB planes Bp and $Bp+1$ of the ROI. The second watermark consists of the BLM used for tamper localization. During embedding the first 524 bits of the first watermark is used as the side information. Fig. 5.7 describes the generation procedure of WM_{EMB}. The watermark generation and insertion procedure is described as follows:

Inputs: Original image (OI) of size $P \times Q$, EHR/DICOM metadata (PI), Secret Key (K_S), n_v, $v(x, y)$, indexing keywords (IDX), doctor's identification code (DIC) and side information (SI).

Outputs: Watermarked image (WMI).

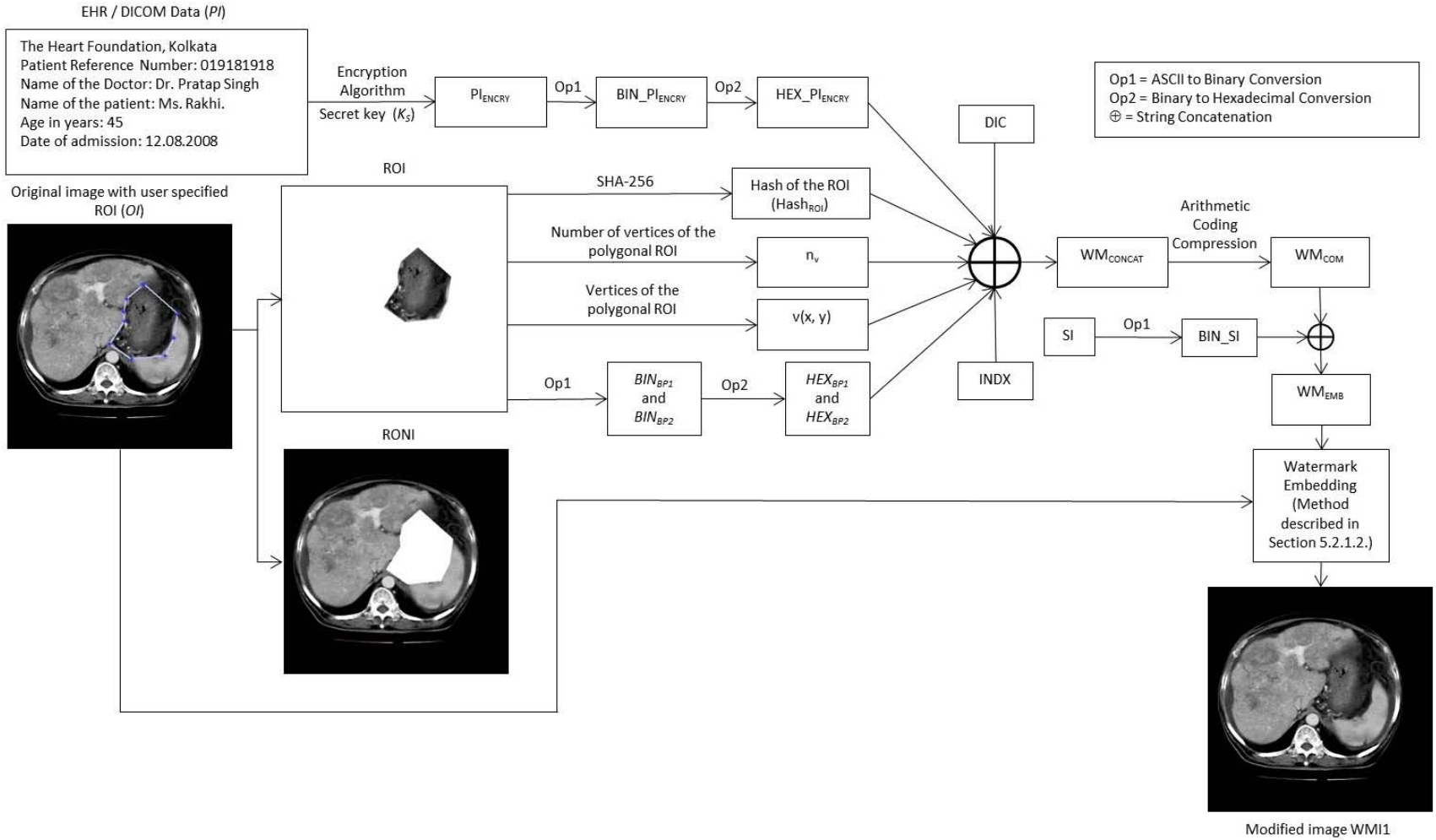

Figure 5.7: Watermark generation and insertion in '*Scheme 1*'.

Steps:

1. Separate OI, into ROI and $RONI$.
2. Compute the message digest $HASH_{ROI}$ of ROI, using $SHA-256$.
3. Assuming, $BP1\_ROI$ and $BP2\_ROI$ represents the bit-planes of the ROI, numbered Bp and $Bp+1$ respectively. Represent the pixels of $BP1\_ROI$ and $BP2\_ROI$, as binary strings BIN_{BP1} and BIN_{BP2} respectively.
4. Change the binary strings BIN_{BP1} and BIN_{BP2} to their hexadecimal representations as HEX_{BP1} and HEX_{BP2}.
5. Encrypt PI using K_S by AES method to get PI_{ENCRY}.
6. Create the binary string representation of PI_{ENCRY} as BIN_PI_{ENCRY}.
7. Represent BIN_PI_{ENCRY} to its equivalent hexadecimal form represented by HEX_PI_{ENCRY}.
8. Concatenate n_v, $v(x,y)$, IDX, DIC, $HASH_{ROI}$, HEX_{BP1}, HEX_{BP2} and HEX_PI_{ENCRY} to get WM_{CONCAT}.
9. Compress WM_{CONCAT} losslessly to WM_{COM} using arithmetic coding compression technique.
10. Concatenate WM_{COM} and the binary representation of side information SI to WM_{EMB}, which is the first watermarked to be embedded in the $Bp+1$ bit-plane.
11. Embed the bits of WM_{EMB} in the $Bp+1$ bit-plane of OI using the method described in Section 5.2.1.2, to get the modified image $WMI1$.

12. If the size of $WMI1$ is not a multiple of 3, then modify it as described in Section 5.2.1.3, and set all the bits of the LSB plane Bp of $WMI1$ to zero to get a modified image $WMI1_{MOD}$.

13. Divide $WMI1_{MOD}$ into B number of 3×3 non-overlapping blocks:

$$BLOCK\_IM_b = block\_im_b(i,j), 1 \leq i,j \leq 3 \tag{5.2}$$

where, $block\_im_b(i,j) \in 0, 1, 2, ..., 2^L - 1$,

14. For each block $BLOCK\_IM_b$, compute its block identification code:

$$BIC_b = BIT\_SEL(HASH(BLOCK\_IM_b)) \tag{5.3}$$

where, $b \in 1, 2, 3, ..., B$; $HASH(\cdot)$ represents the cryptographic hash function used, and $BIT\_SEL(\cdot)$ indicates the 9 bits selection procedure out of 256 bits. Create the final binary location map (BLM) using the method described as follows:

$$BLM = BIC_b, b \in 1, 2, 3, ..., B \tag{5.4}$$

15. Obtain the final watermarked image WMI, by replacing the LSB plane Bp of $WMI1_{MOD}$ by BLM. If the size of $WMI1$ is increased to get $WMI1_{MOD}$ during watermark embedding, then reduce the size of WMI to the original image size by deleting the added rows and/or columns from WMI.

5.2.1.5 Watermark Extraction and Verification

The block diagram of the watermark extraction and verification process is shown in Fig. 5.8. The salient steps of this process are enumerated as follows:

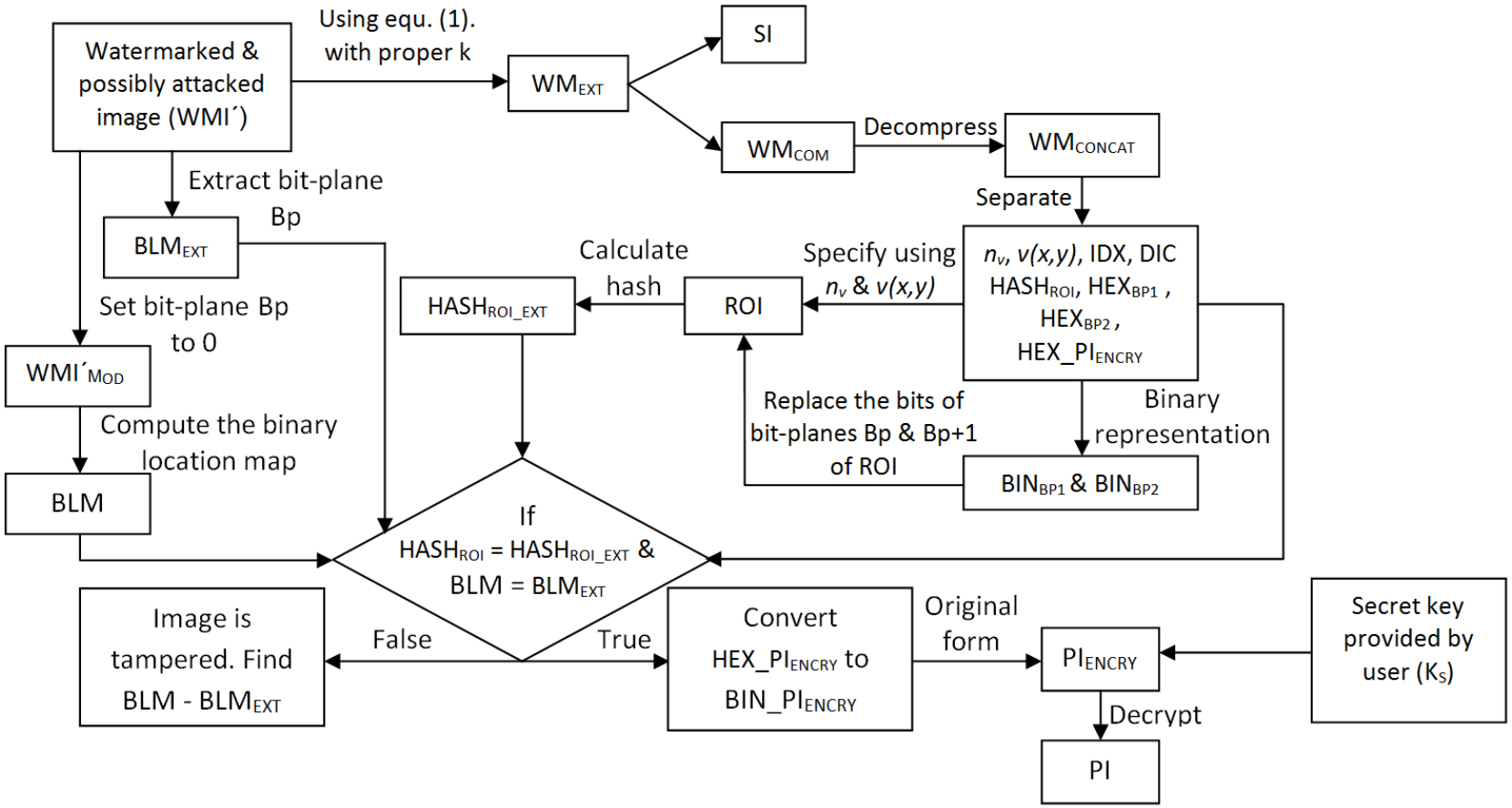

Figure 5.8: Watermark extraction and verification in '*Scheme 1*'.

Inputs: Watermarked and possibly attacked image (WMI') of size $P \times Q$, Secret Key K_S.

Outputs: Authenticity result ($AUTH_{RES}$) and/or watermark extracted image (WMI_{EXI}), PI, IDX, DIC.

Steps:

1. Using the same function (as Eq. 5.1) used for watermark insertion, with proper key k, extract the bit string representation of the embedded watermark, from the bit-plane $Bp + 1$ of WMI'. Let it be denoted by WM_{EXT}.

2. Divide WM_{EXT} into two parts. One as the side information SI (first 524 bits from WM_{EXT}) and the rest as WM_{COM}.

3. Decompress WM_{COM} using the arithmetic coding with the help of SI to WM_{CONCAT}.

4. Separate the embedded information n_v, $v(x, y)$, IDX, DIC, $HASH_{ROI}$, HEX_{BP1}, HEX_{BP2} and HEX_PI_{ENCRY} from WM_{CONCAT}.

5. Using nv and coordinates $v(x, y)$ information, the proposed scheme automatically specify the ROI in WMI'.

6. Convert HEX_{BP1}, HEX_{BP2} to their bit string representations as BIN_{BP1} and BIN_{BP2}, respectively.

7. Replace the bits of the Bp and $Bp + 1$ bit-planes in the ROI of WMI' by the bits of BIN_{BP1} and BIN_{BP2}, respectively.

8. Calculate the hash $Hash_{ROI\_EXT}$ of the ROI of WMI' using $SHA - 256$.

9. Extract the Bp bit-plane of WMI' as BLM_{EXT}.

10. Set all the bits of the Bp bit-plane of WMI' to 0 to get a modified image as WMI'_{MOD}.

11. Compute the binary location map (BLM) from the WMI'_{MOD} using the steps 12–15 described in Section 5.2.1.4.

12. To get the authenticity result ($AUTH_{RES}$) follow the next procedure:
    if $HASH_{ROI} = Hash_{ROI\_EXT}$ and $BLM = BLM_{EXT}$ then
    $AUTH_{RES}$ =True
    Do steps 13 to 15
    else
    $AUTH_{RES}$ =False
    Do step 16
    end if

13. Convert HEX_PI_{ENCRY} to its equivalent binary string representation as BIN_PI_{ENCRY}.

14. Change BIN_PI_{ENCRY} to its original representation as PI_{ENCRY}.

15. Decrypt PI_{ENCRY} using K_S by AES method to get PI.

16. Find the difference between BLM and BLM_{EXT} to get the tampered regions.

5.2.2 Results and Discussion

430 medical images of 7 different modalities (CT, MRI, USG, X-ray, Barium Study, Mammogram, etc.), various sizes, file formats (BMP, TIF, GIF, DICOM), and bit-depths (8, 12, 16) have been used to test the performance of '*Scheme 1*'. Among these 430 images, 140 images are of size 128 × 128 pixels, 140 images are of size

The Heart Foundation, Kolkata
Patient Reference Number: 019181918
Name of the Doctor: Dr. Pratap Singh
Name of the patient: Ms. Rakhi
Age in years: 45
Residential address: #44, 5th F.G. Road, I Block, E phase, Kolkata - 109
Date of admission: 12.08.2008
Case History: Dyspnea on exertion NYHA Class IV. Chest pain.
Pain radiating to the left side of the neck and mastoid.
Patient had h/o a similar attack 4 months ago.
Test performed: Lead II E.C.G.
Results: T wave inversion.
Diagnosis: Suspected myocardial infarction.
Treatment: Sublingual Nitroglycerin.
Required tests: Balloon angioplasty
Referred to: Dr. M. Pathak, Future Hospital, Kolkata

Figure 5.9: An example of EHR used in the experiment.

256×256 pixels and 140 images are of size 512×512 pixels. Each of the 7 different modalities has 60 images individually. Therefore, each modality of medical images consists of 20 images of size 128×128, 256×256 and 512×512 pixels separately. The rest 10 images are DICOM images having different sizes and bit-depths. EHR of different sizes are used in the experiments. Fig. 5.9 shows an example of the EHR used in the experiment.

To show the effectiveness of '*Scheme 1*', both subjective as well as quantitative analysis have been carried out. The quantitative measures, PSNR (Eq.(1.33)) and WPSNR (Eq.(1.53)) have been used to measure the distortion produced after watermark embedding. Higher value of PSNR and WPSNR indicates less distortion in the watermarked image. MSSIM (Eq.(1.35)) is used to measure the similarity between the original image and the watermarked image [383]. MSSIM value 1 indicates that the images are similar. Visual degradation is quantitatively measured

Table 5.1: Performance evaluation of '*Scheme 1*'

Image Modality	Average PSNR	Average WPSNR	Average MSSIM	Average TPE
Abdomen CT	43.5219	45.2290	0.9527	0.0635
Barium study	44.8029	45.8453	0.9786	0.0322
Brain MRI	43.6067	45.5822	0.9486	0.0649
Chest X-ray	44.3848	45.4122	0.9891	0.0250
Head CT	44.0263	45.6086	0.9635	0.0542
Mammogram	43.0897	43.6464	0.8707	0.0923
USG	43.8484	45.4997	0.9751	0.0419

using the TPE measurement calculated from the Watson Metric [336].

Some of the medical images used in the experiment are shown in Fig. 5.10, with their corresponding intensity histograms. It also shows the corresponding watermarked and watermark extracted medical images. Table 5.1, shows the result of watermark insertion in terms of the used quantitative measures in average. The results given in Table 5.1, denotes the average results obtained by watermarking the 60 test images for that particular modality of image. Table 5.2 shows the results for 3 DICOM images among the 10 different test DICOM images with different modalities, sizes and bit-depthes. The graph of Fig. 5.11, shows that relationship between ROI data size and watermarking payload. The performance of '*Scheme 1*' is compared with several state-of-the-art existing MIW techniques and the findings are given in Table 5.3. Fig. 5.12 describes the tamper localization capability of '*Scheme 1*'.

During subjective evaluation, original, watermarked and watermark extracted images obtained by '*Scheme 1*' are shown to an expert clinician. He has been asked to classify the images shown to him into different category: original, watermarked and watermark extracted. He has agreed with our claim that it is nearly impossible to distinguish the original, watermarked and watermark extracted images.

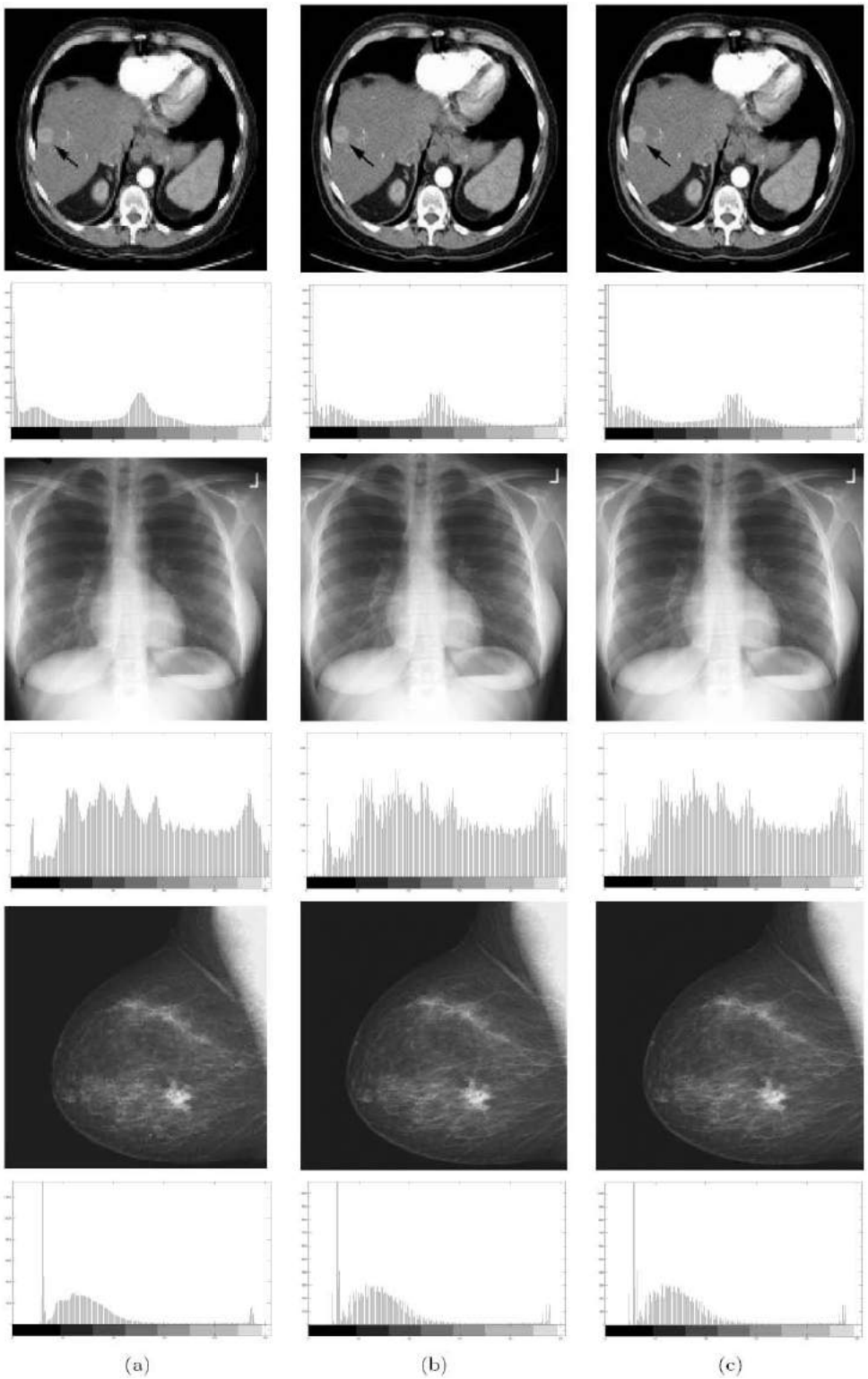

Figure 5.10: Sample medical images used in the experiments of '*Scheme 1*': (a) original images, (b) watermarked images, (c) watermark extracted images.

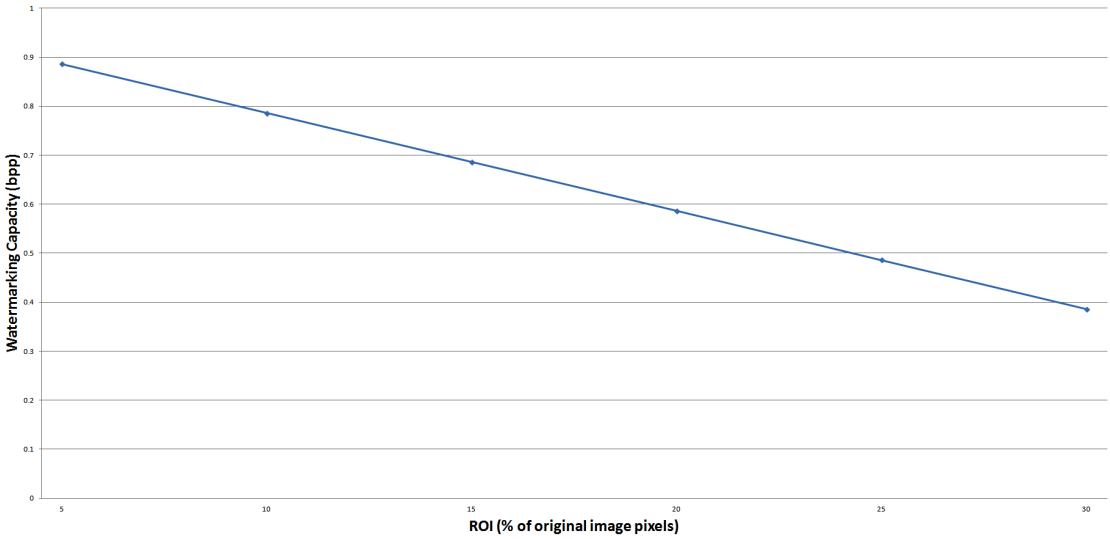

Figure 5.11: Performance of '*Scheme 1*' in terms of watermark capacity versus ROI size (% original image pixels).

He has found no significant visual difference between the original, watermarked and watermark extracted medical images, which suggests that there are no noticeable visual and/or informational degradation in the watermarked and watermark extracted images. The clinician has been also asked to evaluate '*Scheme 1*' for its usability. He has confirmed that the system is easy to use and described the system as a quality product, which satisfies the strict ethical and legislative requirements of medical information paradigm. The images of Fig. 5.10, indicates that the visual degradation caused by watermark insertion and extraction cannot be identified easily. The intensity histograms of Fig. 5.10, also supports the low visual degradation caused by '*Scheme 1*', as the intensity histograms of the watermarked and watermark extracted images, are very similar to the intensity histograms of the original images.

The watermark capacity of '*Scheme 1*', also has been measured by extensive experiments. As mentioned earlier, the second watermark is the BLM, having the same size of the corresponding image. Since the second watermark is solely used for tamper localization purpose, it should not be included in the computation

of watermark payload. Only the first watermark can be of different sizes. The fixed 524 bits needed for SI is also not considered in the watermark payload computation. In this experiment we have considered different sizes ROIs ($5 - -30\%$ of the original image's pixels). The bits needed for two bitplanes (Bp and $Bp+1$) of ROI are excluded in the watermark payload calculation. Then we have calculated how much other information (EPR, Hash of ROI, DIC, etc.) can be embedded in the medical image keeping in mind the imperceptibility requirement of MIW. Considering an image of size $P \times Q$ pixels and a ROI of size $Y\%$ of the whole image, the watermarking capacity is approximately $(PQ(100 - 2Y) - 52,400)/100PQ$ bpp[3]. In other words, the results given in Table 5.1, indicates the highest visual degradation considering the maximum possible watermarking payload. The results shown in Table 5.1 are of the watermark extracted images. It is clear from Table 5.1 that '*Scheme 1*' works well for all the different modalities of medical images. Furthermore, it is referred in [268], medical image distortion should be maintained in the range of $40 - -50$ dB (PSNR value). The PSNR and WPSNR values in Table 5.1 are well over 40 dB, which indicates that the distortion in the watermark extracted images is low, considering the maximum possible watermark payload. The average MSSIM values for all the modalities of medical images are near about 1. This indicates that the perceived change in structural information in the watermark extracted images is insignificant, and that these are similar to the original un-watermarked images. The low average TPE values show that '*Scheme 1*' causes low visual degradation in the watermark extracted images.

As DICOM (Digital Imaging and Communications in Medicine) is the international standard for handling, storing, printing, and transmitting information

[3]Number of bits needed for 2 bitplanes of $ROI = 2PQY/100$ bits, number of bits available for information (EPR, HASH, DIC, etc.) insertion $= PQ - 524 - (2PQY/100)$ bits, watermarking payload capacity $= PQ(100 - 2Y) - 52,400/(100PQ)$ bpp.

Table 5.2: Performance of '*Scheme 1*' for DICOM images.

Image Modality	Size and Bit-depths	Average PSNR	Average WPSNR	Average MSSIM	Average TPE
MR-shoulder	1024×1024, 12	43.0234	44.2318	0.9192	0.0619
CT-abdomen	512×512, 8	42.1649	43.1469	0.8096	0.0634
MR-knee	253×256, 16	43.9823	44.0346	0.9904	0.0102

in medical imaging, '*Scheme 1*' has been also experimented with several DICOM images of different modalities, having different size and bit-depths. In those experiments, we have first extracted the metadata part of the DICOM data and then embedded this information into the medical images. Table 5.2 shows the performance of '*Scheme 1*' in watermarking DICOM images. The results given in Table 5.2 shows the performance of the watermark extracted images. In this experiment, the same experimental setup is used as of for the non-DICOM images. It is obvious from the results of Table 5.2 that '*Scheme 1*' also performs efficiently for DICOM images. The graph of Fig. 5.11 shows there exists an inverse relationship between ROI size and watermarking payload. We can see from the given graph of Fig. 5.11, that for low ROI size (5% of original image's pixels), '*Scheme 1*' has achieved watermarking payload of approximately 0.89 bpp, and that of for 30% ROI is approximately 0.39 bpp. The watermarking payload decreases approximately 10% with 5% increase in the ROI size. For example, for a 512×512 medical image (today's digital medical images often have high resolution) considering a ROI with 30% of total image pixels, '*Scheme 1*' can embed approximately 12 kb information (near about $14,500$ characters considering 7 bits ASCII characters). Decreasing the ROI size to 5% of the total image pixels, the amount of embedded information increase to approximately 28 kb. This amount of information is enough for modern EHR data. It should also be noted that in most of the cases in real life, the size of the watermark payload is much less than

the maximum available embedding payload capacity. Therefore, in those cases we will have much better visual results using our scheme. Moreover, '*Scheme 1*' uses lossless compression technique to compress the information to be embedded in the medical image. The amount of compression that can be achieved is different for different ROIs and EHR. The results given in Table 5.1 and 5.2 and Fig. 5.11 are without using the compression technique. In this regard, it should also be noted that if we consider the compression scheme, the watermarking payload of '*Scheme 1*' will be higher.

The '*Scheme 1*' has also been evaluated for security analysis. The key used to encrypt the EHR data, is the first level of security in this scheme. Without the proper encryption key the unintelligible EHR cannot be decrypted correctly. The secret prime key (integer) and the dispersion function used for dispersing the watermark bits in the embedding region, is the second security measure used in the method. As the watermark bits are not embedded sequentially in the medical image, so for correct watermark extraction the proper dispersion function and the secret prime key is needed. Even if an attacker correctly guesses the bitplane numbers, where the watermarks have been embedded, he/she cannot do much with that information. Assuming, an attacker has correctly guessed the bitplane numbers $Bp + 1$ for inserting the first watermark and Bp for inserting the second watermark, respectively. The first watermark consists of encrypted EHR/DICOM metadata part, ROI information, Side information, INDX and DIC. The attacker has to know the proper order of in which these data are concatenated. Even if he/she knows the proper order of concatenation, the attacker has to know the key for encryption/decryption and the dispersion function along with the secret prime number used to scatter the watermark's bits. If the attacker changes one or more bits in the Bp and/or $Bp + 1$ bit-planes, the extraction and verification algorithm can correctly detect it. If the attacker removes the whole bitplane Bp

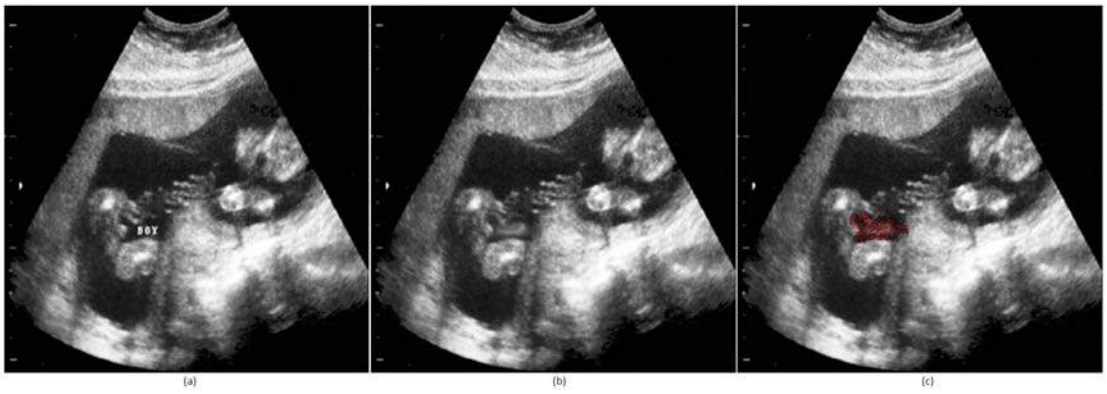

Figure 5.12: Tamper localization capability of '*Scheme 1*': (a) original watermarked image, (b) tampered watermarked image, (c) tampered region.

and/or $Bp + 1$, the algorithm can detect it correctly. Furthermore, the novel tamper localization procedure is based on selecting 9 bits out of available 256 bits, generated by $SHA - 256$ scheme. This selection of 9 bits makes the tamper localization technique secure in the sense, that the attacker has to know which 9 bits out of 256 bits are used.

As mentioned earlier, '*Scheme 1*' is fragile in nature. Therefore, any kind of alteration in the watermarked image, would destroy the hidden watermark and the proposed tamper localization scheme, would identify the tampered locations. Moreover, the technique is secured against common fragile watermarking attacks, such as the copy or the collage attack. Two different watermarks are inserted in the medical images using '*Scheme 1*'. Both of these two watermarks are image content dependent. As a result, for each different image different watermarks are embedded. The first watermark consists of the image content dependent image hash and the second watermark contains the image content dependent binary location map. Both the image hash and binary location map is different for different images. Hence, '*Scheme 1*' is secured against the common fragile watermark attacks.

To demonstrate the efficiency of the novel tamper localization scheme, values of

some pixels in an USG image is modified. Fig. 5.12 shows the result of the tamper localization experiment. The USG image shown in Fig. 5.12(a) is watermarked with '*Scheme 1*'. Fig. 5.12(b) shows the tampered watermarked image, in which the region containing a text ("BOY") is tampered. The tampered region was successfully detected as shown in Fig. 5.12(c). The '*Scheme 1*' marks the tampered regions with red color.

The '*Scheme 1*' has been compared with several state-of-the-art MIW techniques. The advantages/ disadvantages of the compared method are tabulated in Table 5.3. The problem with the method proposed in [300] is that it embeds data in a mark image which is an image of hospital's mark (used to identify the origin of an EHR). No medical image is used in the scheme. Depending on the size of the mark image and the amount of data embedded, the proposed technique produces hidden image with low visual quality (PSNR 33.57 dB). Acharya et al. have used the technique of [297] to interleave EHR and graphical signal (ECG) in the medical images. As mentioned in Table 5.3, this method is of low watermark capacity, without reversibility and tamper localization capabilities. Even though the scheme uses encryption of EHR and graphical signals before interleaving, the system lacks the modern digital data security concerns. In [289], only the hash ($SHA-256$) of the whole image is embedded in the RONI part of the image. The method depends on the size ROI. Moreover, the authors claim that their method is lossless, with the assumption that all the pixels in the RONI of all medical images are zeros. This assumption is not true for all the medical images and so the claim of the reversibility of the technique. Furthermore, the method is not secured. The MIW scheme of [271] lacks the security measures needed in modern digital data management domain. The tamper detection procedure can easily be forged. The method of [295] uses a pre-processing step for changing the pixel value of the original from the range $0-255$ to $3-252$. This pre-processing step makes the

Table 5.3: Performance comparison of '*Scheme 1*'

Scheme	Objectives	Hiding Capacity	ROI Based	Tamper Localization	Lossless	Blind
Chao et al. [300]	Authentication, integration and confidentiality of EHR	Relatively low	No	No	No	No
Acharya et al. [297]	EHR/graphic signal hiding	Low, approximately $0.125 - 0.25$ bpp	No	No	No	Yes
Zain et al. [289]	Authentication and integrity of DICOM images	Only authentication data, no EPR	Yes	No	Near-lossless	Yes
Woo et al. [271]	Authentication, data hiding	Very low, only the border of the image is used for EHR hiding	No	Yes	No	Yes
Wu et al. [295]	Authentication	Low, only authentication data, no EPR	Yes	Yes	Near-lossless	Yes
Guo et al. [272]	Authentication, data hiding	Theoretically 0.75 bpp. However, the authors did not use the scheme for EPR hiding	Yes	No	Yes	Yes
Guo et al. [270]	Authentication, data hiding	Theoretically 0.75 bpp. However, the authors did not use the scheme for EPR hiding	Yes	Yes	ROI lossless	Yes
Nambakhsh et al. [249]	Authentication, EHR hiding (as image)	Low, approximately 0.25 bpp	No	No	No	Yes
'*Scheme 1*'	Authentication, integrity, data hiding	$0.89 - 0.39$ bpp for ROI size of $5 - 30\%$	Yes	Yes	ROI lossless	Yes

scheme a near-lossless technique. During tamper detection, the proposed scheme gives a block of size 256×256 as the tampered block. This limits the tamper localization accuracy. Moreover, the method is tested only for mammogram images. Its effect on other modalities of medical images is not experimented. The method proposed by Guo et al. in [272], is based on region of embedding (ROE) selection automatically or semi-automatically. The watermark is embedded in ROE only. This restricts the watermark capacity. Moreover, two essential requirements of the proposed scheme are that the ROE should not intersect the ROI, and ROE should be in the smooth region (mostly background) of the image. This also reduces the applicability of the method. In [270] Guo et al. proposed an improved version of the method described in [272] with tamper localization capability. Apart from the shortcomings of the technique [272], the tamper localization procedure of [270] will fail if the tampering occurs in the ROE. The MIW scheme proposed by Nambakhsh et al. in [249] is based on Secret Key of size ≥ 13 bytes and tested on PET image only. This key needs to be stored separately and securely. It uses ECG signal and text image as watermarks. In the reconstructed 1D image, some characters are not completely extracted but are visually recognizable. Increase in the size of ECG also decreases the visual quality drastically (for 512 bytes PSNR 50 dB and for 4 kb PSNR 27db). It is clear from the above-mentioned discussion that most of the compared methods are task specific with low hiding capacity or imperceptibility. Moreover, most of the methods shown in Table 5.3, lack one or more useful properties that are very much needed for a modern MIW system. In general, '*Scheme 1*' is modality and task independent, having high imperceptibility and payload capacity. Moreover, '*Scheme 1*' is highly secure having several layers of security mechanisms. Watermarking by combining lossless data compression and encryption techniques, scattered embedding of the watermark bits in the embedding region, use of binary location map for tamper localization pur-

pose, all these aspects make '*Scheme 1*' an effective MIW technique. The '*Scheme 1*' conforms to the strict specifications and requirements regarding medical data handling by preserving their visual/information quality and diagnostic value.

During the development of the above described fragile, spatial domain MIW scheme, it has been realized that even though '*Scheme 1*' provides satisfactory results (compared to many state-of-the-art MIW methods), but there are some other requirements that should be addressed for effective and ethical management and distribution of medical images and related information. In the next section, a transform domain based MIW scheme ('*Scheme 2*') is described fulfilling these requirements.

5.3 *Scheme 2*: Transform Domain MIW Technique

Large production of medical images and related information by medical centers has raised several problems for effectively and ethically manage and distribute this information. The memory requirement to store these medical images and related information (like EHR) is ever increasing, so as the cost associated with it. Moreover, bandwidth is a valuable asset in network applications. The transmission cost of this huge amount of medical images and related information is very high. Keeping these aforementioned issues in mind, in this section another blind MIW technique ('*Scheme 2*') based on CNT is described, which is robust to high compression (both JPEG and JPEG2000) and several common watermarking attacks. The '*Scheme 2*' can be used as an all-in-one solution tool to address various concerns like integrity, authenticity and confidentiality of the medical data management domain. It also conforms to the strict specifications and requirements

regarding medical data handling by preserving their visual/information quality and diagnostic value. In '*Scheme 2*', EHR, DIC, INDX and optionally ROI's information are hidden in the medical images. The confidentiality of the EHR is improved by embedding the data in the medical images. DIC works as a source authenticator and INDX serves as a querying keyword for use in medical image databases for effective image retrieval. If ROI's information is embedded in the image, then it works as a caption or annotation watermark which can be used for future reference, physician's guidance and/or teaching of medical personnel. In addition to that, both the storage and transmission bandwidth requirements as well as the possibility of EHR detachment are reduced.

5.3.1 Proposed Method

The watermark insertion and extraction algorithms of '*Scheme 2*' are described in this section. Block diagrams of both the insertion and extraction methods are also given to clarify these schemes.

5.3.1.1 Watermark Generation and Insertion

As mentioned earlier, in '*Scheme 2*' EHR/PHR (refereed in this section as EPR), DIC, INDX and optionally ROI's information are inserted in the medical image. If the user wants to embed ROI's information, then the user first manually draw a polygonal ROI in the medical image. Polygonal ROI is used, because in most of the cases the ROI is irregular in shapes. A polygon can be fully described by its number of vertices (V_n) and their coordinates $\{v_i(x, y) : v_i$ is the i-th vertex at coordinate (x, y) and $i = 1, 2, ..., V_n\}$. So, ROI's information contains these V_n and $\{v_i(x, y) : v_i$ is the i-th vertex at coordinate (x, y) and $i = 1, 2, ..., V_n\}$. The salient steps of the insertion process are as follows:

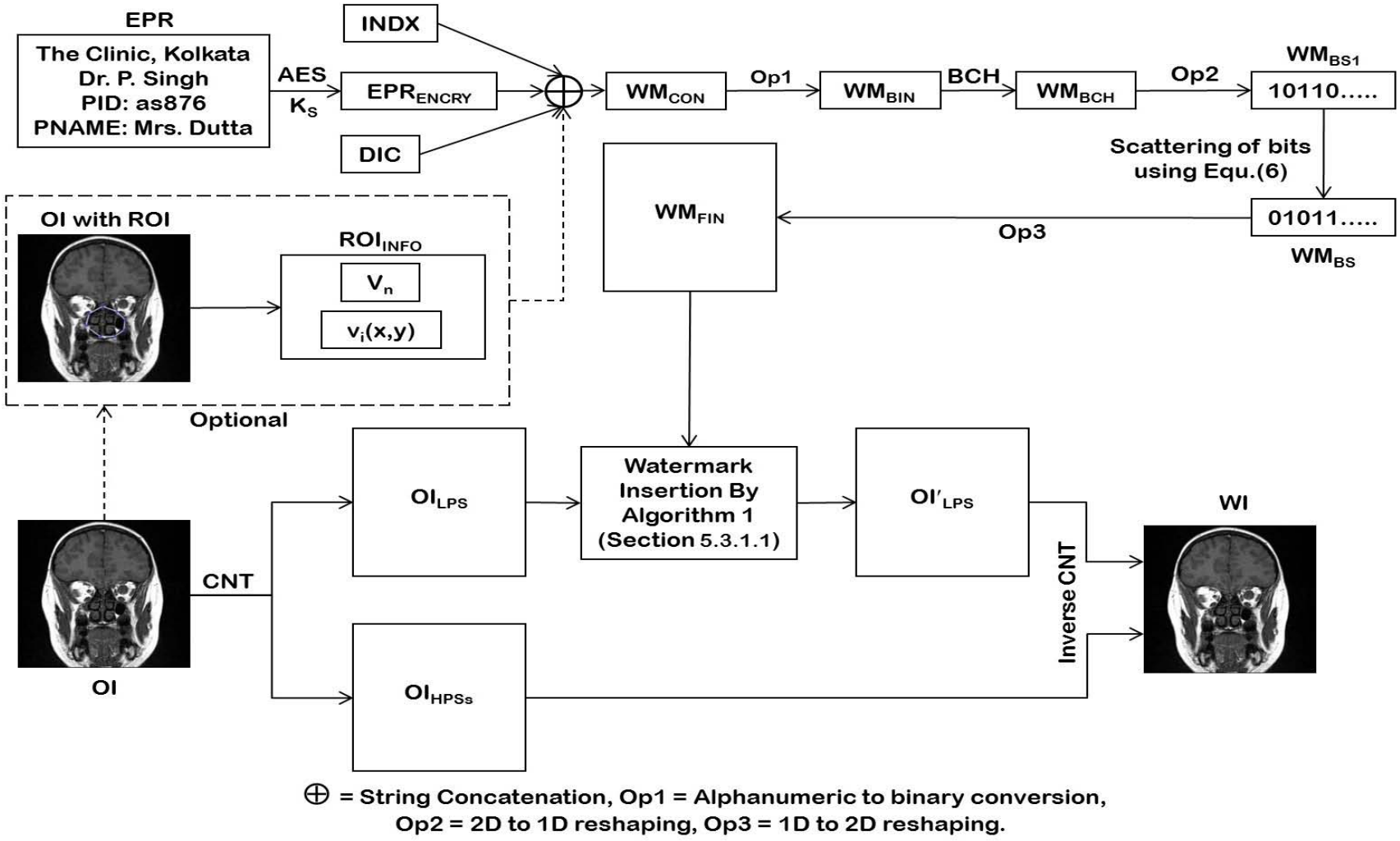

Figure 5.13: Watermark generation and insertion in '*Scheme 2*'.

Inputs: Original Medical Image (OI) of size $M \times N$,

EPR, DIC, IDX, Secret Key (K_S) and

optionally ROI's Information (ROI_{INFO}).

Outputs: Watermarked image (WI), Modified secret

key (K'_S).

Steps:

1. Apply CNT on the original image OI to get low pass subband (OI_{LPS}) and high pass subbands (OI_{HPSs}). Let the size of OI_{LPS} be $S \times T$.

2. Encrypt the EPR by Advanced Encryption Standard (AES) method using a secret key K_S to get EPR_{ENCRY} (the EPR is encrypted to increase the security of the proposed scheme).

3. If $V_n > 2$, then concatenate ROI_{INFO}, DIC, $INDX$, EPR_{ENCRY} to WM_{CON} and represent WM_{CON} to its binary form as WM_{BIN} and set $ROI = 1$. If no ROI's information is present or $V_n \leq 2$, then construct WM_{BIN} from DIC, $INDX$ and EPR_{ENCRY} and set $ROI = 0$.

4. If $ROI = 1$, then modify the secret key K_S to K'_S by concatenating 1 to K_S. Otherwise, if $ROI = 0$ (i.e., no ROI), then concatenate 0 with K_S to get K'_S. (As an example, if K_S = 'xxxxxxxx' and $ROI = 1$ then K'_S = 'xxxxxxxx1', otherwise K'_S = 'xxxxxxxx0'.)

5. Apply Bose, Chaudhuri and Hocquenghem (BCH) error correcting code [384, 385] to WM_{BIN} to get WM_{BCH}.

6. Reshape WM_{BCH} as a 1D-binary string (WM_{BS1}) and scatter the bits of WM_{BS1} using the function given below to get (WM_{BS}) :

$$f(x) = px \ mod \ n + 1 \tag{5.5}$$

Algorithm 1 : Modifying the coefficients of OI_{LPS}

for $i = 1$ to S **do**
  for $j = 1$ to T **do**
    $r(i,j) = round(\frac{OI_{LPS}(i,j)}{\alpha})$
    if $mod((r(i,j) + WM_{FIN}(i,j)), 2) = 1$ **then**
      $OI'_{LPS}(i,j) = [r(i,j) + 1] * \alpha$
    else
      $OI'_{LPS}(i,j) = OI_{LPS}(i,j)$

where,

n = size of the subband $OI_{LPS}(= S \times T)$;

p = secret prime number ε $[1, n]$;

x = bit position in WM_{BS1} and

$x \in [1, length(WM_{BS1})]$;

(This scattering of bits improves the security of the proposed scheme, as to correctly extract the watermark bits, one should have knowledge about the used scattering function (Equation 5.5), as well as the value of p.)

7. Reshape the resultant string in a matrix of equal size as OI_{LPS} (i.e., $S \times T$) to get the final watermark payload WM_{FIN}.

8. Modify the coefficients of OI_{LPS} using the procedure given in Algorithm 1; where, OI'_{LPS} = modified low pass subband, (i, j) = co-ordinates of the coefficients, $round(\bullet)$ = rounding operation, and α = watermarking strength factor. The robustness as well as the imperceptibility of '*Scheme 2*' depends on α. If it is high, the robustness is high, however, the image quality is worse and the vice versa.

9. Finally to get the watermarked image WI, apply Inverse CNT on the OI'_{LPS}, along with other non-modified directional subbands (OI_{HPSs}).

The block diagram of '*Scheme 2*' watermark generation and insertion method is given in Figure 5.13. The dashed lines in the Figure 5.13, indicates that these

activities are optional. If $ROI = 1$, then ROI_{INFO} is used to get WM_{CON}, otherwise not.

5.3.1.2 Watermark Extraction and Verification

The Fig. 5.14, shows the block diagram of the watermark extraction and verification procedure of '*Scheme 2*'. The steps of the extraction process are as follows:

Inputs: Watermarked (and possibly attacked) medical image (WI') of size $M \times N$ and secret Key (K'_S).

Outputs: Extraction and verification Report, EPR, DIC, INDX, and ROI highlighted medical image (optional).

Steps:

1. Separate K'_S to two parts, K_S and ROI.

2. Apply CNT on WI' with the same decomposition configuration of the embedding process, to get the low pass subband (WI'_{LPS}) of size $S \times T$ and high pass subbands (WI'_{HPSs}).

3. Extract the watermark WM'_{FIN} using the procedure given in Algorithm 2.

Algorithm 2 : Extraction of watermark WM'_{FIN}

```
for i = 1 to S do
  for j = 1 to T do
    r(i,j) = round(WI'_LPS(i,j) / α)
    if mod((r(i,j),2)) = 1 then
      WM'_FIN(i,j) = 1
    else
      WM'_FIN(i,j) = 0
```

4. Reshape WM'_{FIN} as a binary string WM'_{BS} and rearrange the bits to their original positions using the Equation 5.5, to get WM'_{BS1}.

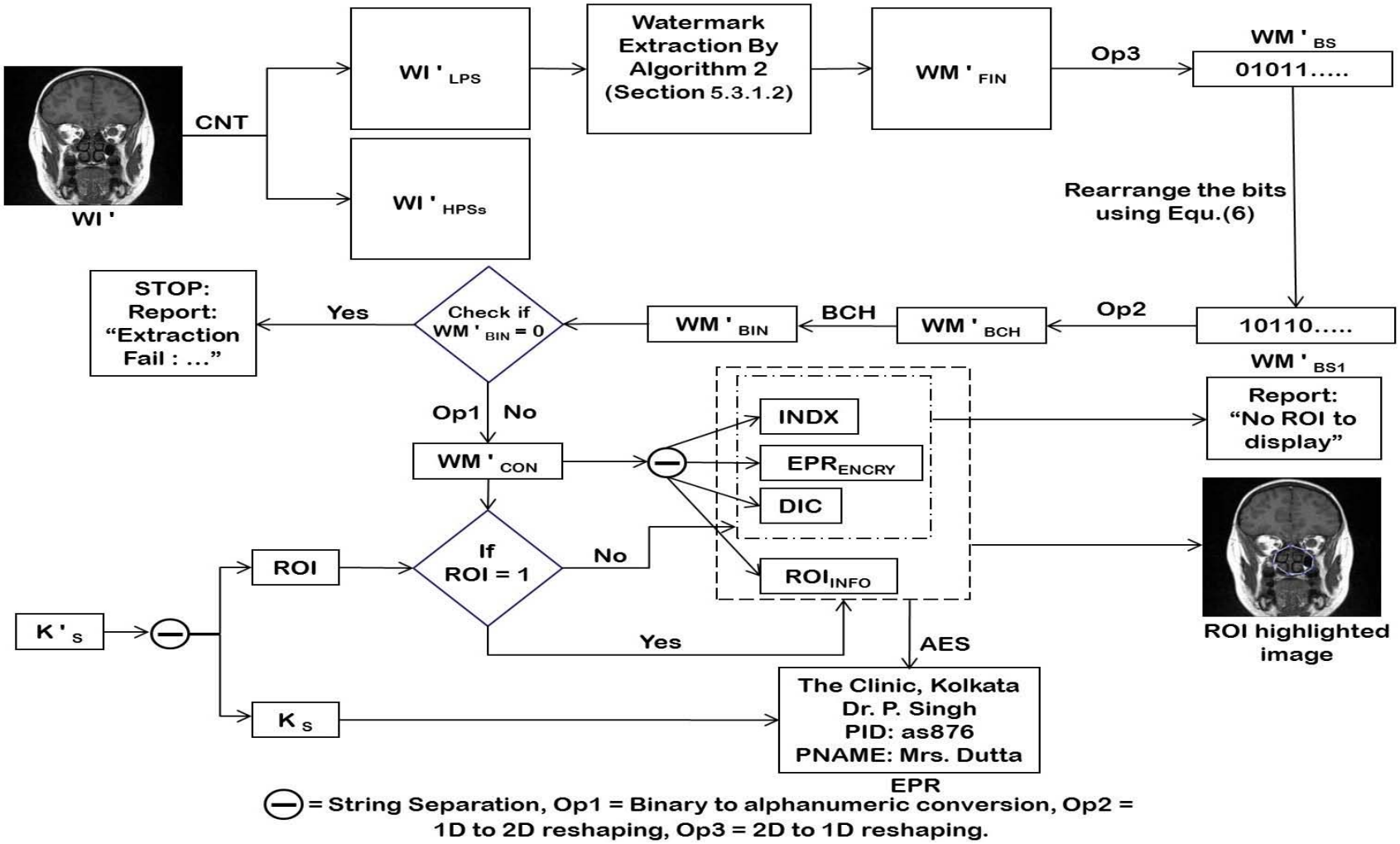

Figure 5.14: Watermark extraction and verification in '*Scheme 2*'.

5. Reshape WM'_{BS1} to WM'_{BCH} and apply BCH error correcting procedure on WM'_{BCH}, to get WM'_{BIN}. Now if WI' is the original watermarked image (i.e., $WI' = WI$) or, WI' is a modified watermarked image where modification level is such that, the BCH error correcting procedure can correctly rectify the errors due to this modification, then the output of BCH error correcting process will be $WM'_{BIN} = WM_{BIN}$. Otherwise, BCH will not be able to rectify the errors correctly and will provide output as $WM'_{BIN} = 0$.

6. If $WM'_{BIN} = 0$, then stop the process and report the result: "*Extraction Fail: Un-watermarked image or modification level exceed maximum acceptable level*". Otherwise, transform WM'_{BIN} to its original format WM_{CON} and go to step 6.

7. Now check if $ROI = 1$, then separate WM_{CON} to ROI_{INFO}, DIC, $INDX$, and EPR_{ENCRY}, otherwise, if $ROI = 0$, then separate WM_{CON} to DIC, INDX, and EPR_{ENCRY}.

8. Decrypt EPR_{ENCRY} using the same secret key K_S to get the original EPR.

9. If $ROI = 0$, then report "*No ROI to display*". Otherwise if, $ROI = 1$, then the algorithm automatically draws the polygonal ROI using the ROI_{INFO}.

5.3.2 Results and Discussion

To evaluate the performance effectiveness of '*Scheme 2*', extensive experiments have been carried out on various modalities (CT, MRI, USG, X-Ray etc.) of grayscale (8 bpp) medical images of size 512×512. The DIC and $INDX$ consisted of 20 ($20 \times 7 = 140$ bits) and 15 ($15 \times 7 = 105$ bits) characters respectively. EHR of different sizes (128 and 144 characters) are used in the experiments, along with two different configurations for BCH error correcting process. EHR of size 128 char-

acters with BCH(255,115,21) is used in case when ROI's information is specified, and in case of no ROI, EHR/PHR of size 144 characters with BCH(255,139,15) have been used. After three level CNT $(2, 4, 8)$ decomposition of the image with '*9-7*' pyramid filter and '*pkva*' directional filter, the size of the low pass subband is 64×64. We have used $p = 23$ in the Eq.(5.5). The value of α is set to 55 after lots of experiments.

To show the effectiveness of the proposed MIW technique both subjective as well as quantitative analysis have been carried out. All the quantitative measures mentioned in '*Scheme 1*' have been used for this purpose. The conventional measures used for authentication of the extracted watermark like Normalized Correlation (NC), Bit Error Rate (BER) etc., are not applicable for '*Scheme 2*'. The MIW technique ('*Scheme 2*') described above, can successfully extract the embedded watermark without any error, from the original watermarked image or a modified watermarked image, where the modification level is below a maximum acceptable modification amount. Otherwise, if an un-watermarked image or a modified watermarked image, where the modification level exceed the maximum acceptable modification amount, is used during the extraction process, then '*Scheme 2*' will give output: "*Extraction Fail: Un-watermarked image or modification level exceed maximum acceptable level*". Therefore, NC and/or BER are not suitable to evaluate the performance of '*Scheme 2*'.

An expert clinician has been asked to subjectively evaluate the effectiveness of '*Scheme 2*'. After careful manual inspection, the clinician has conformed to the effectiveness of the described '*Scheme 2*'. He has found no significant visual difference between the original and the watermarked medical images, which suggests that there is no noticeable visual and/or informational degradation in the watermarked images.

Figure 5.15, shows the visual effect of watermark insertion in some of the test

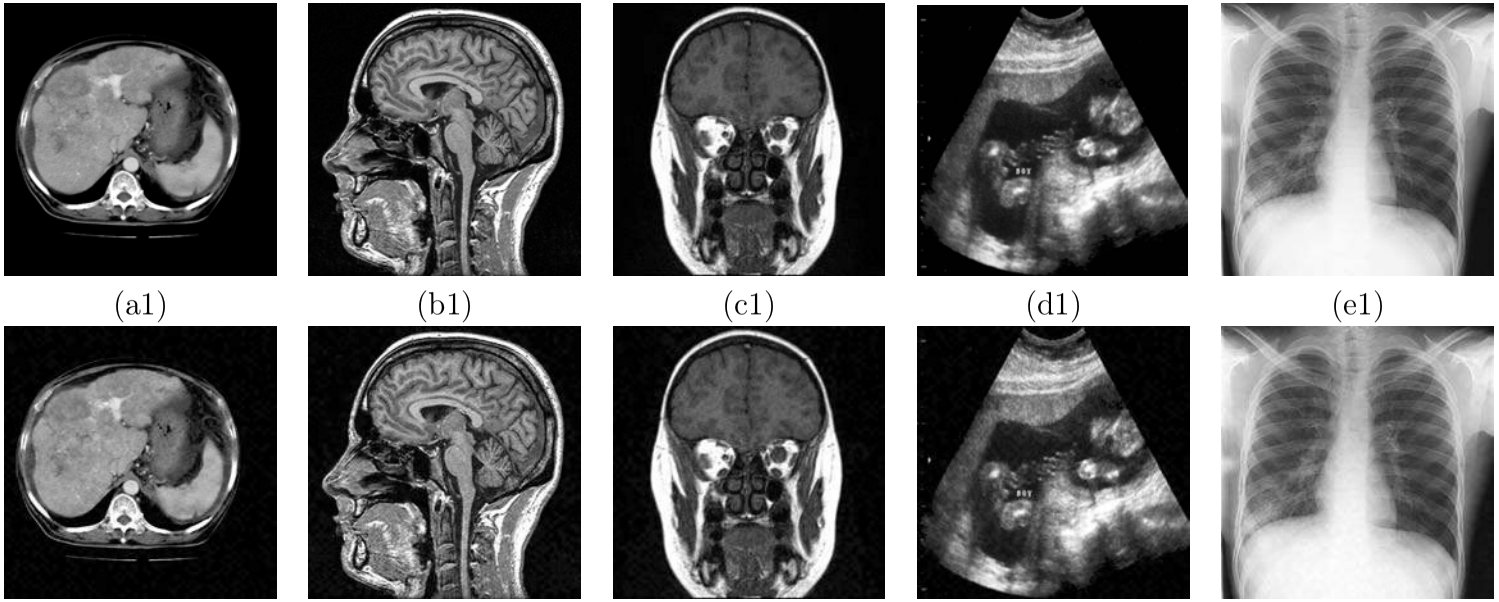

Figure 5.15: Original images (above ((a1)-(e1)) and their corresponding watermarked images produced by '*Scheme 2*' (below ((a2)-(e2)).

Table 5.4: Performance of '*Scheme 2*' when no ROI is specified

Image	**PSNR**	**WPSNR**	**MSSIM**	**Watson's Metric (TPE)**
abdomeCT	34.8498	35.952	0.7887	0.19
cthead	34.3799	35.982	0.9054	0.10
mriBrain	34.0404	37.159	0.9344	0.08
usg	34.6249	36.412	0.8932	0.14

Table 5.5: Performance of '*Scheme 2*' when ROI is specified

Image	**PSNR**	**WPSNR**	**MSSIM**	**Watson's Metric (TPE)**
abdomeCT	34.5594	35.583	0.7703	0.20
cthead	34.3763	35.970	0.9007	0.11
mriBrain	34.0338	37.117	0.9343	0.08
usg	34.5218	36.214	0.8838	0.14

medical images used in the experiments. The results show that there is no significant visual difference between the original and the watermarked images. Table 5.4, shows the PSNR, WPSNR, MSSIM and TPE values, when no ROI is specified. The PSNR and WPSNR values of the different test medical images show that, the visual differences between the original and the watermarked images are very low. Acquired values for MSSIM indicate that the original and the watermarked images are very much similar. The low values for TPE suggests that, the visual degradation caused by '*Scheme 2*' is also very low.

Performance of the '*Scheme 2*' in case when ROI is specified is shown in Table 5.5, for the same set of test images, which are used to produce the results of Table 5.4. During this performance evaluation, a polygonal ROI having 10 vertices are used for all the test images. From Table 5.4 and Table 5.5, it can be seen that the values of PSNR, WPSNR, MSSIM and TPE differs very slightly, which indicates that '*Scheme 2*' perform equally well in both the cases when ROI is specified or not.

In '*Scheme 2*', the watermark is embedded in the LPS of the medical images,

after 3 level of contourlet decomposition. The size of the original image and LPS is 512×512 and 64×64 respectively. So the maximum payload capacity of '*Scheme 2*' is $(64 \times 64)/(512 \times 512) = 0.0156$ bpp. But if we embed this maximum amount of watermark payload in the image by '*Scheme 2*', the watermarked image would be unacceptably distorted. The watermark to be embedded consists of DIC, INDX, EHR/PHR and optionally ROI Information. If ROI is specified then the size of the embedded watermark is 1369 bits and incase when ROI is not specified, then the size of the embedded watermark is 1253 bits. So the hiding capacity of the proposed scheme considering acceptable distortion is 0.0052 bpp (with ROI) or 0.0047 bpp (without ROI).

As mentioned previously that the value of the watermarking strength factor (α) determines the robustness and imperceptibility of '*Scheme 2*'. The higher the value of α, the more robust the method is, and the imperceptibility becomes low. The reverse is also true. The graph of the Figure 5.16, shows the variation of image quality (in terms of PSNR in dB) with respect to watermarking strength factor α of '*Scheme 2*' for a particular test medical image (abdomenCT Figure 5.15(a1)). Similar results have been found for other test images used in the experiments.

To evaluate the effectiveness of '*Scheme 2*', against JPEG compression, different watermarking strength factors (α) are used and the watermarked images are JPEG compressed with different quality factors (high quality factor indicates low compression and better image quality and low quality factor means high compression and worse image quality). The graph of the Figure 5.17, indicates the effectiveness of '*Scheme 2*' for a particular test medical image (abdomenCT Figure 5.15(a1)). In the graph of the Figure 5.17, the JPEG quality factor at a certain α denotes the highest JPEG compression, that can be achieved with that α, without any error in the extracted watermark. For the other test images used in the experiments, similar results have been obtained.

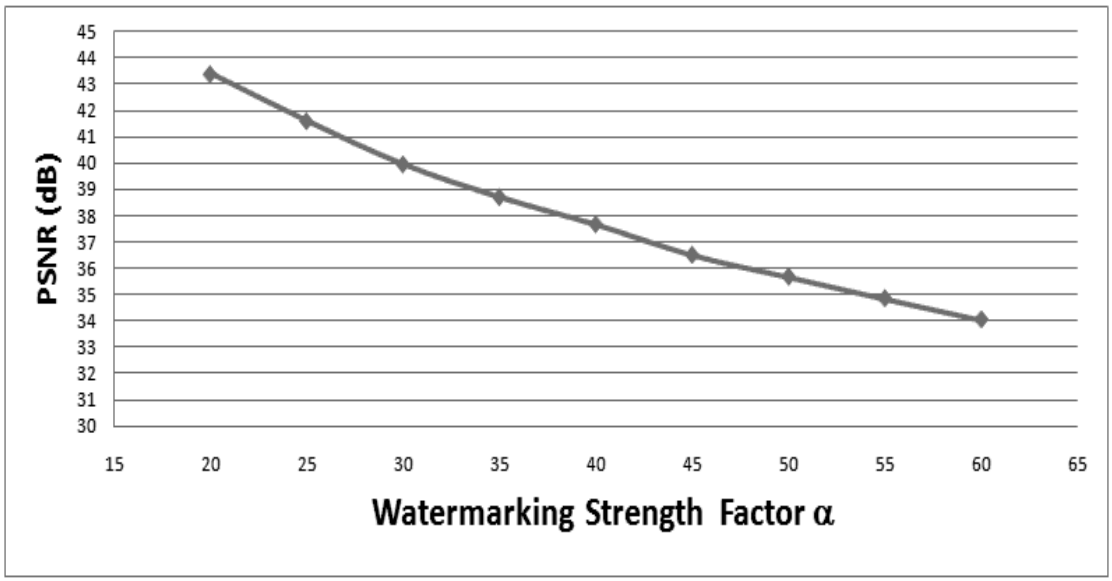

Figure 5.16: Watermarking strength factor (α) vs PSNR (dB).

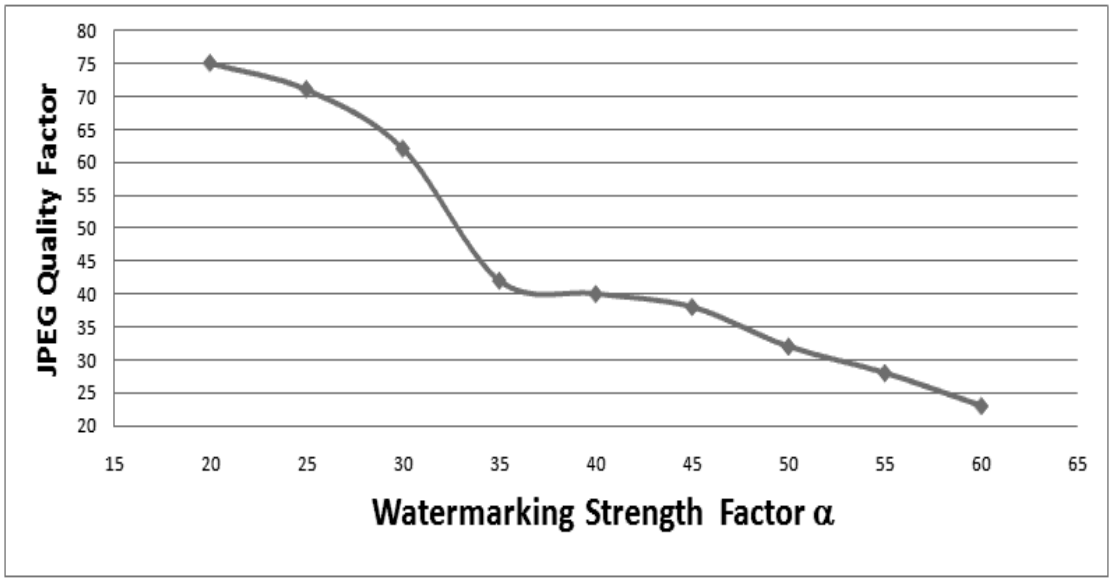

Figure 5.17: Watermarking strength factor (α) vs JPEG Quality Factor.

Table 5.6: Attacks where '*Scheme 2*' successfully extracted the watermark

Attack	**Parameters**
Copy Attack	——
Gaussian Filtering1	3×3 window
Gaussian Filtering2	5×5 window
Mean Filtering	3×3 window
Median Filtering	3×3 window
Trimmed Mean Filtering	7×7 window, 2 samples trimmed
Wiener Filtering	3×3 window
Hard Thresholding	3×3 window
Sample Down Up1	Downsample factor 0.75, Upsample factor 1.333
Sample Down Up2	Downsample factor 0.50, Upsample factor 2.000
Template Removal	——
Salt & Pepper Noise	Noise Density = 0.002
Speckle Noise	Mean = 0, Var = 0.004

Checkmark benchmark software [386] has been used to evaluate the performance of '*Scheme 2*' in case of JPEG2000 compression. The watermarked images are compressed with varying bitrates using JPEG2000 wavelet compression (the JASPER compression program) as mentioned in the Checkmark benchmark. We have compressed the watermarked images using bit rates [8, 3.5, 1.5, 0.8, 0.6, 0.5, 0.4, 0.3, 0.2]. It has been found that the '*Scheme 2*' can successfully extract the embedded watermark in all the cases.

Even though, the main motivation of this above mentioned MIW scheme is to resists high compression attacks (both JPEG and JPEG2000), we have also tested the robustness of '*Scheme 2*' against other watermark attacks (mostly using Checkmark benchmark software and some others). The performance of '*Scheme 2*' is given in Table 5.6, which shows only the attacks (with parameters) where '*Scheme 2*' successfully extracted the inserted watermark.

Comparison with Ref. [293] reveals that, the method is more imperceptible (in terms of PSNR), but less robust than '*Scheme 2*'. In Ref. [293] only the ROI of

the image can be embedded, but no EHR/PHR or DIC or INDX. If the method of Ref. [293] is used to insert EHR/PHR, DIC and INDX, it will not be able to extract the watermark without error, even with a small JPEG compression. Comparison with Ref. [281] shows that, '*Scheme 2*' is more imperceptible (in terms of PSNR) and also more robust. The MIW methods described in Refs. [281, 293] are non-blind, that means the original un-watermarked medical image is needed for correct extraction of the watermark. Whereas, '*Scheme 2*' is blind, which makes it suitable for real-life applications. The watermarking technique described in Ref. [283] is less secured and needs a reference image of size 128×128 for blind extraction of the embedded watermark. Whereas, in '*Scheme 2*', we only need the secret key during watermark extraction. The hiding capacity of '*Scheme 2*' (0.0052 bpp (with ROI) or 0.0047 bpp (without ROI)) is higher than the hiding capacity (0.0036 bpp) of the scheme described in Ref. [283]. Moreover, the MIW technique of Ref. [283], is less robust against JPEG compression attack (up to quality factor $80\% - 75\%$) and no result is given against JPEG2000 compression. Comparison with the method of Ref. [282] shows that both the hiding capacity (0.0077 bpp) and imperceptibility in terms of PSNR (60 dB) is higher than'*Scheme 2*'. But, the scheme of Ref. [282] is less robust against various watermarking attacks than '*Scheme 2*'. Also, the scheme of Ref. [282] is not robust against JPEG and JPEG2000 compression. The '*Scheme 2*' is also much more secure than the methods described above. The use of EHR/PHR encryption by AES with a secret key makes the EHR/PHR secured, which is very much required, as EHR/PHR is highly confidential, critical as well as sensitive in nature. Also the scattering of watermark bits in the embedding region makes '*Scheme 2*' safe and protected. From the above mentioned results and discussion, it can be observed that '*Scheme 2*' is an effective blind and secure MIW technique when high compression and robustness is desired.

Chapter 6

Conclusion and Future Work

This chapter summarizes the major contributions of findings and the research activities reported in the present thesis. It also provides certain pointers for future research in various fields of the medical imaging computing paradigm.

6.1 Contributions

In this thesis work, certain aspects of medical image computing domain have been explored, existing problems have been identified and several feasible solutions have been proposed. Specifically, the major contributions of the present thesis work can be summarized as follows:

- Presence of different kinds of noise in various modalities of medical images, results in degradation in the image quality. Rician noise in MR images, often makes it difficult to properly analyze and interpret the acquired images. There exists several state-of-the-art MR image denoising methods based on different noise removal mechanisms. Recently, MR image denoising schemes based on the NLM paradigm, have gained popularity for their superior noise removal performance. But, NLM based MR image denoising techniques have one major shortcoming, i.e., high computational cost. Moreover, negative contributions of non-significant pixels in the denoising procedure also result in sub-optimal quality of denoised images. Most of the state-of-the-art

NLM based noise removal schemes for MR images, concentrate on either improving the denoising quality or reducing the computational burden. In Chapter 2 of this thesis, we have described a novel and alternate way to pre-select a subset of pixels in the non-local neighbors of NLM paradigm, depending on their similarities with the pixel of interest. The pre-selection of pixels is achieved by the time-matrix information of the noisy image obtained through PCNN with null interconnection. Denoised MR images, obtained by this introduced noise removal technique do not suffer from the problem of over-smoothing of fine textural and structural details, compared to existing denoising schemes. Experimental results and comparisons show that the pre-selection of significant pixels, through the use of synchronous pulse burst output property of PCNN results in faster computation without sacrificing the denoising performance of NLM.

- Most of the state-of-the-art MIF techniques suffer from various problems of image degradation like contrast reduction, blocking effects, blurring and loss of image details etc. Moreover, most of these schemes are modality and task specific. Keeping the above mentioned issues in mind, in Chapter 3 of this present thesis, we have used the shift invariance, multiscale and multidirectional properties of NSCT along with the global coupling and pulse synchronization characteristics of PCNN to develop two novel MIF schemes (termed as '*Scheme 1*' and '*Scheme 2*'). These MIF techniques can capture the subtle differences as well as the fine details present in the source medical images into the fused image without reducing the contrast. In '*Scheme 1*', the use of MSF (capable of efficiently representing the subtle directional details of the medical images) along with the use of different fusion rules for different subbands produces fused images with higher spatial resolution,

fewer unwanted degradations with lesser deviations from the source medical images. It has been observed from the obtained results and comparisons with state-of-the-art schemes that the fused images produced by '*Scheme 1*' are more intelligible, more informative and have higher contrast which is very helpful for clinicians in their diagnosis and treatment planning.

In Chapter 3 of this thesis, we have also introduced another novel MIF method ('*Scheme 2*') based on a hybrid neuro-fuzzy approach in the NSCT domain. To overcome the drawbacks of the traditional MIF schemes, and to integrate as much information as possible into the fused images, we have exploited the advantages of the NSCT, RPCNN, and fuzzy logic. The linking strengths of the neurons in the RPCNNs are adaptively computed based on the fuzzy characteristics (reflecting the ambiguity of HVS response) of the image, which results in high-quality fused images. The parameter estimation problem of PCNN is handled by modifying the structure of PCNN (containing far fewer number of adjustable parameters) and adaptively setting the value of only the most impacting parameter (linking strengths). The experimental results show that '*Scheme 2*' can preserve more useful information in the fused image with higher spatial resolution and lesser deviation from the source images.

- Chapter 4 of this thesis deals with the problem of '*effective information retrieval*' from large and ever growing medical image repositories. In this chapter, two different solutions are provided for two different kinds of medical image search problems. In the first part of this chapter, we have described the benefits of the combination of MGA of RT, and a computationally less expensive SVM (LS-SVM) to build a fully automatic and accurate brain MR image classification system. With this combination, we not only have

achieved higher feature reduction, but also obtained superior performance than the state-of-the-art schemes. One of the major shortcomings of the existing brain MR image classification systems is their performance degradation in presence of common MRI artifacts (rotation, noise, different dynamic range, blurring etc.). Later in this chapter, an improvement of the aforementioned brain MR image classification scheme is described, which performs satisfactorily even in the presence of common MRI artifacts. This improvement is based on the use of both the LFS and HFSs information of the underlying transform domain. Moreover, we have also included a performance comparison study of several recently proposed transform domains like curvelet, contourlet and type-I ripplet. Comparative study of the performances of these transforms show that CNT performs superiorly considering both the classification accuracy and the dimension of the feature vector.

The second part of this chapter contains the description of a medical image retrieval system. From our experiments, we have noticed that NSCT based image coding is suitable for representing low level features of the medical images. Due to low feature vector dimension and use of LS-SVM classifier, the described CBMIR system is able to achieve satisfactory results with lower computational cost. Moreover, the proposed CBMIR system has been found to be general, in the sense that it works efficiently for different modalities of medical image databases.

- Digital watermarking has the potential of becoming an all-in-one solution tool to address various issues regarding effective and ethical management and distribution of medical information. In this regard, two different MIW schemes (termed as '*Scheme 1*' and '*Scheme 2*') have been demonstrated in the last contributory chapter (Chapter 5) of this thesis. '*Scheme 1*' is a

blind, fragile watermarking technique with good imperceptibility, high payload and enhanced security. This scheme can be used for different modalities of medical images. It can be applied to a variety of digital medical images with different size, format, and bit-depth. The tamper localization capability of '*Scheme 1*' can successfully locate even a single tampered pixel and can detect the corresponding 3×3 block as the tampered region.

Storage and transmission of huge number of medical images and related information in a network environment has proven to be highly costly. This also requires special security measures to withstand different kinds of attacks, designed to destroy the integrity, authenticity, reliability and confidentiality of the critical and sensitive medical information. The '*Scheme 2*' of Chapter 5, describes a blind, robust MIW technique with good imperceptibility and enhanced security. This method is not only robust against both high JPEG and JPEG2000 compression, but can also resist a large number of other watermarking attacks. The '*Scheme 2*' can be used for different medical image modalities. The experimental results and comparisons with state-of-the-art MIW techniques, indicate that both the aforementioned MIW schemes are efficient and given their relative simplicity, they can be applied to medical images right after acquisition, to serve in many medical applications concerned with privacy protection, safety, archiving, access control, retrieval and management.

6.2 Future Work

Medical image computing paradigm is a rapidly expanding field and new challenges are arising everyday. The work reported in this present thesis is an attempt to solve certain problems of the medical image computing paradigm. Although

the solutions proposed in this thesis have been found to be useful and efficient, they need further investigations to be widely applicable in various medical image application domains. These may include theoretical analysis of performance, development of quantitative indices for evaluation, and study of sensitivity of the methodologies to noise. Some of the possible future extensions of the work presented in thesis are pointed out here.

- The MRI denoising scheme described in Chapter 2 can be incorporated with more improved version of the NLM filter to get superior results. Also, the extension of this denoising technique for 3D MR images should be carried out in future.

- In Chapter 3 of this thesis, main emphasis is given on fusion of multimodal (inter-modality) medical images. The demonstrated IF schemes may also be used for unimodal (intra-modality) medical image (with different configuration settings) fusion. The effects of different fusion rules, and new techniques to compute the parameters of PCNN, are also some of the future scope of research.

- The effectiveness of other feature representation schemes along with other supervised and unsupervised classification techniques should be investigated in future to improve the brain MR image classification scheme described in Chapter 5. The proposed image representative feature vector may also be used to classify other modalities of medical images. The retrieval accuracy of the proposed medical image retrieval system may be improved by incorporating relevance feedback mechanism into it.

- The spatial domain MIW scheme described in Chapter 5 can be improved to insert higher payload by making it independent of ROI's size. This proposed MIW technique has the capability to localize tampering in the medical

images. Investigation is required to improve this MIW scheme by incorporating tamper correction capability. In the proposed transform domain MIW scheme, the value of α plays a vital role. The value of α is experimentally set in the proposed technique. It would be better if α can be set adaptively and automatically. Moreover, effectiveness of others transforms like curvelet, ripplet, non-subsampled contourlet can be tested to improve the results. Both the proposed MIW schemes may be improved by applying different insertion and extraction rules.

- This thesis contains several solutions only for gray-level 2D medical images. In future, these proposed solutions can be extended to work also on color and volumetric (3D) medical images. The use of the developed schemes in more real-life applications should be demonstrated. Finally, it would be worthwhile to study their implementation in hardware.

Bibliography

[1] M. Nadeski and G. Frantz, "The future of medical imaging," Texas Instruments, Dallas, Texas, White Paper, 2008. [Online]. Available: http://www.ti.com/lit/wp/slyy020/slyy020.pdf

[2] W. R. Hendee and E. R. Ritenour, *Medical Imaging Physics*, 4th ed. Canada: Wiley-Liss, 2002.

[3] I. Bankman, *Handbook of Medical Image Processing and Analysis*, 2nd ed., ser. Academic Press Series in Biomedical Engineering. USA: Academic Press, 2008.

[4] G. Dougherty, *Digital Image Processing for Medical Applications*, 1st ed. UK: Cambridge University Press, 2009.

[5] M. Sonka and J. M. Fitzpatrick, *Handbook of Medical Imaging: Medical Image Processing and Analysis*. SPIE Publications, 2009, vol. 2.

[6] P. Suetens, *Fundamentals of Medical Imaging*, 2nd ed. UK: Cambridge University Press, 2009.

[7] O. F. Erondu, *Medical Imaging*. Croatia: InTech, 2011.

[8] H. Handels and J. Ehrhardt, "Medical image computing for computer-supported diagnostics and therapy," *Methods of Information in Medicine*, vol. 48, no. 1, pp. 11–17, 2009.

[9] G. Frieder, G. T. Herman, C. Meyer, and J. Udupa, "Large software problems for small computers: an example from medical imaging," *IEEE Software*, vol. 2, no. 5, pp. 37–47, 1985.

[10] T. M. Lehmann, H. P. Meinzer, and T. Tolxdorff, "Advances in biomedical image analysis – past, present and future challenges," *Methods of Information in Medicine*, vol. 43, no. 4, pp. 308–314, 2004.

[11] H. Handels, A. Horsch, and H. P. Meinzer, "Advances in medical image computing," *Methods of Information in Medicine*, vol. 46, no. 3, pp. 251–253, 2007.

[12] T. M. Deserno, *Biomedical Image Processing*, ser. Biology and Medical Physics, Biomedical Engineering. Springer, 2011.

[13] A. Pizurica, A. M. Wink, E. Vansteenkiste, W. Philips, and J. B. T. M. Roerdink, "A review of wavelet denoising in MRI and ultrasound brain imaging," *Current Medical Imaging Reviews*, vol. 2, no. 2, pp. 247–260, 2006.

[14] E. R. McVeigh, R. M. Henkelman, and M. J. Bronskill, "Noise and filtration in magnetic resonance imaging," *Medical Physics*, vol. 12, no. 5, pp. 586–591, 1985.

[15] H. Zhu, Y. Li, J. G. Ibrahim, X. Shi, H. An, Y. Chen, W. Gao, W. Lin, D. B. Rowe, and B. S. Peterson, "Regression models for identifying noise sources in magnetic resonance imaging," *Journal of the American Statistical Association*, vol. 104, no. 486, pp. 623–637, 2009.

[16] A. Pizurica, W. Philips, I. Lemahieu, and M. Acheroy, "A versatile wavelet domain noise filtration technique for medical imaging," *IEEE Transactions on Medical Imaging*, vol. 22, no. 3, pp. 323–331, 2003.

[17] P. F. Stetson, F. G. Sommer, and A. Macovski, "Lesion contrast enhancement in medical ultrasound imaging," *IEEE Transactions on Medical Imaging*, vol. 16, no. 4, pp. 416–425, 1997.

[18] H. Rabbani, R. Nezafat, and S. Gazor, "Wavelet-domain medical image denoising using bivariate laplacian mixture model," *IEEE Transactions on Biomedical Engineering*, vol. 56, no. 12, pp. 2826–2837, 2009.

[19] C. Westbrook, *Handbook of MRI Technique*, 3rd ed. USA: Wiley-Blackwell, 2008.

[20] L. Landini, V. Positano, and M. F. Santarelli, *Advanced Image Processing in Magnetic Resonance Imaging.* Taylor & Francis, Edited, 2005.

[21] P. Gravel, G. Beaudoin, and J. A. D. Guise, "A method for modeling noise in medical images," *IEEE Transactions on Medical Imaging*, vol. 23, no. 10, pp. 1221–1232, 2004.

[22] L. J. Erasmus, D. Hurter, M. Naude, H. G. Kritzinger, and S. Acho, "A short overview of MRI artefacts," *SA Journal of Radiology*, pp. 13–17, 2004.

[23] Y. Zhuge, J. K. Udupa, J. Liu, and P. K. Saha, "Image background inhomogeneity correction in MRI via intensity standardization," *Computerized Medical Imaging and Graphics*, vol. 33, no. 1, pp. 7–16, 2008.

[24] A. Wong and A. K. Mishra, "Quasi-Monte carlo estimation approach for denoising MRI data based on regional statistics," *IEEE Transactions on Biomedical Engineering*, vol. 58, no. 4, pp. 1076–1083, 2011.

[25] J. Mohan, V. Krishnaveni, and Y. Guo, "A survey on the magnetic resonance image denoising methods," *Biomedical Signal Processing and Control*, vol. 9, pp. 56–69, 2014.

[26] J. Sijbers and A. den Dekker, "Maximum likelihood estimation of signal amplitude and noise variance form MR data," *Magnetic Resonance in Medicine*, vol. 51, pp. 586–594, 2004.

[27] J. Sijbers, A. den Dekker, J. V. Audekerke, M. Verhoye, and D. V. Dyck, "Estimation of the noise in magnitude MR images," *Magnetic Resonance Imaging*, vol. 16, no. 1, pp. 87–90, 1998.

[28] R. M. Henkelman, "Measurement of signal intensities in the presence of noise in MR images," *Medical Physics*, vol. 12, no. 2, pp. 232–233, 1985.

[29] H. Gudbjartsson and S. Patz, "The rician distribution of noisy MRI data," *Magnetic Resonance in Medicine*, vol. 34, no. 6, pp. 910–914, 1995.

[30] O. Dietrich, J. G. Raya, S. B. Reeder, M. Ingrisch, M. F. Reiser, and S. O. Schoenberg, "Influcence of multichannel combination, parallel imaging and other reconstruction techniques on MRI noise characteristics," *Magnetic Resonance Imaging*, vol. 26, no. 6, pp. 754–762, 2008.

[31] P. Perona and J. Malik, "Scale-space and edge detection using anisotropc diffusion," *IEEE Transactions Pattern Analysis and Machine Intelligence*, vol. 12, no. 7, pp. 629–639, 1990.

[32] G. Gerig, O. Kubler, R. Kikinis, and F. A. Jolesz, "Nonlinear anisotropic filtering of MRI data," *IEEE Transactions on Medical Imaging*, vol. 11, no. 2, pp. 221–232, 1992.

[33] J. Sijbers, A. J. den Dekker, A. V. D. Linden, M. Verhoye, and D. V. Dyck, "Adaptive anisotropic noise filtering for magnitude MR data," *Magnetic Resonance Imaging*, vol. 17, no. 10, pp. 1533–1539, 1999.

[34] M. Lysaker, A. Lundervold, and T. Xue-Cheng, "Noise removal using fourth-order partial differential equation with applications to medical magnetic resonance images in space and time," *IEEE Transactions on Image Processing*, vol. 12, no. 12, pp. 1579–1590, 2003.

[35] K. Krissian and S. Aja-Fernandez, "Noise driven anisotropic diffusion filtering of MRI," *IEEE Transactions on Image Processing*, vol. 18, no. 10, pp. 2265–2274, 2009.

[36] C. Tomasi and R. Manduchi, "Bilateral filtering for gray and color images," in *Proceedings of 6th IEEE International Conference on Computer Vision*, 1998, pp. 839–846.

[37] S. Walker, D. Miller, and J. Tanabe, "Bilateral spatial filtering: refining methods for localizing brain activation in the presence of parenchymal abnormalities," *Neuroimage*, vol. 33, no. 2, pp. 564–569, 2006.

[38] J. Xie, P. Heng, and M. Shah, "Image diffusion using saliency bilateral filter," *IEEE Transactions on Information Technology in Biomedicine*, vol. 12, no. 6, pp. 768–771, 2008.

[39] W. C. K. Wong and A. C. S. Chung, "A nonlinear and non-iterative noise reduction technique for medical images: concept and methods comparison," in *Proceedings of International Congrress Series, Elsevier*, vol. 1268, 2004, pp. 171–176.

[40] W. C. K. Wong, A. C. S. Chung, and S. C. H. Yu, "Trilateral filter for biomedical images," in *Proceedings of IEEE International Symposium on Biomedical Imaging*, vol. 1, 2004, pp. 820–823.

[41] A. Buades, B. Coll, and J. Morel, "A review of image denoising algorithms, with a new one," *SIAM Journal on Multiscale Modelling and Simulation*, vol. 4, no. 2, pp. 490–530, 2005.

[42] J. V. Manjon, J. C. Caballero, J. J. Lull, G. G. Marti, L. M. Bonmati, and M. Robles, "MRI denoising using non-local means," *Medical Image Analysis*, vol. 12, no. 4, pp. 514–523, 2008.

[43] P. Coupe, P. Yger, S. Prima, P. Hellier, C. Kervrann, and C. Barillot, "An optimized blockwise nonlocal means denoising filter for 3-D magnetic resonance images," *IEEE Transactions on Medical Imaging*, vol. 27, no. 4, pp. 425–441, 2008.

[44] J. V. Manjon, M. Robles, and N. A. Thacker, "Multispectral MRI denoising using non-local means," in *Proceedings of International Conference on Medical Image Understanding and Analysis*, 2007, pp. 41–46.

[45] H. Liu, C. Yang, N. Pan, E. Song, and R. Green, "Denoising 3D MR images by the enhanced non-local means filter for rician noise," *Magnetic Resonance Imaging*, vol. 28, pp. 1485–1496, 2010.

[46] A. Buades, B. Coll, and J. Morel, "A non local algorithm for image denoising," in *Proceedings IEEE International Conference on Computer Vision and Pattern Recognition*, vol. 2, 2005, pp. 60–65.

[47] B. Kang, O. Choi, J. D. Kim, and D. Hwang, "Noise reduction in magnetic resonance images using adaptive non-local means filtering," *IEEE Electronics Letters*, vol. 49, no. 5, pp. 324–326, 2013.

[48] P. Coupe, P. Yger, and C. Barillot, "Fast non local means denoising for 3D MR images," in *Proceedings of International Conference on Medical Image Computing and Computer Assisted Intervention*, 2006, pp. 33–40.

[49] M. Mahmoudi and G. Sapiro, "Fast image and video denoising via nonlocal means of similar neighborhoods," *IEEE Signal Processing Letters*, vol. 12, no. 12, pp. 839–842, 2005.

[50] A. T. Vega, A. V. G. Perez, S. A. F., and C. F. Westin, "Efficient and robust nonlocal means denoising of MR data based on salient features matching," *Computer methods and programs in biomedicine*, vol. 105, pp. 131–144, 2012.

[51] P. Coupe, P. Hellier, S. Prima, C. Kervrann, and C. Barillot, "3D wavelet subbands mixing for image denoising," *International Journal of Biomedical Imaging*, vol. 2008, pp. 1:1–1:11, 2008.

[52] N. W. Daessle, S. Prima, P. Coupe, S. P. Morrissey, and C. Barillot, "Rician noise removal by non-local means filtering for low signal-to-noise ratio MRI: applications to DT-MRI," in *Proceedings of International Conference on Medical Image Computing and Computer Assisted Intervention*, 2008, pp. 344–351.

[53] Y. Gal, A. J. Mehnert, A. P. Bradley, K. McMahon, D. Kennedy, and S. Crozier, "Denoising of dynamic contrast-enhanced MR images using dynamic nonlocal means," *IEEE Transactions on Medical Imaging*, vol. 29, no. 2, pp. 302–310, 2009.

[54] J. V. Manjon, P. Coupe, L. M. Bonmati, D. Collins, and M. Robles, "Adaptive nonlocal means denoising of MR images with spatially varying noise levels," *Journal of Magnetic Resonance Imaging*, vol. 31, no. 1, pp. 192–203, 2010.

[55] J. V. Manjon, P. Coupe, A. Buades, D. Collins, and M. Robles, "New methods for MRI denoising based on sparseness and self-similarity," *Medical Image Analysis*, vol. 16, no. 1, pp. 18–27, 2012.

[56] P. Coupe, J. V. Manjon, M. Robles, and D. L. Collins, "Adaptive multiresolution non-local means filter for 3D MR image denoising," *IET Image Processing*, vol. 6, no. 5, pp. 558–568, 2012.

[57] J. B. Weaver, Y. Xu, D. M. Healy, and L. D. Cromwell, "Filtering noise from images with wavelet transforms," *Magnetic Resonance Imaging*, vol. 21, no. 2, pp. 288–295, 1991.

[58] R. D. Nowak, "Wavelet-based rician noise removal for magnetic resonance imaging," *IEEE Transactions on Image Processing*, vol. 8, no. 10, pp. 1408–1419, 1999.

[59] J. C. Wood and K. M. Johnson, "Wavelet packet denoising of magnetic resonance images: importance of rician noise at low SNR," *Magnetic Resonance in Medicine*, vol. 41, no. 3, pp. 631–635, 1999.

[60] M. E. Alexander, R. Baumgartner, A. R. Summers, C. Windischberger, M. Klarhoefer, E. Moser, and R. L. Somorjai, "A wavelet-based method for improving signal-to-noise ration and contrast in MR images," *Magnetic Resonance Imaging*, vol. 18, no. 2, pp. 169–180, 2000.

[61] Z. Q. Wu, J. A. Ware, and J. Jiang, "Wavelet-based rayleigh background removal in MRI," *IEEE Electronics Letters*, vol. 39, no. 7, pp. 603–605, 2003.

[62] C. S. Anand and J. S. Sahambi, "Wavelet domain non-linear filtering for MRI denoising," *Magnetic Resonance Imaging*, vol. 28, no. 6, pp. 842–861, 2010.

[63] F. Luisier, T. Blu, and P. J. Wolfe, "A CURE for noisy magnetic resonance images: Chi-square unbiased risk estimation," *IEEE Transactions on Image Processing*, vol. 21, no. 8, pp. 3454–3466, 2012.

[64] J. L. Starck, E. J. Candes, and D. L. Donoho, "The curvelet transform for image denoising," *IEEE Transactions on Image Processing*, vol. 11, no. 6, pp. 670–684, 2002.

[65] M. N. Do and M. Vetterli, "The contourlet transform: an efficient directional multiresolution image representation," *IEEE Transactions on Image Processing*, vol. 14, no. 12, pp. 2091–2106, 2005.

[66] L. Parthiban and R. Subramanian, "Medical image denoising using X-lets," in *Proceedings of Annual IEEE India Conference*, 2006, pp. 1–6.

[67] J. Ma and G. Plonka, "Combined curvelet shrinkage and nonlinear anisotropic diffusion," *IEEE Transactions on Image Processing*, vol. 16, no. 9, pp. 2198–2206, 2007.

[68] V. G. Ashamol, G. Sreelekha, and P. S. Sathidevi, "Diffusion-based image denoising combining curvelet and wavelet," in *Proceedings of 15th International Conference on Systems, Signals and Image Processing*, 2008, pp. 169–172.

[69] M. A. Erturk, P. A. Bottomley, and A. M. M. E. Sharkawy, "Denoising MRI using spectral subtraction," *IEEE Transactions on Biomedical Engineering*, vol. 60, no. 6, pp. 1556–1562, 2013.

[70] G. McGibney and M. R. Smith, "An unbiased signal-to-noise ratio measure for magnetic resonance images," *Medical Physics*, vol. 20, pp. 1077–1078, 1993.

[71] J. Sijbers, D. Poot, A. J. den Dekker, and W. Pintjenst, "Automatic estimation of the noise variance from the histogram of a magnetic resonance image," *Physics in Medical Biology*, vol. 52, no. 5, pp. 1335–1348, 2007.

[72] L. He and I. Greenshields, "A nonlocal maximum likelihood estimation methodfor rician noise reduction in MR images," *IEEE Transactions on Medical Imaging*, vol. 28, no. 2, pp. 165–172, 2009.

[73] J. Rajan, D. Poot, J. Juntu, and J. Sijbers, "Noise measurement from magnitude MRI using local estimates of variance and skewness," *Physics in Medicine and Biology*, vol. 55, no. 16, pp. 441–449, 2010.

[74] J. Rajan, B. Jeurissen, M. Verhoye, J. Audekerke, and J. Sijbers, "Maximum like-lihood estimation-based denoising of magnetic resonance images usingrestriced local neighborhoods," *Physics in Medicine and Biology*, vol. 56, no. 16, pp. 5221–5234, 2011.

[75] J. Rajan, J. Veraat, J. V. Audekerke, M. Verhoye, and J. Sijbers, "Nonlocal maximum likelihood estimation method for denoising multiple-coil magnetic resonance images," *Magnetic Resonance Imaging*, vol. 30, no. 10, pp. 1512–1518, 2012.

[76] S. Aja-Fernandez, C. A.-Lopez, and C. Westin, "Noise and signal estimationin magnitude MRI and rician distributed images: a LMMSE approach," *IEEE Transactions on Image Processing*, vol. 17, no. 8, pp. 1383–1398, 2008.

[77] H. M. Golshan, R. P. Hasanzedeh, and S. C. Yousefzadeh, "An MRI denoising method using data redundancy and local SNR estimation," *Magnetic Resonance Imaging*, vol. 31, no. 7, pp. 1206–1217, 2013.

[78] S. Awate and R. Whitaker, "Nonparametric neighborhood statistics for MRI denoising," in *Proceedings of International Conference on Information Processing in Medical Imaging*, vol. 19, 2005, pp. 677–688.

[79] S. Awate and R. Whitaker, "Feature-preserving MRI denoising: a nonparametric empirical bayes approach," *IEEE Transactions on Medical Imaging*, vol. 26, no. 9, pp. 1242–1255, 2007.

[80] E. L. Rubio and M. N. F. Nunez, "Kernel regression based feature extraction for 3D MR image denoising," *Medical Image Analysis*, vol. 15, no. 4, pp. 498–513, 2011.

[81] P. Coupe, J. V. Manjon, E. Gedamu, D. Arnold, M. Robles, and D. L. Collins, "An object-based method for rician noise estimation in MR images," in *Proceedings of International Conference on Medical Image Computing and Computer Assisted Intervention*, vol. 12, 2009, pp. 601–608.

[82] P. Coupe, J. V. Manjon, E. Gedamu, D. Arnold, M. Robles, and D. L. Collins, "Robust rician noise estimation for MR images," *Medical Image Analysis*, vol. 14, no. 4, pp. 483–493, 2010.

[83] O. Ukimura, *Image Fusion.* Croatia: InTech, 2011.

[84] R. S. Blum and Z. Liu, *Multi-Sensor Image Fusion and Its Applications (Signal Processing and Communications).* USA: CRC Press, 2005.

[85] T. Stathaki, *Image Fusion: Algorithms and Applications.* UK: Academic Press, 2008.

[86] H. B. Mitchell, *Image Fusion: Theories, Techniques and Applications*, 1st ed. India: Springer, 2010.

[87] P. A. Elsen, E. J. D. Pol, and M. A. Viergever, "Medical image matching-a review with classification," *IEEE Engineering in Medicine and Biology Magazine*, vol. 12, no. 1, pp. 26–39, 1993.

[88] V. Barra and J. V. Boire, "A general framework for the fusion of anatomical and functional medical images," *NeuroImage*, vol. 13, no. 3, pp. 410–424, 2001.

[89] S. P. Constantinos, E. M.-Tzanakou, and M. S. Pattichis, "Medical imaging fusion applications: An overview," in *Proceedings of 35th Asilomar Conference on Signals, Systems and Computers*, vol. 2, 2001, pp. 1263–1267.

[90] B. V. Dasarathy, "Information fusion in the realm of medical applications-a bibliographic glimpse at its growing appeal," *Information Fusion*, vol. 13, no. 1, pp. 1–9, 2012.

[91] A. Galande and R. Patil, "The art of medical image fusion: A survey," in *Proceedings of International Conference on Advances in Computing, Communications and Informatics*, 2013, pp. 400–405.

[92] A. P. James and B. V. Dasarathy, "Medical image fusion: A survey of the state of the art," *Information Fusion*, vol. 19, pp. 4–19, 2014.

[93] G. Piella, "A general framework for multiresolution image fusion: from pixels to regions," *Information Fusion*, vol. 4, no. 4, pp. 259–280, 2003.

[94] M. Chandana, S. Amuth, and N. Kumar, "A hybrid multi-focus medical image fusion based on wavelet transform," *International Journal of Research & Reviews in Computer Science*, vol. 2, no. 4, pp. 948–953, 2011.

[95] R. Shen, I. Cheng, and A. Basu, "Cross-scale coefficient selection for volumetric medical image fusion," *IEEE Transactions on Biomedical Engineering*, vol. 60, no. 4, pp. 1069–1079, 2013.

[96] G. Bhatnagar, Q. M. J. Wu, and Z. Liu, "Directive contrast based multimodal medical image fusion in NSCT domain," *IEEE Transactions on Multimedia*, vol. 15, no. 5, pp. 1014–1024, 2013.

[97] S. M. Darwish, "Multi-level fuzzy contourlet-based image fusion for medical applications," *IET Image Processing*, vol. 7, no. 7, pp. 694–700, 2013.

[98] L. Wang, B. Li, and L. Tian, "Multimodal medical volumetric data fusion using 3-D discrete shearlet transform and global-to-local rule," *IEEE Transactions on Biomedical Engineering*, vol. 61, no. 1, pp. 197–206, 2014.

[99] P. Ganasala and V. Kumar, "CT and MR image fusion scheme in nonsubsampled contourlet transform domain," *Journal of Digital Imaging*, vol. 27, pp. 407–418, 2014.

[100] Z. Wang, D. Ziou, C. Armenakis, D. Li, and Q. Li, "A comparative analysis of image fusion methods," *IEEE Transactions on Geoscience and Remote Sensing*, vol. 43, no. 6, pp. 1391–1402, 2005.

[101] S. Li and B. Yang, "Multifocus image fusion using region segmentation and spatial frequency," *Image and Vision Computing*, vol. 26, no. 7, pp. 971–979, 2008.

[102] C. He, Q. Liu, H. Li, and H. Wang, "Multimodal medical image fusion based on IHS and PCA," in *Procedia Engineering: Symposium on Security Detection and Information Processing*, vol. 7, 2010, pp. 280–285.

[103] S. Daneshvar and H. Ghassemian, "MRI and PET image fusion by combining IHS and retina-inspired models," *Information Fusion*, vol. 11, no. 2, pp. 114–123, 2010.

[104] S. V. Petrovic and C. S. Xydeas, "Gradient-based multi-resolution image fusion," *IEEE Transactions on Image Processing*, vol. 13, no. 2, pp. 228–237, 2004.

[105] G. Pajares and J. M. de la Cruz, "A wavelet-based image fusion tutorial," *Pattern Recognition*, vol. 37, no. 9, pp. 1855–1872, 2004.

[106] A. A. Goshtasby and S. Nikolov, "Image fusion: Advances in the state of the art," *Information Fusion*, vol. 8, no. 2, pp. 114–118, 2007.

[107] S. Das, M. Chowdhury, and M. K. Kundu, "Medical image fusion based on ripplet transform type-I," *Progress in Electromagnetic Research B*, vol. 30, pp. 355–370, 2011.

[108] S. Li, B. Yang, and J. Hu, "Performance comparison of different multiresolution transforms for image fusion," *Information Fusion*, vol. 12, no. 2, pp. 74–84, 2011.

[109] S. Das and M. K. Kundu, "Ripplet based multimodality medical image fusion using pulse-coupled neural network and modified spatial frequency," in *Proceedings of IEEE International Conference on Recent Trends in Information Systems*, 2011, pp. 229–234.

[110] S. Das and M. K. Kundu, "Fusion of multimodality medical images using combined activity level measurement and contourlet transform," in *Proceedings of IEEE International Conference on Image Information Processing*, 2011, pp. 1–6.

[111] K. Feng, X. Zhang, and X. Li, "A novel method of medical image fusion based on bidimensional empirical mode decomposition," *Journal of Convergence Information Technology*, vol. 6, no. 12, pp. 84–91, 2011.

[112] P. S. Pradhan, R. L. King, N. H. Younan, and D. W. Holcomb, "Estimation of the number of decomposition levels for a wavelet-based multiresolution multisensor image fusion," *IEEE Transactions on Geoscience and Remote Sensing*, vol. 44, no. 12, pp. 3674–3686, 2006.

[113] N. Al-Azzawi, H. A. M. Sakim, A. K. W. Abdullah, and H. Ibrahim, "Medical image fusion scheme using complexd contoulet transform based on PCA," in *Proceedings of 31th IEEE International Conference on Engineering in Medicine and Biology*, 2009, pp. 5813–5816.

[114] Z. Wang and Y. Ma, "Medical image fusion using m-PCNN," *Information Fusion*, vol. 9, no. 2, pp. 176–185, 2008.

[115] S. Li, J. T. Kwok, and Y.Wang, "Multifocus image fusion using artificial neural networks," *Pattern Recognition Letters*, vol. 23, no. 8, pp. 985–997, 2002.

[116] J. Teng, S. Wang, J. Zhang, and X. Wang, "Neuro-fuzzy logic based fusion algorithm of medical images," in *Proceedings of 3rd International Congress of Image and Signal Processing*, 2010, pp. 1552–1556.

[117] Y. Na, H. Lu, and Y. Zhang, "Content analysis based medical images fusion with fuzzy inference," in *Proceedings of 5th International Conference on Fuzzy Systems and Knowledge Discovery*, vol. 3, 2008, pp. 37–41.

[118] A. Das and M. Bhattacharya, "Evolutionary algorithm based automated medical image fusion technique: Comparative study with fuzzy fusion ap-

proach," in *Proceedings of World Congress Nature & Biologically Inspired Computing*, vol. 3, 2009, pp. 269–274.

[119] A. Mumtaz, A. Majid, and A. Mumtaz, "Genetic algorithms and its application to image fusion," in *Proceedings of 5th International Conference on Emerging Technologies*, 2008, pp. 6–10.

[120] J. Teng, S. Wang, J. Zhang, and X. Wang, "Fusion algorithm of medical images based on fuzzy logic," in *Proceedings of 7th International Conference on Fuzzy Systems and Knowledge Discovery*, 2010, pp. 546–550.

[121] Y. Liu, J. Yang, and J. Sun, "PET/CT medical image fusion algorithm based on multiwavelet transform," in *Proceedings of International Conference on Advanced Computer Control*, vol. 2, 2010, pp. 264–268.

[122] W. X. Jun and M. Ying, "A medical image fusion algorithm based on lifting wavelet transform," in *Proceedings of International Conference on Artificial Intelligence and Computational Intelligence*, 2010, pp. 474–476.

[123] Y. Yang, D. S. Park, S. Huang, and N. Rao, "Medical image fusion via an effective wavelet-based approach," *EURASIP Journal on Advances in Signal Processing*, vol. 2010, pp. 44:1–44:13, 2010.

[124] H. Tian, Y. N. Fu, and P. G. Wang, "Image fusion algorithm based on regional variance and multi-wavelet bases," in *Proceedings of 2nd International Conference on Future Computer and Communication*, vol. 2, 2010, pp. 792–795.

[125] Z. Bin, Z. Y. Guo, F. Wei, and C. L. Min, "A new image fusion algorithm based on second generation wavelet transform," in *Proceedings of 2nd Inter-*

national Conference on Computational Intelligence and Natural Computing, 2010, pp. 390–393.

[126] J. Xu, L. Yang, and D. Wu, "Ripplet: A new transform for image processing," *Journal of Visual Communication and Image Representation*, vol. 21, no. 7, pp. 627–639, 2010.

[127] L. Yang, B. L. Guo, and W. Ni, "Multimodality medical image fusion based on multiscale geometric analysis of contourlet transform," *Neurocomputing*, vol. 72, no. 1-3, pp. 203–211, 2008.

[128] F. E. Ali, I. M. El-Dokany, A. A. Saad, and F. E. A. El-Samie, "Curvelet fusion of MR and CT images," *Progress in Electromagnetics Research C*, vol. 3, pp. 215–224, 2008.

[129] T. Li and Y. Wang, "Multiscaled combination of MR and SPECT images in neuroimaging: A simplex method based variable-weight fusion," *Computer Methods and Programs in Biomedicine*, vol. 105, pp. 31–39, 2012.

[130] T. C. Wong, "Medical image databases," *LLC: Springer-Verlag, New York*, 1998.

[131] H. Muller, N. Michoux, D. Bandon, and A. Geissbuhler, "A review of content-based image retrieval systems in medical applications – clinical benefits and future directions," *International Journal of Medical Informatics*, vol. 73, no. 1, pp. 1–23, 2004.

[132] C. Moritz, V. Haughton, D. Cordes, M. Quigley, and M. Meyerand, "Whole-brain functional MR imaging activation from finger tapping task examined with independent component analysis," *American Journal of Neuroradiology*, vol. 21, pp. 1629–1635, 2000.

[133] R. Begg, M. Palaniswami, and B. Owen, "Support vector machines for automated gait classification," *IEEE Transactions on Biomedical Engineering*, vol. 52, no. 5, pp. 828–838, 2005.

[134] D. Zhang, M. M. Islam, and G. Lu, "A review on automatic image annotation techniques," *Pattern Recognition*, vol. 45, pp. 346–362, 2012.

[135] D. J. Hemanth, C. K. S. Vijil, A. I. Selvakumar, and J.Anitha, "Performance improved iteration-free artificial neural networks for abnormal magnetic resonance brain image classification," *Neurocomputing*, vol. 130, pp. 98–107, 2014.

[136] K. H. Hwang, H. Lee, and D. Choi, "Medical image retrieval: Past and present," *Healthcare Informatics Research*, vol. 1, no. 18, pp. 3–9, 2012.

[137] T. M. Lehmann, M. O. Guld, T. Deselaers, D. Keysers, H. Schubert, K. Spitzer, H. Ney, and B. B. Wein, "Automatic categorization of medical images for content-based retrieval and data mining," *Computerized Medical Imaging and Graphics*, vol. 29, pp. 143–155, 2005.

[138] M. N. Wernick, Y. Yang, J. G. Brankov, G. Yourganov, and S. C. Strother, "Machine learning in medical imaging," *IEEE Signal Processing Magazine*, vol. 27, pp. 25–38, 2010.

[139] J. M. Medina, S. J.-Castillo, C. D. Barranco, and J. R. Campana, "On the use of a fuzzy object-relational database for flexible retrieval of medical images," *IEEE Transactions on Fuzzy Systems*, vol. 20, no. 4, pp. 786–803, 2012.

[140] H. D. Tagare, C. C. Jaffe, and J. Duncan, "Medical image databases: a content-based retrieval approach," *Journal of the American Medical Informatics Association*, vol. 4, no. 3, pp. 184–198, 1997.

[141] L. Yang, R. Jin, L. Mummert, R. Sukthankar, A. Goode, B. Zheng, S. C. H. Hoi, and M. Satyanarayanan, "A boosting framework for visuality-preserving distance metric learning and its application to medical image retrieva," *IEEE Transactions on Pattern Analysis and Machine Intelligence*, vol. 32, no. 1, pp. 30–44, 2010.

[142] C. Lacoste, J.-H. Lim, J.-P. Chevallet, and D. T. H. Le, "Medical-image retrieval based on knowledge-assisted text and image indexing," *IEEE Transactions on Circuits and Systems for Video Technology*, vol. 17, no. 7, pp. 889–900, 2007.

[143] I. F. A. Amaral, "Content-based image retrieval for medical applications," *Ph.D. Thesis, Faculdade De Ciencias,Univeridade Do Porto*, 2010.

[144] G. Quellec, M. Lamard, G. Cazuguel, B. Cochener, and C. Roux, "Wavelet optimization for content-based image retrieval in medical databases," *Medical Image Analysis*, vol. 14, pp. 227–241, 2010.

[145] J. A. V. Ramirez, "Medical image retrieval using multimodal semantic indexing," *Ph.D. Thesis, Engineering School, Universidad Nacional De Colombia*, 2013.

[146] S. Bhadoria and C. G. Dethe, "Study of medical image retrieval system," in *Proceedings of International Conference on Data Storage and Data Engineering*, 2010, pp. 192–196.

[147] Y. Liu, D. Zhanga, G. Lua, and W. Y. Ma, "A survey of content-based image retrieval with high-level semantics," *Pattern Recognition*, vol. 40, pp. 262–282, 2007.

[148] T. Deselaers, T. Weyand, D. Keysers, W. Macherey, and H. Ney, "FIRE in imageCLEF 2005: combining content-based image retrieval with textual information retrieval," in *Proceedings of the 6th International Conference on Cross-Language Evalution Forum: accessing Multilingual Information Repositories*, 2005, pp. 652–661.

[149] X. S. Zhou, S. Zillner, M. Moeller, M. Sintek, Y. Zhan, A. Krishnan, and A. Gupta, "Semantics and CBIR: A medical imaging perspective," in *Proceedings of International Conference Image and Video Retrieval*, 2008, pp. 571–580.

[150] D. L. Rubin, P. Mongkolwat, V. Kleper, K. Supekar, and D. S. Channin, "Medical imaging on the semantic web: annotation and image markup," in *Proceedings of Semantic Scientific Knowledge Integration*, 2008, pp. 93–98.

[151] Y. Zhuang, N. Jiang, Z. Wu, Q. Li, D. K. W. Chiu, and H. Hu, "Efficient and robust large medical image retrieval in mobile cloud computing environment," *Information Sciences*, vol. 263, no. 1, pp. 60–86, 2014.

[152] M. O. Guld, C. Thies, B. Fischer, and T. M. Lehmann, "A generic concept for the implementation of medical image retrieval systems," *International Journal of Medical Informatics*, vol. 76, pp. 252–259, 2007.

[153] T. M. Lehmann, M. O. Guld, C. Thies, B. Fischer, K. Spitzer, D. Keysers, H. Ney, M. Kohnen, H. Schubert, and B. B. Wein, "Content-based image retrieval in medical applications," *Methods of Information in Medicine*, vol. 43, pp. 354–361, 2004.

[154] H. Greenspan and A. T. Pinhas, "Medical image categorization and retrieval for PACS using the GMM-KL framework," *IEEE Transactions on Information Technology in Biomedicine*, vol. 11, no. 2, pp. 190–202, 2007.

[155] M. O. Guld, M. Kohnen, D. Keysers, H. Schubert, B. B. Wein, J. Bredno, and T. Lehmann, "Quality of DICOM header information for image categorization," in *Proceedings of SPIE: Medical Imaging*, 2002, pp. 280–287.

[156] P. Welter, B. Fischer, R. W. Gunther, and T. M. Deserno, "Generic integration of content-based image retrieval in computer-aided diagnosis," *Comput Methods and Programs in Biomedicine*, vol. 108, no. 2, pp. 589–599, 2012.

[157] A. W. M. Smeulders, M. Worring, S. Santini, A. Gupta, and R. Jain, "Content-based image retrieval at the end of the early years," *IEEE Transactions on Pattern Analysis and Machine Intelligence*, vol. 22, no. 12, pp. 1349–1380, 2000.

[158] M. Acharyya and M. K. Kundu, "M-band wavelets: Application to texture segmentation for real life image analysis," *International Journal of wavelets, Multiresolution and Information Processing*, vol. 1, no. 1, pp. 115–149, 2003.

[159] J. P. Eakins, "Towards intelligent image retrieval," *Pattern Recongintion*, vol. 35, pp. 3–14, 2002.

[160] K. Mikolajczyk and C. Schmid, "A performance evaluation of local descriptors," *IEEE Transactions on Pattern Analysis and Machine Intelligence*, vol. 27, no. 10, pp. 1615–1630, 2005.

[161] I. F. Amaral, F. Coelho, J. F. P. da Costa, and J. S. Cardoso, "Hierarchical medical image annotation using SVM-based approaches," in *Proceedings of*

2nd International Conference on Information Technology and Applications in Biomedicine, 2010, pp. 1–5.

[162] A. Kumar, J. Kim, L. Wena, M. Fulham, and D. Feng, "A graph-based approach for the retrieval of multi-modality medical images," *Medical Image Analysis*, vol. 18, pp. 330–342, 2014.

[163] M. Acharyya and M. K. Kundu, "Extraction of noise tolerant, gray-scale transform and rotation invariant features for texture segmentation using wavelet frames," *International Journal of wavelets, Multiresolution and Information Processing*, vol. 6, no. 3, pp. 391–417, 2008.

[164] S. C. Orphanoudakis, C. Chronaki, and S. Kostomanolakis, "I^2C: a system for the indexing storage and retrieval of medical images by content," *Medical Informatics*, vol. 19, no. 2, pp. 109–122, 1994.

[165] P. M. Kelly and M. Cannon, "Query by image example: the comparison algorithm for navigating digital image databases (CANDID) approach," in *Proceedings of 6th International Conference on Storage and Retrieval for Image and Video Databases*, 1995, pp. 238–248.

[166] A. Marchiori, C. Brodley, L. Broderick, and A. M. Aisen, "CBIR for medical images – an evaluation trial," in *IEEE Workshop on Content-Based Access of Image and Video Libraries*, 2001, pp. 89–93.

[167] O. Commowick and G. Malandain, "Efficient selection of the most similar image in a database for critical structures segmentation," in *Proceedings of the 10th International Conference on Medical Image Computing and Computer-Assisted Intervention*, vol. 4792, 2007, pp. 203–210.

[168] P. Ghosh, S. Antani, L. R. Long, and G. R. Thoma, "Review of medical image retrieval systems and future directions," in *Proceedings of 24th International Symposium on Computer-Based Medical Systems*, 2011, pp. 1–6.

[169] Y. Liu, F. Dellaert, and W. E. Rothfus, "Classification driven semantic based medical image indexing and retrieval," in *Technical Report CMU-RI-TR-98-25, The Robotics Institute, Carnegie Mellon University, Pittsgurgh, PA*, 1998.

[170] D. Keysers, J. Dahmen, H. Ney, B. B. Wein, and T. M. Lehmann, "Statistical framework for model-based image retrieval in medical applications," *Journal of Electronic Imaging*, vol. 12, no. 1, pp. 59–68, 2003.

[171] S. Hong, C. W.-Cheng, and T. Li, "Medical image description in content-based image retrieval," in *Proceedings of 27th IEEE International Conference on Engineering in Medicine and Biology*, 2005, pp. 6336–6339.

[172] H. C. Akakin and N. N. Gurcan, "Content-based microscopic image retrieval system for multi-image queries," *IEEE Transactions on Information Technology in Biomedicine*, vol. 16, no. 4, pp. 758–769, 2012.

[173] C. R. Shyu, C. E. Brodley, A. C. Kak, A. Kosaka, A. M. Aisen, and L. S. Broderick, "ASSERT,: A physician-in-the-loop content-based retrieval system for HRCT image databases," *Computer Vision and Image Understanding*, vol. 75, no. 1–2, pp. 111–132, 1999.

[174] Y. E. A. El-Kwae, H. Xu, and M. R. Kabuka, "Content-based retrieval in picture archiving and communication systems," *IEEE Transactions on Knowledge Data Engineering*, vol. 13, no. 2, pp. 70–81, 2000.

[175] H. Muller, A. Rosset, J. P. Vallee, and A. Geissbuhler, "Integrating content-based visual access methods into a medical case database," in *Proceedings of Medical informatics Europe*, 2003, pp. 480–485.

[176] H. Shen, D. Ma, Y. Zhao, H. Sun, S. Sun, R. Ye, L. Huang, B. Lang, and Y. Sun, "MIAPS: A web-based system for remotely accessing and presenting medical images," *Computers Methods and Programs in Biomedicine*, vol. 113, pp. 266–283, 2014.

[177] W. Hsu, S. Antani, L. R. Long, L. Neve, and G. R. Thoma, "SPIRS,: a web-based image retrieval system for large biomedical databases," *International Journal of Medical Informatics*, vol. 78, no. 1, pp. S13–S24, 2009.

[178] J. Dahmen, T. Theiner, D. Keysers, H. Ney, T. M. Lehmann, and B. B. Wein, "Classification of radiographs in the image retrieval in medical application system IRMA," in *Proceedings of 6th International RIAO Conference on Content Based Multimedia Information Accesss*, 2000, pp. 551–566.

[179] T. M. Lehmann, H. Schubert, D. Keysers, M. Kohnen, and B. B. Wein, "The IRMA code for unique classification of medical images," in *Proceedings of SPIE: Medical Imaging*, 2003, pp. 440–451.

[180] M. O. Guld, C. Thies, B. Fischer, and T. M. Deserno, "A framework and baseline results for the CLEF medical automatic annotation task," *Pattern Recognition Letters*, vol. 29, pp. 2025–2031, 2008.

[181] A. Quddus and O. Basir, "Semantic image retrieval in magnetic resonance brain volumes," *IEEE Transactions on Information Technology in Biomedicine*, vol. 16, no. 3, pp. 348–355, 2012.

[182] D. Unay, A. Ekin, and R. S. Jasinschi, "Local structure-based region-of-interest retrieval in brain MR images," *IEEE Transactions on Information Technology in Biomedicine*, vol. 14, no. 4, pp. 897–903, 2010.

[183] Q. Li, F. Li, J. Shiraishi, S. Katsuragawa, S. Sone, and K. Doi, "Investigation of new psychophysical measures for evaluation of similar images on thoracic computed tomography for distinction between benign and malignant nodules," *Medical Physics*, vol. 30, no. 10, pp. 2584–2593, 2003.

[184] J. E. E. de Oliveira, A. M. C. Machado, G. C. Chavez, A. P. B. Lopes, T. M. Deserno, and A. de A. Araujo, "Mammosys: a content-based image retrieval system using breast density patterns," *Computer Methods and Programs Biomedicine*, vol. 3, no. 99, pp. 289–297, 2010.

[185] A. M. Aisen, L. S. Broderick, H. W.-Muram, C. E. Brodleya, A. C. Kak, C. Pavlopoulou, J. Dy, C. R. Shyu, and A. Marchiori, "Automated storage and retrieval of thin-section CT images to assist diagnosis: system description and preliminary assessment," *Radiology*, vol. 228, no. 1, pp. 265–270, 2003.

[186] B. Fischer, P. Welter, R. W. Gunther, and T. M. Deserno, "Web-based bone age assessment by content-based image retrieval for case-based reasoning," *International Journal of Computer Assisted Radiology and Surgery*, vol. 7, no. 3, pp. 389–399, 2012.

[187] T. Deselaers, "Features for image retrieval," *Ph.D. Thesis, Aachen, Germany: Rheinisch-Westfalische Technische Hochschule Aachen*, 2003.

[188] L. H. Y. Tang, R. Hanka, and H. H. S. Ip, "A review of intelligent content-based indexing and browsing of medical images," *Health Informatics Journal*, vol. 5, pp. 40–49, 1999.

[189] P. Aggarwal, H. K. Sardana, and G. Jindal, "Content based medical image retrieval: Theory, gaps and future directions," *International Journal of Graphics, Vision and Image Processing*, vol. 9, no. 3, pp. 25–38, 2009.

[190] C. B. Akgul, D. L. Rubin, S. Napel, C. F. Beaulieu, H. Greenspan, and B. Acar, "Content-based image retrieval in radiology: Current status and future directions," *Journal of Digital Imaging*, vol. 2, no. 24, pp. 208–222, 2011.

[191] A. P. Bhagat and M. Atique, "Medical image retrieval, indexing and enhancement techniques: A survey," in *Proceedings of International Conference on Communication, Computing & Security*, 2011, pp. 387–390.

[192] P. H. Bugatti, D. S. Kaster, M. P. Silva, C. T. Jr., P. M. A.-Marques, and A. J. M. Traina, "PRoSPer: Perceptual similarity queries in medical CBIR systems through user profiles," *Computers in Biology and Medicine*, vol. 45, pp. 8–19, 2014.

[193] C. Kurtz, C. F. Beaulieu, S. Napel, and D. L. Rubin, "A hierarchical knowledge-based approach for retrieving similar medical images described with semantic annotations," *Journal of Biomedical Informatics*, vol. 49, pp. 227–244, 2014.

[194] M. Wu, Q. Chen, and Q. Sun, "Medical image retrieval with relevance feedback via pairwise constraint propagation," *KSII Transactions on Internet and Information Systems*, vol. 8, no. 1, pp. 249–268, 2014.

[195] S. F. da Silva, M. X. Ribeiro, J. do E. S. B. Neto, C. T.-Jr., and A. J. M. Traina, "Improving the ranking quality of medical image retrieval using a genetic feature selection method," *Decision Support Systems*, vol. 51, pp. 810–820, 2011.

[196] P. V. Prasad, "Magnetic resonance imaging: Methods and biologic applications (methods in molecular medicine)," *Humana Press*, 2005.

[197] P. Maji, M. K. Kundu, and B. Chanda, "Second order fuzzy measure and weighted co-occurrence matrix for segmentation of brain MR images," *Fundamenta Informaticae*, vol. 88, no. 1-2, pp. 161–176, 2008.

[198] S. A. Rombouts, F. Barkhof, and P. Scheltens, "Clinical applications of functional brain MRI," *Oxford University Press*, 2007.

[199] P. Maji, B. Chanda, M. K. Kundu, and S. Dasgupta, "Deformation correction in brian MRI using mutual information and genetic algorithm," in *Proceedings of International Conference on Computing: Theory and Applications*, 2007, pp. 372–376.

[200] Y. Zhang, L. Wu, and S. Wang, "Magnetic resonance brain image classification by an improved artificial bee colony algorithm," *Progress In Electromagnetics Research*, vol. 116, pp. 65–79, 2011.

[201] S. Chaplot, L. M. Patnaik, and N. R. Jagannathan, "Classification magnetic resonance brain images using wavelets as input to support vector machine and neural network," *Biomedical Signal Processing and Control*, vol. 1, no. 1, pp. 86–92, 2006.

[202] Y. Zhang, Z. Dong, L. Wu, and S. Wang, "A hybrid method for MRI brain image classification," *Expert Systems with Applications*, vol. 38, no. 8, pp. 10 049–10 053, 2011.

[203] Y. Zhang and L. Wu, "An MR brain images classifier via principal component analysis and kernel support vector machine," *Progress In Electromagnetics Research*, vol. 130, pp. 369–388, 2012.

[204] M. Maitra and A. Chatterjee, "A slantlet transform based intelligent system for magnetic resonance brain image classification," *Biomedical Signal Processing and Control*, vol. 1, pp. 299–306, 2006.

[205] M. Maitra, A. Chatterjee, and F. Matsuno, "A novel scheme for feature extraction and classification of magnetic resonance brain images based on slantlet transform and support vector machine," in *Proceedings of International Conference on Instrumentation, Control and Information Technology*, 2008, pp. 1130–1134.

[206] M. Maitra and A. Chatterjee, "Hybrid multiresolution slantlet transform and fuzzy c-means clustering approach for normal-pathological brain MR image segregation," *Medical Engineering and Physics*, vol. 30, pp. 615–623, 2008.

[207] D. Selvathi, R. S. R. Prakash, and S. T. Selvi, "Performance evaluation of kernel based techniques for brain MRI data classification," in *Proceedings of International Conference on Computational Intelligence and Multimedia Applications*, 2007, pp. 456–460.

[208] E.-S. A. El-Dahshan, T. Hosny, and A.-B. M. Salem, "Hybrid intelligent techniques for MRI brain images classification," *Digital Signal Processing*, vol. 20, no. 2, pp. 433–441, 2010.

[209] Y. Zhang, S. Wang, and L. Wu, "A novel method for magnetic resonance brain image classification based on adaptive chaotic PSO," *Progress In Electromagnetics Research*, vol. 100, pp. 325–343, 2010.

[210] A. Kharrat, K. Gasmi, M. B. Messaoud, N. Benamrane, and M. Abid, "Automated classification of magnetic resonance brain images using wavelet genetic algorithm and support vector machine," in *Proceedings of 9th International Conference on Congnitive Informatics*, 2010, pp. 369–374.

[211] Y. Zhang, S. Wang, Y. Huo, L. Wu, and A. Liu, "Feature extraction of brain MRI by stationary wavelet transform and its applications," *Journal of Biological Systems*, vol. 18, pp. 115–132, 2010.

[212] N. H. Rajini and R. Bhavani, "Classification of MRI brain images using k-nearest neighbor and artificial neural network," in *Proceedings of International Conference on Recent Trends in Information Technology*, 2011, pp. 863–868.

[213] N. Abdullah, L. W. Chuen, U. K. Ngah, and K. A. Ahmad, "Improvement of MRI brain classification using principal component analysis," in *Proceedings of International Conference on Control System, Computing and Engineering*, 2011, pp. 557–561.

[214] H. Mohsen, E. S. A. E. Dahshan, and A. B. M. Salem, "A machine learning technique for MRI brain images," in *Proceedings of 8th International Conference on Informatics and Systems*, 2012, pp. 161–165.

[215] B. Singh and J. Singh, "Classification of brain MRI in wavelet domain," *International Journal of Electronics and Computer Science Engineering*, vol. 1, no. 3, pp. 879–885, 2012.

[216] V. A. Kovalev and F. Kruggel, "Retrieving 3D MRI brain images," in *Proceedings of International Conference on Medical Image Computing and Computer Assisted Intervention Society*, 2001, pp. 53–56.

[217] J. Moustakas, K. Marias, S. Dimitriadis, and S. C. Orphanoudakis, "A two-level CBIR platform with application to brain MRI retrieval," in *Proceedings of IEEE International Conference on Multimedical and Expo.*, 2005, pp. 1278–1281.

[218] R. F. Tungaraza, J. Guan, S. Rolfe, I. Atmosukarto, A. Poliakov, N. M. Kleinhans, E. Aylward, J. Ojemann, J. F. Brinkley, and L. G. Shapiro, "A similarity retrieval method for functional magnetic resonance imaging (fMRI) statistical maps," in *Proceedings of SPIE Medical Imaging 2009: Image Processing*, vol. 7259, 2009, pp. 1–12.

[219] K. Yuan, S. Feng, W. Chen, S. Jia, and P. Xiao, "Diagnosis system of computer-aided brain MRI using content-based image retrieval," in *Proceedings of SPIE 5th International Conference on Information Technology and Applications in Biomedicine*, 2008, pp. 152–156.

[220] D. Unay, A. Ekin, and R. S. Jasinschi, "Local structure-based region-of-interest retrieval in brain MR images," *IEEE Transactions on Information Technology in Biomedicine*, vol. 14, no. 4, pp. 897–903, 2010.

[221] P. V. Ingole and K. D. Kulat, "A morphological segmentation based features for brain MRI retrieval," in *Proceedings of 4th IEEE International Conferenec on Emerging Trends in Engineering and Technology*, 2011, pp. 210–214.

[222] Y. Qian, X. Gao, M. Loomes, R. Comley, B. Barn, R. Hui, and Z. Tian, "Content-based retrieval of 3D medical images," in *Proceedings of 3rd International Conference on eHealth, Telemedicine, and Social Medicine*, 2011, pp. 7–12.

[223] P. V. Ingole and K. D. Kulat, "A chain code based fuzzy features for brain MRI retrieval," in *Proceedings of 5th IEEE International Conference on Emerging Trends in Engineering and Technology*, 2012, pp. 185–190.

[224] Y. F. Fathabad and M. A. Balafar, "Application of content based image retrieval in diagnosis brain disease," *International Journal on Technical and Physical Problems of Engineering*, vol. 13, no. 4, pp. 133–138, 2012.

[225] M. Saritha, K. P. Joseph, and A. T. Mathew, "Classification of MRI brain images using combined wavelet entropy based spider web plots and probabilistic neural network," *Pattern Recognition Letters*, vol. 34, pp. 2151–2156, 2013.

[226] M. M. Rahman, P. Bhattacharya, and B. C. Desai, "A framework for medical image retrieval using machine learning and statistical similarity matching techniques with relevance feedback," *IEEE Transactions on Information Technology in Biomedicine*, vol. 11, no. 1, pp. 58–69, 2007.

[227] H. Wu, H. Zhang, and C. Li, "Medical image classification with multiple kernel learning," in *Proceedings of 2nd IEEE International Conference on Internet Multimedia Computing and Service*, 2010, pp. 189–192.

[228] T. Deselaers and T. Desemo, "Medical image annotation in imageCLEF 2008," in *Proceedings of CLEF Workshop 2008/ Evaluating Systems for Multilingual and Multimodal Information Access, Aarhus, Denmark*, 2009.

[229] T. Tommasi, B. Caputo, P. Welter, M. O. Guld, and T. M. Desemo, "Overview of the CLEF 2009 medical image annotation track," in *Proceedings 9th CLEF workshop 2009, ser. LNCS, Corfu, Greece*, 2009, pp. 85–93.

[230] H. Shen, D. Tao, and D. Ma, "Multiview locally linear embedding for effective medical image retrieval," *PLOS one*, vol. 8, no. 12, pp. 1–21, 2013.

[231] H. Shen, D. Tao, and D. Ma, "Dual-force ISOMAP: A new relevance feedback method for medical image retrieval," *PLOS one*, vol. 8, no. 12, pp. 1–21, 2013.

[232] U. Avni, H. Greenspan, E. Konen, M. Sharon, and J. Goldberger, "X-ray categorization and retrieval on the organ and pathology level, using patch-based visual words," *IEEE Transactions on Medical Imaging*, vol. 30, no. 3, pp. 733–746, 2011.

[233] I. Dimitrovski, D. Kocev, S. Loskovska, and S. Dzeroski, "Hierarchical annotation of medical images," *Pattern Recognition*, vol. 44, pp. 2436–2449, 2011.

[234] J. Wang, Y. Li, Y. Zhang, C. Wang, H. Xie, G. Chen, and X. Guo, "Bag-of-features based medical image retrieval via multiple assignment and visual words weighting," *IEEE Transactions on Medical Imaging*, vol. 30, no. 11, pp. 1996–2011, 2011.

[235] P. Clough, H. Muller, T. Deselaers, M. Grubinger, T. M. Lehmann, J. Jensen, and W. Hersh, "The CLEF 2005 cross-language image retrieval track," in *Proceedings of Working notes of the 2005 CLEF workshop, Vienna, AUstria*, 2005.

[236] H. Muller, T. Deselaers, T. M. Lehmann, P. Clough, E. Kim, and W. Hersh, "Overview of the imageCLEFmed 2006 medical retrieval and medical annotation tasks," in *Proceedings of in CLEF 2006 Proceedings, ser. (LNCS), Spriger*, vol. 4730, 2007, pp. 595–608.

[237] T. Deselaers, T. M. Deserno, and H. Muller, "Automatic medical image annotation in lmageCLEF 2007: Overview, results, and discussion," *Pattern Recognition Letters*, vol. 29, no. 15, pp. 1988–1995, 2008.

[238] H. Pourghassem and H. Ghassemian, "Content-based medical image classification using a new hierarchical merging scheme," *Computerized Medical Imaging and Graphics*, vol. 32, pp. 651–661, 2008.

[239] T. Deselaers and H. Ney, "Deformations, patches, and discriminative models for automatic annotation of medical radiographs," *Pattern Recognition Letters*, vol. 29, pp. 2003–2010, 2008.

[240] T. Tommasi, F. Orabona, and B. Caputo, "Discriminative cue integration for medical image annotation," *Pattern Recognition Letters*, vol. 29, no. 15, pp. 1996–2002, 2008.

[241] L. Setia, A. Teynor, A. Halawani, and H. Burkhardt, "Grayscale medical image annotation using local relational features," *Pattern Recognition Letters*, vol. 29, pp. 2039–2045, 2008.

[242] M. M. Rahman, B. C. Desai, and P. Bhattacharya, "Medical image retrieval with probabilistic multi-class support vector machine classifiers and adaptive similarity fusion," *Computerized Medical Imaging and Graphics*, vol. 32, pp. 95–108, 2008.

[243] D. K. Iakovidis, N. Pelekis, E. E. Kotsifakos, I. Kopanakis, H. Karanikas, and Y. Theodoris, "A pattern similarity scheme for medical image retrieval," *IEEE Transactions on Information Technology in Biomedicine*, vol. 13, no. 4, pp. 442–450, 2009.

[244] M. M. Rahman, S. K. Antani, and G. R. Thoma, "A learning-based similarity fusion and filtering approach for biomedical image retrieval using SVM classification and relevance feedback," *IEEE Transactions on Information Technology in Biomedicine*, vol. 15, no. 4, pp. 640–646, 2011.

[245] E. L. Seigel and R. M. Kolodner, *Flimless Radiology.* USA: Springer, 1999.

[246] D. Anand and U. C. Niranjan, "Watermarking medical images with patient information," in *Proceedings of 20th IEEE International Conference on Engineering in Medicine & Biology*, vol. 20, no. 2, 1998, pp. 703–706.

[247] U. R. Acharya, D. Ananad, P. S. Bhat, and U. C. Niranjan, "Compact storage of medical images with patient information," *IEEE Transactions on Information Technology in Biomedicine*, vol. 5, no. 4, pp. 320–323, 2001.

[248] X. Kong and R. Feng, "Watermarking medical signals for telemedicine," *IEEE Transactions on Information Technology in Biomedicine*, vol. 5, no. 3, pp. 195–201, 2001.

[249] M.-S. Nambakhsh, A. Ahmadian, and H. Zaidi, "A contextual based double watermarking of PET images by patient ID and ECG signal," *Computer Methods and Programs in Biomedicine*, vol. 104, no. 3, pp. 418–425, 2011.

[250] H. Munch, U. Engelmann, A. Schroeter, and H. Meinzer, "Web-based distribution of radiological images from PACS to EHR," *International Congress Series*, vol. 1256, pp. 873–879, 2003.

[251] M. L. Richardson, M. S. Frank, and E. J. Stern, "Digital image manipulation: what constitutes acceptable alteration of a radiologic image?„" *American Journal of Roentgenology*, vol. 164, no. 1, pp. 228–229, 1995.

[252] G. Coatrieux, H. Maitre, B. Sankur, Y. Rolland, and R. Collorec, "Relevance of watermarking in medical imaging," in *Proceedings of IEEE International Conference on Engineering in Medicine & Biology*, 2000, pp. 250–255.

[253] G. Coatrieux, H. Maitre, and B. Sankur, "Strict integrity control of biomedical images," in *Proceedings of SPIE Security Watermarking Multimedia Contents III*, 2001, pp. 229–240.

[254] Y. Cho, B. Ahn, J.-S. Kim, I.-Y. Kim, and S. I. Kim, "A study for watermark methods appropriate to medical images," *Journal of Digital Imaging*, vol. 14, no. 2, pp. 184–185, 2001.

[255] G. Coatrieux, L. Lecornu, B. Sankur, and C. Roux, "A review of image watermarking applications in healthcare," in *Proceedings of 28th IEEE International Conference on Engineering in Medicine and Biology*, 2006, pp. 4691–4694.

[256] S. Kaihara, "Realisation of the computerised patient record relevance and unsolved problems," *International Journal of Medical Informatics*, vol. 49, no. 1, pp. 1–8, 1998.

[257] K. Navas and M. Sasikumar, "Survey of medical image watermarking algorithms," in *Proceedings of 4th International Conference on Sciences Electronic Technologies Information and Telecommunications*, 2007, pp. 1–6.

[258] H. Nyeem, W. Boles, and C. Boyd, "A review of medical image watermarking requirements for teleradiology," *Journal of Digital Imaging*, vol. 26, no. 2, pp. 326–343, 2013.

[259] F. A. P. Petitcolas, R. J. Anderson, and M. G. Kuhn, "Information hiding–a survey," *IEEE Proceedings*, vol. 87, no. 7, pp. 1062–1078, 1999.

[260] N. Nikolaidis and I. Pitas, "Digital image watermarking: an overview," in *Proceedings of IEEE International Conference on Multimedia Computing and Systems*, vol. 1, 1999, pp. 1–6.

[261] I. J. Cox, M. L. Miller, and J. A. Bloom, "Digital watermarking," *Morgan Kaufmann Publishers*, 2001.

[262] M. Barni and F. Bartolini, "Watermarking systems engineering: Enabling digital assets security and other applications," *CRC Press*, 2004.

[263] I. J. Cox, M. L. Miller, J. A. Bloom, J. Fridrich, and T. Kalker, *Digital Watermarking and Steganography*, 2nd ed. USA: Morgan Kaufmann Publishers, 2007.

[264] I. J. Cox and M. L. Miller, "The first 50 years of electronic watermarking," in *Proceedings of IEEE Special Issue on Protection of Multimedia Content*, vol. 87, 1999, pp. 1062–1078.

[265] S. P. Maity and M. K. Kundu, "Genetic algoirthms for optimality of data hiding in digital images," *Soft Computing*, vol. 13, pp. 361–373, 2009.

[266] S. P. Maity and M. K. Kundu, "DHT domain digital watermarking with low loss in image information," *International Journal of Electronics and Communications*, vol. 64, no. 3, pp. 243–257, 2010.

[267] A. Giakoumaki, K. Perakis, A. Tagaris, and D. Koutsouris, "Digital watermarking in telemedicine applications–towards enhanced data security and accessibility," in *Proceedings of 28th IEEE International Conference on Engineering in Medicine & Biology*, 2006, pp. 6328–6331.

[268] K. Chen and T. Ramabadran, "Near-lossless compression of medical images through entropy coded DPCM," *IEEE Transactions on Medical Imaging*, vol. 13, no. 3, pp. 538–548, 1994.

[269] J. M. Zain and M. Clarke, "Reversible region of non-interest (RONI) watermarking for authentication of DICOM, images," *International Journal of Computer Science and Network Security*, vol. 7, no. 9, pp. 19–28, 2007.

[270] X. Guo and T.-G. Zhuang, "Lossless watermarking for verifying the integrity of medical images with tamper localization," *Journal of Digital Imaging*, vol. 22, no. 6, pp. 620–628, 2009.

[271] C.-S. Woo, J. Du, and B. Pham, "Multiple watermark method for privacy control and tamper detection in medical images," in *Proceedings of APRS workshop on Digital Image Computing Pattern Recognition and Imaging for Medical Applications*, 2005, pp. 43–48.

[272] X. Guo and T. Zhuang, "A region-based lossless watermarking scheme for enhancing security of medical data," *Journal of Digital Imaging*, vol. 22, no. 1, pp. 53–64, 2009.

[273] G. Coatrieux, H. Huang, H. Shu, L. Luo, and C. Roux, "A watermarking-based medical image integrity control system and an image moment signature for tampering characterization," *IEEE Journal of Biomedical and Health Informatics*, vol. 17, no. 6, pp. 1057–1067, 2013.

[274] M. K. Kundu and S. Das, "Lossless ROI medical image watermarking technique with enhanced security and high payload embedding," in *Proceedings of 20th International Conference on Pattern Recognition*, 2010, pp. 1457–1460.

[275] M. S. Emami and K. Omar, "A low-cost method for reliable ownership identification of medical images using SVM and lagnrange duality," *Expert Systems with Applications*, vol. 40, pp. 7579–7587, 2013.

[276] J. M. Zain, "Digital watermarking in medical images," *Ph.D. Thesis, Brunel University*, 2005.

[277] D. Osborne, "Embedded watermarking for image verification in telemedicine," *Ph.D. Thesis, University of Adelaide*, 2005.

[278] N. A. Memon, "Watermarking of medical images for content authentication and copyright protection," *Ph.D. Thesis, GIK Institute of Engineering Sciences and Technology*, 2010.

[279] M. Li, R. Poovendran, and S. Narayanan, "Protecting patient privacy against unauthorized release of medical images in a group communication environment," *Computerized Medical Imaging and Graphics*, vol. 29, no. 5, pp. 367–383, 2005.

[280] F. Y. Shih and Y.-T. Wu, "Robust watermarking and compression for medical images based on genetic algorithms," *Information Sciences*, vol. 175, pp. 200–216, 2005.

[281] T. Manasrah and A. Al-Haj, "Management of medical images using wavelets-based multi-watermarking algorithm," in *Proceedings of IEEE International Conference on Innovations in Information Technology*, 2008, pp. 697–701.

[282] F. Rahimi and H. Rabbani, "A dual adaptive watermarking scheme in contourlet domain for DICOM images," *BioMedical Engineering OnLine*, vol. 10, no. 53, pp. 1–18, 2011.

[283] S. A. K. Mostafa, N. E. El-sheimy, A. S. Tolba, F. M. Abdelkader, and H. M. Elhindy, "Wavelet packets-based blind watermarking for medical image management," *Open Biomedical Engineering Journal*, vol. 4, pp. 93–98, 2010.

[284] M. Arsalan, S. A. Malik, and A. Khan, "Intelligent reversible watermarking in integer wavelet domain for medical images," *The Journal of Systems and Software*, vol. 85, pp. 883–894, 2012.

[285] B. Lei, E.-L. Tan, S. Chen, D. Ni, T. Wang, and H. Lei, "Reversible watermarking scheme for medical image based on differential evolution," *Expert Systems with Applications*, vol. 41, pp. 3178–3188, 2014.

[286] P. Fakhari, E. Vahedi, and C. Lucas, "Protecting patient privacy from unauthorized release of medical images using a bio-inspired wavelet-based watermarking approach," *Digital Signal Processing*, vol. 21, pp. 433–446, 2011.

[287] A. Wakatani, "Digital watermarking for ROI medical images by using compressed signature image," in *Proceedings of 35th International Conference on System Sciences*, 2002, pp. 2043–2048.

[288] A. Giakoumaki, S. Pavlopoulos, and D. Koutsouris, "Multiple image watermarking applied to health information management," *IEEE Transactions on Information Technology in Biomedicine*, vol. 10, no. 4, pp. 722–732, 2006.

[289] J. Zain, L. Baldwin, and M. Clarke, "Reversible watermarking for authentication of DICOM images," in *Proceedings of 26th Annual IEEE International Conference on Engineering in Medicine & Biology*, 2004, pp. 3237–3240.

[290] F. Bao, R. H. Deng, B. C. Ooi, and Y. Yang, "Tailored reversible watermarking schemes for authentication of electronic clinical atlas," *IEEE Transactions on Information Technology in Biomedicine*, vol. 9, no. 4, pp. 554–563, 2005.

[291] X. Q. Zhou, H. K. Huang, and S. L. Lou, "Authenticity and integrity of digital mammography images," *IEEE Transactions on Medical Imaging*, vol. 20, no. 8, pp. 784–791, 2001.

[292] U. R. Acharya, P. S. Bhat, S. Kumar, and L. C. Min, "Transmission and storage of medical images with patient information," *Computers in Biology and Medicine*, vol. 33, pp. 303–310, 2003.

[293] H.-K. Lee, H.-J. Kim, K.-R. Kwon, and J.-K. Lee, "ROI medical image watermarking using DWT and bit-plane," in *Proceedings of Asia-Pacific Conference Communication*, 2005, pp. 512–515.

[294] J. M. Zain and A. M. Fauzi, "Medical image watermarking with tamper detection and recovery," in *Proceedings of 28th IEEE International Conference on Engineering in Medicine & Biology*, 2006, pp. 3270–3273.

[295] J. Wu, R. Chang, C. Chen, C. Wang, T. Kuo, W. Moon, and D. Chen, "Tamper detection and recovery for medical images using near-lossless information hiding technique," *Journal of Digital Imaging*, vol. 21, no. 1, pp. 59–76, 2008.

[296] A. Giakoumaki, S. Pavlopoulos, and D. Koutsouris, "A medical image watermarking scheme based on wavelet transform," in *Proceedings of 25th IEEE International Conference on Engineering in Medicine and Biology*, vol. 1, 2003, pp. 856–859.

[297] U. Acharya, U. Niranjan, S. Iyengar, N. Kannathal, and L. Min, "Simultaneous storage of patient information with medical images in the frequency domain," *Computer Methods and Programs in Biomedicine*, vol. 76, pp. 13–19, 2004.

[298] J. Nayak, P. S. Bhat, U. R. Acharya, and U. C. Niranjan, "Simultaneous storage of medical images in the spatial and frequency domain: A comparative study," *BioMedical Engineering Online*, vol. 3, pp. 13–19, 2004.

[299] A. Giakoumaki, S. Pavlopoulos, and D. Koutsouris, "Multiple digital watermarking applied to medical imaging," in *Proceedings of 27th Annual IEEE International Conference on Engineering in Medicine & Biology*, 2005, pp. 3444–3447.

[300] H. Chao, C. Hsu, and S. Miaou, "A data-hiding technique with authentication, integration, and confidentiality for electronic patient records," *IEEE Transactions on Information Technology in Biomedicine*, vol. 6, no. 1, pp. 46–53, 2002.

[301] M. Kamran and M. Farooq, "An information-preserving watermarking scheme for right protection of EMR systems," *IEEE Transactions on Knowledge and Data Engineering*, vol. 24, no. 11, pp. 1950–1962, 2012.

[302] D. Bouslimi, G. Coatrieux, M. Cozic, and C. Roux, "A joint encryption/watermarking system for verifying the reliability of medical images," *IEEE Transactions on Information Technology in Biomedicine*, vol. 16, no. 5, pp. 891–899, 2012.

[303] N. A. Memon and S. A. M. Gilani, "Watermarking of chest CT scan medical images for content authentication," *International Journal of Computer Mathematics*, vol. 88, no. 2, pp. 265–280, 2011.

[304] N. A. Memon, A. Chaudhry, M. Ahmad, and Z. A. Keerio, "Hybrid watermarking of medical images for ROI authentication and recovery," *International Journal of Computer Mathematics*, vol. 88, no. 10, pp. 2057–2071, 2011.

[305] G. Coatrieux, C. L. Guillou, J.-M. Cauvin, and C. Roux, "Reversible watermarking for knowledge digest embedding and reliability control in medical images," *IEEE Transactions on Information Technology in Biomedicine*, vol. 13, no. 2, pp. 158–165, 2009.

[306] A. K. Navas, M. Sasikumar, and S. Sreevidya, "A benchmark for medical image watermarking," in *Proceedings of 6th International Conference on EURASIP Speech and Image Processing, Multimedia Communications and Services*, 2007, pp. 237–240.

[307] R. Norcen, M. Podesser, A. Pommer, H.-P. Schmidt, and A. Uhl, "Confidential storage and transmission of medical image data," *Computers in Bioloty and Medicine*, vol. 33, pp. 277–292, 2003.

[308] D.-C. Lou, M.-C. Hu, and J.-L. Liu, "Multiple layer data hiding scheme for medical images," *Computer Standards & Interfaces*, vol. 31, pp. 329–335, 2009.

[309] N. V. Rao and V. M. Kumari, "Watermarking in medical imaging for security and authentication," *Information Security Journal: A Global Perspective*, vol. 20, pp. 148–155, 2011.

[310] M. N. Do, "Directional multiresolution image representations," PhD Dissertation, Ecole polytechnique fédérale de Lausanne, Europe, 2001.

[311] M. N. Do and Y. M. Lu, "Multidimensional filter banks and multiscale geometric representations," *Foundations and Trends in Signal Processing*, vol. 5, no. 3, pp. 157–264, 2011.

[312] D. H. Hubel and T. N. Wiesel, "Receptive fields, binocular interaction and functional architecture in the cat's visual cortex," *Journal of Physiology*, vol. 160, pp. 106–154, 1962.

[313] B. A. Olshausen and D. J. Field, "Emergence of simple-cell receptive field properties by learning a sparse code for natural images," *Nature*, pp. 607–609, 1996.

[314] I. Daubechies, *Ten Lectures on Wavelets*. Philadelphia: PA: SIAM, 1992.

[315] G. Strang and T. Nguyen, *Wavelets and Filter Banks*. Boston: Wellesley Cambridge Press, 1996.

[316] M. Do and M. Vetterli, "The finite ridgelet transform for image representation," *IEEE Transactions on Image Processing*, vol. 12, no. 1, pp. 16–28, 2003.

[317] P. J.Burt and E. H. Adelson, "The laplacian pyramid as a compact image code," *IEEE Transactions on Communications*, vol. 31, pp. 532–540, 1983.

[318] R. H. Bamberger and M. J. T. Smith, "A filter bank for the directional decomposition of images: theory and design," *IEEE Transactions on Signal Processing*, vol. 40, no. 4, pp. 882–893, 1992.

[319] D. Cunha, J. Zhou, and M. Do, "The nonsubsampled contourlet transform: theory, design, and applications," *IEEE Transactions on Image Processing*, vol. 15, no. 10, pp. 3089–3101, 2006.

[320] R. Eckhorn, H. J. Reitboec, M. Arndt, and P. Dicke, "Feature linking via synchronization among distributed assemblies: Simulations of results from cat visual cortex," *Neural Computation*, vol. 2, no. 3, pp. 293–307, 1990.

[321] I. A. Rybak, N. A. Shevtsova, L. N. Podladchikova, and A. V. Golovan, "A visual cortex domain model and its use for visual information processing," *Neural Networks*, vol. 4, pp. 3–13, 1991.

[322] J. L. Johnson and M. L. Padgett, "PCNN models and applications," *IEEE Transactions on Neural Network*, vol. 10, no. 3, pp. 480–498, May 1999.

[323] H. S. Ranganath, G. Kuntimad, and J. L. Johnson, "Pulse coupled neural networks for image processing," in *Proceedings of Southeast Conference on Visualize the Future*, 1995, pp. 37–43.

[324] T. Lindblad and J. M. Kinser, *Image Processing Using Pulse Coupled Neural Networks*, 2nd ed. Berlin: Springer, 2005.

[325] Z. Wang, Y. Ma, F. Cheng, and L. Yang, "Review of pulse-coupled neural networks," *Image and Vision Computing*, vol. 28, no. 1, pp. 5–13, 2010.

[326] M. M. Subashini and S. K. Sahoo, "Pulse coupled neural networks and its applications," *Expert Systems with Applications*, vol. 41, pp. 3965–3974, 2014.

[327] J. L. Johnson and D. Ritter, "Observation of periodic waves in a pulse-coupled neural network," *Optical Letter*, vol. 18, no. 15, pp. 1253–1258, 1993.

[328] V. Vapnik, *The nature of statistical learning theory.* New-York: Springer-Verlag, 1995.

[329] J. A. K. Suykens and J. Vandewalle, "Least squares support vector machine classifiers," *Neural Processing Letters*, vol. 9, no. 3, pp. 293–300, 1999.

[330] T. V. Gestel, J. Suykens, B. Baesens, S. Viaene, J. Vanthienen, G. Dedene, B. D. Moor, and J. Vandewalle, "Benchmarking least squares support vector machine classifiers," *Machine Learning*, vol. 54, no. 1, pp. 5–32, 2004.

[331] Y. Rubner, C. Tomasi, and L. J. Guibas, "The Earth Mover's distance as a metric for image retrieval," *International Journal of Computer Vision*, vol. 40, no. 2, pp. 99–121, 2000.

[332] Z. Wang, A. C. Bovik, H. R. Sheikh, and E. P. Simoncelli, "Image quality assessment: from error visibility to structural similarity," *IEEE Transactions on Image Processing*, vol. 13, no. 4, pp. 600–612, 2004.

[333] S. A. Fernandez, R. S. J. Estepar, C. A.-Lopez, and C.-F. Westin, "Image quality assessment based on local variance," in *Proceedings of 28th IEEE International Conference on Engineering in Medicine & Biology*, 2006, pp. 4815–4818.

[334] G. H. Qu, D. L. Zhang, and P. F. Yan, "Information measure for performance of image fusion," *Electronics Letters*, vol. 38, no. 7, pp. 313–315, 2002.

[335] C. S. Xydeas and V. Petrovic, "Objective image fusion performance measure," *Electronics Letters*, vol. 36, no. 4, pp. 308–309, 2000.

[336] A. Watson, "DCT quantization matrices visually optimized for individual images," in *Proceedings of SPIE Human Vision, Visual Processing and Digital Display IV*, vol. 1913, 1993, pp. 202–216.

[337] A. Mayache, T. Eude, and G. Cherifi, "A comparison of image quality models and metrics based on human visual sensitivity," in *Proceedings of IEEE International Conference on Image Processing*, vol. 3, 1998, pp. 409–413.

[338] S. Das and M. K. Kundu, "MRI denoising using visual system response model simulating PCNN," in *Proceedings of 2nd International Conference on Perception and Machine Intelligence*, 2015,(to appear).

[339] S. Das and M. K. Kundu, "PCNN based non-local means for MRI denoising," *Submitted to Biomedical Signal Processing and Control*, 2014.

[340] S. Das and M. K. Kundu, "NSCT-based multimodal medical image fusion using pulse-coupled neural network and modified spatial frequency," *Medical and Biological Engineering and Computing*, vol. 50, no. 10, pp. 1105–1114, 2012.

[341] S. Das and M. K. Kundu, "A neuro-fuzzy approach for medical image fusion," *IEEE Transactions on Biomedical Imaging*, vol. 60, no. 12, pp. 3347–3353, 2013.

[342] S. Das, M. Chowdhury, and M. K. Kundu, "Brain MR image classification using multi-scale geometric analysis of ripplet," *Progress In Electromagnetics Research*, vol. 137, pp. 1–17, 2013.

[343] S. Das and M. K. Kundu, "Robust classification of MR brain images based on multiscale geometric analysis," in *Proceedings of 5th International Conference on Pattern Recognition and Machine Intelligence*, vol. LNCS 8251, 2013, pp. 482–488.

[344] M. Chowdhury, S. Das, and M. K. Kundu, "Effective classification of radiographic medical images using LS-SVM and NSCT based retrieval system," in *Proceedings of 5th International Conference on Computers and Devices for Communication*, 2012, pp. 1–4.

[345] S. Das and M. K. Kundu, "Effective management of medical information through ROI-lossless fragile image watermarking technique," *Computer Methods and Programs in Biomedicine*, vol. 111, no. 3, pp. 662–675, 2013.

[346] S. Das and M. K. Kundu, "Effective management of medical information through a novel blind watermarking technique," *Journal of Medical Systems*, vol. 36, no. 5, pp. 3339–3351, 2012.

[347] H. Zhang, Z. Zhang, D. Lin, and Y. Ma, "A novel image de-noising algorithm combined PCNN with morphology," in *Proceedings of IEEE International Conference on Neural Networks and Signal Processing*, 2007, pp. 208–211.

[348] Y. Ma, D. Lin, B. Zhang, Q. Liu, and J. Gu, "A new algorithm for noise reducing of image based on PCNN time matrix," *Journal of Electronics & Information Technology*, vol. 30, no. 8, pp. 1869–1873, 2008.

[349] Y. Ma, S. Fei, and L. Lian, "Gaussian noise filter based on PCNN," in *Proceedings of IEEE International Conference on Neural Networks and Signal Processing*, vol. 1, 2003, pp. 149–151.

[350] M. M. I. Chacon and A. S. Zimmerman, "Image processing using the PCNN time matrix as a selective filter," in *Proceedings of IEEE International Conference on Image Processing*, vol. 1, 2003, pp. 877–880.

[351] J. Zhang, J. Dong, and M. Shi, "An adaptive method for image filtering with pulse-coupled neural networks," in *Proceedings of IEEE International Conference on Image Processing*, vol. 2, 2005, pp. 133–136.

[352] L. Ji and Z. Yi, "A mixed noise image filtering method using weighted-linking pcnns," *Neurocomputing*, vol. 71, pp. 2986–3000, 2008.

[353] Y. Ma, D. Lin, B. Zhang, Q. Liu, and J. Gu, "A novel algorithm of image gaussian noise filtering based on PCNN time matrix," in *Proceedings of IEEE International Conference on Signal Processing and Communications*, 2007, pp. 1499–1502.

[354] D. L. Collins, A. P. Zijdenbos, V. Kolloki, J. G. Sled, N. J. Kabani, C. J. Holmes, and A. C. Evans, "Design and construction of a realistic digital brain phantom," *IEEE Transcations on Medical Imaging*, vol. 17, no. 3, pp. 463–468, 1998.

[355] "http://www.bic.mni.mcgill.ca/brainweb/."

[356] M. Li, W. Cai, and Z. Tan, "A region-based multi-sensor image fusion scheme using pulse-coupled neural network," *Pattern Recognition Letters*, vol. 27, no. 16, pp. 1948–1956, 2006.

[357] S. Yang, M. Wang, Y. Lu, W. Qi, and L. Jiao, "Fusion of multiparametric SAR images based on SW-nonsubsampled contourlet and PCNN," *Signal Processing*, vol. 89, no. 12, pp. 2596–2608, 2009.

[358] Z. Wang, Y. Ma, and J. Gu, "Multi-focus image fusion using PCNN," *Pattern Recognition*, vol. 43, no. 6, pp. 2003–2016, June 2010.

[359] M. M. Deepika and V. Vaithyanathan, "An efficient method to improve the spatial property of medical images," *Journal of Theoretical and Applied Information Technology*, vol. 35, no. 2, pp. 141–148, 2012.

[360] H. Deng and Y. Ma, "Image fusion based on steerable pyramid and PCNN," in *Proceedings of 2nd International Conference on Applications of Digital Information and Web Technologies*, 2009, pp. 569 –573.

[361] Q. X.-Bo, Y. J.-Wen, X. H.-Zhi, and Z. Z.-Qian, "Image fusion algorithm based on spatial frequency-motivated pulse coupled neural networks in nonsubsampled contourlet transform domain," *Acta Automatica Sinica*, vol. 34, no. 12, pp. 1508–1514, 2008.

[362] G. Xin, B. Zou, J. Li, and Y. Liang, "Multi-focus image fusion based on the nonsubsampled contourlet transform and dual-layer PCNN model," *Information Technology Journal*, vol. 10, no. 6, pp. 1138–1149, 2011.

[363] A. Eskicioglu and P. S. Fisher, "Image quality measures and their performance," *IEEE Transactions on Communications*, vol. 43, no. 12, pp. 2959–2965, Dec 1995.

[364] Y. Zheng, E. A. Essock, B. C. Hansen, and A. M. Haun, "A new metric based on extended spatial frequency and its application to DWT based fusion algorithms," *Information Fusion*, vol. 8, no. 2, pp. 177–192, 2007.

[365] J. M. Kinser, "Foveation by a pulse-coupled neural network," *IEEE Transactions on Neural Network*, vol. 10, no. 3, pp. 621–626, 1999.

[366] M. K. Kundu and S. K. Pal, "A note on grey level-intensity transformaion: effect on HVS thresholding," *Pattern Recognition Letters*, vol. 8, pp. 257–269, 1988.

[367] M. K. Kundu and S. K. Pal, "Automatic selection of object enhancement operator with quantitative justification based on fuzzy set theoretic measure," *Pattern Recognition Letters*, vol. 11, pp. 811–829, 1990.

[368] J. M. Kinser, "Pulse coupled image fusion," *Optical Engineering*, vol. 36, no. 3, pp. 737–742, 1997.

[369] J. A. Karvonen, "Baltic sea ice SAR segmentation and classification using modified pulse-coupled neural networks," *IEEE Transactions on Geoscience and Remote Sensing*, vol. 42, no. 7, pp. 1566–1574, 2004.

[370] G. Buchsbaum, "An analytical derivation of visual nonlinearity," *IEEE Transactions on Biomedical Engineering*, vol. 27, no. 5, pp. 237–242, 1980.

[371] M. K. Kundu and S. K. Pal, "Thresholding for edge detection using human psycho visual phenomena," *Pattern Recognition Letters*, vol. 4, pp. 433–441, 1986.

[372] H. D. Cheng and H. Xu, "A novel fuzzy logic approach to contrast enhancement," *Pattern Recognition*, vol. 33, no. 5, pp. 809–819, 2000.

[373] T. Kadir and M. Brady, "Saliency, scale and image description," *International Journal of Computer Vision*, vol. 45, no. 2, pp. 83–105, 2001.

[374] M. Khosrowpour, *Encyclopedia of Information Science and Technology*, 3rd ed. USA: IGI Global, 2014.

[375] I. Selesnick, "The slantlet transform," *IEEE Transactions on Signal Processing*, vol. 47, no. 5, pp. 1304–1313, 1999.

[376] I. T. Jolliffe, "Principal component analysis," *Springer*, 2002.

[377] P. Groskerry, "The throry and practice of clinical decision-making," *Canadian Journal of Anesthesia*, vol. 52, pp. 1–8, 2005.

[378] R. L. Siegle, E. M. Baram, S. R. Reuter, E. A. Clarke, and J. L. Lancaster, "Rates of disagreement in imaging interpretation in a group of community hospitals," *Academic Radiology*, vol. 5, pp. 148–154, 1998.

[379] J. K. Cramer and W. Hersh, "Effectiveness of global features for automatic medical image classification and retrieval – the experiences of OHSU at imageCLEFmed," *Pattern Recognition Letters*, vol. 29, pp. 2032–2038, 2008.

[380] F. P. 180-4, "Secure hash standard (SHS)," National Institute of Standards and Technology, Gaithersburg, USA, Technical Paper, 2012. [Online]. Available: http://csrc.nist.gov/publications/fips/fips180-4/fips-180-4.pdf

[381] F. P. 197, "Announcing the ADVANCED ENCRYPTION STANDARD (AES)," National Institute of Standards and Technology, USA, Technical Paper, 2001. [Online]. Available: http://csrc.nist.gov/publications/fips/fips197/fips-197.pdf

[382] I. H. Witten, R. M. Neal, and J. G. Cleary, "Arithmetic coding for data compression," *Communications of the ACM*, vol. 30, no. 6, pp. 520–540, 1987.

[383] W. Zhou, A. Bovik, H. Sheikh, and E. Simoncelli, "Image quality assessment: from error visibility to structural similarity," *IEEE Transactions on Image Processing*, vol. 13, no. 4, pp. 600–612, 2004.

[384] A. Hocquenghem, "Codes correcteurs d'erreurs," *Chiffres*, vol. 2, pp. 147–156, 1959.

[385] R. C. Bose and D. K. Ray-Chaudhuri, "On a class of error correcting binary group codes," *Information and Control*, vol. 3, no. 1, pp. 68–79, 1960.

[386] S. Pereira, S. Voloshynovskiy, M. Madueno, S. M.-Maillet, and T. Pun, "Second generation benchmarking and application oriented evaluation," in *Proceedings of 4th International Workshop on Information Hiding*, 2001, pp. 340–353.

Author's Publications

- **Journals:**

1. **Sudeb Das**, Manish Chowdhury and Malay Kumar Kundu, "Medical Image Fusion based on Ripplet Transform Type-I", *Progress In Electromagnetics Research B*, Vol. 30, pp. 355–370, 2011.
2. **Sudeb Das** and Malay Kumar Kundu, "Effective Management of Medical Information through A Novel Blind Watermarking Technique", *Journal of Medical Systems*, Springer, Vol. 36, No. 5, 3339–3351, 2012.
3. Manish Chowdhury, **Sudeb Das** and Malay Kumar Kundu,"Novel CBIR System Based on Ripplet Transform Using Interactive Neuro-Fuzzy Technique", *Electronic Letters on Computer Vision and Image Analysis*, CVC Press, Vol. 11, No. 1, 1–13, 2012.
4. **Sudeb Das** and Malay Kumar Kundu, "NSCT-based Multimodal Medical Image Fusion using Pulse-coupled Neural Network and Modified Spatial Frequency", *Medical and Biological Engineering and Computing*, Springer, Vol. 50, No. 10, 1105–1114, 2012.
5. **Sudeb Das**, Manish Chowdhury and Malay Kumar Kundu, "Brain MR Image Classification using Multi-scale Geometric Analysis of Ripplet", *Progress in Electromagnetics Research*, Vol. 137, 1–17, 2013.
6. **Sudeb Das** and Malay Kumar Kundu, "Effective Management of Medical Information through ROI-Lossless Fragile Image Watermarking Technique", *Computer Methods and Programs in Biomedicine*, Elsevier, Vol. 111, No. 3, 662–675, 2013.
7. **Sudeb Das** and Malay Kumar Kundu, "A Neuro-Fuzzy Approach for Medical Image Fusion", *IEEE Transactions on Biomedical Engineering*, IEEE, Vol. 60, No. 12, 3347–3353, 2013.
8. **Sudeb Das** and Malay Kumar Kundu,"PCNN based Non-Local Means for MRI Denoising", *Biomedical Signal Processing and Control*, Elsevier (under review).

- **Conferences:**

1. Malay Kumar Kundu and **Sudeb Das**, "Lossless ROI Medical Image Watermarking Technique with Enhanced Security and High Payload Embedding", *in Proceedings of 20th IEEE International Conference on Pattern Recognition (ICPR–2010)*, IEEE, pp. 1457–1460, Istanbul, Turkey, August 2010.
2. **Sudeb Das** and Malay Kumar Kundu, "Hybrid Contourlet-DCT Based Robust Image Watermarking Technique Applied to Medical Data Management", *in Proceedings of 4th International Conference on Pattern recognition and Machine Intelligence (PReMI–2011)*, Springer LNCS 6744, pp. 286–291, Higher School of Economics, National Research University , Moscow, Russia, June 2011.
3. **Sudeb Das** and Malay Kumar Kundu, "Fusion of Multimodality Medical Images Using Combined Activity Level Measurement and Contourlet transform", *in Proceedings of 1st IEEE International Conference on Image Information Processing (ICIIP–2011)*, IEEE, pp. 1–6, JAYPEE University of Information Technology, Shimla, India, November 2011.
4. **Sudeb Das** and Malay Kumar Kundu, "Ripplet Based Multimodality Medical Image Fusion Using Pulse-Coupled Neural Network and Modified Spatial Frequency", *in Proceedings of IEEE International Conference on Recent Trends in Information Systems (ReTIS–2011)*, IEEE, pp. 229–234, Jadavpur University ,Kolkata, India, December 2011.
5. Manish Chowdhury, **Sudeb Das** and Malay Kumar Kundu, "Interactive Content based Image Retrieval using Ripplet Transform and Fuzzy Relevance Feedback", *in Proceedings of 1st International Conference on Perception and Machine Intelligence (PerMIn–2012)*, Springer LNCS 7143, pp. 243–251, CDAC, Kolkata, India, January 2012.
6. Manish Chowdhury, **Sudeb Das** and Malay Kumar Kundu, "Effective Classification of Radiographic Medical Images Using LS-SVM and NSCT based Retrieval System", *in Proceedings of 5th IEEE International Conference on computers and devices for communication (CODEC–*

2012), IEEE, pp. 1–4, Institute of Radio Physics and Electronics, University of Calcutta, Kolkata, India, December 2012.

7. Manish Chowdhury, **Sudeb Das** and Malay Kumar Kundu, "Compact Image Signature Generation: An Application in Image Retrieval", *in Proceedings of 5th IEEE International Conference on Computer Science and Information technology (CSIT–2013)*, IEEE, pp. 1–7, Applied Science University, Amman, Jordan, March 2013.

8. Manish Chowdhury, **Sudeb Das** and Malay Kumar Kundu, "A ripplet transform based statistical framework for natural color image retrieval", *in Proceedings of 17th International Conference on Image Analysis and Processing (ICIAP–2013)*, Springer LNCS 8156, pp. 492–502, Naples, Italy, September 2013.

9. **Sudeb Das** and Malay Kumar Kundu, "Robust classification of MR brain images based on multiscale geometric analysis", *in Proceedings of 5th International Conference on Pattern Recognition and Machine Intelligence (PReMI–2013)*, Springer LNCS 8251, pp. 482–488, Indian Statistical Institute, Kolkate, India, December 2013.

10. **Sudeb Das** and Malay Kumar Kundu, "MRI Denoising using Visual System Response Model Simulating PCNN", *in Proceedings of 2nd International Conference on Perception and Machine Intelligence (PerMIn–2015)*, ACM, CDAC, Kolkata, India, February 2015 (to appear).